

Lawrence Berkeley National Laboratory

Recent Work

Title

High Resolution X-Ray Fluorescence Spectroscopy - A New Technique for Site- and Spin-Selectivity

Permalink

<https://escholarship.org/uc/item/5sc4n7nz>

Author

Wang, Xin

Publication Date

1996-12-01

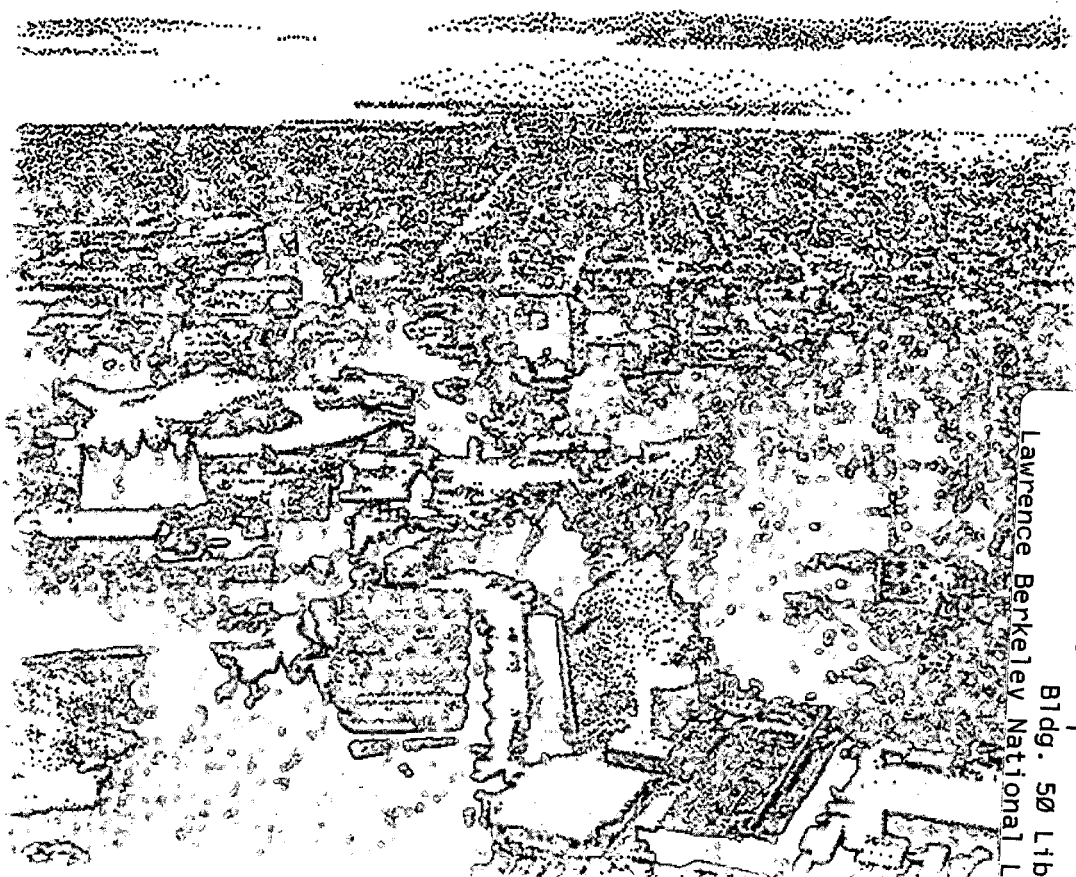


ERNEST ORLANDO LAWRENCE BERKELEY NATIONAL LABORATORY

High Resolution X-Ray Fluorescence Spectroscopy—A New Technique for Site- and Spin-Selectivity

Xin Wang
Energy and Environment Division

December 1996
Ph.D. Thesis



Lawrence Berkeley National Laboratory
Bldg. 50 Library - Ref.

REFERENCE COPY
Does Not
Circulate

Copy 1

LBL-39801

DISCLAIMER

This document was prepared as an account of work sponsored by the United States Government. While this document is believed to contain correct information, neither the United States Government nor any agency thereof, nor the Regents of the University of California, nor any of their employees, makes any warranty, express or implied, or assumes any legal responsibility for the accuracy, completeness, or usefulness of any information, apparatus, product, or process disclosed, or represents that its use would not infringe privately owned rights. Reference herein to any specific commercial product, process, or service by its trade name, trademark, manufacturer, or otherwise, does not necessarily constitute or imply its endorsement, recommendation, or favoring by the United States Government or any agency thereof, or the Regents of the University of California. The views and opinions of authors expressed herein do not necessarily state or reflect those of the United States Government or any agency thereof or the Regents of the University of California.

LBL-39801
UC-404

High Resolution X-Ray Fluorescence Spectroscopy
- A New Technique for Site- and Spin-Selectivity

by

Xin Wang
Ph.D. Thesis

Department of Applied Science
University of California
Davis, California 95616

and

Energy & Environment Division
Ernest Orlando Lawrence Berkeley National Laboratory
University of California
Berkeley, California 94720

December 1996

This work was funded by the Director, Office of Energy Research, Office of Health and Environmental Research, of the U.S. Department of Energy under Contract No. DE-AC03-76SF00098, by the National Institutes of Health under Contract No. GM-44380 and GM-48145.

To my parents and my sisters
who live far but feel close to my heart
and
james
who is always there to support

Acknowledgments

During the last five years of working towards my Ph.D., I have benefited from the help of many people, and I would like to thank them all.

In the first place I thank professor Steve Cramer, who gave me inspiration and stimulation on x-ray research, as well as freedom for trying out my ideas. I also thank the collaborative opportunity he provided, it became possible to learn so much from many people. The excitement and frustration of synchrotron research have certainly been well experienced all the way through my thesis.

Most of the experiments presented in this thesis were performed at the Stanford Synchrotron Radiation Laboratory (SSRL) and National Synchrotron Light Source (NSLS). I thank the help of the support staff at these facilities, especially the x-ray group at SSRL.

I would like to thank all the collaborators who supplied both inorganic model compounds and proteins. I thank Larry Que from University of Minnesota, Mike Adams and Amy Huang from University of George, Allen Balsh from University of California at Davis and Pradip Mascharak from University of California at Santa Cruz. Thanks to them and their students especially to Yan Zang, who made an effort to synthesize an 'ideal' sample for my spin-polarized EXAFS experiment.

A special thanks to Frank de Groot who taught me the crystal field multiplet calculation. I am grateful to have the opportunity to learn from him, and to work with him, both in person and over emails. Many exchange of ideas has made him a good friend. Thanks to him, learning is still a pure joy.

I thank all the people from the Cramer group. I thank Melissa Grush for the collaboration on experiments and preparing manuscripts; Corie Ralston for her attention to details, and her help for proof reading some of my papers. I thank Jason Christiansen for his help on the EXAFS simulations, Brenda Weiss for the enjoyable synchrotron experience. I want to thank technician Andy Froeschner, who built parts for the spectrometer, and helped on assembling them during beamtimes. A special thanks to George Meigs for his help to organize the experiments and to proof read my thesis, and to Mark Legros for 'pushing' me to make my abstract more understandable.

Also I like to thank the postdocs I worked with and learned from: Jie Chen, Gang Peng, Jan van Elp and Simon George. They are the first 'bunch' of the Cramer group, and I started to learn about x-ray research by watching over their shoulders. I have benefited from their help, especially from the collaboration with Gang. Together with Hongxin Wang, Clay Randall, Craig Bryant and Jue Wang, I have enjoyed my student days in the Cramer group (including group meetings at Strawberry Ranch).

I have learned much from the discussions with Alexei Ankudinov and John Rehr. I also thank them for their help on the SPEXAFS and FEFX simulations.

Bo Yu and Graham Smith not only developed the two dimensional detector, they have also served as technical consultants whenever I have questions.

I had the pleasure to work with Oliver Mullins at Schlumberger-Doll Research. I had enjoyed very much to learn about industry research as well as crude oils during my four months stay in Connecticut. There was also a 'unique' canoeing experience I would not forget.

A special thanks to Professor Akio Kotani for insightful discussions on core spectroscopy. I have also enjoyed our exploration of the southern French country.

Last but not least, I thank helpful discussions with Marie-Anne Arrio and Christian Brouder. I also thank Marie-Anne for her hospitality during my visit to Paris.

This work was funded by the Director, Office of Energy Research, Office of Health and Environmental Research, of the U.S. Department of Energy under Contract No. DE-AC03-76SF00098, by the National Institutes of Health under Contract No. GM-44380 and GM-48145.

Abstract

X-ray spectroscopy has long been used to elucidate electronic and structural information of molecules. One of the weaknesses of x-ray absorption is its sensitivity to all of the atoms of a particular element in a sample. Through out this thesis, a new technique for enhancing the site- and spin-selectivity of the x-ray absorption has been developed.

By high resolution fluorescence detection, the chemical sensitivity of K emission spectra can be used to identify oxidation and spin states; it can also be used to facilitate site-selective X-ray Absorption Near Edge Structure (XANES) and site-selective Extended X-ray Absorption Fine Structure (EXAFS). The spin polarization in K fluorescence could be used to generate spin selective XANES or spin-polarized EXAFS, which provides a new measure of the spin density, or the nature of magnetic neighboring atoms. Finally, dramatic line-sharpening effects by the combination of absorption and emission processes allow observation of structure that is normally unobservable. All these unique characters can enormously simplify a complex x-ray spectrum.

Applications of this novel technique have generated information from various transition-metal model compounds to metalloproteins. The absorption and emission spectra by high resolution fluorescence detection are interdependent. The ligand field multiplet model has been used for the analysis of $K\alpha$ and $K\beta$ emission spectra.

First demonstration on different chemical states of Fe compounds has shown the applicability of site selectivity and spin polarization. Different interatomic distances of the same element in different chemical forms have been detected using site-selective EXAFS.

To make high resolution experiments on metalloproteins possible, a new spectrometer with higher efficiency was developed. Some first metalloprotein results have shown that the strength of both site- and spin-selectivity could complement the structural information from other spectroscopies.

The first spin polarized EXAFS (SPEAXFS) of an antiferromagnetically coupled system using $K\beta$ detection is reported. Utilizing the internally referenced spin-up and spin-down transitions, the SPEAXFS effects are 2 order of magnitude larger than that of the method previously used, and it is suited for both antiferromagnetic systems as well as ferromagnetic systems.

Table of Contents

Chapter 1. Introduction	1
Chapter 2. Theory of X-ray Absorption and Emission Spectra	6
2.1 X-ray Spectroscopy	6
2.2 X-ray Inelastic Scattering	10
2.3 X-ray Emission	16
Chapter 3. Spin-Polarized and Site-Selective X-ray Absorption of Fe Compounds	54
3.1 Spin-Selective X-ray Spectroscopy	55
3.2 Site-Selective and Spin-Polarized X-ray Absorption of Fe Porphyrins	64
Chapter 4. Site-Selective X-ray Absorption Spectroscopy of Prussian Blue	76
4.1 Introduction	76
4.2 Experimental	79
4.3 Results and Discussions	81
4.3.1. $K\beta$ Emission Spectra	81
4.3.2 Site-Selectivity and Spin-Polarization	83
4.3.3 Site-Selective XANES	87
4.3.4 Site-Selective EXAFS	89
4.4 Conclusions	93
Chapter 5. High Resolution X-ray Spectroscopy of Metalloproteins	97
5.1 Instrumentation and Initial Results	98
5.2 Experimental Results of Rubredoxin	121
5.2.1 $K\beta$ Emission Spectra	121
5.2.2 Spin-Polarized Excitation Spectra	126
5.2.3 Line-Sharpening Effect	130
5.2.4 Photoreduction	133
Chapter 6. Spin Polarized EXAFS using $K\beta$ Detection	135
Appendix I. XMCD Spectra and Distortions of Fe^{2+} $L_{2,3}$ Edges	149
Appendix II. Manual for the Two-Dimensional Position Sensitive Detector	157

Chapter 1. Introduction

X-ray absorption and emission spectroscopies have long been used to elucidate electronic and structural information [1.1]. One of the strengths and weaknesses of x-ray absorption spectroscopy is that it is sensitive to all of the atoms of a particular element. In the K absorption edge, the features due to a particular site in an absorption spectrum are often unsolved, because of the natural line width of the 1s core hole, which could be 1~10 eV for transition metals. Techniques such as isotopic labeling are useful for other spectroscopic methods such as EPR and NMR to assign features to discrete species, but for x-ray absorption, such effects are generally too small to be useful.

This thesis will demonstrate the power of a new technique developed for enhancing the resolution and selectivity of x-ray absorption - High Resolution X-Ray Fluorescence Spectroscopy. With this new technique, the chemical sensitivity of K emission spectra can be used to identify oxidation and spin states; it can also be used to facilitate site-selective X-ray Absorption Near Edge Structure (XANES) and site-selective EXAFS. The extra spin selectivity in K fluorescence detection can be used to generate spin selective XANES or spin-polarized EXAFS, which provides a new measure of the spin dependent density of states (DOS) above the Fermi level, or the nature of the magnetic neighboring atoms. Finally, dramatic line-sharpening effects by the combination of absorption and emission processes allow observation of structure that is normally unobservable. Applications of all aspects of this novel technique have generated information previously unobtainable from samples of various inorganic model compounds and metalloproteins.

Transition metals are important in both redox reactions [1.2] and magnetic interactions [1.3]. Examples where Fe changes oxidation state or spin states in redox cycles are the reduction of oxygen to water by cytochrome oxidase [1.4], the conversion between dinitrogen and ammonia by nitrogenase [1.5], and the conversion between dihydrogen and protons by Fe-Ni hydrogenase [1.6]. The proposed models for the active sites of the latter two enzymes are shown in Figure 1.1. Although the current experimental sensitivity is not great enough to apply the high resolution fluorescence technique to those systems, much of the ground work on model compounds and proteins presented in this thesis has shown a promising future.

The theoretical aspect of x-ray K edge absorption and K emission is discussed in Chapter 2. The absorption (excitation) and emission spectra by high resolution fluorescence detection are interdependent. Fortunately, the lack of interference effects between the intermediate state (1s hole core) and the final state (np core hole) makes it possible to analyze the absorption and

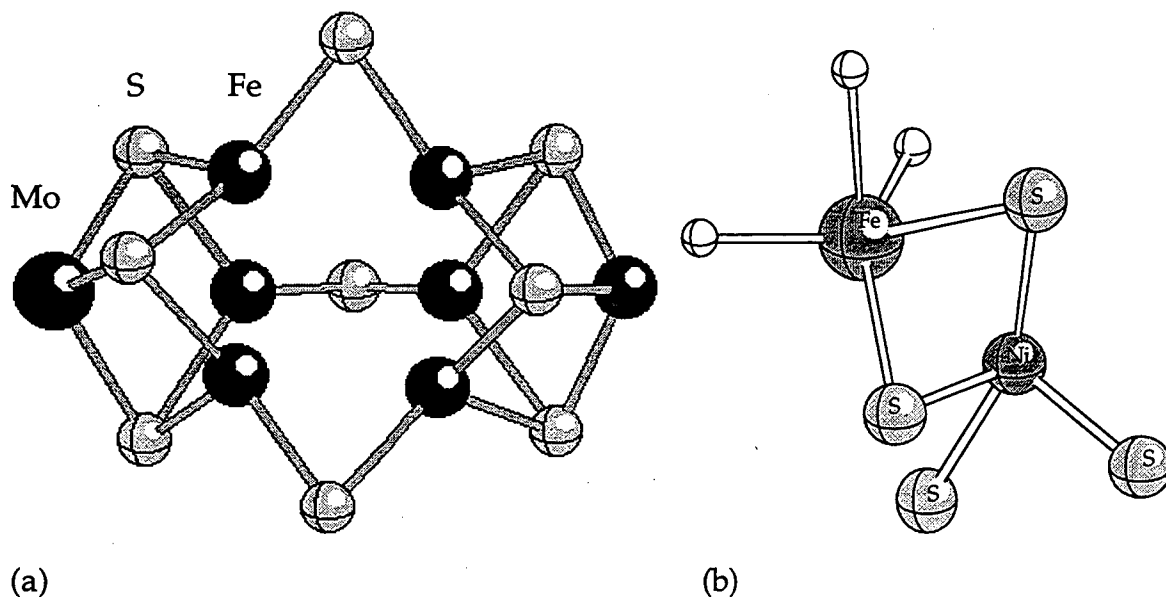


Figure 1.1 (a) The current model for the M center of nitrogenase; (b) Proposed structure for the hydrogenase Fe-Ni site.

emission spectra discretely. The ligand field multiplet model has been used for $K\alpha$ and $K\beta$ emission spectra analysis through out the thesis.

First applications of the spin and site selectivity by high resolution spectroscopy on different Fe model compounds are reported in Chapters 3 and 4. The chemical sensitivity and spin-polarization of $K\beta$ emission have been demonstrated on different spin states of iron porphyrins, and the 0.1 Å difference in the Fe(II)-C and Fe(III)-N bond lengths has been detected using site-selective EXAFS on the mixed valence prussian blue.

High resolution experiments on metalloproteins are clearly starved for photons. The combination of the hottest synchrotron beamline in the country and the 'first generation' spectrometer still could not provide enough photon counts. To increase solid angle and the overall efficiency, we developed a 'second generation' spectrometer, with the capability of accommodating six collecting crystals. This development and some first high resolution metalloprotein results are presented in Chapter 5.

The first spin polarized EXAFS (SPEAXFS) of an antiferromagnetically coupled system using $K\beta$ detection is reported in Chapter 6. Photoelectron spin polarization effects have found some success previously by using circular polarized x-rays and a magnetic field [1.7], but the K edge MCD signals are weak ($\sim 10^{-4}$), and it is generally limited to ferromagnetic or paramagnetic systems. Utilizing the internally referenced spin-up and spin-down transitions in $K\beta$ emission spectrum, the SPEAXFS effects could be 2 order of magnitude larger, and it is suited for both antiferromagnetic systems as well as ferromagnetic systems. This new technique should have broad applications on magnetic materials and eventually biological clusters.

This thesis also contains two appendices. The first one is a paper on the correlation of symmetry distortion and the Magnetic Circular Dichroism

(MCD) spectra; the second is a manual for the two-dimensional position sensitive detector used to take x-ray image data.

References

- 1.1 *X-ray absorption fine structure*, edited by Hasnain, S.S., E. Horwood, New York, 1991; *X-ray Absorption Principles, Applications, Techniques of EXAFS, SEXAFS, and XANES*, edited by Konigsberger, D.C., Prins, R., Jone, Wiley and Sons, Inc., New York, 1988.
- 1.2 Lippard, S.J., and Berg, J.M., *Principles of Bioinorganic Chemistry*, University Science Books, Mill Valley, 1994.
- 1.3 Jiles, D., *Introduction to Magnetism and Magnetic Materials*, Chapman and Hall, New York, 1991.
- 1.4 Morgan, J.E., Li, P.M., Jang, D.J., El-Sayed, M.A., and Chan, S.I., *Biochemistry.*, **28**, 6975 (1989).
- 1.5 Orme-Johnson, W.H., *Annu. Rev. Biophy. Chem.*, **14**, 419 (1985).
- 1.6 Kumar, M., Day, R.O., Colpas, G.J., and Maroney, M.J., *J. Am. Chem. Soc.*, **111**, 5974 (1989).
- 1.7 Schütz, G., Wagner, W., Wilhelm, W., Kienle, P., Zeller, R., Frahm, R., and Materlik, G. *Phys. Rev. Lett.* **58**, 737 (1987).

Chapter 2. Theory of X-ray Absorption and Emission Spectra

2.1. X-ray Spectroscopy

The two most popular kinds of x-ray spectroscopy are x-ray absorption spectroscopy (XAS) and x-ray emission spectroscopy (XES). Both have been popular tools to determine geometric and electronic structures, which are also linked since one is the consequence of the another [2.1]. When the incoming x-ray energy is comparable to the binding energy of core electrons of an atom, absorption occurs. During the absorption process the electron is either ejected out of the atom with a certain kinetic energy or it makes a transition to the lowest available bound state. After absorption the atom with a core hole is in an excited state. Transitions to fill the core hole via different decay processes have very large possibilities. X-ray emission (fluorescence) occurs when higher level electron makes the transition to fill the core hole; Auger decay happens when the energy from the electronic transition to the core state is absorbed by an electron at higher level, which is then ejected with a characteristic energy.

The nomenclature of x-ray spectroscopy has not always been consistent [2.2]. For our purposes, the x-ray labels K, L, M correspond to states with the main quantum number 1, 2, 3 in their energy levels, and the angular quantum number l is denoted as s, p, d, respectively. For example, the absorption from a 1s core state is called K absorption, where the 1s electron makes the transition to higher level. The transition represented by $K \rightarrow L$ ($K\alpha$) and $K \rightarrow M$ ($K\beta$) correspond to the electron jumps $2p \rightarrow 1s$ and $3p \rightarrow 1s$, respectively, in the x-ray emission process.

Figure 2.1 shows an absorption spectrum obtained from Prussian Blue. The stepwise increase in the absorption intensity around 7120 eV is called the absorption edge. The dependence of the absorption edge energy on the atomic number is given through the Moseley relation

$$E \sim (Z - \sigma)^2 \quad (2.1)$$

where E is the photon energy, Z is the atomic number of the absorbing atom, and σ is a screening constant. Because of the Z dependence, x-ray

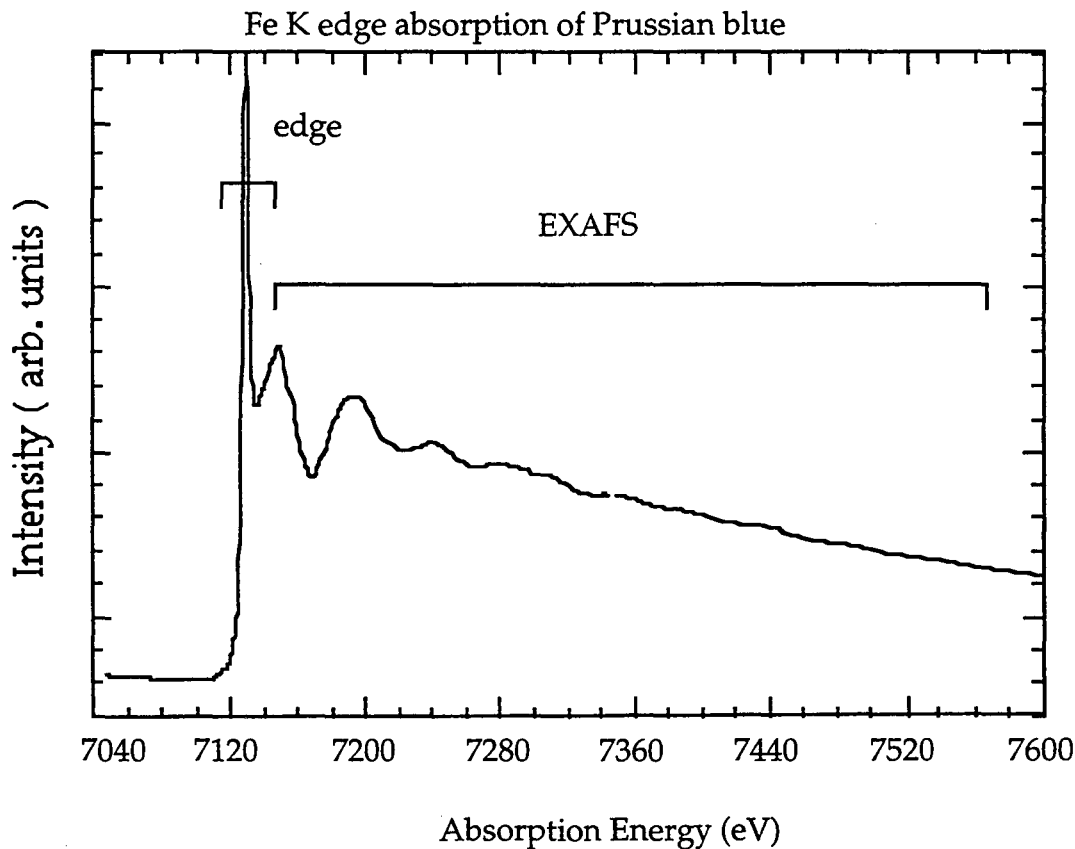


Figure 2.1. An x-ray absorption spectrum of Fe(III) compound. The K edge corresponds to an electron excited from the 1s core state. XANES (edge) and EXAFS are different regions in the spectrum (labeled in figure).

absorption is element specific. In K absorption edge, the constant σ arises due to the screening of the 1s electron by all other electrons. Since the value of σ changes for the atom in chemical binding, one expects the energy values of the absorption edges in different compounds to vary.

The absorption coefficient decreases towards higher energies above $\omega = E$, where E corresponds to the absorption edge. When recording x-ray absorption spectra with high resolution, more or less pronounced oscillations are observed in the immediate vicinity of the edge which extend to higher energy. This is called edge structure or X-ray Absorption Near Edge Structure (XANES). In the simplest model, the near edge fine structure is interpreted as the product of site and symmetry selected density of states and transition matrix element. Strong deviations, however, between the local density of states and the XANES features indicate clear influences of the core-hole potential. In other cases, a totally different approach, such as multiple scattering, is used to explain the fine structure [2.3]. Theoretical interpretation is complex in this region; fortunately, the qualitative interpretation is sometimes enough for certain information to be extracted.

When the ejected electron with enough kinetic energy scatters off with neighboring atoms, the interference of scattering wave and backscattered wave can be constructive and destructive; this is the source of Extended X-ray Absorption Fine Structure (EXAFS). The photoelectron of an isolated atom can be represented as an outgoing wave as shown in Figure 2.2. The transition-matrix element for the absorption process is determined by the overlap of the wave function for the core state and final state, which depends on the relative phase of the outgoing and backscattered waves [2.3]. The EXAFS is expressed as following formula:

$$\chi(k) = \sum_j N_j f_j(\pi, k) e^{-2k^2 \sigma_j^2} e^{-2R_j/\lambda_j} \frac{\sin[2kR_j + \Phi_{ij}(k)]}{kR_j^2} \quad (2.2)$$

where i is the absorbing atom, j is the backscattering atom, N_j is the number of backscatterers, $f_j(\pi, k)$ is the backscattering amplitude, R_j is the distance between the absorbing atom and the j th scatterer, σ_j^2 is the root mean square deviation of R_j , λ_j is the mean free path for inelastic scattering of the photoelectron, Φ_{ij} is the total phase shift for atoms i and j , and

$$k = [(8\pi^2 m_e / h^2)(E - E_0)]^{1/2} \quad (2.3)$$

where m_e is the electron mass, h is Planck's constant, E is excitation energy, and E_0 is the ionization potential of the absorbing element.

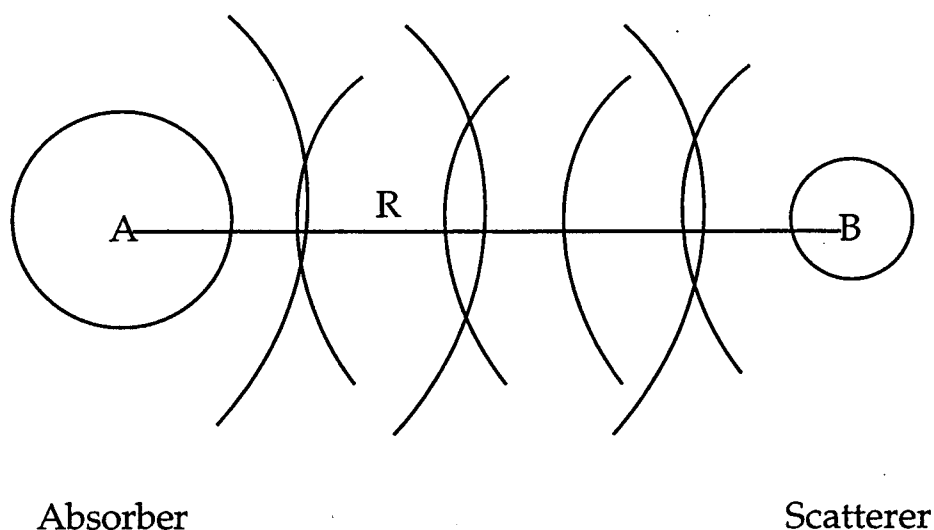


Figure 2.2. Schematic drawing of the radial portion of the photoelectron wave function in a typical EXAFS effect.

Equation 2.2 demonstrates the important influence of interatomic distances of the absorbing atom on the position of the extrema. The extended fine structure can be explained as a superposition of periodic contributions from separate coordination spheres around the absorbing atom. Detailed analysis of the spectra yields information on the absorber-scatterer distances, coordination, and type of neighboring atoms. Development of dedicated synchrotron radiation sources has strengthened the usage of EXAFS for determination of the local geometrical structure [2.4].

2.2. X-ray Inelastic Scattering

The combination of x-ray absorption and x-ray emission is sometimes called X-ray Inelastic Scattering (XIS) [2.5] or X-ray Raman Scattering (XRS) [2.6], the processes involved are shown in Figure 2.3. The XAS is a probe for the unoccupied states above the Fermi level, while XES probes the occupied levels. Unlike XAS and XES, XIS is a two-photon process. A theoretical basis for understanding this process can be found in the Kramers-Heisenberg equation, which is derived by treating the electromagnetic-radiation field as a time-dependent perturbation. By using a dipole approximation, and averaging over all angles, the cross section of K-edge XIS is given by:

$$I(\omega, \omega') = [L_{np}(\omega, \omega') \cdot G_E] \cdot \sum_{np} \left| \sum_{1s} \frac{\langle np | r_q | 1s \rangle \langle 1s | r_q | \epsilon \rangle}{\omega - E_{1s} - i\Gamma_{1s}} \right|^2 \quad (2.4)$$

where ω represents the excitation energy, ω' the emission energy, L_{np} the

Lorentzian broadening of the final np core state Γ_{1s} is the lifetime broadening of the $1s$ hole, G_E the experimental Gaussian broadening.

Equation (2.4) has been used in a simulation of K XIS by $2p$ electrons in Mn [2.7], by $2p$ and $3p$ electrons in Ar [2.8]. L edge XIS can also be simulated by a similar equation in CaF_2 [2.9]. According to equation (2.4), the cross section of XIS depends on ω and ω' . The denominator indicates that a resonance occurs if the incoming photon energy ω equals the $1s$ binding energy E_{1s} . There is an important consequence when the $1s$ core state is the intermediate state, such as the absence of interference effects, because there is only one core state per spin that resonates. In L XIS, however, the interference effects between the $2p$ intermediate state and the final state are not negligible, as

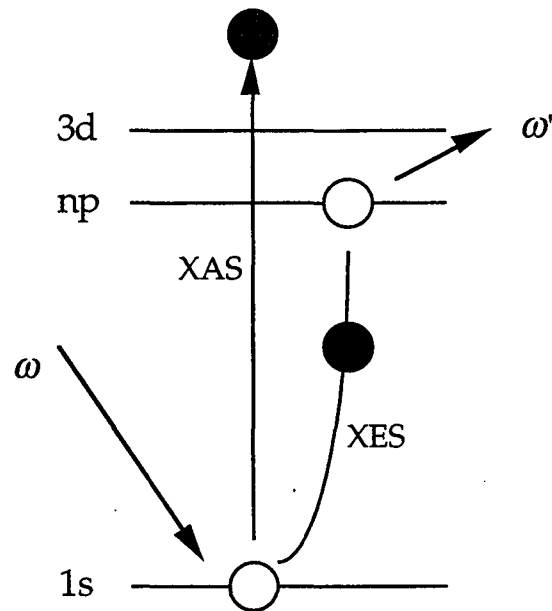


Figure 2.3. Illustration of processes involved in x-ray absorption (XAS), x-ray emission (XES), and x-ray inelastic scattering (XIS).

discussed by Carra, Fabrizio, and Thole [2.10]. When interference effects are not important as in K XIS, one can separately simulate the absorption and emission processes by treating the inelastic scattering as the absorption-followed-by-emission approach [2.11], except at the near edge region. Although the transition rate of XIS is not the product of the absorption and emission transition rates, as it was generally believed before [2.12], one can obtain the x-ray absorption cross section at a given emission energy, and the x-ray emission cross section at a particular excitation energy.

The emission spectral shape changes with the excitation energy. Resonant Raman scattering occurs when the incoming photon energy ω approaches but does not equal E_{1s} . The emission spectral width is determined by the final state core hole broadening Γ_{np} and the experimental width G_E , rather than Γ_{1s} , until $\omega = E_{1s}$ is reached. This is related to energy conservation which prohibits the high energy emission flank from being fully broadened by Γ_{1s} until $\omega > E_{1s}$. The halfwidth of the emission spectra appears to narrow as a function of ω before it becomes independent of the experimental broadening and equals to $\Gamma_{1s} + \Gamma_{np}$ if $G_E < \Gamma_{1s}$. This is not analogous to the situation in resonance fluorescence [2.13] but rather is a result of energy conservation. The experimental results of Ni²⁺ K α (2p \rightarrow 1s) line narrowing at the pre-edge excitation is demonstrated in Figure 2.4, as compared with normal excitation.

The excitation spectra are emission energy dependent. There are two major results from recent high resolution XIS experiments. First, in the absorption (excitation) spectra monitoring at certain emission energies, the lifetime broadening of the intermediate state disappears [2.14]. This line-sharpening effect has been observed in L edge dysprosium [2.14], K edge Mn and Fe [2.15]. This is due to the coherence of the absorption and

Figure 2.4. $K\alpha$ emission spectra are excitation energy dependent. The halfwidth-narrowing effect of Ni^{2+} $K\alpha$ emission is shown when comparing the spectrum at pre-edge excitation energy (dotted line) with normal emission (solid line) at excitation energy far above the edge.

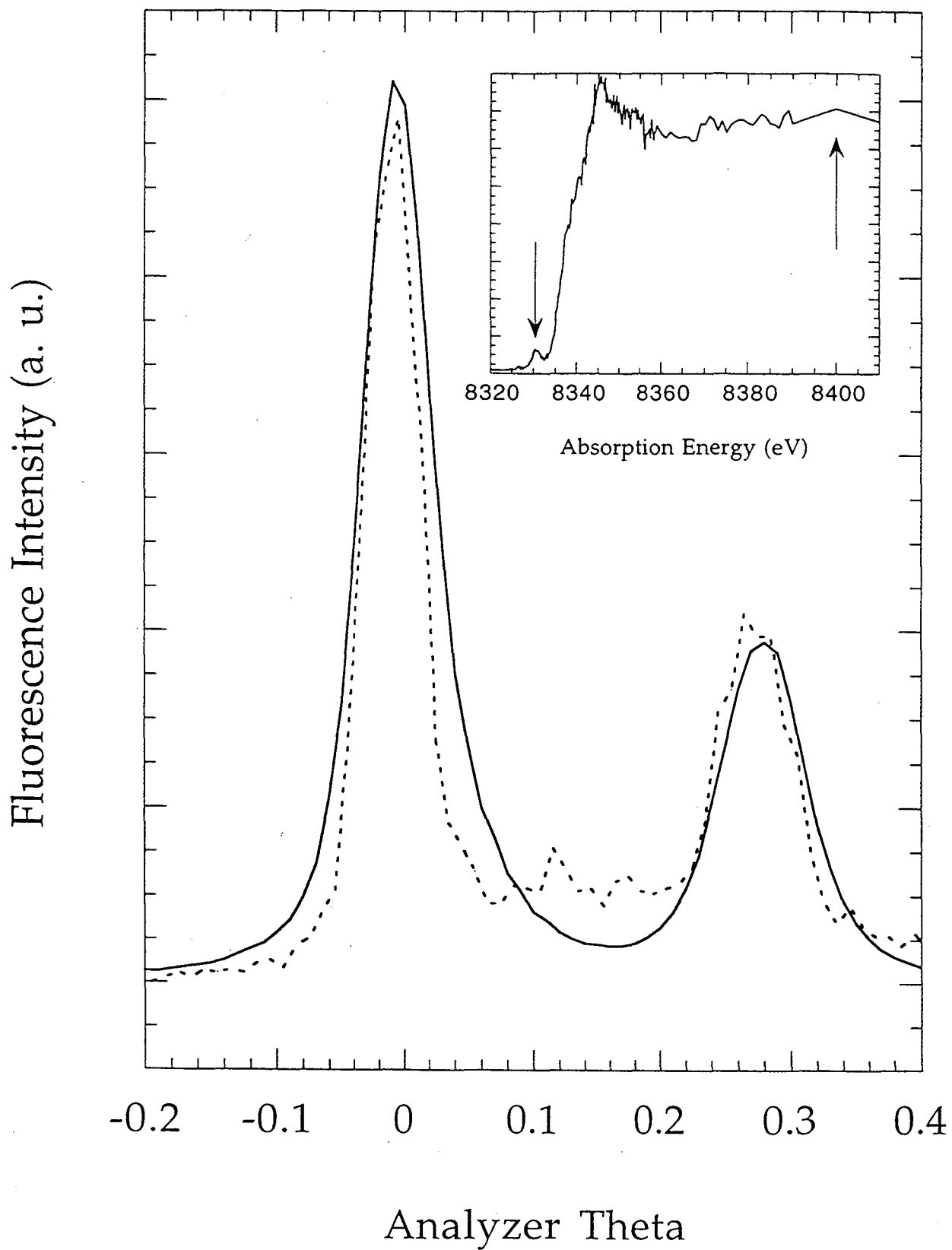
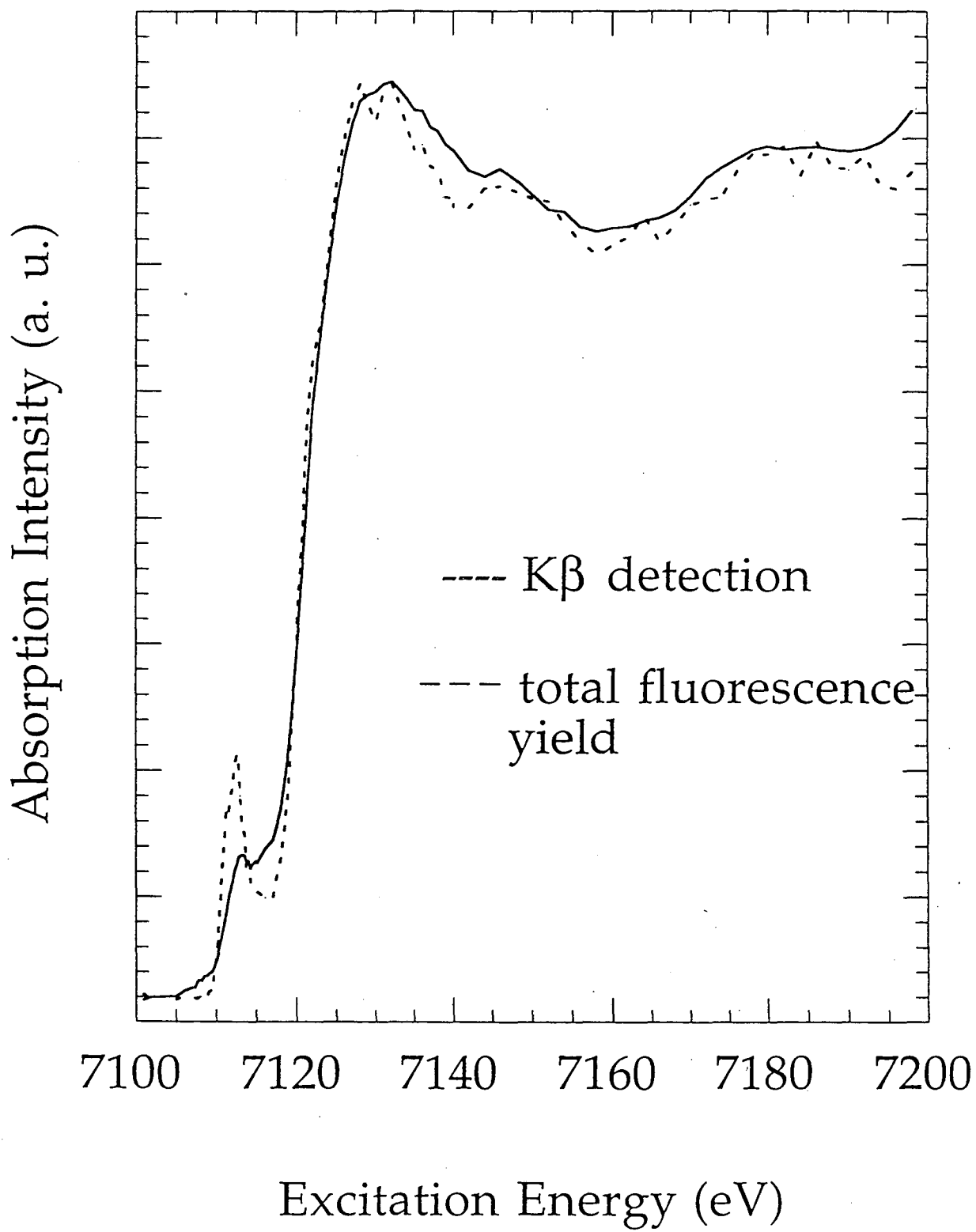


Figure 2.5. Line-sharpening effect of excitation (absorption) spectra by $K\beta$ detection. The excitation spectrum of Fe_2O_3 monitoring Fe $K\beta$ (solid line) shows sharper features than the spectrum by total fluorescence yield (dotted line), due to the disappearance of the lifetime broadening of the $1s$ core hole intermediate state.



emission processes, which can also be explained by a simple picture of energy conservation. Suppose the photoelectron ejected in the absorption process has an energy ε . Because the energy is conserved in the absorption process,

$$\varepsilon = \omega - E_{1s} \quad (2.5)$$

In transmission or an equivalent total fluorescence experiment, ω is scanned across E_{1s} while recording the beam attenuation of the sample. Thus the photoelectron is used as a probe and has an uncertainty of

$$\Delta\varepsilon = \Delta\omega + \Gamma_{1s} \quad (2.6)$$

Therefore the lifetime width Γ_{1s} is the resolution limit. In some heavy elements the 1s lifetime broadening can be as high as 10 eV [2.16], which could smear out the whole near edge structure. After absorption, the 1s core hole is filled by another electron through various decay channels. The transmission measurement integrates over all possible decays. In fluorescence it involves an electron with p character filling the 1s hole and emitting a photon ω' , therefore the photoelectron energy is:

$$\varepsilon = \omega - \omega' - E_{np} \quad (2.7)$$

The fluorescence photon energy is determined by the energy difference of the corresponding binding energies as $\omega' = E_{1s} - E_{np}$ and has a natural linewidth $\Gamma_{1s} + \Gamma_{np}$. Since the Γ_{np} is normally much smaller than Γ_{1s} , the uncertainty of photoelectron is still determined by equation (2.5).

However, when fixing the incoming photon energy ω and measuring the fluorescence energy ω' , the uncertainty of the photoelectron energy is

$$\Delta\varepsilon = \Delta\omega + \Delta\omega' + \Gamma_{np} \quad (2.8)$$

which is only limited by the (usually) much smaller natural width Γ_{np} . Therefore by analyzing the fluorescence energy at a narrow energy window (about 0.45 eV in our experiment) while scanning the incident energy, one can obtain an absorption spectra without the K shell lifetime broadening. The spectral width is limited only by the experimental resolution together with the final state lifetime width. This line-sharpening effect by detecting K β fluorescence energy with 0.45 eV energy window while scanning the incoming energy is illustrated in Figure 2.5 for Fe₂O₃.

The second important result in high resolution XIS is due to the fact that different parts of the emission spectra correspond to different decays [2.17]. Since the intensity distributions of spin-up and spin-down transitions are well separated, the absorption spectra at different emission energies are spin polarized. The spin dependence of excitation spectra when detecting certain emission energies is caused by the strong two electron interactions in the final state of K emission process; this will be discussed in detail in the following section.

2.3 X-ray Emission

The following paper, submitted to Physical Review B, discusses the spin polarization character of K α and K β x-ray emission of 3d transition-metal ions, as well as the corresponding x-ray excitation spectra. The ligand

field multiplet model was used to simulate the K emission spectra, its validity and limitations are discussed in detail.

Spin Polarized X-ray Emission of 3d transition-metal ions - A Comparison via $K\alpha$ and $K\beta$ detection

Xin Wang^{1,2}, Frank M. F. de Groot³ and Stephen P. Cramer^{1,2}

(1) Department of Applied Science, University of California, Davis, CA 95616.

(2) Lawrence Berkeley National Laboratory, Berkeley, CA 94720.

(3) Solid State Physics, University of Groningen, Nijenborgh 4, 9747 AG Groningen, Netherlands

Abstract: This paper demonstrates that spin polarized x-ray excitation spectra can be obtained using $K\alpha$ emission as well as $K\beta$ line. The first spin-polarized analysis of $K\alpha$ x-ray emission and the excitation spectra by $K\alpha$ detection on a Ni compound are reported. Systematical analysis of the first row transition-metal ions using the ligand field multiplet calculation are presented for $K\alpha$ and $K\beta$ emission spectra.

I. INTRODUCTION

X-ray absorption spectroscopy¹ (XAS) and x-ray emission spectroscopy² (XES) are both powerful tools for probing the electronic structure of transition metal compounds. The x-ray emission spectrum has long been known for its sensitivity to the absorbing element, the population and distribution of valence electrons, the coordination and the electronegativity of the surrounding atoms. K absorption involves the promotion of a 1s electron from a 1s orbital to unoccupied orbitals (bands) or the continuum, while K emission is a result of a p electron filling the 1s core hole. The 2p->1s transition gives K α XES, while K β XES arise from 3p->1s transition. The K β XES of transition metals and their compounds have been studied for many years³.

With the development of brighter synchrotron sources and more efficient fluorescence spectrometers, remarkable progress has recently been made in the combined application of x-ray absorption and emission spectroscopy. Hämäläinen et al.⁴ measured high resolution spin-dependent excitation spectra for different Mn compounds using the spin-polarized final states in the Mn K β XES. The spin dependent x-ray absorption spectra were obtained by fixing emission energy at the main peak (K $\beta_{1,3}$) and the satellite (K β'), respectively, while scanning the excitation energy through the Mn K absorption edge. Interpretation of the spin dependent excitation spectrum of MnF₂ and MnO was originally based on the analogy of the Mn K β XES with the 3p x-ray photoemission spectrum (XPS), which has been supported by multiplet calculations including ligand field effects⁵. Similar spin polarization in K β emission spectra has since been confirmed for Fe complexes^{6,7}, as well as Ni complexes^{8,9}. It can be shown^{5,10} that using the exchange picture first developed by Tsutsumi et al.¹¹, the K β emission

spectrum can be separated into internally referenced spin-up and spin-down part, with the main peak primarily comes from the spin-down transition, while the satellite is almost 100% spin-up. The outgoing 1s electron spin direction is referenced to the spin direction of the 3d valence electrons.

Apart from the spin polarized nature of the spectra, the combination of excitation and emission processes (sometimes called inelastic x-ray scattering¹²) provides other unique advantages, such as the line-sharpening effect¹³ and site-selectivity in a mixed cluster^{14,15}. In the current interpretation of the line-sharpening effect, the coherence of excitation and fluorescence decay processes causes the lifetime of the intermediate state disappear^{10,16}, i.e. the width of excitation spectrum monitoring the fluorescence is determined essentially by the much narrower final core hole state lifetime. The chemical sensitivity of K β emission spectra can also be used to facilitate site-selective x-ray absorption, which could provide useful information on a particular site in a mixed oxidation states or spin states complex.

The purpose of this paper is to demonstrate that spin polarized x-ray excitation spectra can be obtained using K α emission as well as K β line. This is important because the much larger fluorescence yield makes the K α experiment more efficient and usually easier. Since the 2p final states are often narrower than 3p levels, K α excitation spectra may also exhibit greater line sharpening. We first present a systematic theoretical analysis of spin polarized K α XES, as well as K β XES, for all first row transition-metal ions, by using the ligand field multiplet model¹⁷⁻²⁰. We then report the first spin-polarized experiment on a Ni compound by K α detection, and compare these data with spin-polarized Ni K β experimental results.

The paper is organized as follows. Section II discusses the theory involved in the analysis, and we show the calculated results of $K\alpha$ XES in section III. The crystal field effects, 3d spin-orbit effects and the charge transfer effects on the $K\alpha$ emission spectrum are discussed there. In section IV, the calculated results of $K\beta$ XES are presented, as well as similar effects on the $K\beta$ emission spectrum. Section V compares the experimental $K\alpha$ and $K\beta$ XES on Ni compounds, as well as the resultant excitation spectra by $K\alpha$ and $K\beta$ detections. Section VI is devoted to concluding remarks.

II. THEORY

In describing the ligand field multiplet model for the $K\alpha$ and $K\beta$ XES, we start from an atomic model²¹. The ground state of a 3d transition-metal ion can be described as a $3d^n$ configuration. When a 1s electron is excited to the continuum, the $K\alpha$ emission spectrum can be calculated from the dipole transition matrix element for $1s^1 3d^n \rightarrow 2p^5 3d^n$ transitions, and the $K\beta$ emission can be simulated by calculations $1s^1 3d^n \rightarrow 3p^5 3d^n$. In the calculations, the energy levels of the fluorescence initial state and final state multiplets are calculated first, and the spectrum is simulated by means of the dipole transition.

The hamiltonian used for calculating the wavefunctions is given by

$$H = \epsilon_{3d} n_{3d} + U_{dd} n_d n_d + \epsilon_p n_p + \epsilon_{1s} n_{1s} + H_{multiplet} + H_{CF}$$

where the ϵ_{3d} represents the 3d energy state of transition metal-ions, U_{dd} is the Coulomb interaction between 3d electrons, ϵ_{1s} and ϵ_p are the energy levels of the 1s initial core state and final np (n=2 for $K\alpha$ and n=3 for $K\beta$) core hole states, respectively. The $H_{multiplet}$ includes the multiplet

couplings originated from the multipole terms of the 3d-3d interaction, the 1s-3d interaction and the np-3d interaction, as well as the corresponding np spin-orbit couplings. The H_{CF} represents the crystal field effects.

Notice we did not use the Anderson impurity model²² in our hamiltonian, that is, we did not include the inter-atomic hybridization between the metal 3d states and the ligand p states (charge transfer effects). In principle, the charge transfer effects are very important in the 1s electron excitation process. If including the transfer of an electron from the ligand p states to the metal 3d states, the ground state then can be described as $3d^n + 3d^{n+1}\underline{L}$, where \underline{L} represents a ligand hole state with an energy at $\epsilon_{3d} - \epsilon_{2p}$, where ϵ_{2p} is the energy of the ligand 2p state. After a 1s core hole is created, the initial state could be dominated by the $1s^1 3d^{n+1}\underline{L}$ character²³ because the energy difference $\epsilon_{3d} - \epsilon_{2p}$ is decreased or even negative, therefore this electronic configuration is stabilized, as discovered by XPS study²⁴. However, the symmetry of this configuration is still given by that of the $1s^1 3d^n$ configuration, i. e. the symmetry is determined by the 'original' valency of the transition metal-ion even though the configuration is dominated by $1s^1 3d^{n+1}\underline{L}$. Also, in the fluorescence process, the charge transfer effect is not as important, since the 1s core hole potential is similar to the 2p (3p) core potential, the relative energy positions of the valence states do not change. Because the shape of the emission spectrum is more sensitive to the symmetry of the state than to the electronic configurations, we therefore still use one electron configuration symmetry originated from the ground state $3d^n$ to simulate the fluorescence process $1s^1 3d^n \rightarrow (n)p^5 3d^n$. The charge transfer effects will be examined in section III E using a specific example.

The atomic multiplet terms in the fluorescence initial state consist of the 3d-3d Coulomb interaction and the 1s-3d exchange interaction. When the 3d spin-orbit is neglected, all states with the same angular symmetry are degenerate because the spin itself does not influence the energy. In the final state, there are terms related to 3d valence electrons coupled with the 2p (3p) core hole in the K emission process. 2p-3d and 3p-3d Coulomb and exchanges interactions are all important two electron integrals which can be calculated explicitly in the ligand field multiplet model, as well as the corresponding spin-orbit couplings.

The last ingredient of the ligand field multiplet model is introducing the effects of neighboring atoms as the crystal field H_{CF} in both the initial state and final state. In terms of group theory, the crystal field effects reduce the symmetry from $O(3)$ to O_h in a cubic field. The $O(3)$ - O_h branching rule²⁵ is used to project the spherical $O(3)$ multiplets into the O_h symmetry.

In an octahedral environment, the symmetry and strength of surrounding ligands split the 3d orbitals of the transition metal-ions, while the s and p orbitals remain unsplit. The 3d orbitals are split into E and T_{2g} characters, with an energy difference denoted as ligand field strength $10Dq$. For a small crystal field, the initial state is originated from the atomic ground state, which is high-spin according to Hund's rule. The energy level of ground state with a crystal field is given by the Tanabe and Sugano diagram²⁶. The initial state could change character from high-spin to low-spin when ligand field is strong enough. The final state is also split or shifted by the crystal field. The sudden change of the initial state from high-spin to low-spin cause a different set of final states can be reached, and therefore both the spectrum shape and the spin-polarization character

change with the ligand field. The dipole transition operator is not split in O_h symmetry.

III. $K\alpha$ XES RESULTS

Calculations were performed using the chain of groups approach by Butler²⁵, with a program adapted by Thole¹⁶⁻²⁰. This approach starts with the calculation of the reduced matrix elements of the necessary operators in the spherical group using Cowan's atomic multiplet program²¹. Octahedral symmetry is used in all cases to simulate the surrounding effects with $10Dq=0.9$ eV. Since the 1s-3d exchange is only used to correlate up and down spins, a smallest possible value of 0.001 eV is taken in the calculation. The Slater integrals are scaled down to 70% of Hartree-Fock values to account for covalency. The initial state 3d spin-orbit coupling is neglected for the moment for clarity. For illustration purposes, broadening parameters of 0.6 eV (FWHM) are used for both the 1s and 2p core hole widths in Lorentzian function, and 0.5 eV (FWHM) for the Gaussian function for instrumental broadening.

A. Initial State and Final state of $K\alpha$ XES

In Table I, the ground state and fluorescence initial state characters of all configurations are shown in both spherical and octahedral symmetries without the 3d spin-orbit coupling. The 3d-3d Coulomb interaction (F^2 , F^4) splits the atomic state into multiplet terms via LS coupling, where the total momentum J is the sum of orbital momentum L and spin momentum S of the valence electrons, and the ground state in spherical symmetry [$2S+1L$] is given by Hund's rule. In an octahedral environment, the atomic ground state is projected into cubic symmetry by the branching rules, as given in

Table II. The fluorescence initial state is then formed by the excitation of a 1s electron, where the 1s-3d exchange interaction ($G_{s,d}$) further splits the degenerate cubic ground state into a pair of states with high-spin and low-spin symmetries.

The spin-polarized components in $K\alpha$ XES can be constructed from the high-spin and low-spin symmetries of the fluorescence initial state. For a d^n ion with $[2S+1L]$ character, the excitation of a 1s electron is related to $[2S+2L]$ and $[2SL]$ symmetries. The $[2SL]$ symmetry relates 100% to spin-up transition, while the $[2S+2L]$ partitions $\frac{2S+1}{2S+2}$ to spin-down and $\frac{1}{2S+2}$ to spin-up transitions^{27,28}, because there are as many up electrons as down electrons. Thus, the spin-up spectrum is constructed from $[2SL] + [\frac{1}{2S+2}] [2S+2L]$, and the spin-down spectrum from $[\frac{2S+1}{2S+2}] [2S+2L]$, keeping the intensity of spin-up and spin-down equal.

The definition of our spin-up and spin-down spectrum here is somewhat different from the references 4,5,6,7, where the spin-up and spin-down intensities were directly related to $[2SL]$ and $[2S+2L]$ symmetries, and the intensity ratio of spin-up and spin-down was $S : (S+1)$. In a careful analysis, it can be shown²⁹ that the substate $m_j = -(L+S+1/2)$ in $[2S+2L]$ symmetry is actually constructed from the spin-up 1s state instead of spin-down. Therefore, there is always one state in $[2S+2L]$ symmetry with spin-up character, which keeps the intensity ratio equal. This is the same as found in XPS³⁰, where the spin-up character is found related to one state of high-spin symmetry $[2S+2L]$.

When the ligand field is strong enough, the initial state character change from high-spin to low-spin for d^4 , d^5 , d^6 and d^7 configurations in octahedral symmetry. All low-spin symmetries can also form spin-up and

spin-down states except 1A_1 in the case of low-spin d^6 , and since both the spin and orbitals are zero, the spin-up and spin-down states are degenerate as no exchange interaction takes place.

In Table III, the *ab initio* values of the involved parameters are given for each configuration for both the initial state and the final state. In the final state of $K\alpha$ XES, in addition to the Coulomb and exchange interactions (Slater integrals) of 3d-3d, 2p-3d electrons, the spin-orbit coupling (ξ) of the 2p core hole also plays an important role. As shown in Table III, the spin-orbit coupling of the 2p core hole is of the same order of magnitude as the 2p-3d interactions. The core level of 2p is split by the spin-orbit into $2p_{1/2}$ (L_2) and $2p_{3/2}$ (L_3) with an energy difference $(3/2)\xi$, and that gives rise to the two prominent peaks in $K\alpha$ XES, $K\alpha_1$ (L_3) and $K\alpha_2$ (L_2). Although the exchange interaction between the 2p core hole and the 3d valence electrons is smaller than that between 3p and 3d in $K\beta$ XES, it is comparable to the 2p spin-orbit coupling, therefore there are still large spin effects on both peaks, especially on $K\alpha_1$. This will be shown in section III B in the calculated spectra.

Comparing all the atomic values of Slater integrals and the spin-orbit couplings with $L_{2,3}$ X-ray absorption process³¹, it has been found, as expected, that the final state of $K\alpha$ emission is identical to the final state of the $L_{2,3}$ absorption edge with one less electron. For example, the values of $F^2, F^4, F_{p,d}, G^1, G^3, \xi(2p)$ and $\xi(d)$ of the Ti^{2+} final state in $K\alpha$ XES are exactly the same as that of Ti^{3+} final state in $L_{2,3}$ XAS. Although the creation of a 1s core hole only affects the electronic state as one more 'formal charge', the spectrum shape of $K\alpha$ XES is quite different from $L_{2,3}$ XAS because of the totally different transitions. The transition can be described as $2p_{3/2} \rightarrow 3d, 1s$ and $2p_{1/2} \rightarrow 3d, 1s$ for $L_3, K\alpha_1$ and $L_2, K\alpha_2$, respectively. Thus, different

transitions control the transition intensity despite the identical final states, and different branching ratios can be created. The 1s core hole lifetime also contributes to the width of the emission spectra, causing much broader features than that in the absorption spectra.

B. $K\alpha$ Emission Spectra

The spin-polarized $K\alpha$ emission spectra of first row transition-metal ions are presented in Figure 1. The spin-up and spin-down spectra are constructed as previously described. The total fluorescence spectrum is the sum of spin-up and spin-down spectra. The $K\alpha_1$ peaks are aligned at a common energy for comparison. The degeneracy of the ground state for each configuration is taken into account for intensity normalization. Since the 2p spin-orbit coupling increases with atomic number, the splitting between $K\alpha_1$ and $K\alpha_2$ increases from Sc^{2+} to Cu^{2+} . For each configuration, the spin-down character is stronger in $K\alpha_1$, while spin-up is stronger in $K\alpha_2$, shown as positive and negative signs in the difference spectrum in the right panel. The spin-down spectrum is favorable on the high energy shoulder of $K\alpha_1$, while the spin-up at the lower energy shoulder of $K\alpha_2$. In the most favorable case, as in a d^5 system, there is 75% of spin-down character at 1 eV higher energy from the $K\alpha_1$ peak, and 65% spin-up component at the $K\alpha_2$ peak.

For d^1 and d^9 systems, the spin selectivity is very small. For all other systems, though most spin polarization is on $K\alpha_1$, spin polarized excitation experiments by $K\alpha$ detection should be possible because of the two prominent peaks. For example, a spin dependent excitation spectrum can be obtained by detecting at 1 eV higher energy shoulder of $K\alpha_1$ and the lower

energy shoulder of $K\alpha_2$ separately, then extracting the pure spin-up and spin-down components by using the spin selective coefficients.

C. Crystal Field Effects

Figure 2-5 shows the crystal field effects for d^4 - Cr^{2+} , d^5 - Mn^{2+} , d^6 - Fe^{2+} and d^7 - Co^{2+} configurations on the $K\alpha$ emission spectrum. In general, the spin-polarization decreases with the increase of crystal field strength. When the initial state changes from high-spin to low-spin, there are sudden changes in the spin character as well – the spin-polarization becomes very small in low-spin states. For example, the spin-up character becomes much stronger in $K\alpha_1$ and shifts to 1 eV higher energy for Cr^{2+} when $10Dq$ reaches 2.7 eV; for Mn^{2+} , the spin-down spectrum shifts to 1 eV lower energy at $10Dq=2.85$ eV, and the spin-up spectrum is as strong as the spin-down one, which makes the spin selection of a pure component more difficult. For Fe^{2+} , there is 60% spin selectivity at the $K\alpha_1$ peak when $10Dq$ is below 2.1 eV, and the spin-up and spin-down spectra are degenerate when $10Dq$ reaches 2.1 eV. For Co^{2+} , the transition happens at $10Dq=2.4$ eV, with almost no spin-polarization on both $K\alpha_1$ and $K\alpha_2$ when the low-spin state is reached.

Apart from the changes of spin-polarization character, the total fluorescence spectrum shape is not very sensitive to the crystal field, and there are no dramatic branching ratio³² changes from high-spin to low-spin state, as observed in $L_{2,3}$ XAS³³ (and also in $K\beta^7$). As discussed in Section III A, the different transitions are responsible for the different branching ratios. Although the branching ratio of $K\alpha$ is close to that of $L_{2,3}$ before the high-spin low-spin transition (both are $2/3$ without multiplet effect), the transition from $2p$ directly into $3d$ orbitals makes the branchings more

sensitive to the crystal field than the transition from 2p to 1s, where the 3d electrons can be viewed as 'spectators' despite the strong 2p-3d couplings. This can be understood as the origin of the relative insensitivity of crystal field effects in $K\alpha$ XES.

D. 3d Spin-orbit Effects

Until now, we did not include the 3d spin-orbit coupling in our calculations. When it is included, the symmetry of the fluorescence initial state is more complicated, as the total spin momentum S should also be projected from spherical to cubic symmetry as well as angular momentum L , to form the overall final state. In some cases, when the unfilled 3d states have E character, in the first order, the 3d spin-orbit effects on the symmetry can be neglected³⁴. For systems such as Co^{2+} , however, it is important to include the 3d spin-orbit for a complete ground state description, since the unfilled 3d orbitals have T symmetry, and the value of the spin-orbit coupling increases with atomic number.

There are two main changes in the calculation with inclusion of the 3d spin-orbit coupling. First, the ground state is further split, so a different ground state symmetry is formed. For Co^{2+} , the ground state $[^4T_1]$ is split into $[E_1]$, $[E_2]$ and $2[G]$ when the spin-orbit coupling is included, and the degeneracy of 12 states in $[^4T_1]$ is lifted into 2, 2 and 2×4 , as $[E_2]$ symmetry has the lowest energy. Secondly, the effective spin value 'S' becomes much smaller, changing from $3/2$ to $1/2$, so the transition intensity to $[^{2S+2}L]$ is 3 times stronger than that to $[^{2S}L]$ symmetry, increased from a $5/3$ ratio when the 3d spin-orbit is neglected. The spin-polarized spectra including the 3d spin-orbit coupling is compared with the one without in Figure 6. The total spectrum shape is somewhat different in these two spectra, although the

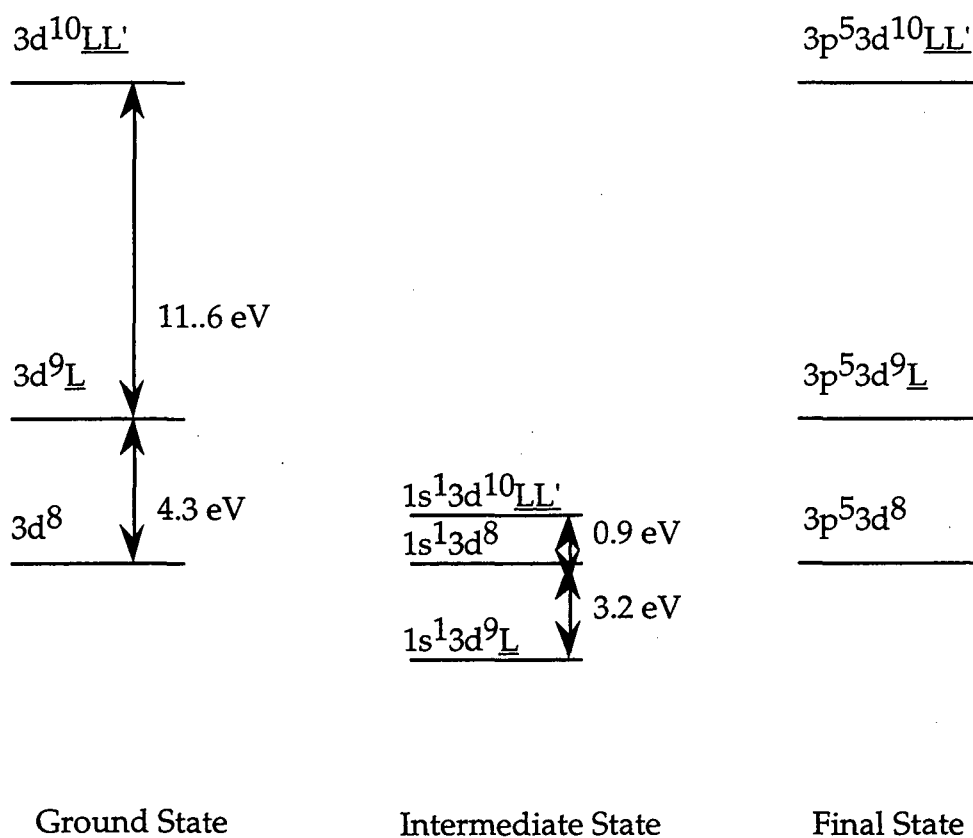
spin-polarization character did not change drastically. Thus, despite of the different state symmetry, the $K\alpha$ XES spectrum shape and spin-polarization characters are not so sensitive to the 3d spin-orbit coupling, so it can be safely neglected in the simulation.

E. Charge Transfer Effects

In this section an example of charge transfer effects on the multiplet calculations of Ni^{2+} $K\alpha$ emission is given. The important improvement with respect to the crystal field multiplet model is that, the ground state is described as a linear combination of the configurations $3d^8$, $3d^9\underline{L}$ and $3d^{10}\underline{L}\underline{L}'$ in the charge transfer multiplet model. \underline{L} denotes a hole in the (ligand) valence band. We start from the initial state of the $K\alpha$ process, where the 1s core hole is created. This state is constructed from the configurations $1s^13d^8$, $1s^13d^9\underline{L}$ and $1s^13d^{10}\underline{L}\underline{L}'$. It is assumed that the potential of a 1s core hole is similar to that of a 2p core hole in the $K\alpha$ final state. The parameters which determine the relative energies of the states are the charge transfer energy Δ , the correlation energy U , the core potential energy Q and the hybridization strength T . The parameter values for NiF_2 are taken from 2p photoemission experiments: $\Delta=4.3$ eV, $U=7.3$ eV, $Q=7.5$ eV and $T=2$ eV³⁵.

The results is that in the initial state of $K\alpha$ x-ray emission the state with the lowest energy is $1s^13d^9\underline{L}$. Its energy is at $\Delta-Q$ with respect to $1s^13d^8$, $\Delta-Q$ being -3.2 eV. In $K\alpha$ (and the same is true for $K\beta$) it is important to include also the third state $1s^13d^{10}\underline{L}\underline{L}'$, which is positioned at an energy $2\Delta-2Q+U$ with respect to $1s^13d^8$ being 0.9 eV. This gives the initial state of $K\alpha$ x-ray emission about 60% $1s^13d^9\underline{L}$ character, 30% $1s^13d^8$ and 10% $1s^13d^{10}\underline{L}\underline{L}'$, with an overall symmetry still the same as that of the $3d^8$ ground state [3A_2].

Charge transfer effects on the calculated Ni^{2+} $K\alpha$ emission are presented in Figure 7. The total spectrum shape does not change much except to be broader, and there is slightly more mixed spin character in the $K\alpha_1$. To some extent, this justifies the use of single configuration ligand field multiplet calculations for K emission spectra, and it supports the argument made in Section II that the emission spectra are more sensitive to the level symmetry instead of the electronic configurations.



Scheme 1. Energy level diagram in charge transfer model for NiF_2 . Each state is a linear combination of three different configurations. Since the configuration $1s^1 3d^9\underline{L}$ has the lowest energy after x-ray absorption process, the hybridized intermediate state has about 60% $1s^1 3d^9\underline{L}$ character.

We also performed the same charge transfer multiplet calculation on Ni^{2+} $\text{K}\beta$ emission spectra in Figure 8. The parameters used are the same as in $\text{K}\alpha$ calculation. It is found that in $\text{K}\beta$ emission, both the spectrum shape and spin polarization character change with charge transfer effects. There is more spin-up character in the main peak as compared with the single configuration multiplet calculation, and the satellite intensity is much more reduced. As argued in reference 8, the increase of covalency, i.e. the increase percentage of $1s^13d^9L$ character in the initial state would reduce the spin selectivity in $\text{K}\beta$. This is more significant for late transition metal ions where the main peak and satellite have smaller splittings. The ligand field multiplet calculation remains to be a good model for ions with large energy splittings.

IV. $\text{K}\beta$ XES RESULTS

The Mn, Fe and Ni $\text{K}\beta$ emission spectra of various compounds have been experimentally recorded, as well as theoretically calculated, using the ligand field multiplet model or the charge transfer model (ref 5-8). For ionic systems with large main peak and satellite separations, the crystal field multiplet model works well. Although similar calculations have been presented before⁶, we first summarize the trends in calculated $\text{K}\beta$ spectra, so that the difference with $\text{K}\alpha$ spectra can be better appreciated.

A. Final State Character of $\text{K}\beta$ XES

The $\text{K}\beta$ XES initial state can be described as the same as in $\text{K}\alpha$ XES, the creation of a $1s$ core hole. The spin polarized component can be constructed also from $2^S L$ and $2^{S+2} L$ symmetries with the same formula given in Section III A. However, the final state in $\text{K}\beta$ is different, where a $3p$ electron instead of a $2p$ electron makes the transition to fill the $1s$ core hole. The main

difference between $K\alpha$ and $K\beta$ XES then is the 3p-3d two electron interactions instead of 2p-3d, as well as the 3p spin-orbit coupling. As shown in table IV, where all the atomic values of Slater integrals and spin-orbit couplings are tabulated, both the Coulomb (Fp,d) and exchange (G^1, G^3) interactions of 3p-3d are much stronger because the 3p wavefunction overlaps much more with the 3d wavefunction, though the 3p spin-orbit coupling is much weaker. The consequences are that the splittings in $K\beta$ XES are largely due to the 3p-3d exchange interaction, as first proposed by Tsutsumi¹⁰. The energy difference between the main peak $K\beta_{1,3}$ and the satellite $K\beta'$ is given by $\Delta E = J(2S+1)$, where J is the exchange parameter, which is on the order of 15 eV, and S is the net valence electron spin. The 3p spin-orbit splits the states further within 1 eV.

B. $K\beta$ Emission Spectra

The calculations were carried out under identical conditions as that of $K\alpha$ XES. In Figure 9, the spin-polarized $K\beta$ emission spectra of first row transition-metal ions are presented. Each spectrum is aligned with its own 'center of gravity' energy. Clearly the satellite is almost 100% spin-up, while the main peak is greater than 60% spin-down. We did not include more realistic broader lifetime for the satellite (because of technical problems) so they appear larger than in the experimental spectra. In most cases, the spin polarization is stronger in $K\beta$ XES than in $K\alpha$ XES, and the spin-up and spin-down x-ray absorption spectrum can be obtained by tuning the detecting channels to the main peak and the satellite, respectively. Even when the main peak is not favorable in spin-down character, the satellite remains purely spin-up, which can be used in the spin-polarized study.

The $K\beta$ spectrum shape is quite different among different transition-metal ions. Since the intensity ratio of $K\beta'$ and $K\beta_{1,3}$ is $S/(S+1)$, for systems such as d^1 and d^9 , the satellite intensities are very small, and the separation of $K\beta_{1,3}$ and $K\beta'$ is also small because of the correlation with the net spin S . Although the degree of spin-polarization is higher in $K\beta$ XES, in those cases detecting $K\alpha$ would be more feasible because there are always two distinct peaks, with primarily spin-up or spin-down characters. The comparison between $K\alpha$ and $K\beta$ will be discussed in detail in section V and VI.

C. Crystal Field Effects

The change of $K\beta$ XES shape of Mn^{2+} with crystal field was calculated in ref 4, where it has been found that only the lower energy shoulder of the main peak is slightly sensitive to the crystal field strength before the high-spin to low-spin transition occurs. Figure 10-13 shows the crystal field effects on the spin polarization character on d^4 - Cr^{2+} , d^5 - Mn^{2+} , d^6 - Fe^{2+} and d^7 - Co^{2+} configurations. In general, the spectrum shape does not change much for a given spin state, while spin polarization decreases from high-spin to low-spin states. The high-spin state has a much stronger satellite, because of the intensity correlation of the net spin S . The transition happens at 2.7 eV for Cr^{2+} , 2.85 eV for Mn^{2+} , 2.1 eV for Fe^{2+} and 2.4 eV for Co^{2+} . As in $K\alpha$, there is no spin selection for low-spin Fe^{2+} because of the zero spin. When the transition occurs, the spin-up spectrum shifts most of its weight to higher energy, and the main peak where the spin-down character dominated shifts ~ 1 eV to lower energy, causing much smaller spin selectivity at both the main peak and the satellite. However, the weakening of satellite intensity and ~ 1 eV lower energy shift of the main peak in the low-spin state make a spin state 'labeling' possible. For an unknown complex, the main peak

energy position and the satellite intensity can be used to determine the spin state conclusively by comparing to known compounds, and the spin state sensitivity in $K\beta$ emission can also be used to generate site-selective x-ray absorption in spin state mixtures^{7,15}, by detecting at emission energies preferable to high-spin or low-spin states.

D. Spin-orbit Effects

We examine the 3d spin-orbit effects on the $K\beta$ XES also on Co^{2+} in Figure 14. When including the 3d spin-orbit coupling in the calculation, the initial state symmetry changes from $[^4T_1]$ to $[E_2]$, and the transition to the high-symmetry component in the spin-up spectrum is increased from 1/5 to 1/3, therefore there are mixed spin characters in both the main peak and the satellite. This is more obvious than in $K\alpha$ XES, because the final state exchange splitting is more sensitive to the 3d spin-orbit coupling. As shown in Figure 13, the spin-down spectrum does have some contributions to the satellite intensity, but it is still largely spin-up character. In the main peak, however, the spin-up intensity is much larger, and the selectivity for spin-down becomes quite small. This result can be generalized into all the electronic configurations with empty E levels which have relative large 3d spin-orbit coupling. We conclude that the 3d spin-orbit coupling should be included in $K\beta$ XES calculations and is quite important for the unfilled orbitals with E levels, where the spin character in the satellite is not purely spin-up, and the spin selectivity at the main peak is also reduced.

V. COMPARISON WITH EXPERIMENTS

Until now, spin-polarized excitation spectra have only been demonstrated for transition metal $K\beta$ spectra. Based on the theoretical

predictions made above, we examined the $K\alpha$ emission and excitation spectra for high spin tetrahedral Ni^{2+} in $(PPh_4)_2[Ni(SePh)_4]^{36}$, as well as Ni $K\beta$ emission and excitation spectra of NiF_2 . The experiments were carried out at beamline X-25³⁷ at the National Synchrotron Light Source, with apparatus and procedures as previously described³⁸. A Ge(620) crystal was used to monochromatize the $K\alpha$ fluorescence, while 4 Ge(642) crystals were used for $K\beta$ experiments. The emission spectra were taken by rotating the analyzer crystal(s) while fixing the excitation energy. Alternatively, the excitation spectrum was also recorded by fixing the analyzer crystal(s) at certain emission energies while scanning monochromator energy.

The experimental Ni $K\alpha$ emission spectrum of $(PPh_4)_2[Ni(SePh)_4]$ (top, dotted line) is presented in Figure 14, with comparison to the total fluorescence spectrum (solid line), as well as spin-up (dotted line) and spin-down (solid line) components calculated using the ligand field multiplet model. The calculation used T_d symmetry with $10Dq=0.9$ eV to simulate the high-spin Ni^{2+} geometry. In a T_d environment, the ground state $3d^8$ has a $[^3A_2]$ symmetry, and the $K\alpha$ spin-dependent initial states are therefore constructed from $(3/4)[^4A_2]$ for spin-down and $(1/4)[^4A_2] + [^2A_2]$ for spin-up transitions. Since the spin-polarization character in $K\alpha$ XES is not sensitive to both the charge transfer effects and the $3d$ spin-orbit coupling, they were neglected in the calculation. All Slater integrals were reduced to 70% of their Hartree-Fock values. Overall, the calculation simulates the emission spectrum quite well, except a bit large $K\alpha_2$ peak.

From the decomposed spin components in the simulation, it is predicted that the high energy side of the $K\alpha_1$ is more favorable for spin-down, while the low energy side of $K\alpha_1$ represents mostly spin-up transitions. On $K\alpha_2$, the spin-up and spin-down are almost averaged. The

excitation spectra bear out this prediction. The $1s \rightarrow 3d$ transition is visible only when monitoring 2.1 eV high energy side of $K\alpha_1$ (solid line), but almost no pre-edge intensity is observed when monitoring 1.3 eV low energy shoulder of $K\alpha_1$ (dotted line), as shown in Figure 15. This is consistent with the fact that the vacant 3d orbitals available in the high-spin d^8 configuration are all spin-down. Therefore, only spin-down $1s \rightarrow 3d$ transitions are allowed. This confirms again the spin polarization in $K\alpha$ emission spectrum, as predicted from the ligand field calculation.

For comparison, we show the $K\beta$ NiF_2 experimental emission spectrum (top) and simulations (bottom) in Figure 16, and the spin polarized excitation spectra in Figure 17. Notice the main peak $K\beta_{1,3}$ has most of the intensity in the spectrum, with some small satellite features. The charge transfer multiplet model was used to correctly simulate the $K\beta$ emission spectrum. The excitation spectra are shown in Figure 18, which picking up mostly spin-up (dotted line) and spin-down (solid line) components at the satellite and the main peak, respectively. There are similar effects at the pre-edge, where the $1s \rightarrow 3d$ is only visible in the spin-down spectrum.

VI. COMPARISON BETWEEN $K\alpha$ and $K\beta$

Theoretical analysis of $K\alpha$ and $K\beta$ XES of first row transition-metal ions, and the examples of experimental results using $K\alpha$ and $K\beta$ XES and excitation spectra reveal that there is similar information content in both spectra. Both emission spectra are spin-polarized. In general, the spin selectivity in $K\beta$ XES is larger than in $K\alpha$ XES, especially at the satellite $K\beta'$, where the spin-up character is almost pure or dominant. However, the intensity of the $K\beta'$ feature is sometimes too small to be useful. In $K\alpha$ XES,

there are always two well separated peaks, and different spin character can be recorded by monitoring at the lower and higher energy shoulder of $K\alpha_1$, or the the lower energy shoulder of $K\alpha_2$. The $K\beta$ spectrum shape is more sensitive to changes from high-spin to low-spin states than $K\alpha$. Experimental results on Mn^{5+} , Fe^{7+} and Ni^{9+} compounds have shown that the $K\beta$ emission spectra are sensitive to both oxidation states and spin states, therefore chemical sensitivity thus site selectivity in a chemically mixed cluster is better achieved by detecting $K\beta$ emission. However, the $K\alpha$ emission and the excitation monitoring different $K\alpha$ features would have special advantages, because of the higher fluorescence yield, and the longer and more constant 2p core hole lifetime:

1. The fluorescence yield of $K\alpha$ is almost 5-10 times stronger than $K\beta$ ³⁹ for first row transition-metal ions. The main obstacle in the excitation combined with emission experiments is the low efficiency of the collecting spectrography. The almost order of magnitude increase in $K\alpha$ fluorescence makes the experiment much easier, and in some cases, the difficult experiments for dilute systems such as metalloproteins become more accessible;
2. The 2p core hole lifetime broadening⁴⁰ is much narrow in average in $K\alpha$ (some complications will be discussed next) than 3p core hole broadening in $K\beta$. Because of the coherence of excitation and emission process, the excitation spectrum width is essentially determined by the narrower final state core hole lifetime. There should be more dramatic line-sharpening effect by detecting $K\alpha$, and the excitation spectrum could reveal new structures previously buried within lifetime broadening. For example, the 0.8 eV lifetime broadening of the Ni 2p core which determines the width of

the $K\alpha$ excitation spectrum is more than a factor of 2 less than the 2 eV 3p core which determines the width of the $K\beta$ excitation.

3. Finally, the lifetime of the $K\alpha$ final state is much less multiplet term dependent than the $K\beta$ final state. The broadening factors vary much more in the 3p multiplets, where the lower energy multiplets have shorter lifetimes⁴¹, because of the strong 3p-3d couplings and the 3p3d3d super Coster-Kronig-like process⁴¹ associated with the 3d states. This means, when monitoring some 3p multiplets, the spectrum could have smaller broadening than monitoring other 3p multiplets, even smaller than the 2p core hole state. On the other hand, the 2p core hole broadening is almost a constant⁴² because of the mixed symmetries due to the 2p core hole spin-orbit coupling. When comparing the excitation spectrum monitoring different $K\beta$ features, care must be taken to 'unify' the broadening factor before processing can be done, while $K\alpha$ excitation spectrum can be treated directly without the complication.

VII. CONCLUSIONS

The spin-polarized $K\alpha$ XES as well as $K\beta$ XES of first row transition-metal ions have been calculated by using the ligand field multiplet model. It is found, that the $K\alpha$ XES has large spin effects especially at $K\alpha_1$, although the two prominent peaks are separated by the 2p spin-orbit coupling. The first experiment based on this prediction has been carried out on an Ni compound, the excitation spectrum shows a strong pre-edge feature when monitoring the higher energy shoulder of $K\alpha_1$ where the spin-down is dominant, with almost no intensity while monitoring the lower energy shoulder of $K\alpha_1$ where it is mostly spin-up. The results on Ni $K\beta$ experiment

have also confirmed the spin polarization assignment from theoretical analysis.

The ground state symmetry determines the spectrum shape in K emission instead of electronic configurations, although the charge transferred state is dominant after the creation of a 1s core hole. The $K\alpha$ XES in general is not sensitive to crystal field and 3d spin-orbit coupling, but the shape and the spin polarization in $K\beta$ XES are. There is no dramatic branching ratio changes in $K\alpha$ when the initial state changes character from high-spin to low-spin, despite the identical final state as in $L_{2,3}$ absorption edges.

Similarities and differences are given when comparing the $K\alpha$ and $K\beta$ XES as well as $K\alpha$ and $K\beta$ detected excitation spectrum. The higher fluorescence yield in $K\alpha$ makes the experiment much easier, and the sharper lifetime broadening of the 2p core hole would have a more dramatic effect on line-sharpening. The large lifetime variations in 3p multiplets complicate the situation. In some cases, $K\beta$ detected excitation spectrum would be narrower even than the $K\alpha$ spectrum.

ACKNOWLEDGMENTS

We are grateful to Professor P. Mascharak (Santa Cruz, University of California) for providing the Ni compound, to Dr. C.R. Randall (Berkeley, Lawrence Berkeley Laboratory) for making the NiF_2 data available. We thank M.M. Grush and J. Wang (Davis, University of California) for experimental help. XW would also like to thank Professor A. Kotani (Tokyo, University of Tokyo) for helpful discussions. This work was funded by the National Institutes of Health (GM-48145) and the Department of Energy, Office of

Health and Environmental Research. National Synchrotron Light Sources is founded by the Department of Energy, Basic Energy Research.

Table I. The character of ground state and initial state for the d^n ion configurations in spherical [O(3)] and octahedral (Oh) symmetry.

Configurations (g.s.)(i.s.)		O(3)	Oh (h.s.)(g.s.)(i.s.)		Oh (l.s.)(g.s.)(i.s.)	
d^1	Sc ²⁺ $s^1 d^1$	${}^2D_{3/2}$	2T_2	3,1T_2		
d^2	Ti ²⁺ $s^1 d^2$	3F_2	3T_1	4,2T_1		
d^3	V ²⁺ $s^1 d^3$	${}^4F_{3/2}$	4A_2	5,3A_2		
d^4	Cr ²⁺ $s^1 d^4$	5D_0	5E	6,4E	3T_1	4,2T_2
d^5	Mn ²⁺ $s^1 d^5$	${}^6S_{5/2}$	6A_1	7,5A_1	2T_2	3,1T_2
d^6	Fe ²⁺ $s^1 d^6$	5D_4	5T_2	6,4T_2	1A_1	
d^7	Co ²⁺ $s^1 d^7$	${}^4F_{9/2}$	4T_1	5,3T_1	2E	3,1E
d^8	Ni ²⁺ $s^1 d^8$	3F_4	3A_2	4,2A_2		
d^9	Cu ²⁺ $s^1 d^9$	${}^2D_{5/2}$	2E	3,1E		

Table II. The $SO_3 \rightarrow O_h$ branching rules.

Spherical	Cubic
S	A1
P	T1
D	E+T2
F	A2+T1+T2
G	A1+T1+T2+E
H	T1+T1+T2+E
I	A1+A2+T1+T1+T2+E

Table III. The *ab initio* values (in eV) of the parameters in the Hartree-Fock calculation for both initial state and final state. The actual values for the Coulomb and exchange interaction used in the calculation have been scaled to 70% of these values.

d^N	Ion	$F^2(i.s.)$	$F^4(i.s.)$	$G_{s,d}$	$F^2(f.s.)$	$F^4(f.s.)$	$F_{p,d}$	$G^1(p,d)$	$G^3(p,d)$	ξ_{2p}	ξ_{3d}
d^1	Sc ²⁺	0.000	0.000	0.033	0.000	0.000	5.096	3.585	2.036	3.032	0.020
d^2	Ti ²⁺	10.218	6.412	0.039	10.343	6.499	5.581	3.991	2.268	3.776	0.027
d^3	V ²⁺	10.863	6.809	0.045	10.974	6.888	6.057	4.392	2.496	4.649	0.036
d^4	Cr ²⁺	11.596	7.199	0.052	11.596	7.270	6.526	4.788	2.722	5.667	0.047
d^5	Mn ²⁺	12.120	7.584	0.059	12.210	7.649	6.988	5.179	2.945	6.845	0.059
d^6	Fe ²⁺	12.736	7.963	0.065	12.818	8.023	7.446	5.566	3.166	8.199	0.074
d^7	Co ²⁺	13.347	8.339	0.072	13.422	8.395	7.900	5.941	3.386	9.746	0.092
d^8	Ni ²⁺	13.953	8.712	0.079	14.022	8.764	8.350	6.332	3.603	11.506	0.112
d^9	Cu ²⁺	0.000	0.000	0.086	0.000	0.000	8.797	6.712	3.820	13.496	0.135

Table IV. The *ab initio* values (in eV) of the parameters in the Hartree-Fock calculations for the final state of $K\beta$ XES.

d^N	Ion	F^2	F^4	$F_{p,d}$	$G^1(p,d)$	$G^3(p,d)$	ξ_{3p}	ξ_{3d}
d^1	Sc^{2+}	0.000	0.000	9.693	12.128	7.369	0.320	0.014
d^2	Ti^{2+}	9.546	5.946	10.395	12.976	7.891	0.410	0.020
d^3	V^{2+}	10.199	6.400	11.075	13.799	8.394	0.519	0.027
d^4	Cr^{2+}	10.839	6.794	11.743	14.603	8.890	0.646	0.036
d^5	Mn^{2+}	11.469	7.182	12.400	15.395	9.376	0.795	0.047
d^6	Fe^{2+}	12.091	7.565	13.050	16.176	9.854	0.969	0.052
d^7	Co^{2+}	12.706	7.944	13.694	16.949	10.328	1.168	0.075
d^8	Ni^{2+}	13.317	8.320	14.333	17.716	10.798	1.397	0.092
d^9	Cu^{2+}	0.000	0.000	14.968	18.479	11.264	1.658	0.113

References:

- ¹ *X-ray Absorption: Principles, Applications, Techniques of EXAFS, SEXAFS and XANES*, eds. by D.C. Konigsberger and R. Prins (John Wiley & Sons, New York, 1988).
- ² A. Meisel, G. Leonhardt, R. Szargan, *X-ray Spectra and Chemical Binding*, edited by R. Gomer (Springer-Verlag, Berlin, 1989).
- ³ B. Ekstig, E. Källne, E. Noreland, E. Manne, *Physica Scripta* **2**, 38 (1970).
- ⁴ K. Hämäläinen, C.-C. Kao, J.B. Hastings, D.P. Siddons, L.E. Berman, V. Stojanoff, and S.P. Cramer, *Phys. Rev. B.*, **63**, 14274 (1992).
- ⁵ G. Peng, F.M.F. de Groot, K. Hämäläinen, J.A. Moore, X. Wang, M.M. Grush, J.B. Hastings, D.P. Siddons, W.H. Armstrong, O.C. Mullins, and S.P. Cramer, *J. Am. Chem. Soc.* **116**, 2914 (1994).
- ⁶ G. Peng, X. Wang, C. Randall, J. Moore, and S.P. Cramer, *App. Phys. Lett.* **65**, 2527 (1994).
- ⁷ X. Wang, C.R. Randall, G. Peng, and S.P. Cramer, *Chem. Phys. Lett.* **243**, 469 (1995).
- ⁸ F.M.F. de Groot, A. Fontaine, C.C. Kao, and M. Krisch, *J. Phys. Cond. Matt.*, **6**, 6875 (1994)
- ⁹ C.R. Randall, A.G. Froeschner, S.P. Cramer, M.F.J.M. Verhagen, and M.W.W. Adams, submitted to *Inorg. Chem.*
- ¹⁰ F.M.F. de Groot, S. Pizzini, A. Fontaine, K. Hämäläinen, C.C. Kao, J.B. Hastings, *Phy. Rev. B*, **51**, 1045 (1995).
- ¹¹ K. Tsutsumi, H. Nakamori, K. Ichikawa, *Phys. Rev. B*, **13**, 929 (1976).
- ¹² *Resonant Anomalous X-Ray Scattering*, eds. by G. Materlik, C.J. Sparks, and K. Fischer (North-Holland, Amsterdam, 1994)

- 13 K. Hämäläinen, D.P. Siddons, J.B. Hastings, and L.E. Berman, *Phys. Rev. Lett.*, **67**, 2850 (1991).
- 14 M.M. Grush, G. Christou, K. Hämäläinen, and S.P. Cramer, *J. Am. Chem. Soc.*, **117**, 5895 (1995).
- 15 X. Wang and S.P. Cramer, in preparation.
- 16 P. Carra, M. Fabrizio, and B.T. Thole, *Phys. Rev. Lett.* **74**, 3700 (1995); M. Taguchi, and A. Kotani, *J. Phys. Soc. Japan.*, **65**, 706, (1996).
- 17 B.T. Thole, G. van der Laan, J.C. Fuggle, and G.A. Sawatzky, *Phys. Rev. B*, **32**, 5107 (1985).
- 18 G. van der Laan, B.T. Thole, G.A. Sawatzky, and M. Verdaguer, *Phys. Rev. B* **37**, 6587 (1988).
- 19 B.T. Thole, G. van der Laan and P. H. Bulter, *Chem. Phys. Lett.*, **149**, 295 (1988).
- 20 B.T. Thole and G. van der Laan, *Phys. Rev. A*, **38**, 1943 (1988).
- 21 R.D. Cowan, *The theory of Atomic Structure and Spectra* (University of California Press, Berkeley, 1981).
- 22 A. Kotani, Y. Koyozana, *Theoretical Aspects of Inner-level Spectroscopy*, in *Synchrotron Radiation: Techniques and Applications*, edited by C. Kurz (Springer-Verlag, Berlin, 1979).
- 23 J. Kawai, M. Takami, C. Satoko, *Phys. Rev. Lett.* **65**, 2193 (1990).
- 24 J. Zaanen, C. Westra and G. A. Sawatzky, *Phys. Rev. B* **33**, 8060 (1986).
- 25 see for example, P.H. Butler, *Point Group Symmetry Application: Methods and Tables* (Plenum, New York, 1981); F.A. Cotton, *Chemical Applications of Group Theory* (John Wiley & Sons, New York, 1972)
- 26 Y. Tanabe and S. Sugano, *J. Phys. Soc. Japan.*, **9**, 753 (1954).
- 27 T. Kachel, C. Carbone and W. Gudat, *Phys. Rev. B*. **47**, 15391 (1993).
- 28 F.M.F. de Groot, M.H. Krisch and F. Sette, in preparation.

²⁹ in $2s+2L$ symmetry, there are total $2J+1=2(L+S)+2$ states, with $m_j = -(L+S+1/2), -(L+S-1/2), \dots, L+S-1/2, L+S+1/2$. For 3d electrons, there are $2(L+S)+1$ states, with $m_j = -(L+S), -(L+S-1), \dots, L+S-1, L+S$. so the state $m_j = -(L+S+1/2)$ is constructed from 3d state $m_j = -(L+S)$ and 1s state $m_j = -1/2$, where the remaining 1s electron is spin-down, therefore the excited 1s electron is spin-up.

³⁰ C.S. Fadley, *Electron Spectroscopy* Vol. II, ed. C.R. Brundle and A.D. Baker (Academic, London, 1978).

³¹ F.M.F. de Groot, J.C. Fuggle, B.T. Thole and G.A. Sawatzky, *Phys. Rev. B*, **42**, 5459 (1990).

³² B.T. Thole and G. van der Laan, *Phys. Rev. B* **38**, 3158 (1988).

³³ The branching ratio in $K\alpha$ XES is defined as the fraction of $K\alpha$ intensity in the $K\alpha_1$ line.

³⁴ F.M.F. de Groot, *J. Elec. Spec.* **67**, 529 (1994),

³⁵ K. Okada, A. Kotani and B.T. Thole, *J. Elec. Spec.* **58**, 325 (1992).

³⁶ the sample is a kind gift from professor P. Mascharak at University of California, Santa Cruz.

³⁷ L.E., Berman, J.B. Hastings, T. Oversluizen, M. Woodle, *Rev. Sci. Instrum.* **63**, 428 (1992).

³⁸ X. Wang, M.M. Grush, A. Freoschner, and S.P. Cramer, accepted by *J. Synchr. Rad.*

³⁹ M. Krause, *J. Phys. Chem. Ref. Data* **8**, 307 (1979).

⁴⁰ J.C. Fuggle and S.F. Alvarado, *Phys. Rev. A*, **22**, 1615 (1990).

⁴¹ Private communication

⁴² K. Okada, A. Kotani, H. Ogasawara, Y. Seino and B.T. Thole, *Phys. Rev. B* **47**, 6203 (1993).

Figure Captions:

Figure 1. Spin-polarized $K\alpha$ x-ray emission spectra of first row transition-metal ions using the ligand field multiplet calculation in O_h symmetry. Plotted are spin-down (solid line) and spin-up spectra (dotted line). For visual clarity, the total fluorescence spectra (spin-down plus spin-up) are omitted. All Slater integrals are reduced to 70% of their Hartree-Fock values. $10Dq$ is 0.9 eV in all cases and 3d spin-orbit coupling is neglected. Broadening parameters used are 0.6 eV Lorentzian (FWHM) and 0.5 eV Gaussian (FWHM). The difference spectra of spin-down and spin-up are shown in the right panel.

Figure 2. Crystal field effects on $K\alpha$ emission spectra in (a) d^4 - Cr^{2+} , (b) d^5 - Mn^{2+} , (c) d^6 - Fe^{2+} and (d) d^7 - Co^{2+} configurations. In all cases spin-down (solid line) and spin-up (dotted line) are plotted. The transition from high-spin to low-spin state occurs at 2.7 eV, 2.85 eV, 2.1 eV and 2.4 eV, respectively, from d^4 - Cr^{2+} to d^7 - Co^{2+} .

Figure 3. 3d spin-orbit effects on $K\alpha$ emission spectra in Co^{2+} . Top: Including 3d spin-orbit coupling. Bottom: Without 3d spin-orbit coupling. Plotted are spin-up (dotted line) and spin-down (solid line) spectra.

Figure 4. Charge transfer effects in Ni^{2+} on (a) $K\alpha$ emission and (b) $K\alpha$ emission. Top: Ligand field multiplet calculation. Bottom: Charge transfer multiplet calculation. Plotted are spin-up (dotted line), spin-down (solid line) and total spectra (dotted dashed line).

Figure 5. Spin-polarized $K\beta$ x-ray emission spectra of first row transition-metal ions using the ligand field multiplet calculation in O_h symmetry. Plotted are spin-down spectra (solid line) and spin-up spectra (dotted line). All Slater integrals are reduced to 70% of their Hartree-Fock values. $10Dq$ is used as 0.9 eV in all cases. Broadening parameters used are 1.5 eV (FWHM) Lorentzian and 0.5 eV (FWHM) Gaussian. The difference spectra of spin-down and spin-up are shown in the right panel.

Figure 6. Crystal field effects on $K\beta$ emission spectra in (a) d^4 - Cr^{2+} , (b) d^5 - Mn^{2+} , (c) d^6 - Fe^{2+} and (d) d^7 - Co^{2+} configurations. In all cases spin-down (solid line) and spin-up (dotted line) are plotted. The transition from high-spin to low-spin state occurs at 2.7 eV, 2.85 eV, 2.1 eV and 2.4 eV, the same as in $K\alpha$ emission spectra.

Figure 7. 3d spin-orbit effects on $K\beta$ emission spectra in Co^{2+} . Top: Including the 3d spin-orbit coupling calculation, the spin-up (dotted line) and spin-down (solid line) spectra. Bottom: Without 3d spin-orbit coupling calculation, the spin-up (dotted line) and spin-down (solid line) spectra.

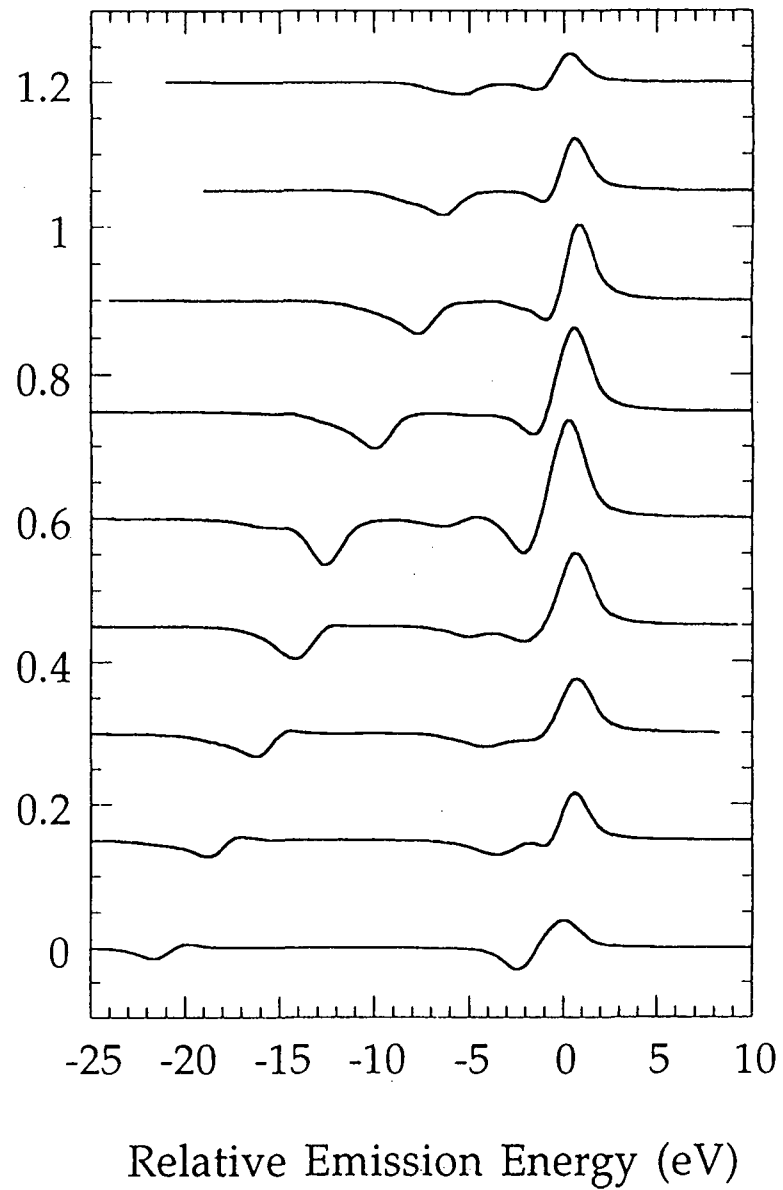
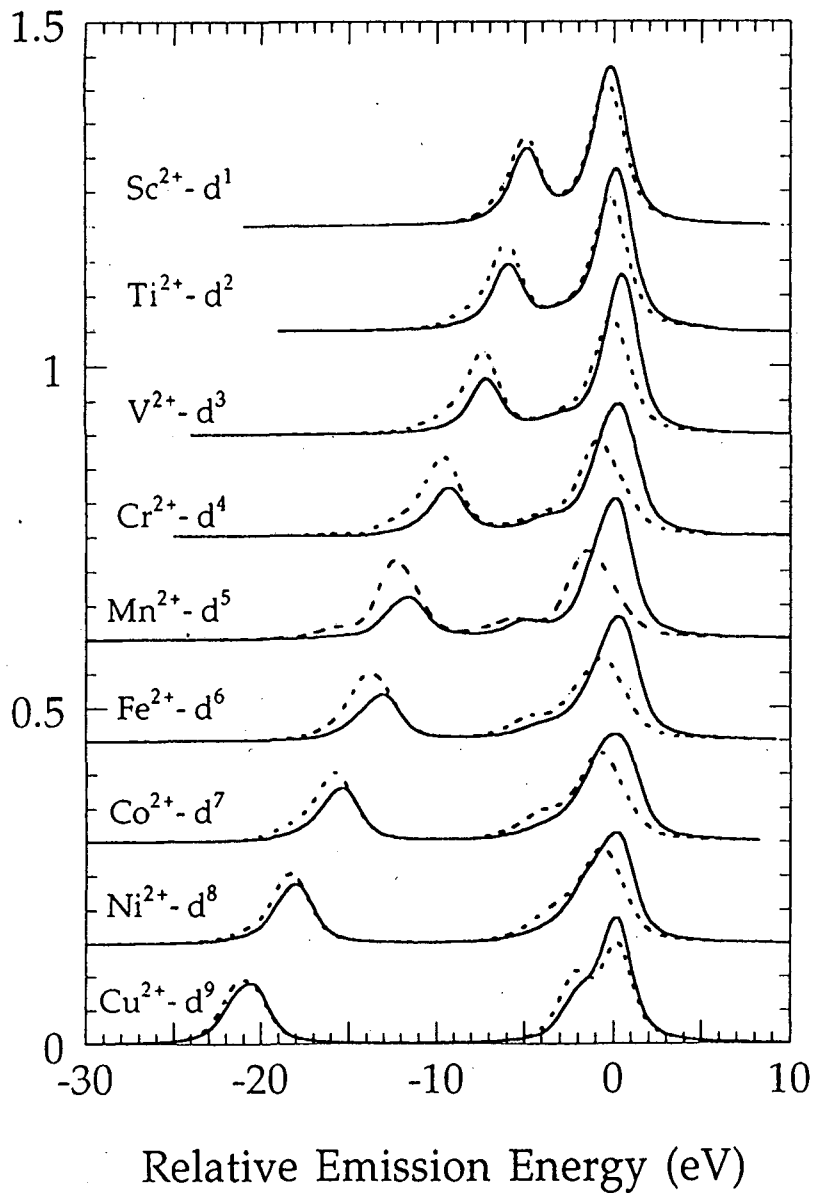
Figure 8. Comparison of experimental $K\alpha$ emission spectrum (top, dotted line) of $(PPh_4)_2[Ni(SePh)_4]$ with the ligand field multiplet calculation (bottom) in T_d symmetry. Calculated spectra are spin-up (dotted line), spin-down (solid line) and total spectra (solid line).

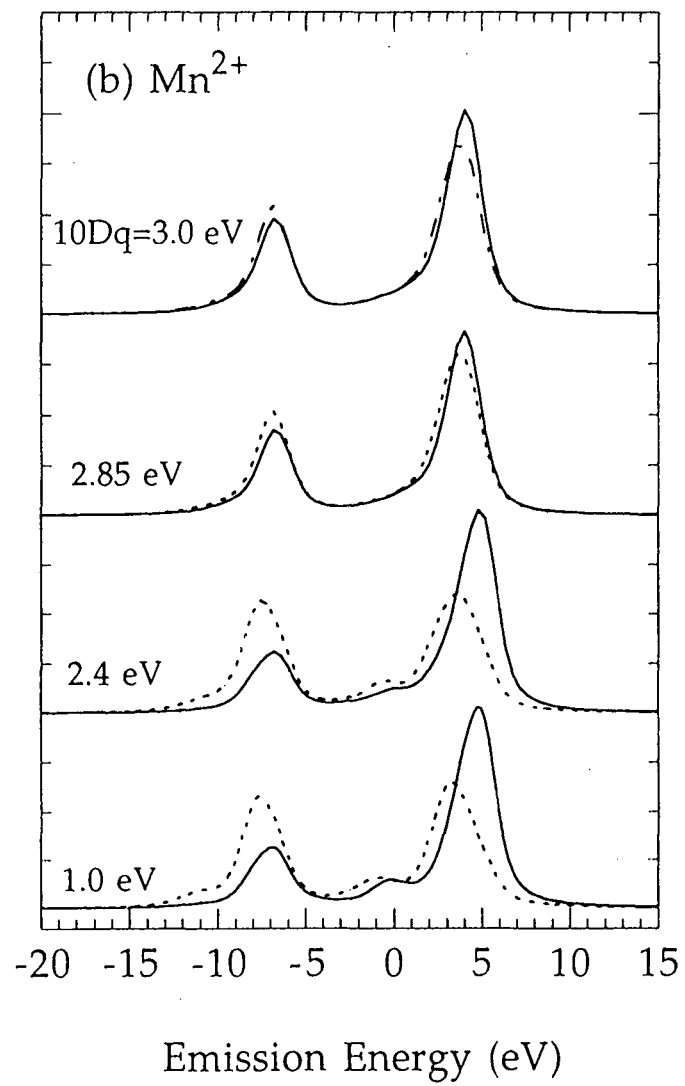
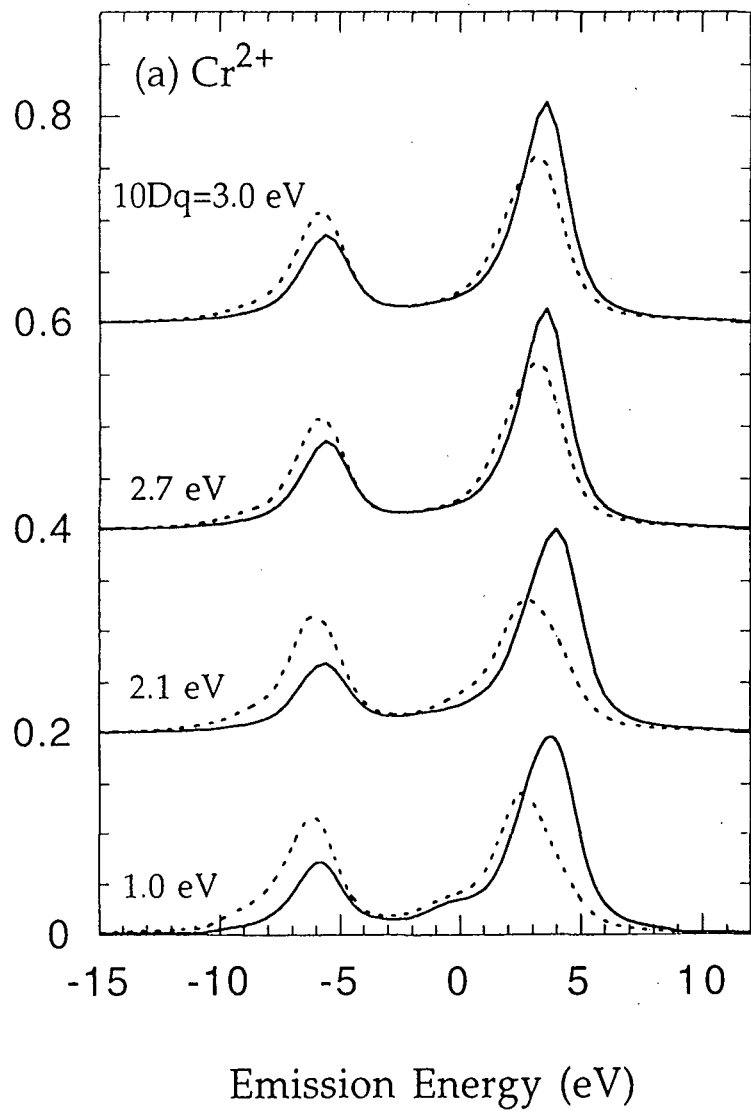
Figure 9. Experimental spin-polarized excitation spectra of $(PPh_4)_2[Ni(SePh)_4]$ by $K\alpha$ detection. Mostly spin-up spectrum (dotted line) was taken monitoring at 2.1 eV lower energy shoulder of $K\alpha_1$, and

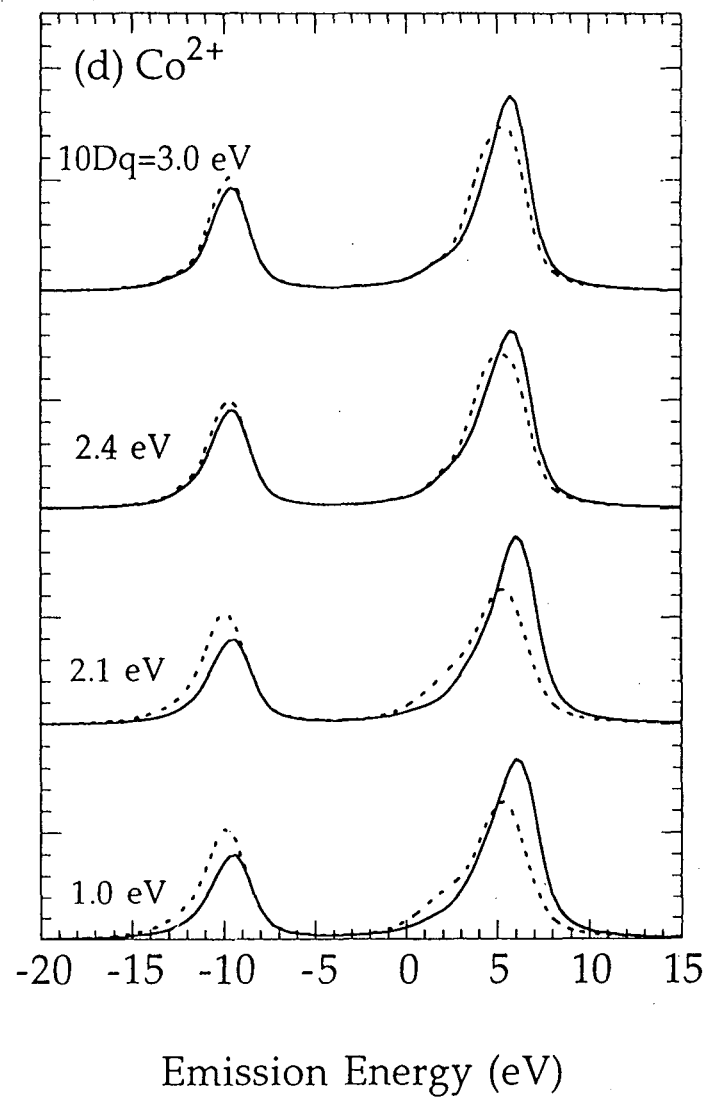
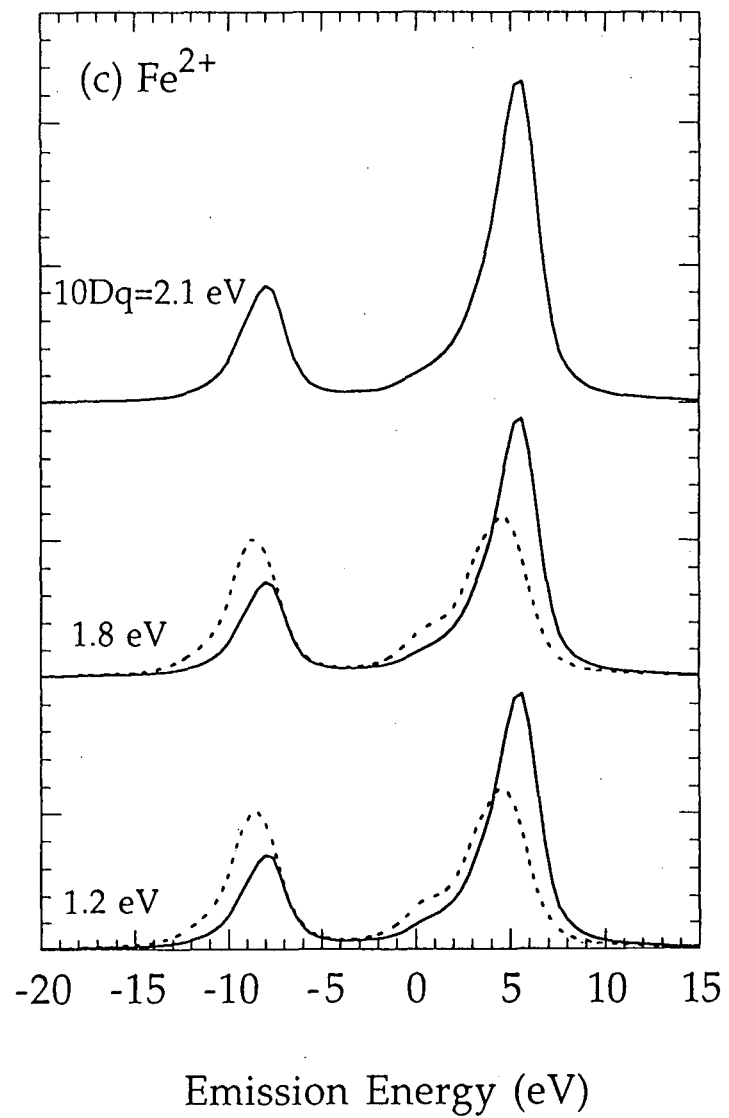
dominantly spin-down spectrum (solid line) at 1.3 eV higher energy shoulder of $K\alpha_1$, as indicated by arrows in Figure 8.

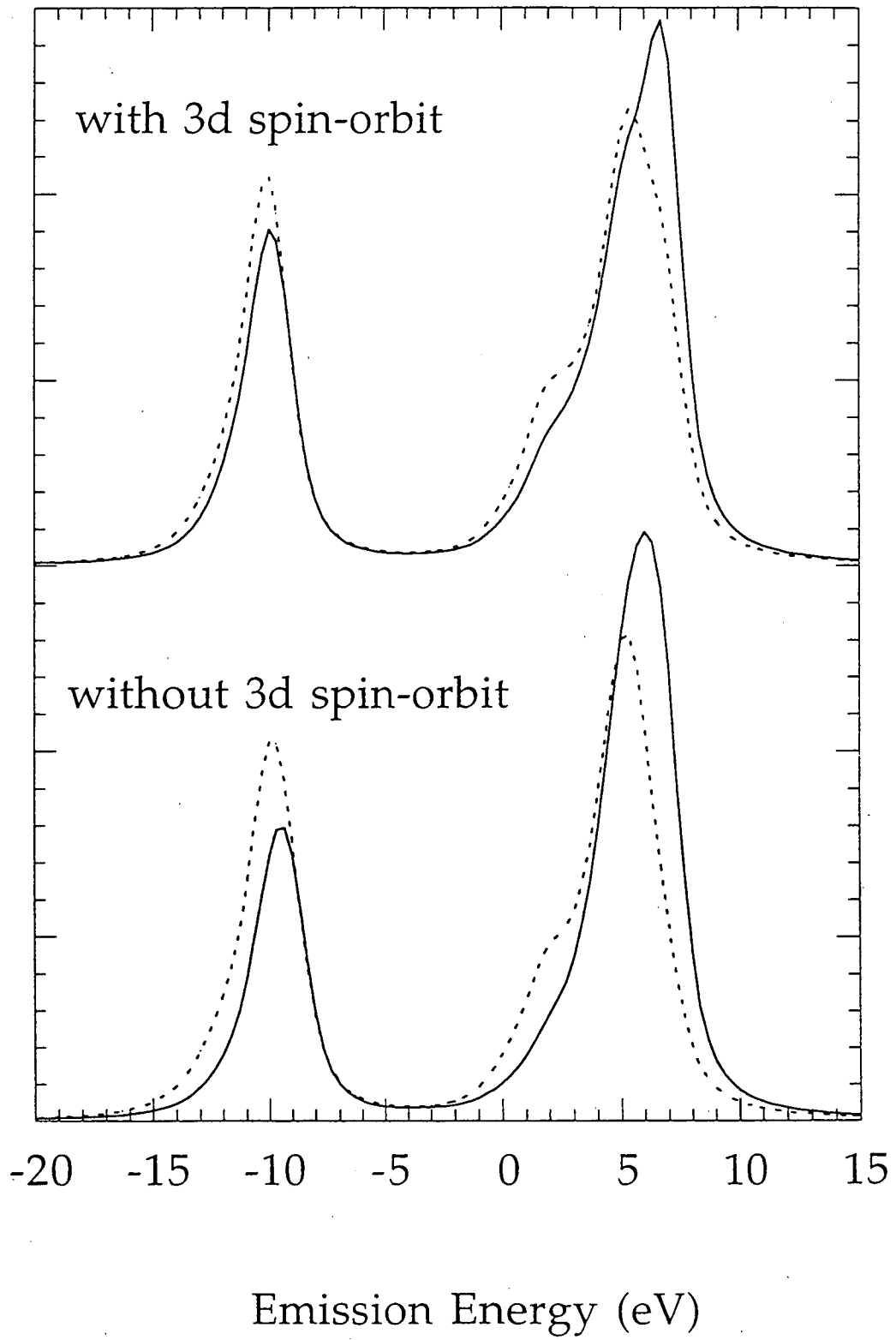
Figure 10. Comparison of experimental $K\beta$ emission spectrum (top, dotted line) of NiF_2 with the charge transfer multiplet calculation (bottom) in O_h symmetry. Calculated spectra are spin-up (dotted line), spin-down (solid line) and total spectra (solid line).

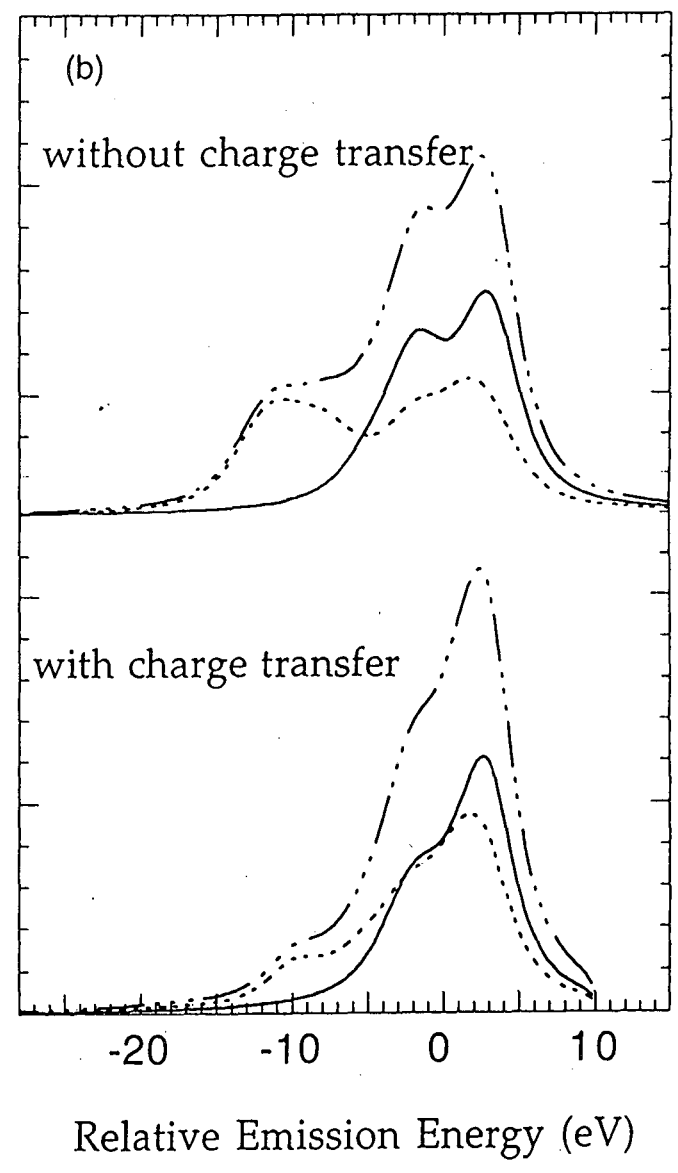
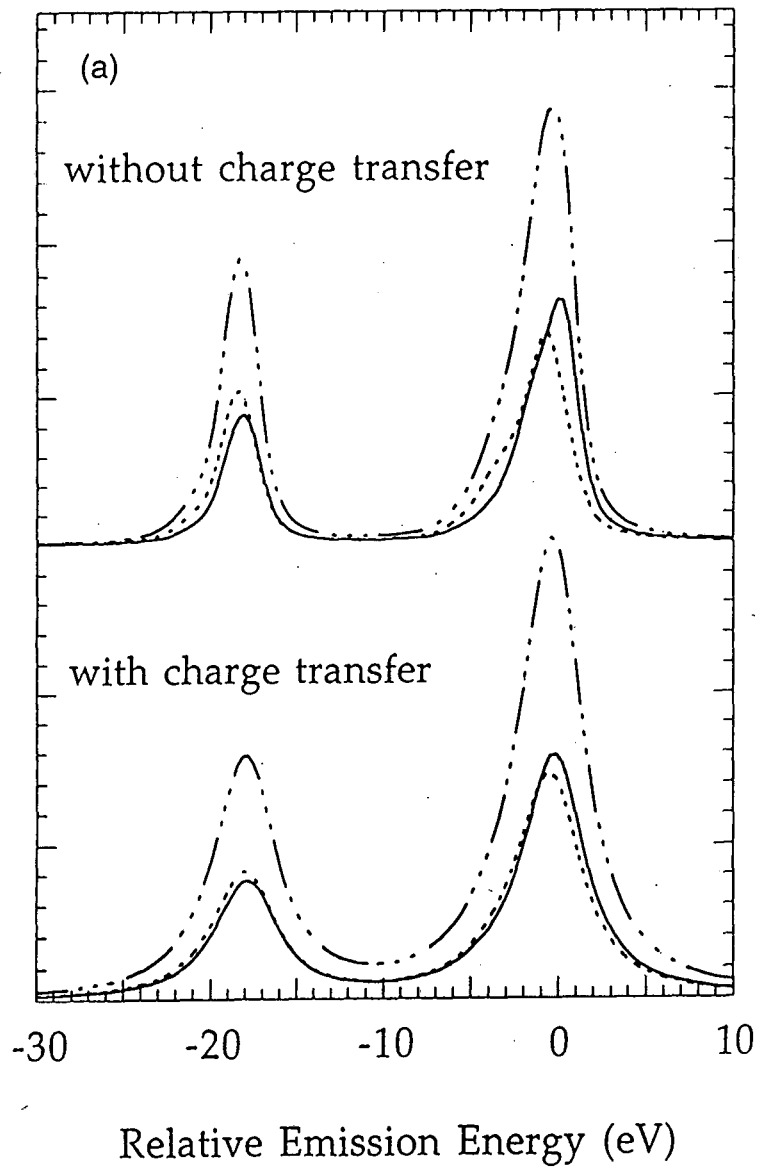
Figure 11. Experimental spin-polarized excitation spectra of NiF_2 by $K\beta$ detection. Spin-up spectrum (dotted line) was taken monitoring at the satellite $K\beta'$, and dominantly spin-down spectrum (solid line) monitoring 1 eV higher energy shoulder of $K\beta_{1,3}$, as indicated by arrows in Figure 10.

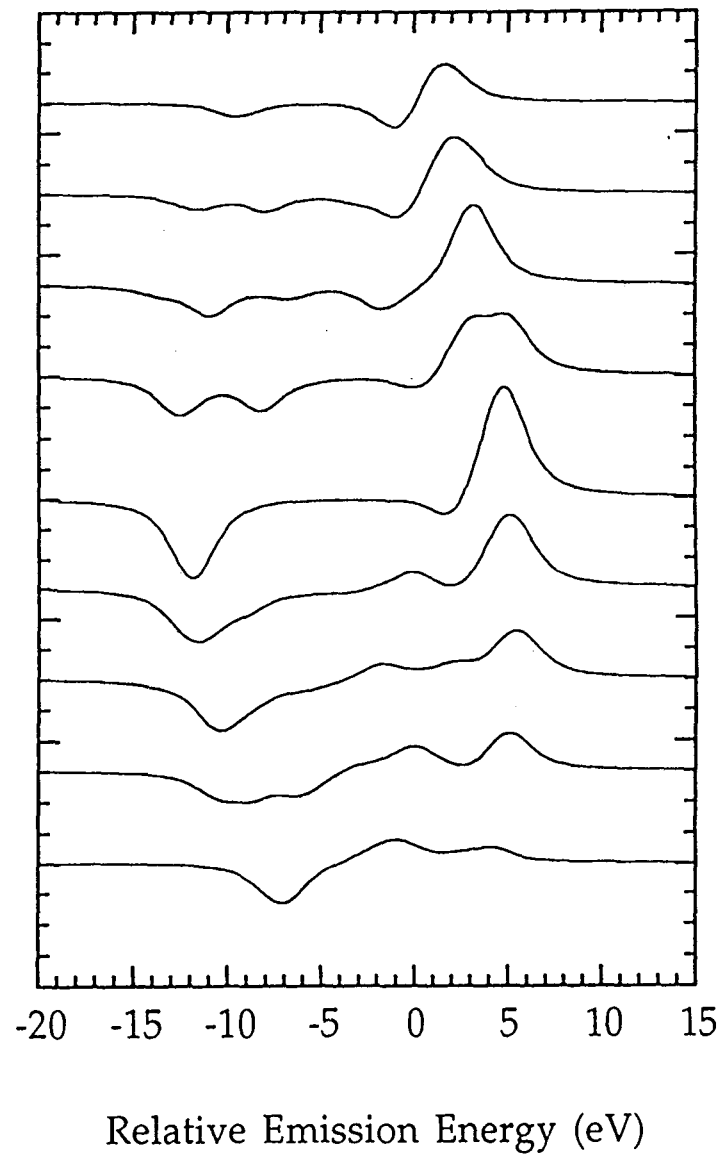
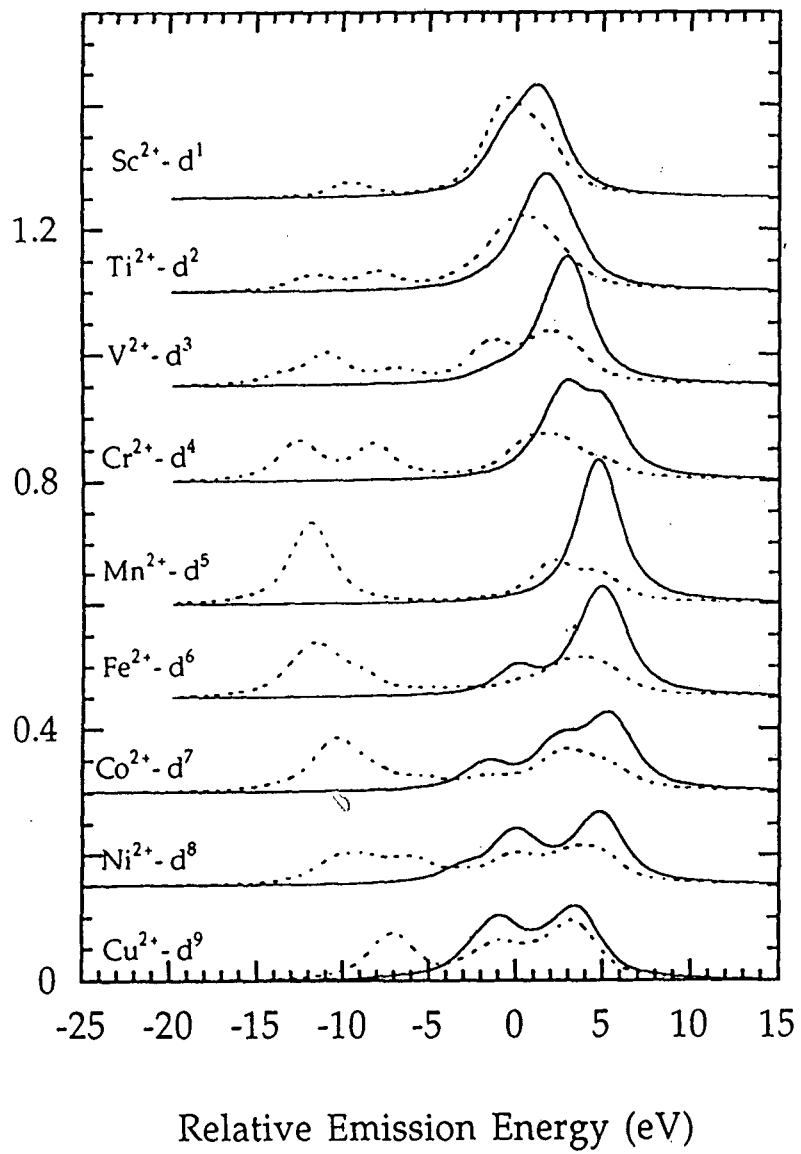


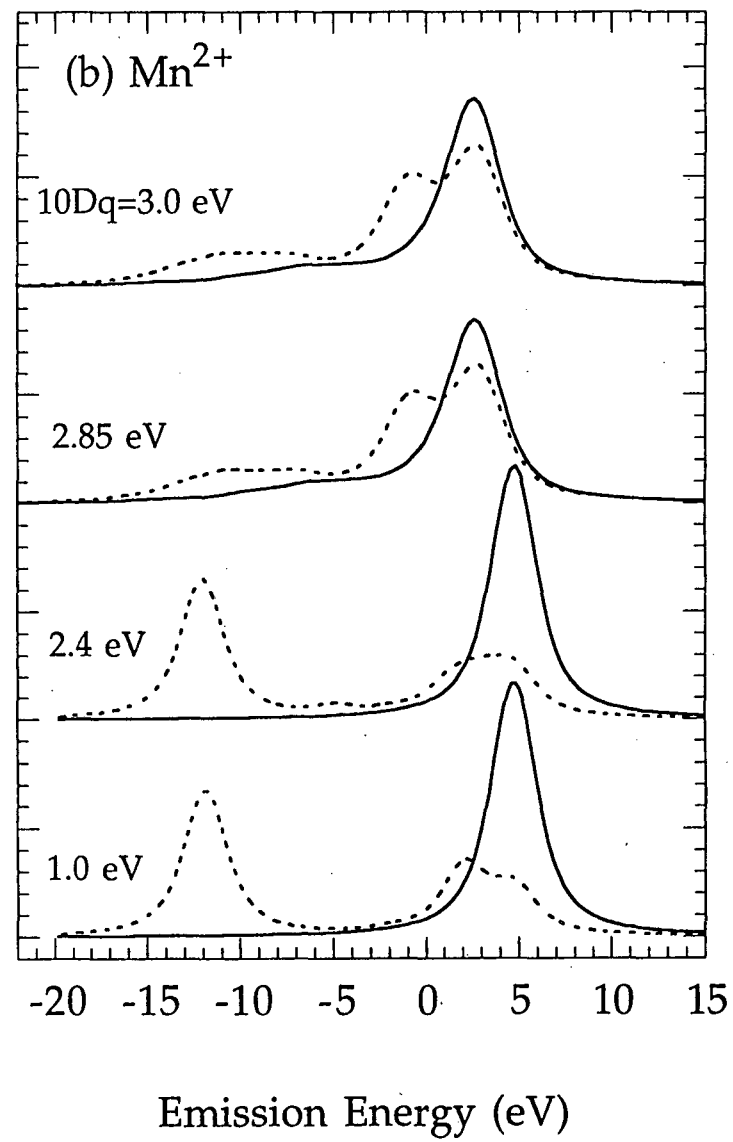
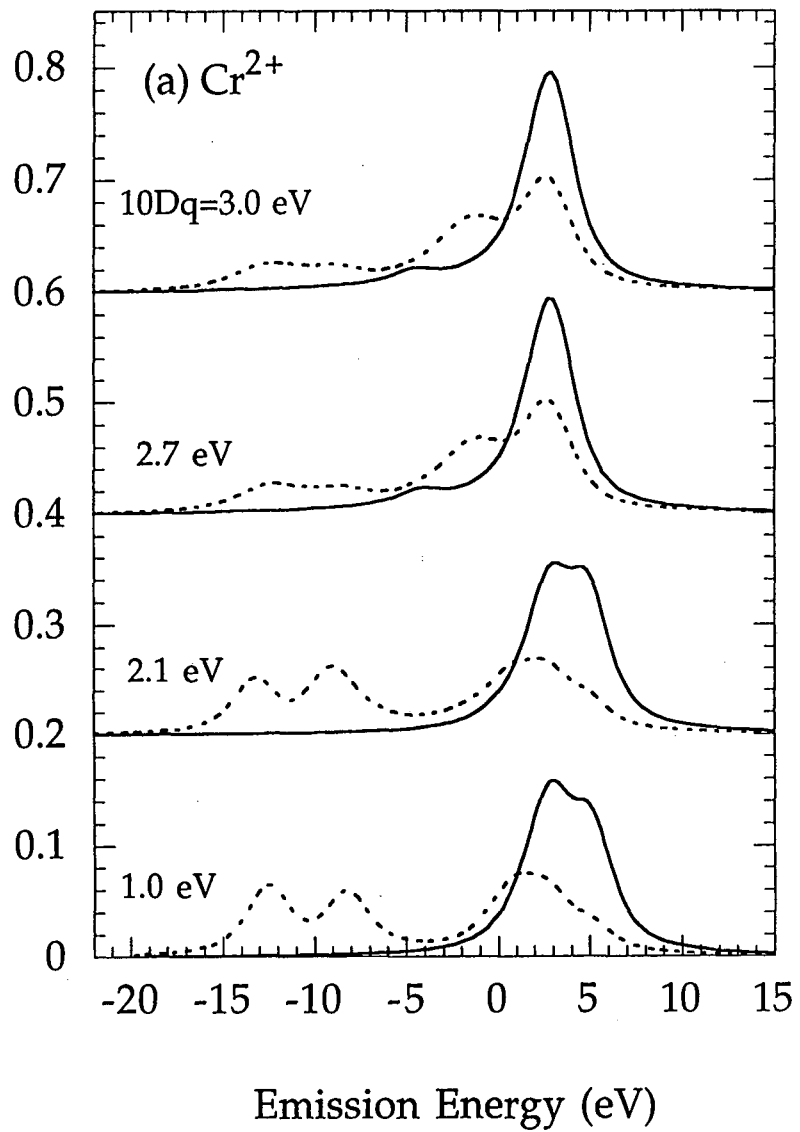


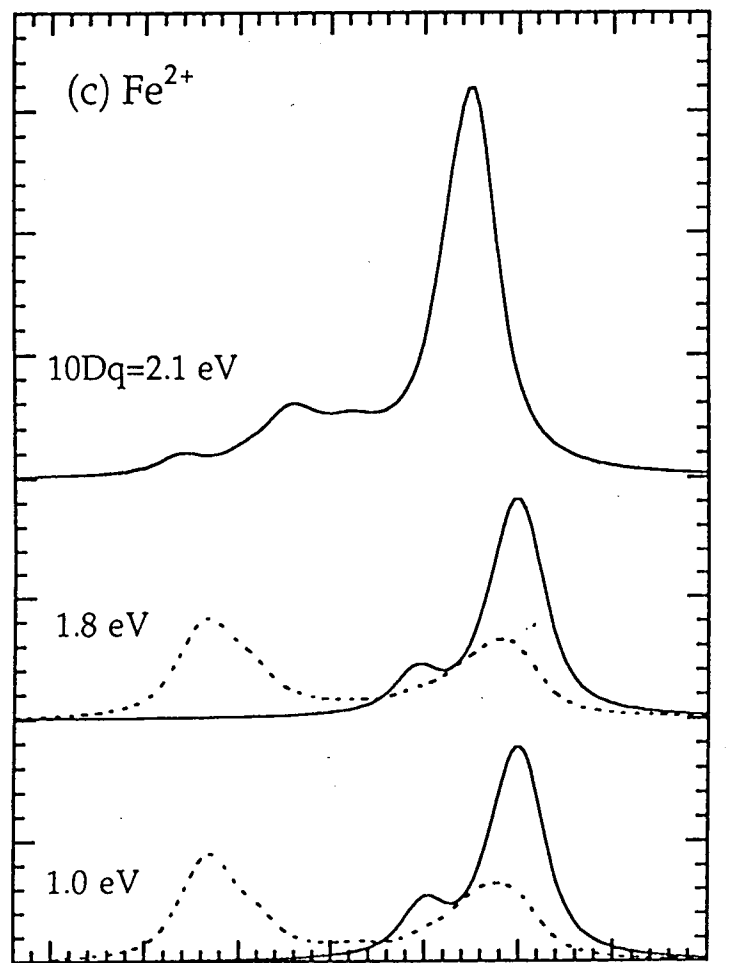






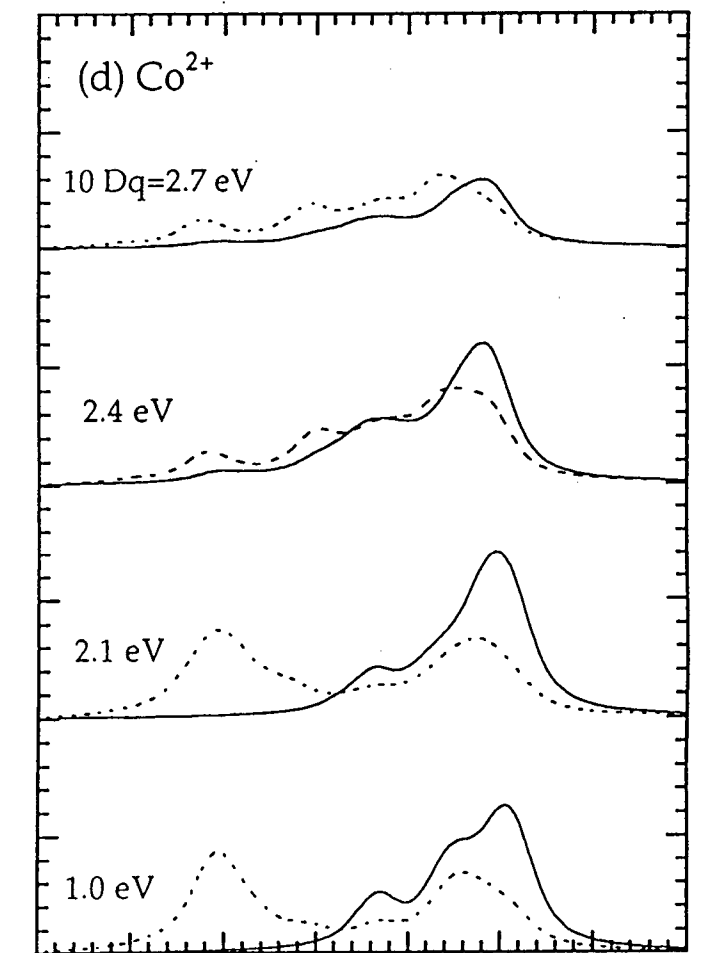






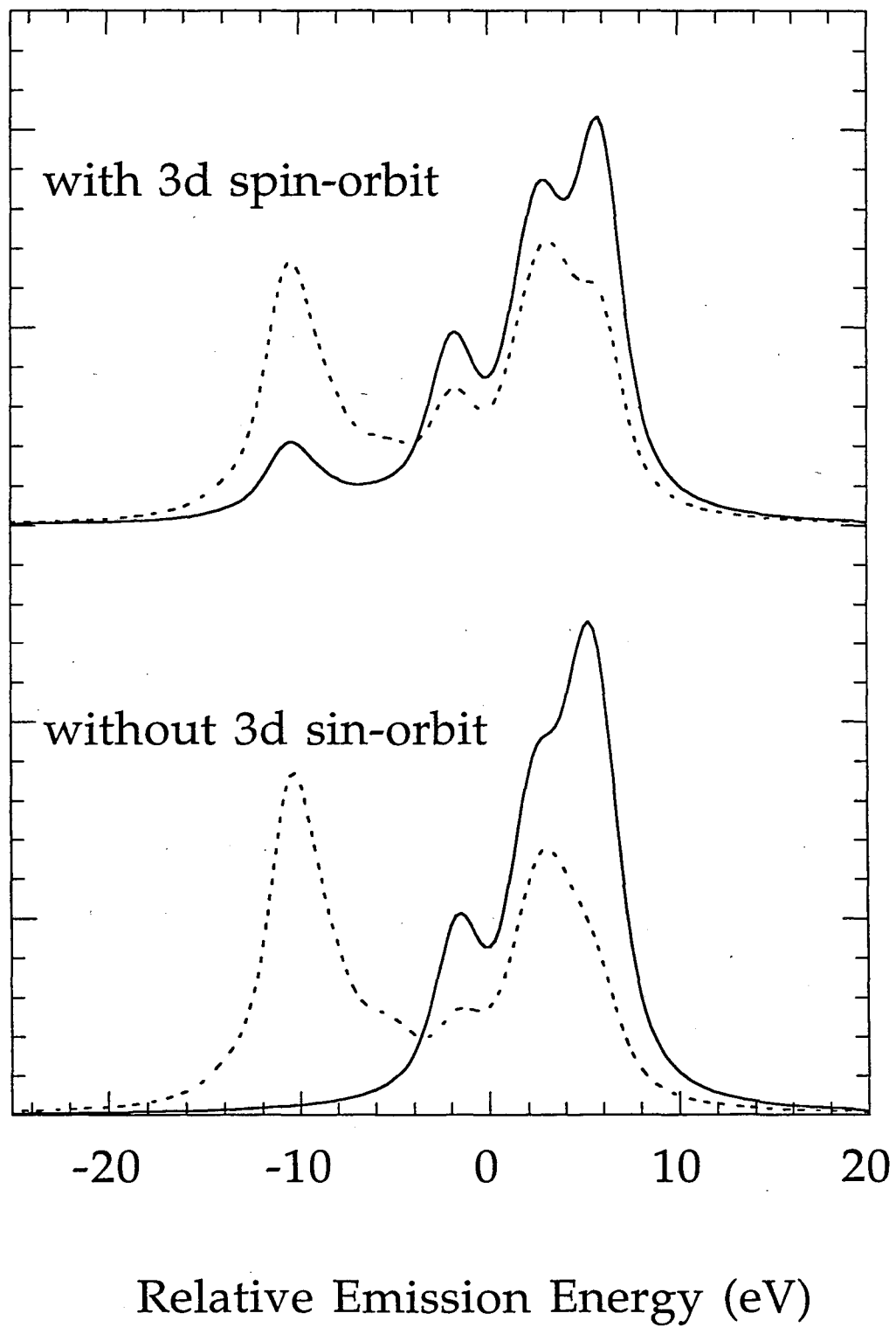
-20 -15 -10 -5 0 5 10 15

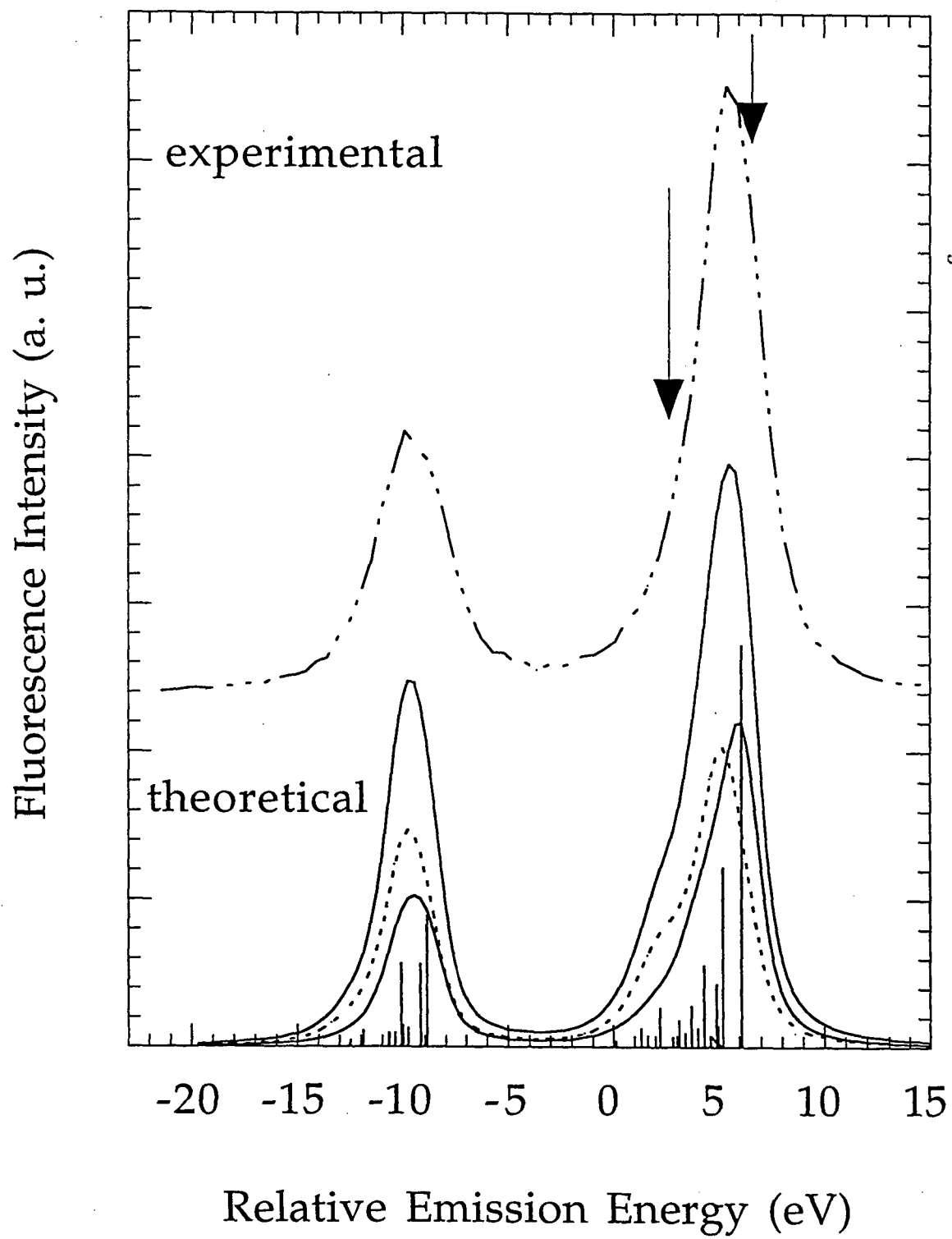
Emission Energy (eV)

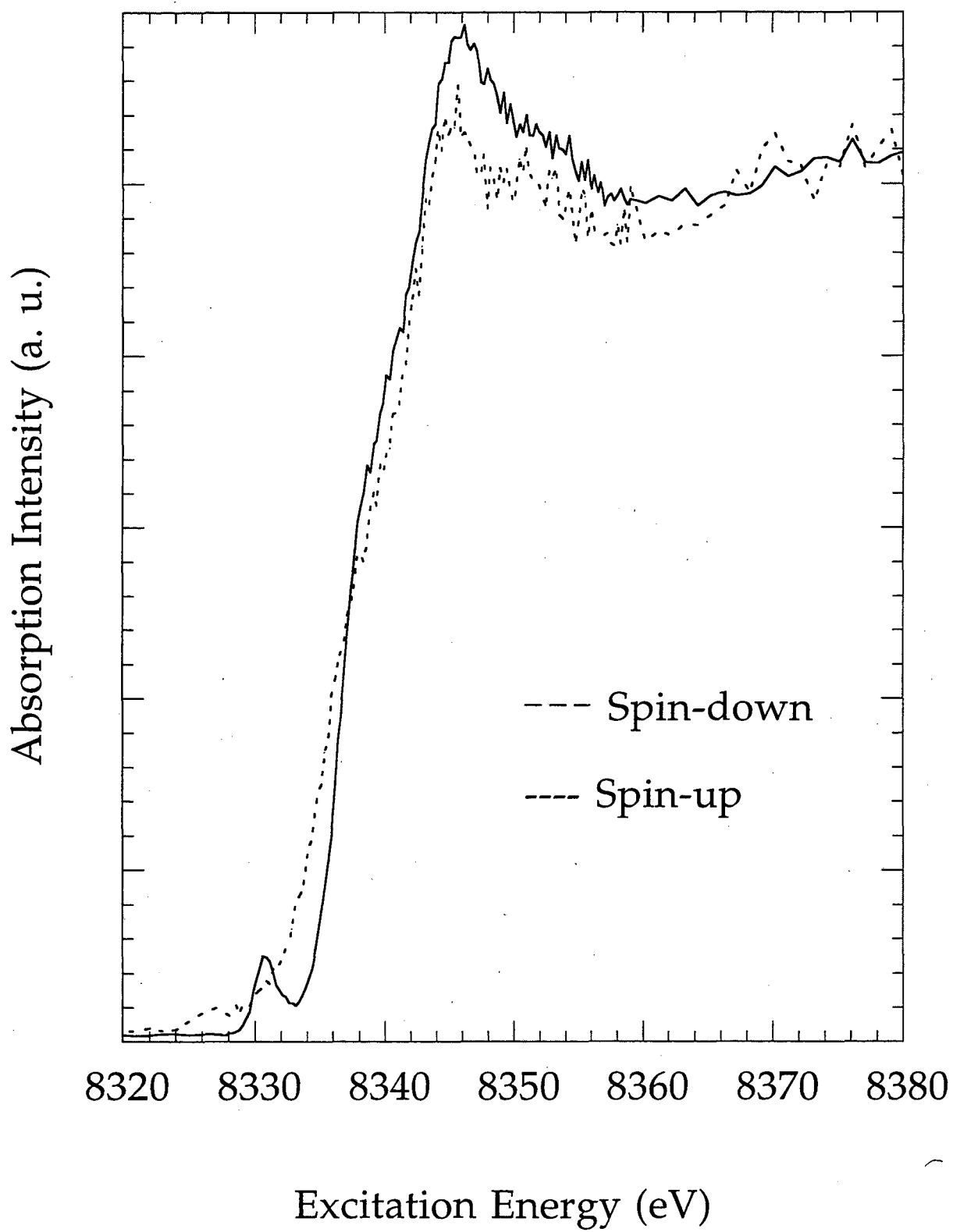


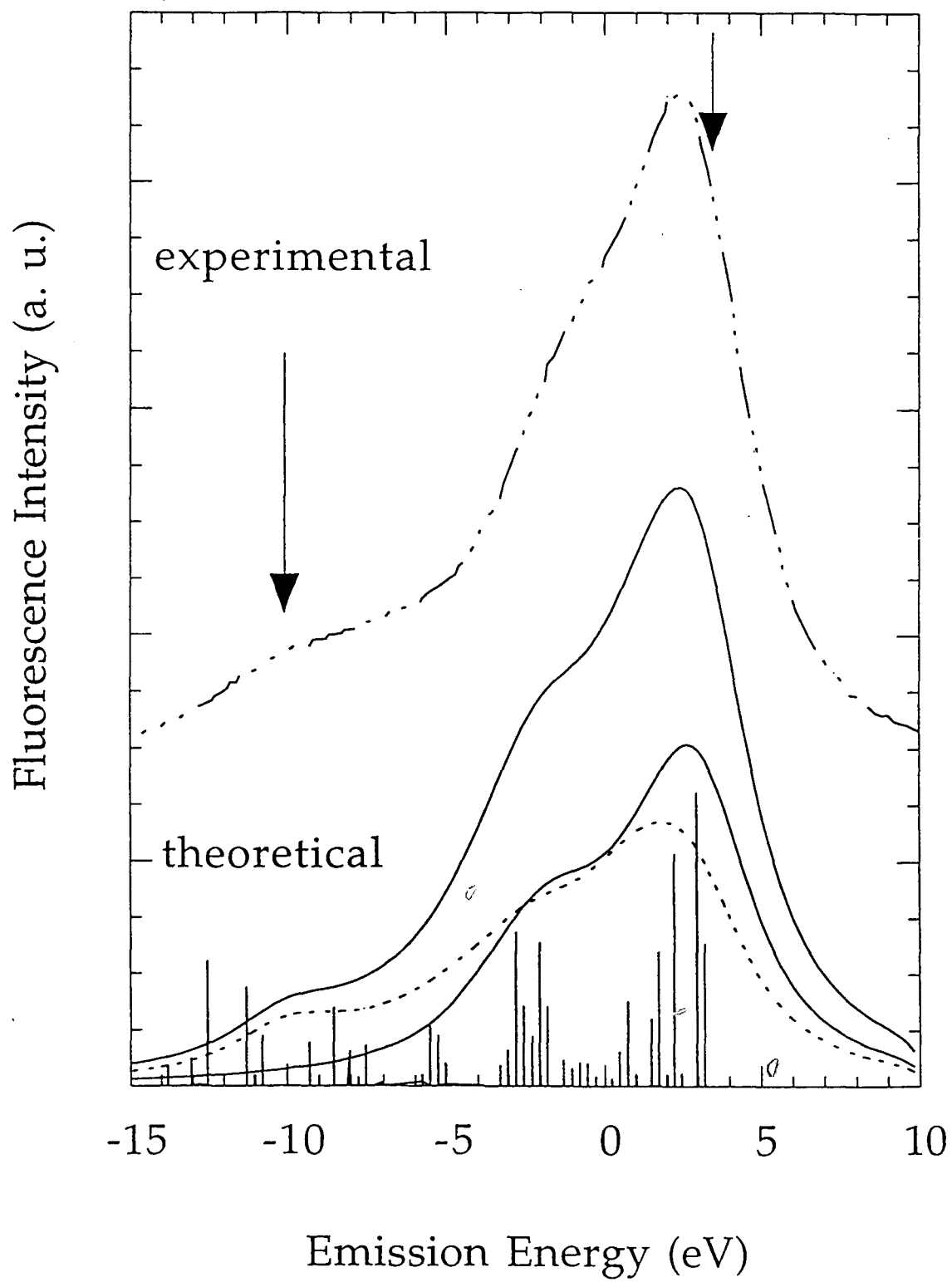
-20 -15 -10 -5 0 5 10 15

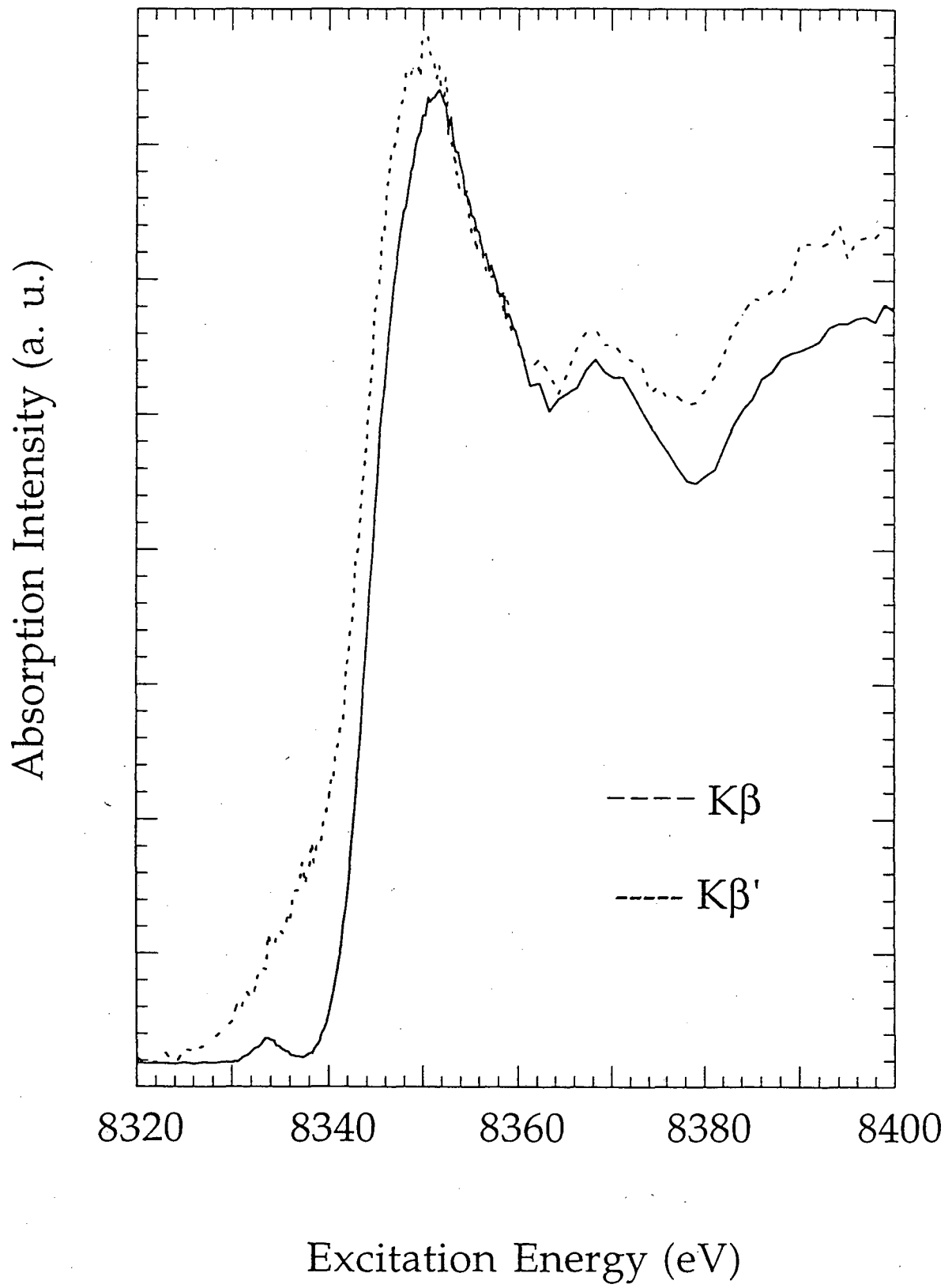
Emission Energy (eV)











References:

- 2.1 *X-ray Absorption Principles, Applications, Techniques of EXAFS, SEXAFS, and XANES*, eds by Konigsberger, D.C., Prins, R., Jone, Wiley and Sons, Inc., New York, 1988. p. 443
- 2.2 Meisel, A., Leonhardt, G. and Szargan, R., in *X-ray Spectra and Chemical Binding*, Springer-Verlag, Berlin, 1989.
- 2.3 Stern, E.A., *Theory of EXAFS in X-ray Absorption Principles, Applications, Techniques of EXAFS, SEXAFS, and XANES*, edited by Konigsberger, D.C., Prins, R., Jone Wiley and Sons, Inc., 1988. p.3.
- 2.4 *J. Physique* 47, C8, 3 (1986) (2 vols.)
- 2.5 *Resonant Anomalous X-Ray Scattering*, edited by Materlik, G., Sparks, C.J. & Fischer, K., North-Holland, Amsterdam, 1994.
- 2.6 Udagawa Y., Hayashi H., Tohji K & Mizushima T., *J. Phys. Soc. Japan.* 63, 1713 (1994).
- 2.7 Tulkki, J. and Åberg T., *J. Phys. B* 15 L435 (1982).
- 2.8 Åberg T. and Tulkki, J., in *Atomic Inner-shell Physics*, edited by Crasemann B. Plenum, New York, 1985. p.419.
- 2.9 de Groot, F.M.F, *Phys. Rev. B*, 53, 7099 (1996).
- 2.10 Carra, P., Fabrizio, M. & Thole, B.T., *Phys. Rev. Lett.* 74, 3700 (1995).
- 2.11 Ma, Y.J., *Phys. Rev. B*, 49, 5799 (1994).
- 2.12 Eisenberger, P., Platzman, P.M. and Winick, H., *Phys Rev. B* 31, 2377 (1976).
- 2.13 Tulkki, J. and Åberg T., *J. Phys. B* 13, 3341 (1980).
- 2.14 Hämäläinen, K., Siddons, D.P., Hastings, J.B., and Berman, L.E.. *Phys. Rev. Lett.*, 67, 2850 (1991).

- 2.15 Wang, X., Randall, C.R., Peng, G., and Cramer, S.P., *Chem. Phys. Lett.* **243**, 469 (1995).
- 2.16 Fuggle J.C. and Alvarado, S.F., *Phys. Rev. A*, **22**, 1615 (1990).
- 2.17 Peng, G., Wang, X., Randall, C., Moore, J. and Cramer, S.P., *App. Phys. Lett.* **65**, 2527 (1994).

Chapter 3. Spin-Polarized and Site-Selective X-ray Absorption of Fe Compounds

3.1. Spin Selective X-ray Spectroscopy

This section contains a published paper from Applied Physics Letter, 65, 2527 (1994), which describes the first high resolution $K\beta$ fluorescence results on an Fe model compound. At the end of the paper, a theoretical predictions of spin polarization of other first row transition-metal ions in $K\beta$ emission spectra are given. The calculations done at that time were not accurate for the spin-up and spin-down spectra, due to the incorrect definitions, as discussed in Chapter 2.3.

Spin Selective X-Ray Absorption Spectroscopy - Demonstration using High Resolution Fe K β Fluorescence

G. Peng^{a)}, X. Wang, C. R. Randall, J. A. Moore^{b)} and S. P. Cramer

Department of Applied Science, U. C. Davis, CA 95616 and Energy & Environment Division, Lawrence Berkeley Laboratory, Berkeley, California 94720

Abstract

In this paper it is shown that high resolution Fe K β excitation spectra can be used to separately probe empty spin-up and spin-down final states. Spin-selective x-ray absorption spectra were obtained by selectively monitoring different regions of the K β emission. The fluorescence was excited with monochromatized synchrotron radiation and analyzed using a spherically bent Ge(620) crystal. Spin-polarization was demonstrated by showing that the 1s \rightarrow 3d transition at the Fe K-edge is seen with K $\beta_{1,3}$ detection, but missing in the excitation spectrum using K β' detection. The spin-polarization is also confirmed by ligand field atomic multiplet calculations that reproduce the K β spectra. Calculations are presented showing the applicability of spin-polarized K β detection to nearly all first transition metal ions.

a), U.C. Davis only.

b), Lawrence Berkeley Laboratory only.

The scientific and technological importance of magnetic materials and their properties has stimulated interest in magnetically sensitive x-ray measurements (1-3). For example, x-ray magnetic circular dichroism measurements have been used to determine the spin and orbital contributions to the magnetic moment of the absorbing atom (4), as well as to provide information about the magnetic properties of neighboring atoms (5). In this paper we show that the exchange splitting of Fe $K\beta$ spectra can be used to extract spin-sensitive x-ray absorption spectra, without the use of circular polarization or magnetic fields. Experimental $K\beta$ emission and excitation spectra are reported for a high-spin iron(III) complex, and atomic multiplet calculations are presented which reproduce the data and elucidate the spin-dependent regions. Calculations for other 3d metals are presented which show the broad applicability of $K\beta$ detection for spin-polarized absorption spectroscopy.

$K\beta$ x-ray emission spectra were recorded on wiggler beam line 6-2 at the Stanford Synchrotron Radiation Laboratory using previously described methods (6,7) with a set of 4 spherically bent Ge(620) crystal spectrometers. Each bent crystal was separately aligned on the Rowland circle, and the diffracted beams were all deflected vertically to a nearly common focus. Fluorescence excitation spectra were obtained by setting the secondary monochromator to a particular energy, and then scanning the upstream Si(111) spectrometer to vary the excitation energy. The incident flux, focused with a toroidal mirror and defined by a 1 mm x 2 mm slit, was approximately 10^{11} photons/sec. The maximum total fluorescence count rate at the NaI detector was ~ 500 photons/sec. Spectra for the pure powdered sample of $(\text{NEt}_4)[\text{FeCl}_4]$ (8) were recorded at room temperature. The absorption spectra

were calibrated by using internal standard of $1s \rightarrow 3d = 7113.0$ eV (9), while the emission energies were calibrated by 7058 eV for the $K\beta_{1,3}$ energy (10).

The $K\beta$ emission spectrum for $(\text{NEt}_4)[\text{FeCl}_4]$, excited using 7180 eV synchrotron radiation, is shown in Figure 1. The stronger peak, near 7058 eV, is known as the $K\beta_{1,3}$ line, while the weaker feature near 7043 eV is the $K\beta'$ region. As early as 1927 (11), Coster and Druyvesteyn proposed that the splitting of $K\beta$ ($3p \rightarrow 1s$) fluorescence into $K\beta_{1,3}$ and $K\beta'$ features came from the interaction between the 3p core hole and the incomplete shell of 3d electrons. As elucidated by Tsutsumi (12), the $K\beta_{1,3}$ region primarily has final states with the net spin of the open $3p^5$ shell parallel to the 3d shell spin. The 3p3d exchange stabilization yields a lower energy state, and the emitted fluorescence is therefore at higher energy. The splitting between these two regions is thus a result of the 3p-3d exchange interaction. Although other explanations have been offered (13), experiments and calculations by both Tsutsumi (12) and Nefedov (14) strongly support this multiplet assignment. Additional support comes from the observation that the strongest $K\beta'$ lines are generally associated with the highest spin complexes (13).

In Figure 1, the measured spectrum is compared with a simulation using ligand field multiplet calculations that include orbital angular momentum and crystal field effects (15). As with previous Mn $K\beta$ calculations (16), we find that the $K\beta'$ region is solely 5P final states, while the $K\beta_{1,3}$ region is predominantly 7P final states, with a group of 5P states contributing a lower energy shoulder. The $K\beta'$ region is consistently broader than the $K\beta_{1,3}$ features, presumably because additional higher energy final states are available.

The previous Mn experiments (6,16) showed that by monitoring the $K\beta_{1,3}$ emission while scanning the excitation energy, absorption by transitions to spin-down vacancies can be monitored, while selecting the $K\beta'$ emission probes spin-up transitions. Results for the analogous experiment on $(\text{NEt}_4)[\text{FeCl}_4]$ are shown in Figure 2. At the foot of the $K\beta_{1,3}$ excitation spectrum there is a distinct absorption feature - the well-known $1s \rightarrow 3d$ transition. Since the high-spin $3d^5 [\text{FeCl}_4]^-$ complex has a filled spin-up shell of 3d electrons, and since the electron spin does not change in an x-ray transition, this transition necessarily involves a spin-down electron. The promotion of a spin-down electron from the 1s core is followed by relaxation of a spin-down 3p electron. This yields a net spin-up $3p^5$ shell, which has an exchange coupling with the 3d electrons. Although there may be some changes in the fluorescence spectrum when on resonance with $1s \rightarrow 3d$ transitions, because of the change in 3d occupation number, in general the exchange stabilization of the final states will persist. Hence, the fluorescence from promoting spin-down electrons will be found at higher energies, while the fluorescence from spin-up transitions will be found at lower energies.

The predictions from the simple exchange picture are confirmed by examination of the $K\beta'$ fluorescence excitation spectrum. The $1s \rightarrow 3d$ feature is no longer observed, since it cannot be reached with spin-up electrons. There are also differences in features at higher energies, but a full analysis will require improved beamline resolution and better statistics. Substantial differences throughout the XANES region were previously shown for various Mn compounds this same technique (6,16).

As noted by Hämäläinen (6), spin-polarized EXAFS (5) measurements are also feasible using $K\beta$ detection. If neighboring atoms have a net spin, then they may scatter spin-up or spin-down electrons differently. So in principal, spin-polarized EXAFS can be used to distinguish magnetic from non-magnetic neighbors and to reveal the relative spin-orientations of neighbors with respect to the absorber. Although Schütz and coworkers have demonstrated spin-polarized EXAFS using circularly polarized x-rays (17,18), at K-edges the spin-polarization of the outgoing electron achieved with circular polarization is only $\sim 1\%$ (17), and the observed effects are quite weak. With high resolution $K\beta$ detection, essentially 100% spin polarization can be achieved, and spin-polarized EXAFS effects should therefore be much stronger.

So far, spin-polarized $K\beta$ spectra have only been reported for Fe and Mn (6,16). Since high-spin Fe(III) and Mn(II) both have half-filled d-shells, they possess the largest spin and biggest $K\beta$ splittings of the first-row transition metals. To evaluate feasibility among less favorable cases, we have calculated emission spectra for d^1 through d^9 complexes across the first transition series. The results (Figure 3) show that $K\beta$ splittings of several volts are expected even in the least favorable cases, hence spin-dependent spectra should be feasible from Sc(II) through Cu(II). Even bigger L β splittings are seen in the rare earths, and exchange splitting effects are also present in second-row transition metal L γ spectra (13).

In summary, we have shown that high resolution Fe $K\beta$ spectra can be recorded with a spherically bent Ge(620) monochromator. Using variable energy synchrotron radiation excitation, a spectrum that primarily probes the

spin-down density of states can be obtained by monitoring the $K\beta_{1,3}$ emission, while $K\beta'$ detection probes solely the spin-up density of states. By choosing appropriate absorption edges and emission lines, high resolution x-ray fluorescence excitation spectra offer the promise of spin-sensitive spectroscopy for a wide range of elements.

The authors would like to thank Drs. Frank de Groot and K. Hämäläinen for useful discussions, as well as the Department of Energy, Office of Health and Environmental Research, the American Chemical Society, Petroleum Research Fund, and the National Institutes of Health (grant GM-48145) for support of this work. SSRL is supported by the Department of Energy, Office of Basic Energy Sciences. and the National Institutes of Health - Division of Research Resources.

References

- (1) B. E. Warren, "X-Ray Diffraction", Dover Publications, New York (1990)
- (2) D. B. McWhan, J. B. Hastings, C. C. Kao, D. P. Siddons, *Rev. Sci. Instr.* **63**, 1404 (1992)
- (3) D. B. McWhan, *NSLS Newsletter*, July (1993), 6-14.
- (4) a) B. T. Thole, P. Carra, F. Sette, and G. van der Laan, *Phys. Rev. Lett.* **68**, 1943 (1992) b) P. Carra, *Synchrotron Radiation News*, **5**, 21 (1992)
- (5) G. Schütz, R. Frahm, P. Mautner, R. Wienke, W. Wagner, W. Wilhelm, and P. Kienle, *Phys. Rev. Lett.* **62**, 2620 (1989)
- (6) K. Hämäläinen, C. C. Kao, J. B. Hastings, D. P. Siddons, L. E. Berman, V. Stojanoff and S. P. Cramer, *Phys. Rev. B*, **46**, 14274 (1992).
- (7) V. Stojanoff, K. Hämäläinen, D. P. Siddons, J. B. Hastings, L. E. Berman, S. P. Cramer, and G. Smith, *Rev. Sci. Instrum.* **63**, 1125 (1992).
- (8) N. S. Gill, *J. Chem. Soc.* 3512 (1961).
- (9) J. A. Bearden and A. F. Burr, *Rev. Mod. Phys.* **39**, 125 (1967)
- (10) 'X-ray Data Booklet', D. Vaughan, Ed, *Lawrence Berkeley Lab Pub-490*, University of California, Berkeley (1986).
- (11) D. Coster and M. Druyvesteyn, *Z. Phys.* **40**, 765 (1927).
- (12) a) K. Tsutsumi, *J. Phys. Soc. Japan* **14**, 1696-1706 (1959),
b) K. Tsutsumi, *J. Phys. Soc. Japan*, **25**, 1418 (1968).
- (13) B. Ekstig, E. Kallne, E. Noreland, R. Manne, *Physica Scripta*, **2**, 38 (1970).
Other explanations for the $K\beta$ structure are reviewed in this reference.
- (14) a) V. I. Nefedov, *Bull. Acad. Sci. USSR. Phys. Ser.* **2**, 724, (1964),
b) V. I. Nefedov, *J. Struct. Chem.* **7**, 672 (1966).
- (15) The ligand field atomic multiplet calculations used to simulate the emission spectra for Fe(III) used a $1s^1 3p^6 3d^5$ initial state and $1s^2 3p^5 3d^5$ final states. Hartree-Fock calculations were used to evaluate the $3d3d$ and $3p3d$

coulomb integrals (F_2^{pd} , F_2^{dd} , F_4^{dd}), which were reduced to 80% of their calculated atomic values, while the 3p3d exchange integrals G_1 and G_3 , which determine the main peak and satellite splitting, were reduced to 55%. To describe the local symmetry a ligand field splitting ($10Dq = -0.5$ eV) was included. The spectra were convoluted with Lorentzians of 1.5 or 3 eV FWHM (for $K\beta$ and $K\beta'$ regions respectively) and with a Gaussian of $s = 0.5$ eV, to describe the lifetime and instrumental broadening respectively.

(16) G. Peng, F. M. F. deGroot, K. Hämäläinen, J. A. Moore, X. Wang, M. M. Grush, J. B. Hastings, D. P. Siddons, W. H. Armstrong, O. C. Mullins and S. P. Cramer, *J. Am. Chem. Soc.* **116**, 2914-2920 (1994).

(17) G. Schütz, *Physica Scripta* **T29**, 172-176 (1989).

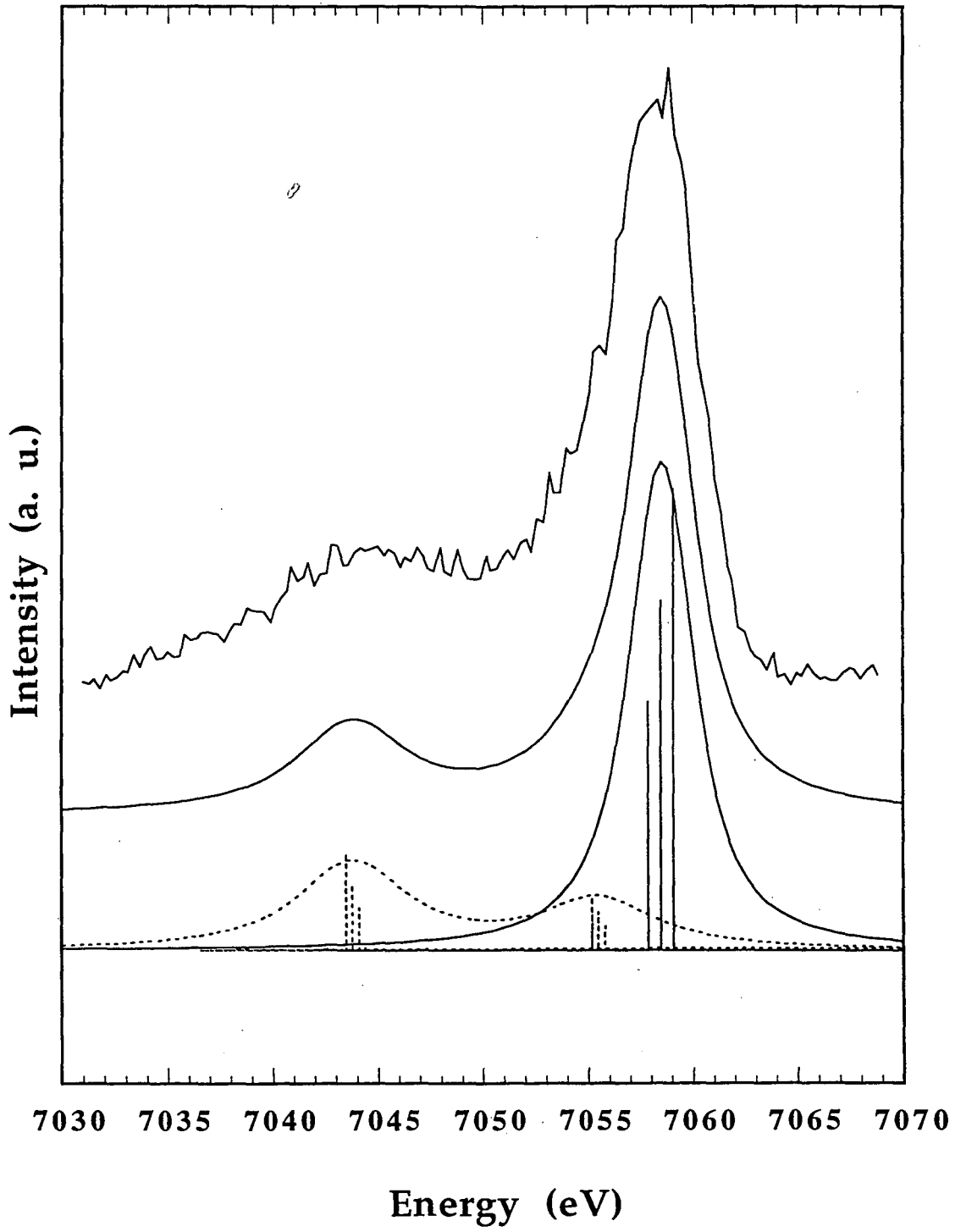
(18) G. Schütz, R. Frahm, P. Mautner, R. Wienke, W. Wagner, W. Wilhelm, and P. Kienle, *Phys. Rev. Lett.* **62**, 2620 (1989).

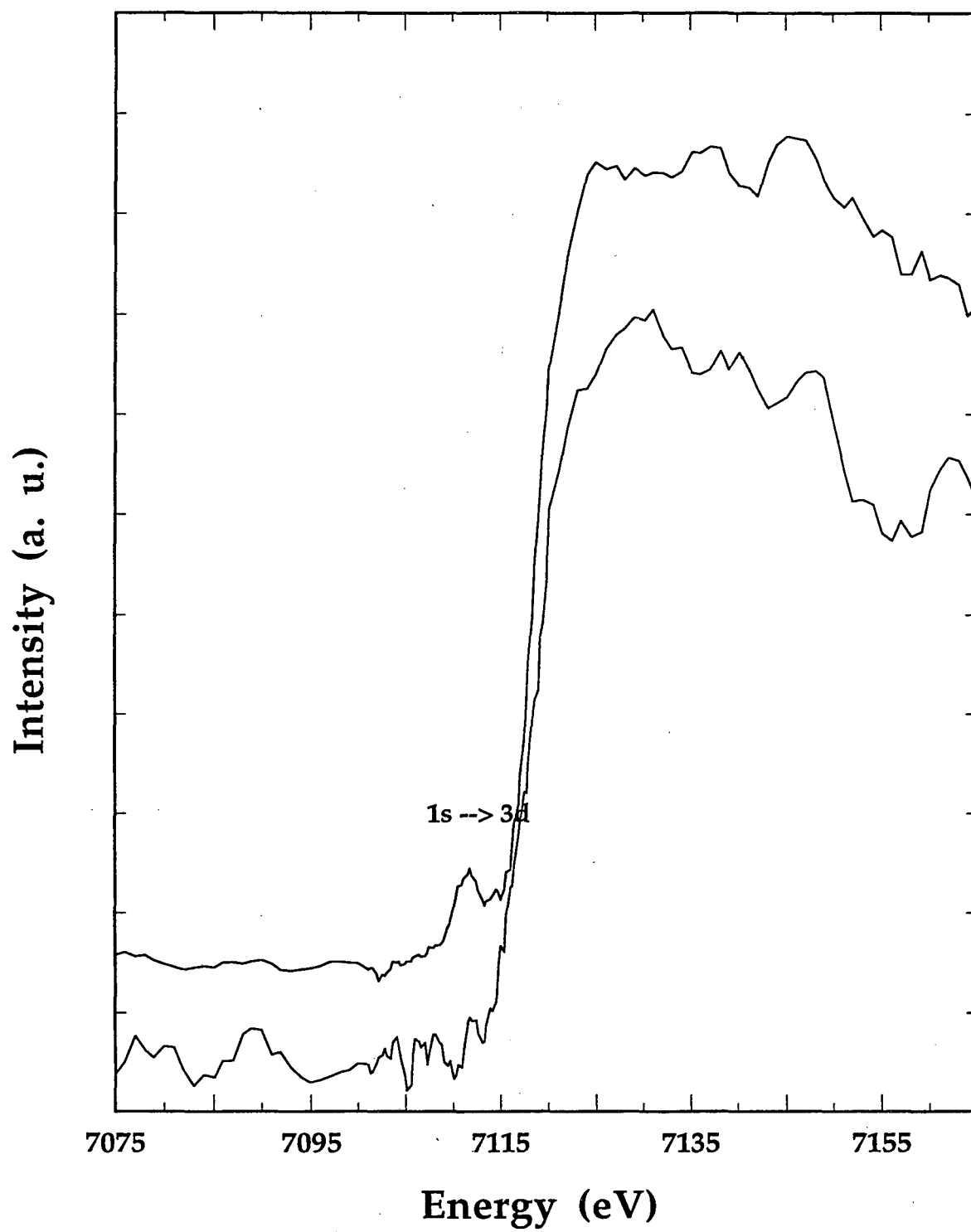
Figure Captions

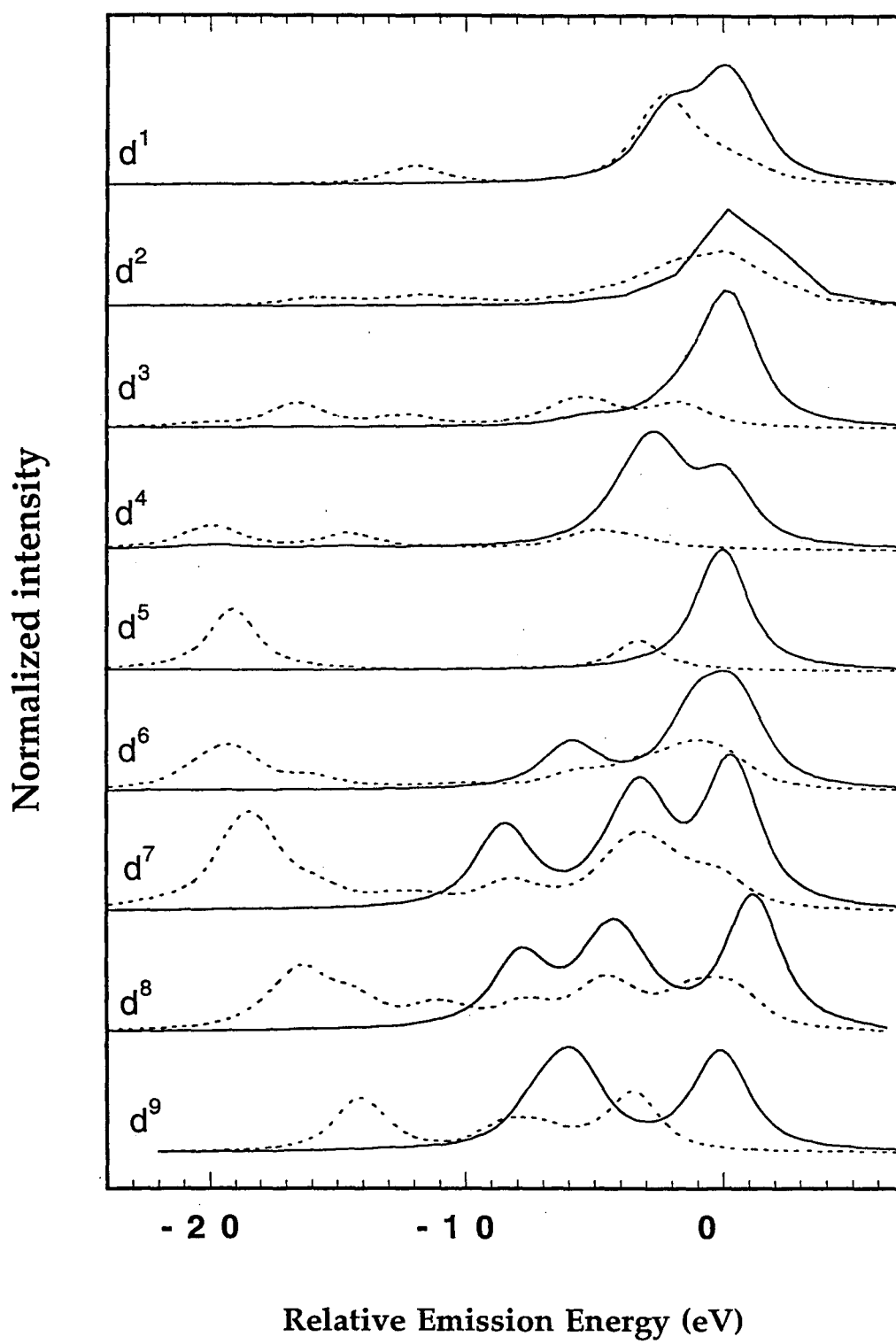
Figure 1 - (Upper trace) Experimental $K\beta$ spectrum for $(\text{NEt}_4)[\text{FeCl}_4]$, recorded using 7180 eV excitation. (Lower traces) Solid line - total calculated $K\beta$ spectrum, using parameters described in text. The sticks represent transitions to different multiplet levels before instrumental and lifetime broadening. Solid sticks and associated curve represent 7P final states, dashed lines and curves are 5P final states.

Figure 2 - Experimental excitation spectra for $(\text{NEt}_4)[\text{FeCl}_4]$, recorded by monitoring the fluorescence intensity at (upper trace) 7058 or (lower trace) 7043 eV.

Figure 3 - Calculated $K\beta$ spectrum for divalent transition metal complexes. The d^1 spectrum is for Sc(II) , and the atomic number increases sequentially up to the d^9 spectrum for Cu(II) . Solid lines - $K\beta$ spectra for a spin-down 3p shell hole (higher multiplicity final states); dashed lines are for spin-up 3p shell holes.







3.2 Site-Selective and Spin-Polarized X-ray Absorption of Fe Porphyrins

This section contains a published paper from *Chemical Physics Letter*, 243, 469 (1995), which discusses the application of high resolution x-ray fluorescence spectroscopy on Fe porphyrins.

Spin-Polarized and Site-Selective X-Ray Absorption - Demonstration with Fe Porphyrins and $K\beta$ Detection

Xin Wang ^{a,b}, Clayton R. Randall ^b, Gang Peng ^a, and Stephen P. Cramer ^{a,b*}

(a) Department of Applied Science, University of California, Davis, CA 95616.

(b) Energy and Environment Division, Lawrence Berkeley Laboratory, Berkeley, CA 94720.

Abstract

High-spin and low-spin Fe(III) porphyrins were studied by high resolution x-ray fluorescence and fluorescence-detected X-ray absorption spectroscopy using synchrotron radiation. The high-spin $K\beta$ spectrum is split into a main peak ($K\beta_{1,3}$) and a satellite ($K\beta'$) at 15 eV lower energy. The low-spin $K\beta_{1,3}$ peak shifted ~ 0.7 eV to lower energy, and the $K\beta'$ feature is almost unobservable. Ligand field multiplet calculations show that spin-up (5A_1) and spin-down (7A_1) states are separated for the high-spin spectrum. Spin polarization of the $K\beta$ -detected absorption was demonstrated by enhancement or elimination of the $1s \rightarrow 3d$ transition, depending on the $K\beta$ region used for detection.

Key Words:

X-ray absorption, Spin-polarized, $K\beta$, X-ray fluorescence and Fe porphyrins.

1. Introduction

X-ray absorption is now a popular tool for structure determination [1]. A strength and limitation of this technique is that it is sensitive to all different species of the same element in a sample; this makes characterization of mixtures difficult. An ideal detection method would allow the spectra for different chemical species to be recorded separately. One approach that appears promising is to use chemical shifts in x-ray emission during fluorescence-detected x-ray absorption [2a] as the means to gain this selectivity [2b].

The chemical sensitivity of $K\beta$ X-ray emission spectra has been known for many years [3], and the advantages of using synchrotron radiation as an excitation source have been demonstrated [4-7]. Typical shifts are on the order of 1 eV per oxidation state change. The final state after $K\beta$ X-ray emission has a 3p core hole for a first transition series metal. Coulomb and exchange interactions between the partially filled 3p and 3d shells make the overall shape of these spectra sensitive to the number and configuration of 3d electrons, hence to the spin state and oxidation state [3-6].

In favorable cases, $K\beta$ emission multiplet splittings can be separated into spin-up and spin-down regions [4-6]. $K\beta$ detection can then be used to record spin-polarized excitation spectra, without the need for circularly-polarized X-rays or spin-polarized samples. This internally referenced spin-polarized X-ray absorption can provide some information comparable to x-ray magnetic circular dichroism (XMCD) [8] and spin-polarized Extended X-ray Absorption Fine Structure (SPEXAFS) measurements [9].

In this paper, we report $K\beta$ emission and spin-selective excitation spectra of high-spin and low-spin Fe porphyrins [10]. Fe Porphyrins serve as electron transfer agents in various cytochromes, in oxygen transport in hemoglobin, as well as in critical enzymes such as cytochrome c oxidase [11a] and cytochrome P-450 [11b]. The $K\beta$ emission spectra are compared with ligand field multiplet calculations, which predict regions of spin-up and spin-down selectivity. These predictions were then confirmed by recording $K\beta_{1,3}$ and $K\beta'$ X-ray excitation spectra for a high-spin porphyrin. The potential for site-selective spectroscopy of high-spin and low-spin mixtures is discussed.

2. Experimental

Fe $K\beta$ high resolution fluorescence spectra were recorded on SSRL beamline 6-2 with a set of 3 spherically bent Si (440) crystal spectrometers [12]. Each bent crystal was separately aligned on the Rowland circle, and the beams were all diffracted vertically onto a common spot. A NaI detector was used for initial alignment and for fluorescence detection. The fluorescence emission spectra were recorded by scanning the detector and a slit vertically as the diffraction angle was changed by rotating the Si(440) crystals. The synchrotron radiation excitation beam was focused with a toroidal mirror to a 1mm x 7mm spot then monochromated using a pair of Si (111) crystals. Finely powdered samples were packed into a sample cell about 2mm thick. The typical count rates at $k\beta$ peak is around 800c/s. The emission spectrum takes about 2 hours (4 scans) and excitation spectrum takes around 5 hours (10 scans). All of the spectra were taken with samples at room temperatures. The

excitation energy was calibrated by reference to the first inflection point of Fe metal as 7111.2 eV [13].

High-spin 2,3,7,8,12,13,17,18-octaethyl-21H,23H-porphine iron(III) chloride (FeOEP₂Cl) was used as received from Aldrich. Low-spin 2,3,7,8,12,13,17,18-octaethyl-21H,23H-porphine iron(III) bis-imidazole, chloride salt (FeOEPIm₂Cl) was prepared by a published method [14].

3. Results and Discussion

3.1 K β Emission Spectra

The K β emission spectra for both high-spin Fe(OEP)Cl and low-spin Fe(OEP)Im₂Cl, excited at 7200 eV, are shown in Fig. 1. For the high-spin complex, the spectrum is split into two regions. The main peak (known as K $\beta_{1,3}$) is found at around 7058 eV, while the satellite (K β') is at 15 eV lower energy side. For the low-spin complex, the centroid of the K $\beta_{1,3}$ peak is shifted ~ 0.7 eV to lower energy as compared to the high-spin Fe(III) complex, and there is also very little K β' intensity. Similar results, although with lower resolution, have been reported by Koster [15].

The differences between high-spin and low-spin Fe(III) spectra can be explained primarily in terms of different final states for x-ray fluorescence, using an interpretation developed by Tsutsumi [16]. Neglecting charge transfer effects [17], the initial state configuration for excitation far above threshold before K β fluorescence is $1s^13d^5$, and the final state is $3p^53d^5$. In an octahedral environment, the 3d orbitals are split into e_g and t_{2g} orbitals with

an energy difference $10 Dq$. Two extreme situations can occur when there are five d electrons. When the ligand field strength is small, Fe(III) adopts a $(t_{2g}^+)^3(e_g^+)^2$ configuration with five parallel spins and 6A_1 ground state. A $(t_{2g}^+)^3(t_{2g}^-)^2$ configuration with 2T_2 symmetry occurs when the ligand field is large. In the final state, the 3p hole interacts very strongly with the partly filled 3d shell, thus the energy splitting in $K\beta$ spectra is caused by the exchange interaction between 3p and 3d levels. In the crystal field multiplet model [18], Coulomb repulsion terms, spin-orbit interactions, and ligand field splittings are also included.

The initial state symmetry determines which final states can be reached by dipole transitions. As seen before, the low-spin $K\beta_{1,3}$ peaks occur at lower energy than fluorescence from the high-spin species [19]. Also, a smaller $K\beta'$ feature is predicted in the low-spin case [16]. This chemical sensitivity of fluorescence $K\beta$ spectra allows selective measurement of high-spin or low-spin Fe absorption in a mixed system, by monitoring at appropriate $K\beta$ energies for each species.

In Fig. 2, the calculated spectra are compared with experimental spectra for both high-spin and low-spin Fe porphyrins. The $K\beta_{1,3}$ peak comes primarily from transitions where a 1s spin down hole is created, the $K\beta'$ peak is derived exclusively from spin-up transitions. This separation between spin-down and spin-up transitions makes $K\beta$ fluorescence a good spin-polarized probe of high-spin Fe(III). In the low-spin case, transitions to 3T_2 and 1T_2 states unfortunately overlap and spin-polarized studies would be more difficult.

Fig. 3 illustrates the theoretical site selectivity that can be achieved for high-spin vs. low-spin ferric by this technique. The ratio of high-spin intensity over the sum of high-spin and low-spin is given as a function of emission energy. There are three regions. Below 7043 eV and above 7061 eV, around 60% of the emission from a 50:50 high-spin low-spin mixture comes from the high-spin component. Between these two energies, the fluorescence is mostly from the low-spin component. Although the selectivity is highest at 7043 eV, the counting rate would be relatively low; detecting at 7061 eV gives much better statistics with almost the same selectivity. The selectivity of low-spin is just the opposite.

3.2 $K\beta$ Excitation Spectra

Spin-polarized X-ray excitation of the high-spin Fe porphyrin FeOEPCl are shown in Fig. 4. The spin-down absorption spectrum was taken by setting the analyzer crystal at 7059 eV, the peak centroid of $K\beta_{1,3}$, while the spin-up spectrum was selected at 7044 eV. The spin-down spectrum has a clear pre-edge peak around 7112 eV, which is assigned as $1s \rightarrow 3d$ transition. This dipole forbidden transition becomes allowed by mixing Fe 4p character with the predominantly 3d orbitals [20]. There is also a small quadrupole component. Despite the complicated nature of the $1s \rightarrow 3d$ transition, the spin selection rule still holds. When mainly spin-down transitions are monitored at 7059 eV, only the spin-down 3d orbitals can be reached. When probing at 7044 eV, only spin-up transitions are monitored; no $1s \rightarrow 3d$ transitions are possible since all five spin-up orbitals are occupied, therefore very little pre-edge features are observed. This confirms the spin dependence of the fluorescence spectrum. However, Lorentzian tail of the main peak will appear in the spin-up

spectrum (so called resonant Raman effect) [8], covalency, configuration interaction and spin-orbit coupling will also complicate the simple spin polarization picture, which might explain the nonvanishing pre-edge features in the spin-up spectrum.

In Fig. 5, we compare the high resolution fluorescence excitation spectra with conventional transmission spectra for high-spin and low-spin porphyrins. The excitation spectra were taken monitoring the $K\beta_{1,3}$ centroid, at 7059 eV and 7058.2 eV, and are similar to the transmission spectra in both cases, but with more intense pre-edge features in excitation spectra [21]. This again confirms the spin component assignment in the fluorescence spectrum. In the high resolution fluorescence excitation spectrum, only spin-down transitions are monitored, which have intense $1s \rightarrow 3d$ transition. The conventional transmission spectrum includes both spin-up and spin-down transitions. As shown in Fig. 4, the spin-up transition has small pre-edge features, therefore a much weaker $1s \rightarrow 3d$ is observed in the 'averaged' transmission spectrum. The edge is also sharper because of the elimination of $1s$ core hole natural line width in the $K\beta$ monitored spectrum [21]. The $1s \rightarrow 3d$ transition in the nearly octahedral low-spin compound is weak since much less $4p$ character mixing with the $3d$ orbitals, even in the fluorescence excitation spectra. The absorption edge shifts about 1 eV to higher energy for the low-spin porphyrin. At higher energy (40 eV above the edge), we observed what Oyanagi and coworkers [22] identified as the spin-state marker bands.

4. Summary

Iron $K\beta$ X-ray fluorescence emission and excitation spectroscopy has been used to study high-spin and low-spin porphyrins. The low-spin Fe $K\beta_{1,3}$ is shifted to lower energy by ~ 0.7 eV from the high-spin Fe, and the $K\beta'$ almost disappears for low-spin compounds. The ligand field multiplet model successfully explains the shapes and positions of the spectra. We find that the spin state shifts are large enough to select for high-spin or low-spin Fe with a crystal spectrograph. These chemical shifts should make site selective EXAFS experiments possible on mixtures of spin states. Potential applications include systems like Prussian Blue, with discrete high spin Fe(III) and low spin Fe(II) sites, as well as enzymes like cytochrome c oxidase and sulfite reductase.

Acknowledgment

The authors would like to thank Dr. F. M. F. deGroot for useful discussions, and M. M. Grush and J. A. Moore for helping with the experiment. This work was funded by the National Institutes of Health (GM-48145), the Department of Energy, Office of Health and Environmental Research, the American Chemical Society, and Petroleum Research Fund. The Stanford Synchrotron Radiation Laboratory is supported by the Department of Energy, Office of Basic Energy Sciences.

References

- [1] *X-ray Absorption: Principles, Applications, Techniques of EXAFS, SEXAFS and XANES*, D. C. Konigsberger and R. Prins eds. John Wiley & Sons: New York, 1988.
- [2a] J. Jaklevic, J. A. Kirby, M. P. Klein and A. S. Robertson, G. S. Brown and P. Eisenberger, *Soild State Communications*, 23, (1977) 679.
- [2b] *NEXAFS Spectroscopy*; Stöhr, J. Spring-Verlag, New York, 1992.
- [3] Börje Ekstig, Elisabeth Kallne, Erik Noreland, and Rolf Manne, *Physica Scripta*. 2, (1970) 38.
- [4] K. Hämäläinen, C. C. Kao, J. B. Hastings, D. P. Siddons, L. E. Berman, V. Stojanoff and S. P. Cramer, *Phys. Rev. B*. 46, (1992) 14274.
- [5] G. Peng, F. M. F. deGroot, K. Hämäläinen, J. A. Moore, X. Wang, M. M. Grush, J. B. Hastings, D. P. Siddons, W. H. Armstrong, O. C. Mullins and S. P. Cramer, *J. Am. Chem. Soc.*. 116, (1994) 2914.
- [6] G. Peng, X. Wang, C. R. Randall, J. A. Moore and S. P. Cramer, *Appl. Phys. Lett.* 65, (1994) 2527.
- [7] P. L. Cowan, *physica Scripta* VT31, (1990) 112.
- [8] F. M. F. DeGroot, S. Pizzini, A. Fontaine, K. Hämäläinen, C. C. Kao and J. B. Hastings, *Phys. rev. B*, 51 (1995) 1045.
- [9] G. Schütz, *physica Scripta* T29, (1989) 172.
- [10] *Iron Porphyrins*, A.B.P. Lever, Harry B. Gary, (eds.); Physical Bioinorganic Chemistry Series, Addison-Wesley, (1983).
- [11a] *Bioinorganic chemistry*, I. Bertini (eds.), University Science Books, Mill Valley, (1994).
- [11b] *Principles of Bioinorganic Chemistry*, S. J. Lippard and J. M. Berg, University Science Books, Mill Valley, (1994).

- [12] V. Stojanoff, K. Hämäläinen, D. P. Siddons, J. B. Hastings, L. E. Berman, S. P. Cramer, and G. Smith, *Rev. Sci. Instrum.* 63, (1992) 1125.
- [13] 'X-ray Data Booklet', D. Vaughan, Ed, *Lawrence Berkeley Lab Pub-490*, University of California, Berkeley (1986).
- [14] J. P. Collman, J. L. Hoard, N. Kim, G. Lang, and C.A. Reed, *J. Am. Chem. Soc.*, 97, (1975) 2676.
- [15] A. S. Koster, *J. Chem. Phys.* 56, (1972) 3161.
- [16] K. Tsutsumi, H., Nakamori, K. Ichikawa, *Phys. Rev. B* (1976), 13,929.
- [17] J. Kawai, M. Takami, C. Satoko, *Phys. Rev. Lett.* 65, (1990), 2193.
- [18] B. T. Thole, R. D. Cowan, G. A. Sawatzky, J. Fink and J. C. Fuggle, *Phys. Rev. B* , 31, (1985), 6856.
- [19] Octahedral symmetry was used for both calculations. The $10Dq$ value used for high-spin and low-spin is 1.2eV and 3.3 eV, respectively. In the high-spin case, the fluorescence initial state could have 7A_1 or 5A_1 symmetry when the escaping 1s electron is spin-down or spin-up with respect to 3d electrons.
- [20] A. L. Reo, D. J. Schneider, R. J. Mayer, J. W. Pyrz, J. Widom, and L. Que, Jr, *J. Am. Chem. Soc.* 106, (1984), 676.
- [21] K. Hämäläinen, D. P. Soddons, J. B. Hastings, L. E. Berman, *Phys. Rev. Lett.* 67, (1991), 2850.
- [22] H. Oyanagi, T. Iizuka, T. Matsushita, S. Saigo, R. Makino, Y. Ishimura, *J. Phys., Colloq.*, C8, Vol. 2 (1986), 1147.

Figure Legends

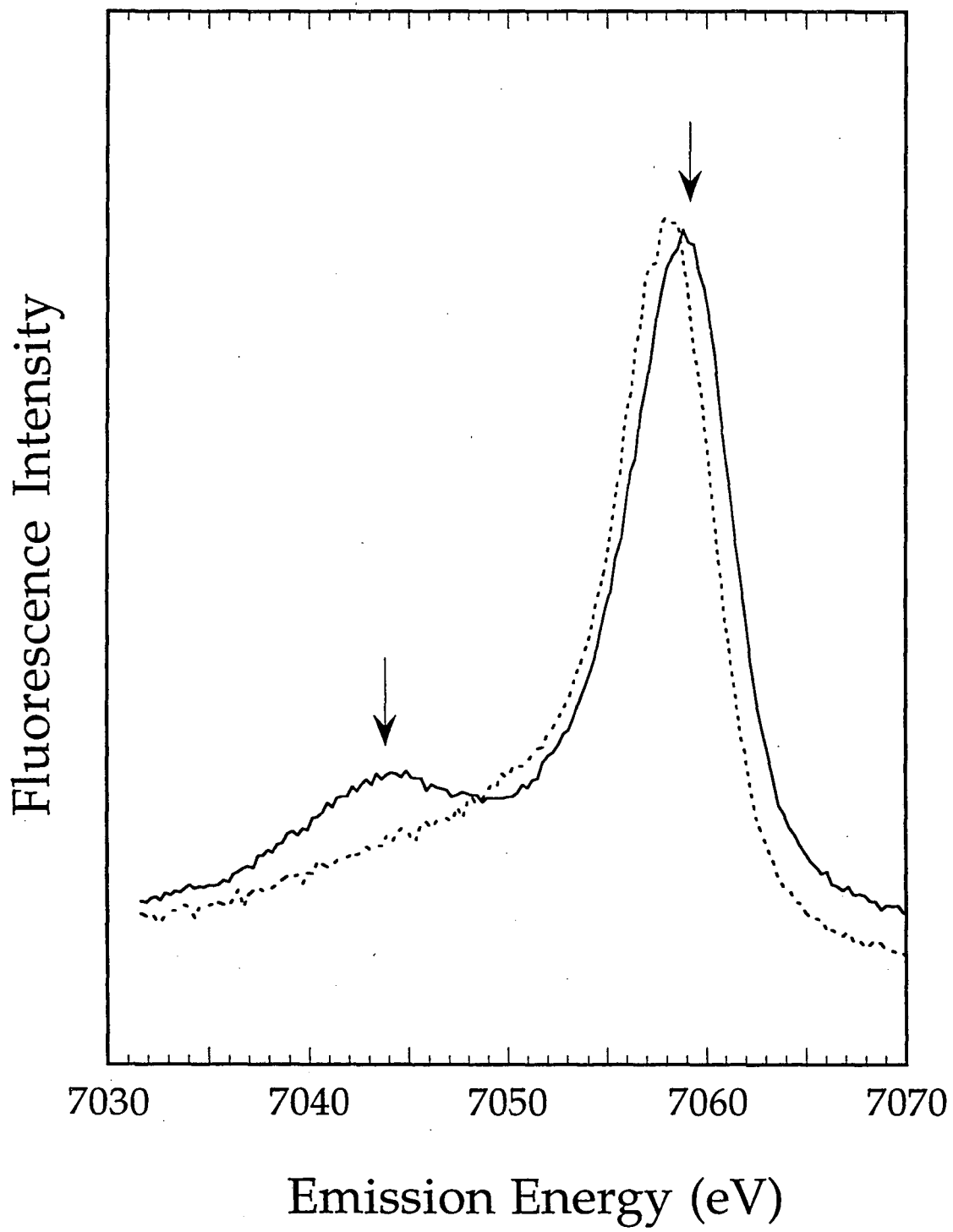
Figure 1. Experimental $K\beta$ emission spectra of high-spin FeOEPCl (solid line) and low-spin FeOEPI_mCl (dotted line) porphyrins. The Spin-polarized X-ray excitation spectra were taken monitoring the energy positions indicated by arrows.

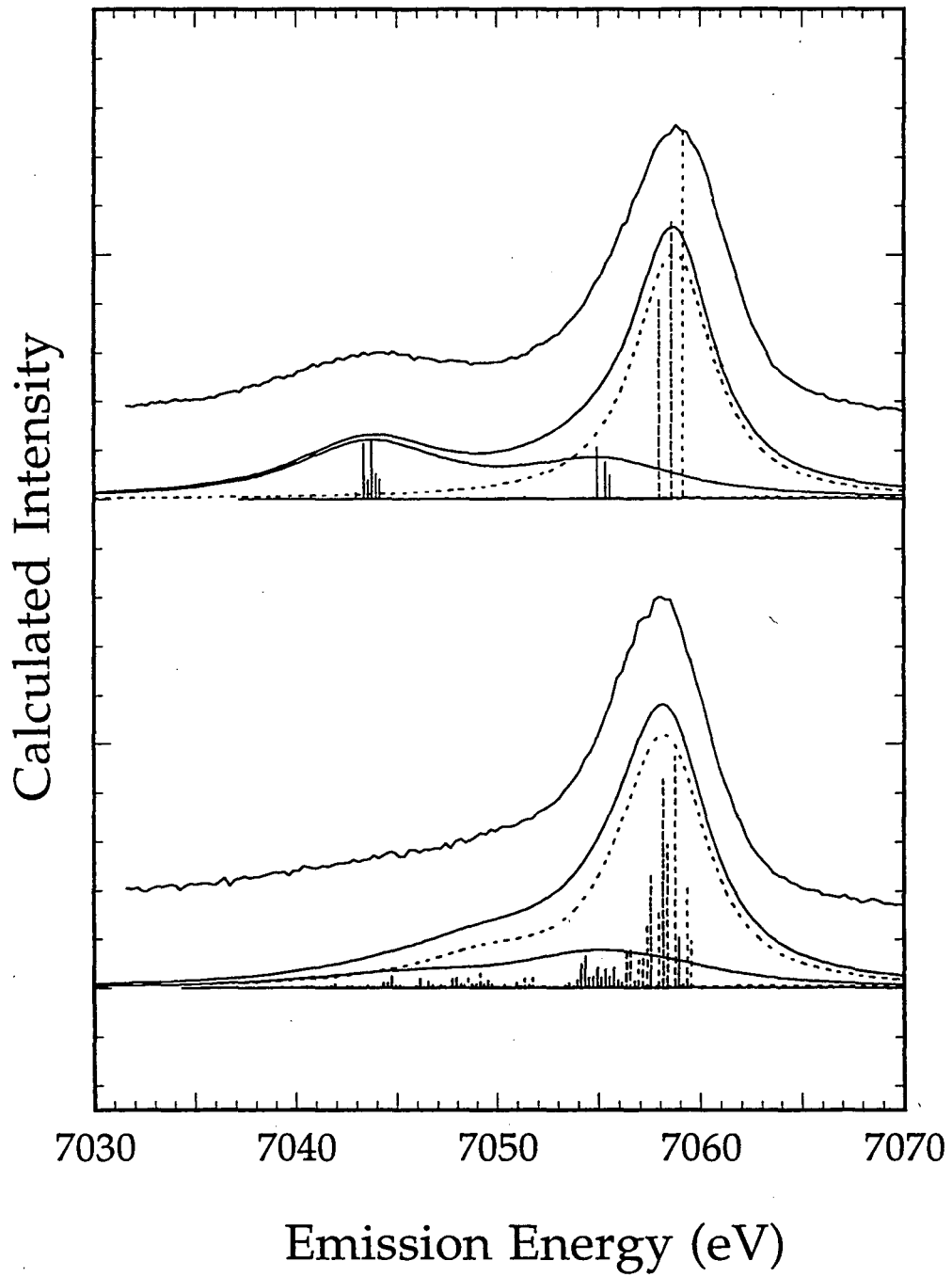
Figure 2. Experimental spectra with ligand field multiplet simulations of high-spin Fe porphyrin FeOEPCl (top) and low-spin FeOEPI_mCl porphyrin (bottom). Dotted line for the 7A_1 and 3T_2 spin-down transitions, dashed line for the 5A_1 and 1T_2 spin-up transitions, and solid line for total spectra. The stick diagrams show the strengths of individual transitions before line-width broadening.

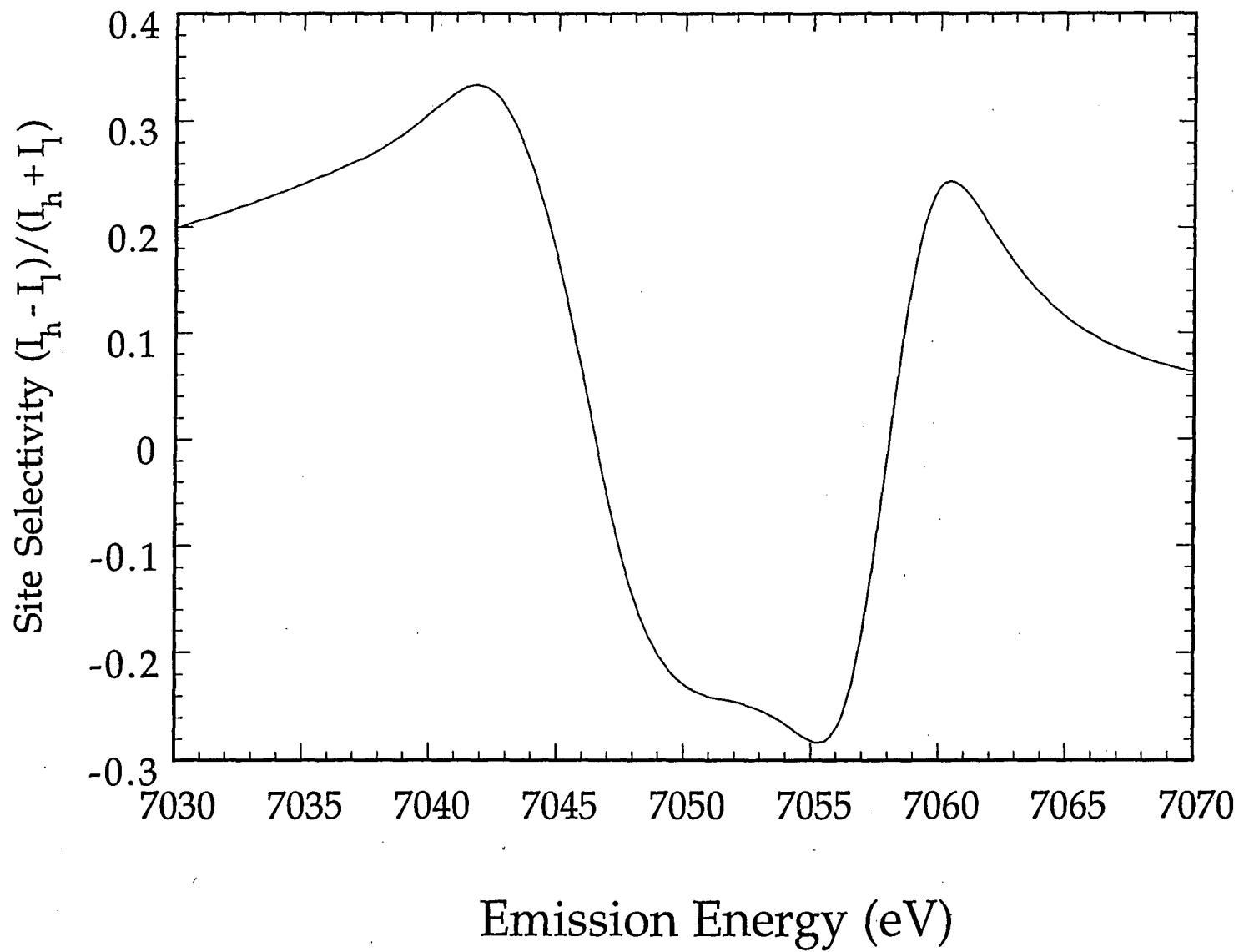
Figure 3. Calculated intensity ratio of high-spin ferric over the sum of high-spin and low-spin ferric as a function of emission energy.

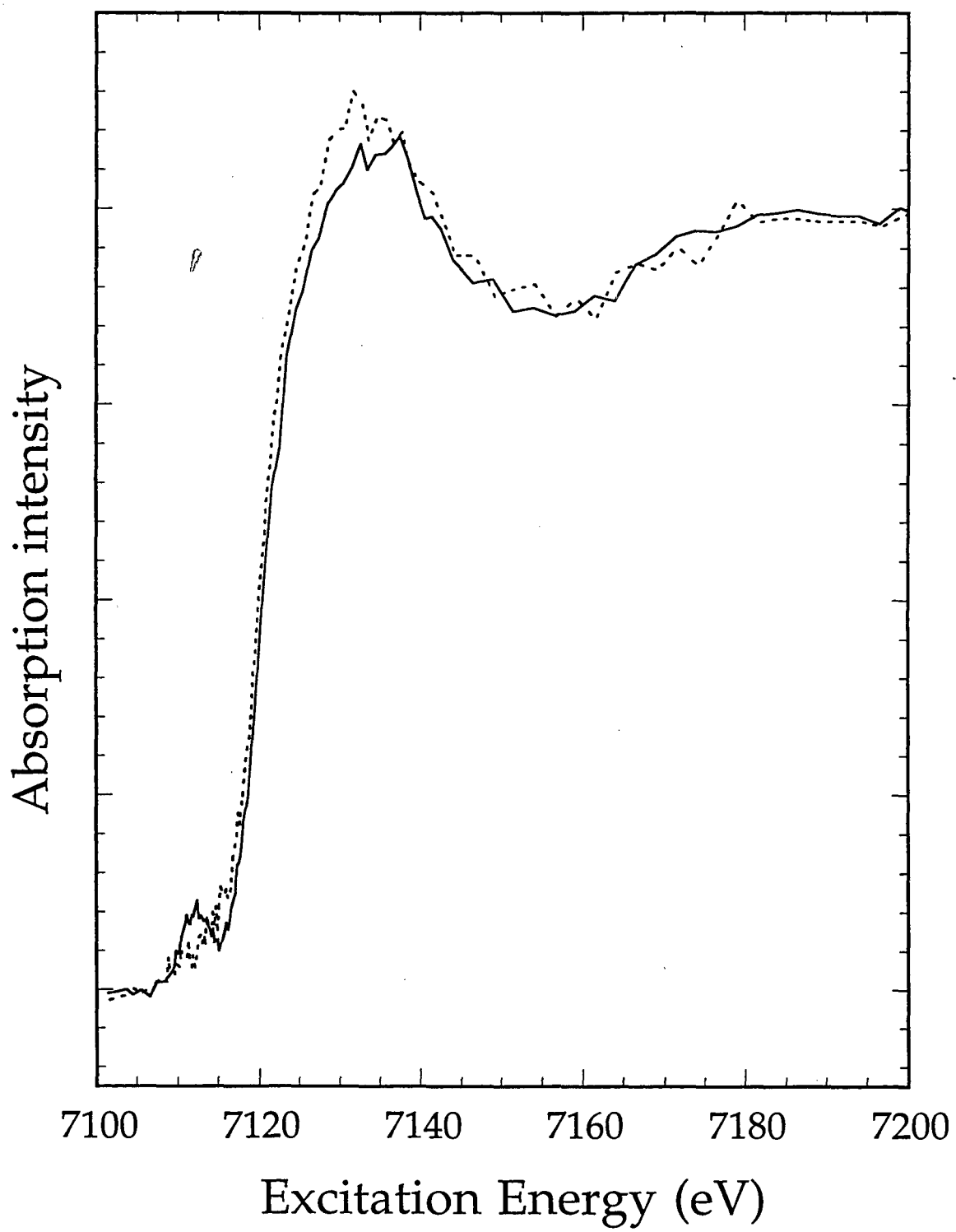
Figure 4. Spin-polarized X-ray excitation spectra of high-spin FeOEPCl. Solid line for spin-down absorption, monitoring 7059 eV; dotted line for spin-up absorption, detecting at 7044 eV.

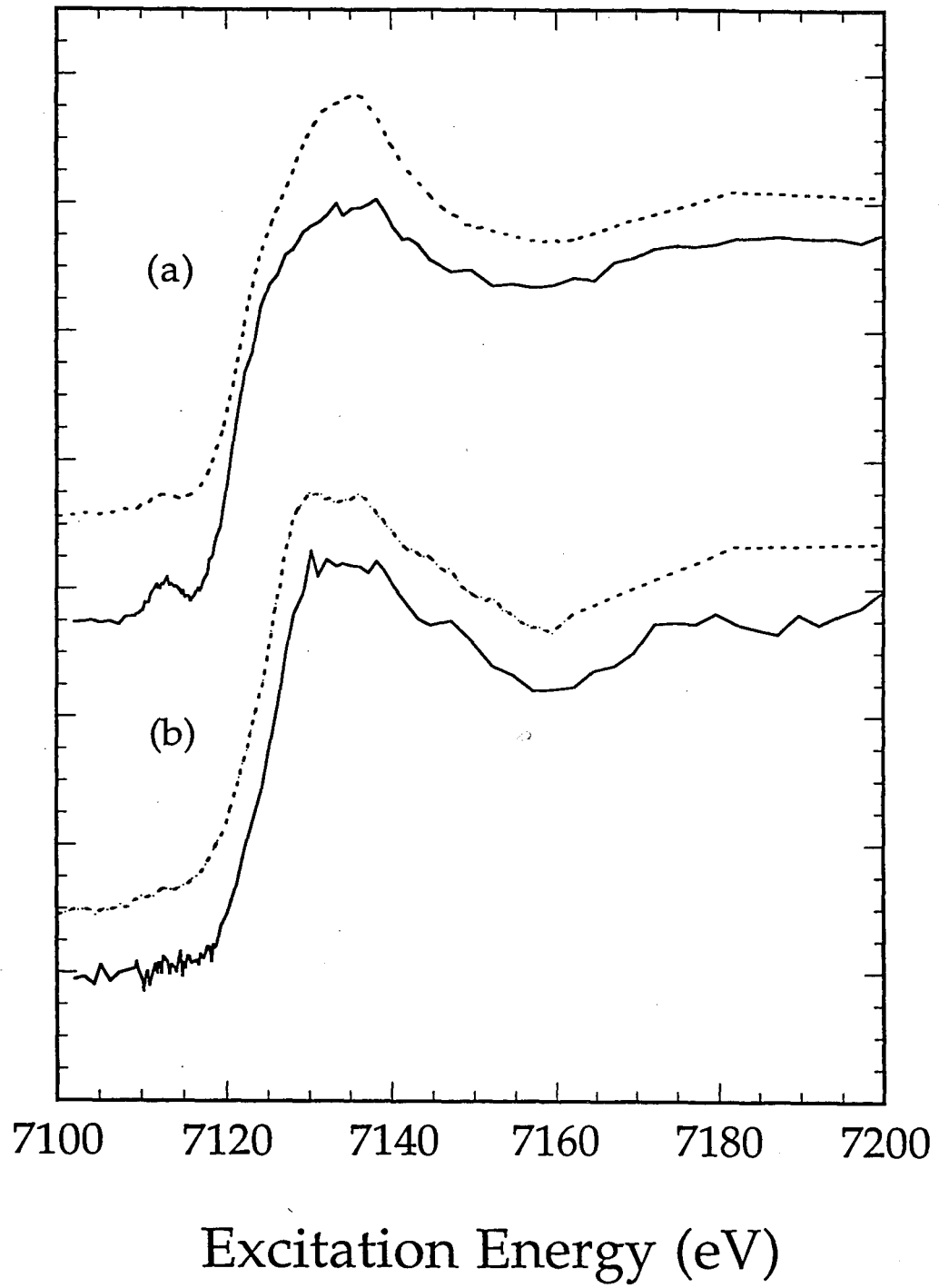
Figure 5. High resolution $K\beta_{1,3}$ fluorescence excitation spectra (solid line) with conventional transmission spectra (dotted line) for (a) high-spin FeOEPCl and (b) low-spin FeOEPI_mCl porphyrins.











Chapter 4: Site-Selective X-ray Absorption Spectroscopy of Prussian Blue

4.1. Introduction

In this chapter, site-selective x-ray absorption spectroscopy using $K\beta$ detection has been applied to the coordination compound Prussian Blue, $\text{Fe(III)}_4[\text{Fe(II)(CN)}_6]_3 \cdot 15\text{H}_2\text{O}$. Prussian Blue is interesting to study for at least two reasons. First, the metal sites and the lattice as a whole are highly symmetrical [4.1], therefore there are strong Fe x-ray absorption signals. In the type II of the mixed valence compounds [4.2], there is about 0.1 Å difference between the Fe(II)-C and Fe(III)-N bond lengths. It is an excellent candidate to test the resolving power and site selectivity of the high resolution fluorescence spectroscopy, by probing Fe(II) and Fe(III) site fluorescence separately. Second, in Prussian-Blue-like phases of general formula $\text{A}_k[\text{B(CN)}_6]_l \cdot n\text{H}_2\text{O}$, the metal sites A and B can be substituted by other transition metal ions; all these compounds have long-range magnetic order, therefore they behave as a magnet below their critical temperatures. The research has emerged as a new field of molecular magnetism [4.3]. These compounds maybe three-dimensional ferromagnets, antiferromagnets, or ferrimagnets, depending on the nature of the A-B interaction. Both A and B are in octahedral surroundings, where the 3d valence orbitals are split into t_{2g} and e_g sublevels. For B, only the t_{2g} orbitals are occupied, so the magnetism shown by the compound overall depends on A. If all the unpaired electrons of A occupy t_{2g} orbitals, the A-B interaction will be anti-ferromagnetic, and the compound will be ferrimagnet. If the unpaired electrons of A occupy some t_{2g} and some e_g orbitals, the A-B interaction will be again

antiferromagnetic, but the ferrimagnet of the compound will have a lower critical temperature. Finally, if the unpaired electrons of A only occupy e_g orbitals, the A-B interaction will be ferromagnetic, and the compound will be ferromagnet.

Prussian Blue can be considered as one of the first coordination compounds [4.2]. The mixed valence iron cyanides have been known for a long time, without being fully explained of its deep blue color. The magnetic susceptibility of Prussian Blue is consistent with high-spin $3d^5$ Fe(III) ions in the nitrogen sites, and low-spin $3d^6$ Fe(II) ions in the carbon sites [4.4]. Mössbauer spectra also confirmed the ferric ferrocyanide assignment [4.5]. There has been numerous investigation to determine the structure of Prussian Blue. The crystal structure [4.6] consists of a three-dimensional cubic Fe(III)-N-C-Fe(II) framework where a certain number of Fe(II) with cyanides missing, as shown in Figure 4.1. The interatomic distance of Fe(II)-C is 1.94 Å, Fe(III)-N 2.06 Å. The deep blue color presented in Prussian Blue is now understood as the intense absorption band at 700 nm, due to a transition from the ground state to an excited state in which an electron is transferred from an Fe(II) to an Fe(III) site (ground $\text{Fe(III)}_A\text{Fe(II)}_B$ to excited $\text{Fe(II)}_A\text{Fe(III)}_B$). These kinds of compounds have played, and continue to play, a crucial role in the study of electron transfer phenomena.

The attraction of Prussian Blue lies also in its long-range ferromagnetic ordering below Curie temperature 5.6 Kelvin [4.7]. Since only the Fe(III) sites carry a spin, whereas the Fe(II) sites are diamagnetic, the magnetic interactions must occur between the next-nearest ions through the 10.6-Å-long Fe(III)-N-C-Fe(II)-C-N-Fe(III) linkages. The possibility of propagating magnetic interactions through extended bridging networks between widely separated spin carriers seems to be specific to molecular compounds; it is due

to the strong spin delocalization from the metal ion towards its nearest neighbors. The presence of strong spin densities on the nitrogen and carbon atoms of the cyano groups has been experimentally observed by polarized neutron diffraction [4.8].

X-ray absorption spectroscopy has become a powerful tool for probing both geometric and electronic structures. Both x-ray absorption near edge (XANES) and extended x-ray absorption fine structure (EXAFS) techniques measure spectra that average over all species of an element in a sample. High resolution fluorescence spectroscopy utilizes the chemical shifts in x-ray

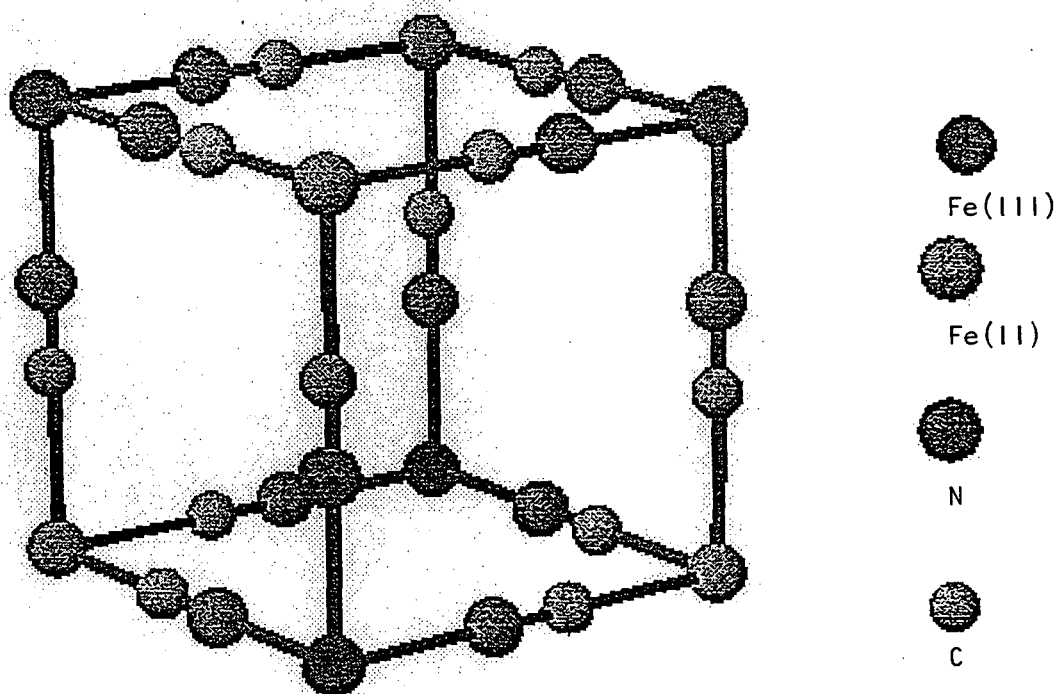


Figure 4.1 The unit cell of Prussian Blue. The atom types and crystallographic positions are indicated by the symbols.

in Chapter 2, the Mn K β emission spectra shift around 1 eV per oxidation state [4.10]; as found in Chapter 3, the Fe K β emission spectra shift also around 1 eV between spin states [4.11], and Ni K β shows the same kind of shifts between oxidation states and spin states [4.12]. Apart from the energy position changes, the spectral shape is also different. Because of this oxidation state and spin state sensitivity, the high-spin Fe(III) and low-spin Fe(II) emission in Prussian Blue should be distinguishable. This suggests that by picking the appropriate fluorescence energy, it is possible to selectively probe the absorption spectrum of high-spin Fe(III) or low-spin Fe(II), and we can extract electronic structure as well as geometrical structure information exclusively for one Fe site.

4.2. Experimental

All the K β emission spectra, site-selective XANES, and EXAFS spectra were recorded on Stanford Synchrotron Radiation Laboratory (SSRL) beamline VI-2 [4.13] using a Si(111) excitation monochromator. Transmission Fe K-edge x-ray absorption spectra were recorded on SSRL beamline IV-2 using a Si(220) monochromator. A description of the spherically bent Ge(620) fluorescence spectrometer which was used to collect Fe fluorescence follows.

The high resolution fluorescence spectrometer using spherically bent Ge(620) crystal arrays is an improvement on that using Si(440) crystals (see Chapter 3), with which the first K β emission and excitation spectra of Fe model compounds were obtained. Since the fluorescence energy is determined by the Bragg equation:

$$\lambda = 2d \sin \theta \quad (4.1)$$

therefore the energy resolution is given by:

$$\frac{\Delta\lambda}{\lambda} = \cot\theta\Delta\theta + \frac{\Delta\tau}{\tau} \quad (4.2)$$

where $2d$ is the crystal lattice spacing, λ is the wavenumber of fluorescence energy, and ϑ is the Bragg diffraction angle. The $\frac{\Delta\tau}{\tau}$ term, in the absence of strain, is just the contribution of the Darwin width. For Ge(620) at 78 Bragg angle, the Darwin width is about $75 \mu\text{rad}$. The resolving power of the analyzer crystals is determined by the Bragg angle ϑ , as well as the projected angle of the sample on the analyzer crystal $\Delta\vartheta$. The closer to backscattering (meaning ϑ closer to 90°), the smaller the $\text{ctg}\vartheta$ value, and the better the resolution. It is also proportional to the sample size. When switching Si(440) to Ge(620), the Bragg angle for Fe $K\beta$ fluorescence changes from 66° to 78° , and the resolving power is therefore increased by a factor of 2. This increased resolution will be used to distinguish the near edge structure of particular chemical forms of Fe.

The fluorescence spectrometer uses Rowland geometry: the source (where the sample emits x-rays), the Ge(620) analyzer crystal, and the NaI scintillation detector are all in the circle with an 850-mm-diameter. The spherically bent crystal has an 850-mm-radius, so all the x-rays collected by the crystal are focused back on the detector. The Rowland circle is on the vertical plane, in order to reduce the scattering. The crystal arrays are formed such that each analyzer crystal is on an intersecting Rowland circle with the same source and the same detector. The spherical crystal bender used is illustrated in Figure 4.2.

The samples used here are Fe_2O_3 , $\text{K}_4\text{Fe}(\text{CN})_6$ and $\text{Fe}_4(\text{Fe}(\text{CN})_6)_3$ (Prussian Blue), all as received from Aldrich Chemical Company. Fe_2O_3 and $\text{K}_4\text{Fe}(\text{CN})_6$ were used as models for pure high-spin Fe(III) and low-spin Fe(II) components in octahedral symmetry, to simulate the two different Fe sites in Prussian Blue. They were all diluted with BN to a concentration of ~10% Fe (w/w). All emission, XANES, and EXAFS spectra were recorded at 30 K, using a He refrigerator.

The emission spectra were calibrated using the $\text{K}\beta_{1,3}$ peak of $(\text{NEt}_4)[\text{FeCl}_4]$ as a reference (7058.0 eV); excitation spectra were calibrated using the $1s \rightarrow 3d$ pre-edge peak of $(\text{NEt}_4)[\text{FeCl}_4]$ (7113.0 eV), or the 1st derivative peak of an Fe foil (7111.2 eV). The EXAFS data were averaged over 80 scans; each took about 40 minutes. The EXAFS spectra were smoothed over a k -range of 0.2 \AA^{-1} for the transmission and site-selective data, and the Fourier transforms were taken over a 2.5 to 10 \AA^{-1} interval.

4.3. Results and Discussions

4.3.1 $\text{K}\beta$ Emission Spectra

The $\text{K}\beta$ fluorescence spectra of Fe_2O_3 , $\text{K}_4\text{Fe}(\text{CN})_6$, and $\text{Fe}_4(\text{Fe}(\text{CN})_6)_3$ were obtained using 7200 eV synchrotron excitation as presented in Figure 4.3. The pure octahedral high-spin Fe(III) compound Fe_2O_3 shows a main feature $\text{K}\beta_{1,3}$ around 7058.4 eV, and a very clear satellite $\text{K}\beta'$ at 7044 eV in the emission spectrum. The pure octahedral low-spin Fe(II) compound $\text{K}_4\text{Fe}(\text{CN})_6$ has a main peak $\text{K}\beta_{1,3}$ at 7056.6 eV and almost no satellite. The 2 eV energy shift can be used to selectively probe the site-specific structure in the mixed valence compound Prussian Blue. As shown in the $\text{K}\beta$ emission

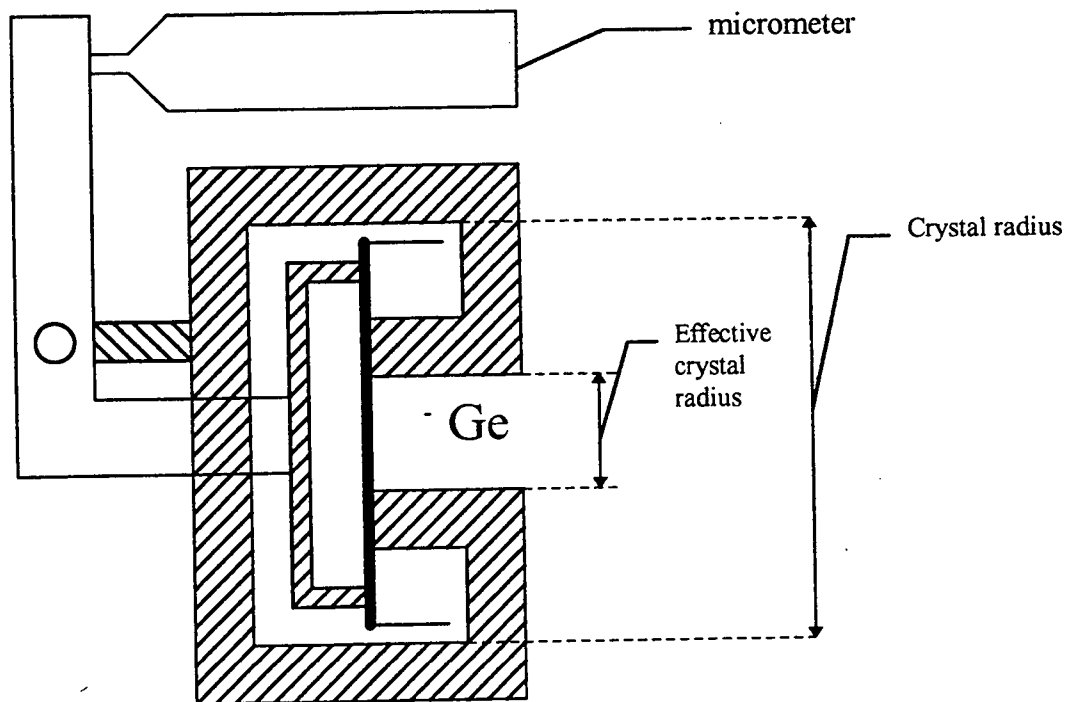


Figure 4.2 Schematic drawing of the spherical crystal bender.

spectrum, the main peak of Prussian Blue falls right in between the $K\beta_{1,3}$ of the pure high-spin Fe(III) and pure low-spin Fe(II), and the $K\beta'$ satellite is almost half of the intensity of pure Fe(III). The weighted average of two pure component spectra nicely simulates the experimental Prussian blue data, as expected.

As discussed in Chapter 2.3 by ligand field multiplet theory, the ground state symmetry determines the shape of the K emission spectra. High-spin Fe(III) has a half-filled stable state 6S , and the 5 unpaired d

electrons form the largest spin moment possible $5/2$. Because the main peak and the satellite energy splitting is caused by the 3p-3d exchange interaction, and the splitting is proportional to the spin moment [4.14], there is a large energy difference between the main peak and the satellite in high-spin Fe(III) system, about 15 eV. The satellite intensity is also proportional to the spin moment [4.14], so the strong and clear satellite is presented in the high-spin Fe(III) system. For low-spin Fe(II), the net spin moment is zero, therefore no satellite is expected. The energy shifts between high-spin Fe(III) and low-spin Fe(II) in the main peak can be used for site selective x-ray absorption measurements. By setting the analyzer crystals at the favorable energies at 2.5 eV higher energy shoulder and 2.0 eV lower energy shoulder of the main peak, as indicated by arrows in Figure 4.3, primarily high-spin Fe(III) and low-spin Fe(II) x-ray absorption can be recorded.

4.3.2 Site-Selectivity and Spin-Polarization

From the weighted emission spectra of pure high-spin Fe(III) and low-spin Fe (II) components, we could get the experimental site selective coefficients at different emission energies for Prussian Blue. When monitoring at 7060.0 eV, 54.6% emission comes from the high-spin Fe(III), 45.4% from low-spin Fe(II). At 7055.4 eV, there is 65.4% low-spin Fe(II) and 34.6% high-spin Fe(III).

There are complications regarding this method for site-selective x-ray absorption. The excitation spectra are emission energy dependent, because different parts of the emission correspond to different final states in the decay process, and the final states are spin polarized and have different lifetime broadenings. The spin composition of a high-spin Fe(III) and a low-spin Fe(II) system are shown in the calculated $K\beta$ emission spectra in Figure

Figure 4.3. $K\beta$ Emission spectra of Fe compounds. Top: $K\beta$ Emission Spectra of high-spin Fe(III) Fe_2O_3 (dotted line) and low-spin Fe(II) $K_4Fe(CN)_6$ (solid line); Bottom: Weighted average of these two pure components (solid line) and $K\beta$ emission spectrum of Prussian Blue $Fe(III)_4(Fe(II)(CN)_6)_3$ (dotted dashed line). The emission energies monitored for site-selective x-ray absorption are indicated by arrows.

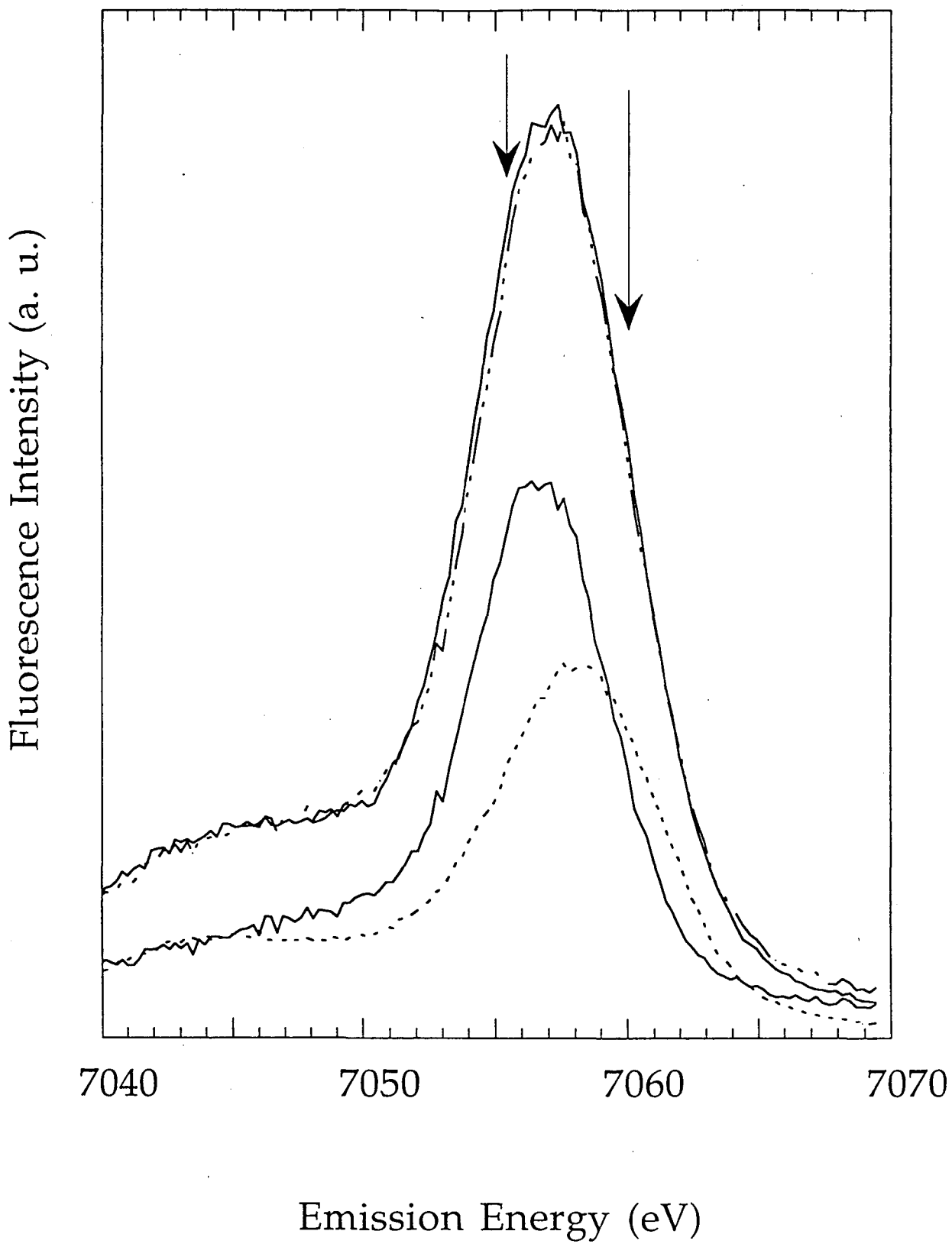
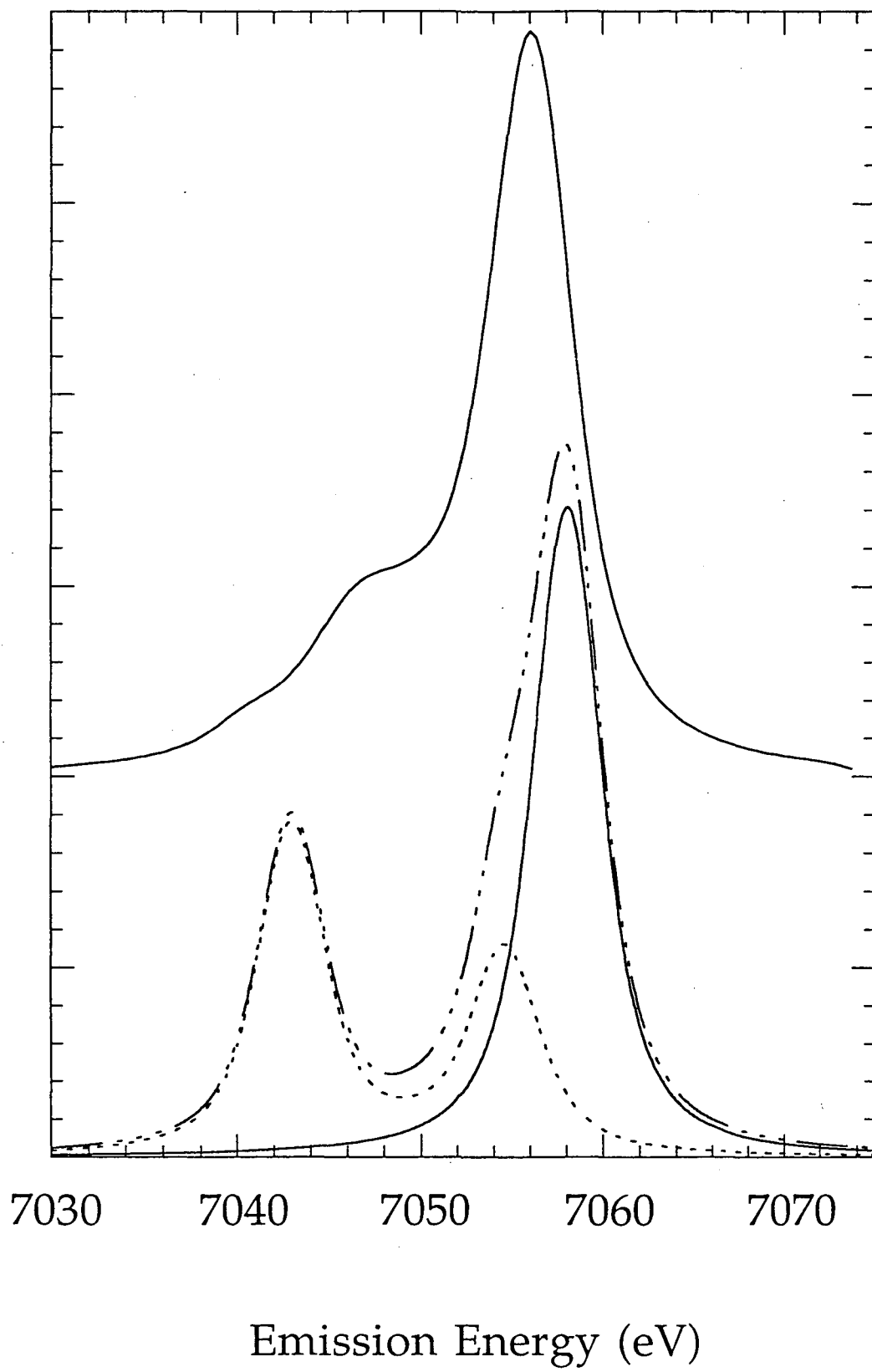


Figure 4.4. Spin components in $K\beta$ emission spectra of high-spin Fe(III) (top) and low-spin Fe(II) (bottom) system using the ligand field multiplet calculation. Plotted are spin-up transition (dotted line), spin-down transition (solid line), and total fluorescence spectrum (dotted dashed line).



4.4. The calculated main peak position of high-spin Fe(III) is aligned with the experimental data, while the energy difference with the low-spin Fe(II) is preserved from the calculation. As discussed in Chapter 2.3, the $K\beta$ main peak is about 85% spin-down and the satellite is about 100% spin-up for a high-spin Fe(III). Because of the spin polarization, when setting analyzer crystals at certain emission energies, the detected fluorescence is mostly for one chemical species, as well as for one spin component. For example, the $K\beta_{1,3}$ corresponds mostly to spin-down transition, meaning the excited 1s electron is spin-down, with respect to the spin direction of 3d valence electrons. When monitoring Prussian Blue fluorescence at 7060.0 eV, we detect 54.3% high-spin Fe(III) absorption, but only the spin-down absorption at that site. The lower energy shoulder of $K\beta_{1,3}$ has some spin-up character in the high-spin Fe(III) emission. Thus, monitoring the Prussian Blue emission at 7055.4 eV, we detect 65.4% low-spin Fe(II) component, but some spin-up absorption at the high-spin Fe(III) site. Low-spin Fe(II) has no spin selectivity because of the zero spin moment. In a more complex system where the emission of both sites are spin polarized, we can envision to detect the spin-up absorption of site A and the spin-down absorption of site B by picking up an emission energy.

This complicates quantitative explanations of the site selective near edge structure. However, a quantitative theoretical approach is not yet available even for simple transmission or total fluorescence K-edge spectra. In one electron theory, different approaches such as band structure [2.15] or multiple scattering analysis [4.16] have been used recently for quantitative simulations of the spin polarized XANES. Still, each has its own deviation from the experimental data. Inclusion of the core hole potential has found some success [4.17] but not all features can be fully understood. This is,

however, beyond the scope of our problems here. Qualitatively, when comparing site-selective near edge spectra of mixed valence compounds with pure components, it is possible to record the corresponding excitation spectra at the same emission energy with the same spin selectivity. With identical spin selectivity, the comparison between the mixed valence compounds and the pure components should be helpful to extract exclusively the electronic structure of a particular site.

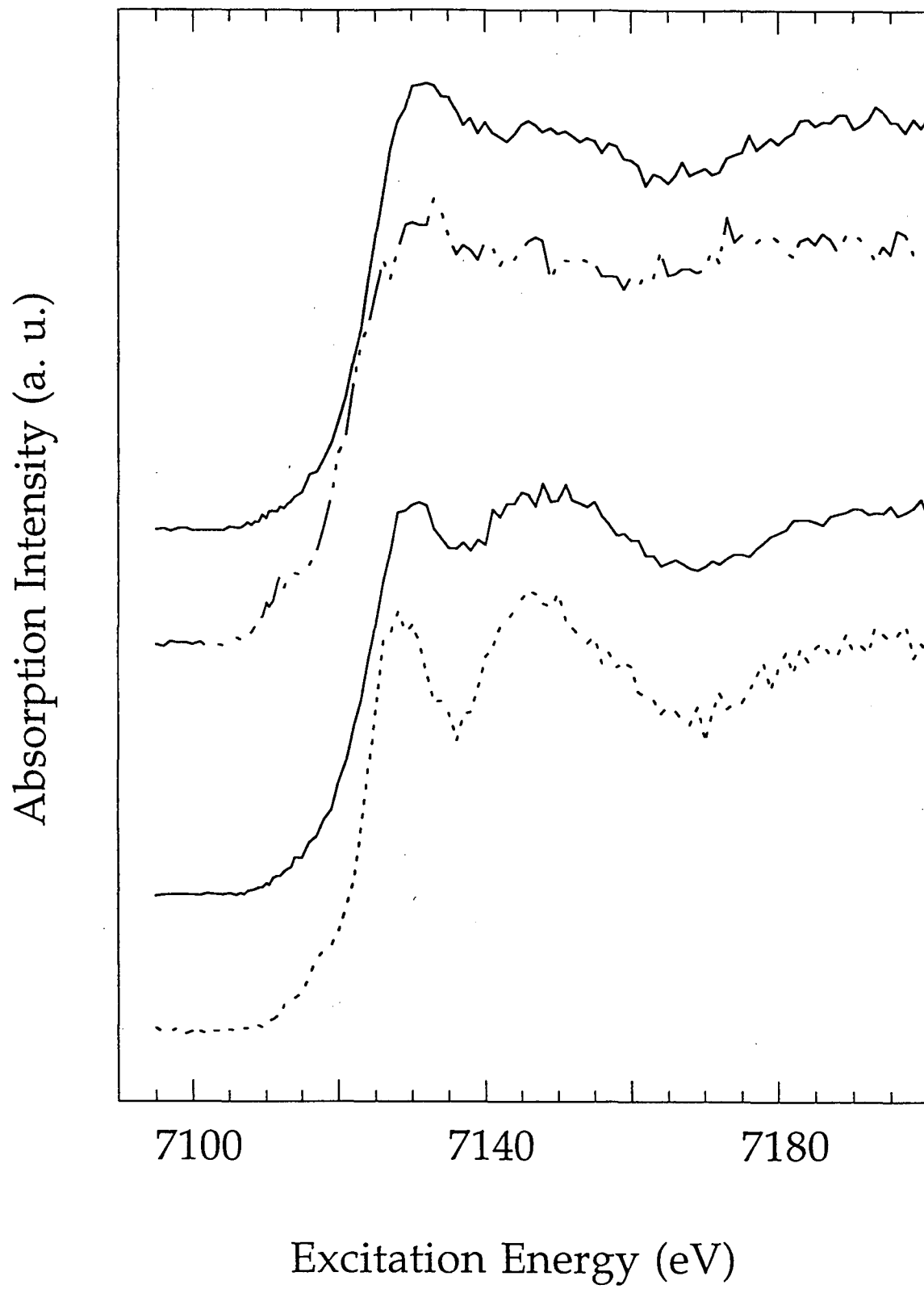
For site-selective EXAFS, the spin polarization of emission spectra will have a small effect in data interpretation, in particular if the interest is on the bond-length differences among different species of the same element. Although the spin polarization still exists, the information obtained by selective measurements will be the same for spin-up or spin-down transitions, with the exception of backscattering amplitudes for magnetic neighbors. The extra exchange term in the scattering potentials of magnetic neighbors makes the spin-up electron scatter off with slightly different probability than the spin-down electron. This spin polarized EXAFS effect will be studied in Chapter 6. Qualitative bond length information of a particular site, however, should still be obtainable in a mixed valence compound by site-selective EXAFS.

4.3.3 Site-Selective XANES

Figure 4.5. shows the XANES spectra selective for the Fe (III) component and Fe(II) component of Prussian Blue, by setting analyzer crystals at 7060.0 eV and at 7055.4 eV, respectively. The pure high-spin Fe(III) of Fe_2O_3 and low-spin Fe(II) of $\text{K}_4\text{Fe}(\text{CN})_6$ spectra were also taken at the corresponding emission energy.

The XANES changes with the surrounding of an absorbing atom. In

Figure 4.5. Site-selective XANES spectra. From top to bottom: Fe(III) site-selective edge of Prussian Blue (solid line) using 7060.0 eV detection as indicted in Figure 4.3, Fe₂O₃ edge at the same detection energy (dotted dashed line); Fe(II) site-selective edge monitoring 7055.4 eV (solid line), and K₄Fe(CN)₆ edge monitoring the same energy (dashed line).



the simplest model, the near edge fine structure is interpreted as the site and symmetry selected density of states (DOS). For octahedral high-spin Fe(III), Fe₂O₃ shows a broad and strong absorption peak around 7130.2 eV, without many oscillations above the edge. The low-spin Fe(II) compound K₄Fe(CN)₆, however, has a much lower edge position at 7128.6 eV, and there are two sharp and strong oscillations above the edge, which are due to the excited electron virtually 'trapped' thereby strongly multiple scattered within the CN groups [4.18]. The Fe(III) has one less electron than Fe(II) on the valence orbitals, therefore the stronger screening effect in Fe(III) requires more energy to ionize the 1s core electron.

Comparing selective Fe(III) and Fe(II) XANES of Prussian Blue with Fe₂O₃ and K₄Fe(CN)₆ XANES, it is clearly shown that there are striking similarities in the site selective edges and the pure components. There is one broad main absorption peak at the Fe(III) site data around 7130 eV. For the Fe(II) site, the period of oscillation is the same as in K₄Fe(CN)₆, although the amplitude of oscillation is understandably smaller, as there is still a 34.5% Fe(III) component in the absorption edge, which is almost structureless. This results show the feasibility of site-selective absorption edge measurement in a mixed valence complex.

4.3.4 Site-Selective EXAFS

EXAFS is the result of the outgoing photoelectron waves being backscattered off of neighboring atoms, producing interference patterns which show up as oscillations in the absorption coefficient. The formula which describes this phenomena is presented in Chapter 2.1. The EXAFS oscillations can be fit with a series of damped sine waves generated either empirically or by *ab initio* calculations for individual absorber-backscatterer pairs. These

simulations yield information on the number, atom type, and distance of backscattering atoms relative to the absorbing atom.

EXAFS data analysis procedures are described nicely in some articles [4.19-20]. A short review follows. First, a background fit to the pre-edge region is subtracted from the raw spectra. It is also necessary to subtract a spline function fit to the data above the edge in order to eliminate the atomic background. Dividing by the free atom fall-off Victoreen leaves the EXAFS oscillations which are then converted from E-space to k -space. The order of polynomial function can be chosen, and the coefficients [4.21] are specific for each absorption edge. The data is generally multiplied by k^3 to compensate for the dampening of oscillations at higher k .

For easier interpretation of the EXAFS spectra, the Fourier transform of the data can be taken and the expression describing the signal becomes a function of real space R instead of momentum space k :

$$f(R) = \int \chi(k)e^{-ikR} dk \quad (4.3)$$

The data is then presented as a radial distribution of scatterers which surround the absorbing atom. The analysis procedure is simplified by first fitting individual peaks which correspond to fewer shells of backscattering atoms. Theoretical phase and amplitude functions as tabulated by McKale [4.22] were used in our case to simulate the EXAFS oscillations in the single scattering approach; FEFF codes obtained from University of Washington [4.23] were used to generate the phase and amplitude functions when multiple scattering was important.

Site-selective EXAFS for Fe(III) and Fe(II) were obtained by monitoring at 7060.0 eV and 7055.4 eV, respectively. Both site-selective EXAFS and

Fourier Transforms are presented in Figure 4.5. Due to the noise in the site-selective data, a k -interval of 2.5 to 10 \AA^{-1} is presented. The site selective data and were smoothed over a k 0.2 \AA^{-1} range.

The transmission EXAFS shown as the combination of the two site-selective data, while the site-selective EXAFS oscillations are clearly different from each other (Figure 4.6). The three main peaks in the Fourier transform correspond to Fe(II)-C/Fe(III)-N, Fe(II)-N/Fe(III)-C, and Fe(II)-Fe(III) interactions. The distance difference between Fe(II)-C (1.92 \AA) and Fe(III)-N (2.03 \AA) is quantitatively shown in the Fourier transform in the site-selective spectra. These data are still difficult to work with since they are mixtures of both components. From two site-selective EXAFS and the corresponding selective coefficients, we extracted out the pure high-spin Fe(III) and pure low-spin Fe(II) EXAFS in Prussian Blue by simply using

$$\text{Site Fe(III)} = 0.546x \text{ pure Fe(III)} + 0.454x \text{ pure Fe(II)} \quad (4.4)$$

$$\text{Site Fe(II)} = 0.346x \text{ pure Fe(III)} + 0.654x \text{ pure Fe(II)} \quad (4.5)$$

The extracted pure Fe(II) and pure Fe(III) components EXAFS in Prussian Blue, their corresponding Fourier transforms and their fittings are shown in Figure 4.7. To clarify the analysis and demonstrate the site selectivity on the first coordinate sphere, we filtered only the first two peaks for fitting. The EXAFS of two pure components are very different, and almost out of phase from each other. The best fit of the pure Fe(II) spectrum gives 6 C at 1.941 \AA and 6 N at 3.080 \AA ; and the fit of the pure Fe(III) spectrum gives 6 N at 2.060 \AA and 6 C at 3.202 \AA , as shown in the fitting parameters in Table 1. This is in good agreement with the crystal structure data, where the average bond length of Fe-C is 1.923 \AA , Fe-N 2.029 \AA , and C-N 1.131 \AA . The 0.12 \AA

Figure 4.6. Left: Site-selective EXAFS data of Prussian Blue monitored predominately for Fe(II) (solid line) and Fe(III) (dotted line); Right: Fourier Transform of the EXAFS data for Fe(II) (solid line) and Fe(III) (dotted line).

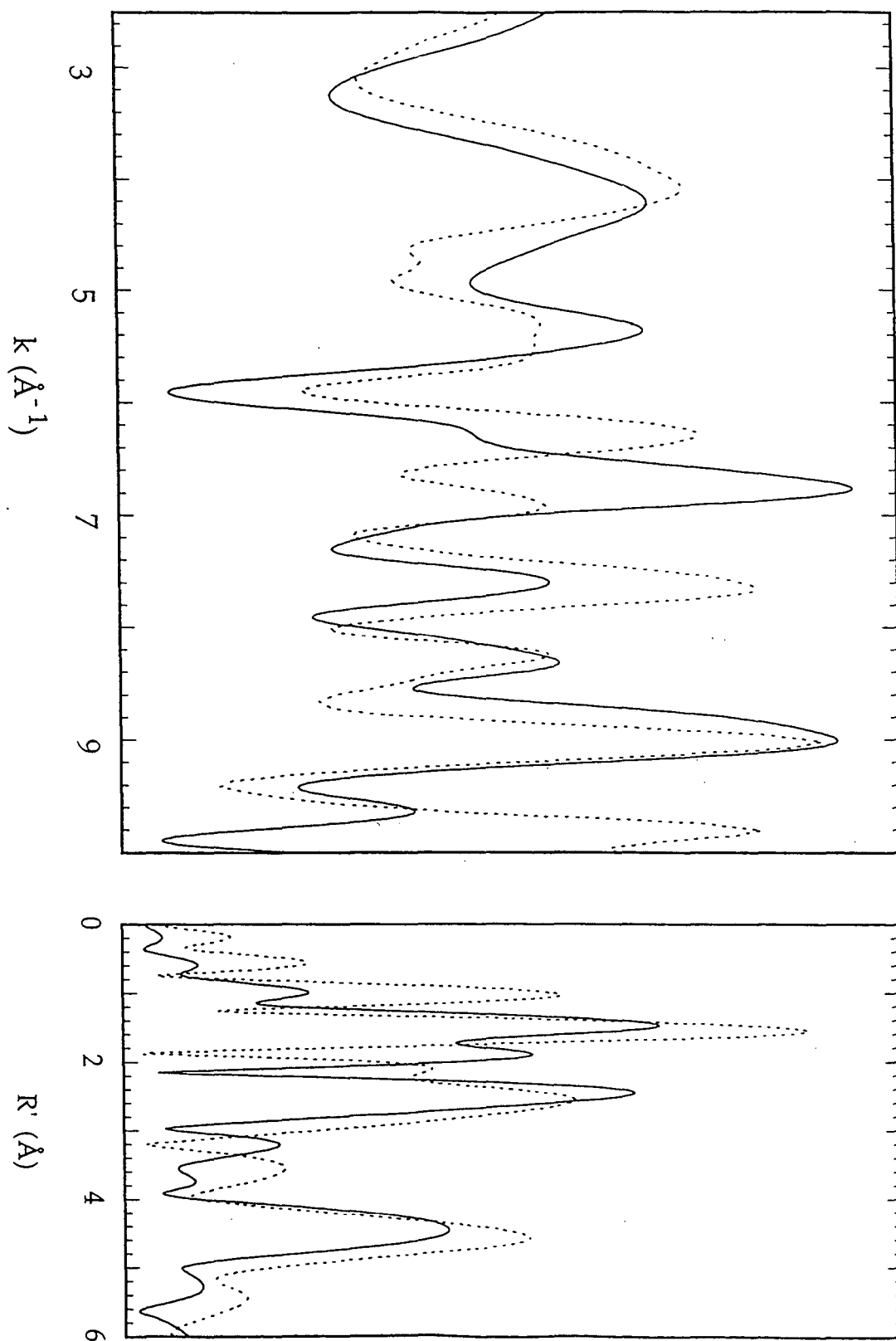
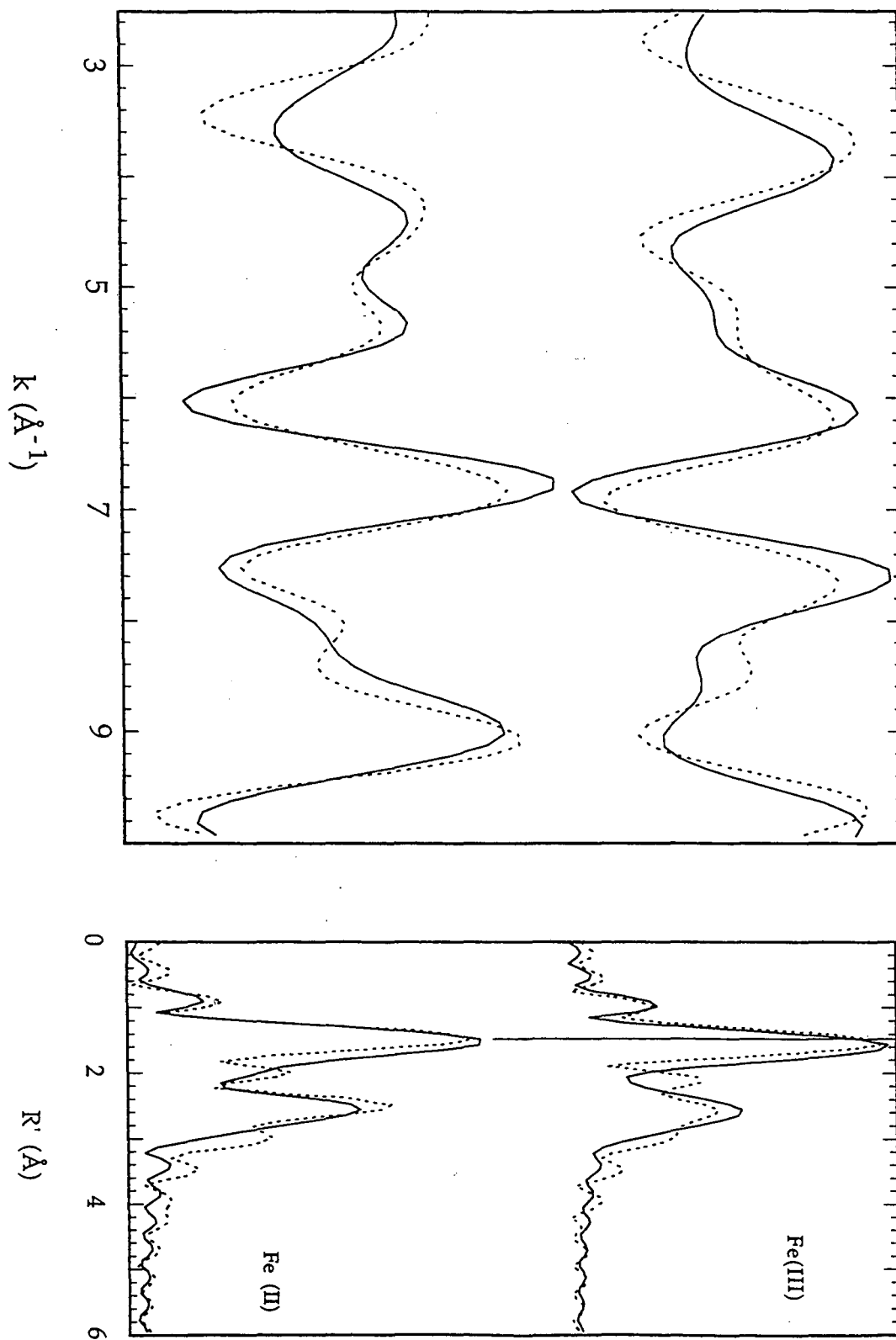
$k^3 \times$ EXAFS

Figure 4.7. Left: Extracted pure Fe(III) EXAFS of Prussian Blue (solid line) and simulations with FEFF (dotted line); pure Fe(II) EXAFS of Prussian Blue (solid line) and simulations (dotted line). Right: Fourier Transform of filtered pure Fe(III) EXAFS (solid line) and simulations (dotted line); and that of Fe(II) EXAFS (solid line) and simulations (dotted line).

$k^3 \times \text{EXAFS}$ 

difference between Fe(II)-C and Fe(III)-N is demonstrated by site-selective EXAFS. There are clear features around 4.5 Å (unphase-shifted) in both pure Fe(II) and pure Fe(III) EXAFS, which should correspond to the Fe(II)-Fe(III) interaction. Better statistics and a wider range of data, however, are needed to allow more accurate determination of longer interactions and different geometries in a mixed valence model.

4.4 Conclusions

In summary, we have demonstrated the feasibility of site-selective x-ray absorption in Prussian Blue by $K\beta$ detection. The different local geometry at different sites of the same element can be distinguished by site-selective EXAFS, which utilizes the chemical shifts on $K\beta$ emission spectra. Electronic structure can also be extracted for a particular site in the near edge structure. While the spin polarization of $K\beta$ emission spectra complicates the determination of the electronic structure of a mixed valence compound, it also generates the possibility of extracting magnetic information of neighboring atoms. Detectable chemical shifts in emission spectra are known for other elements such as the rare earths [4.24], and even for light atoms such as carbon. Site-selective XAS will become a common and valuable technique for electronic and geometric structure determination as new synchrotron radiation sources and improved collecting optics are developed.

References

- 4.1 Keggin, J.F. and Miles, F.D., *Nature*, **4**, 577 (1936).
- 4.2 Robin, M. B. and Day P., *Adv. Inorg. Chem. Radiochem* **10**, 247 (1967).
- 4.3 Kahn, O., *Molecular Magnetism*, VCH, New York, 1993.
- 4.4 Herren, F., Fischer, P., Ludi, A. and Hålg, W., *Inorg. Chem.* **19**, 956 (1980).
- 4.5 Davidson, D., Welo, L.A., *J. Phys Chem.* **32**, 1191 (1928).
- 4.6 Buser, H.J., Schwaezenbach, D., petter, W., and Ludi, A., *Inorg. Chem.* **16**, 2704 (1977).
- 4.7 Hoden, A.N., Mattias, B.T., Anderson, P.W., and Lewis, H.W., *Phys. Rev.* **102**. 1463 (1956).
- 4.8 Figgis, B.N., Kuchaeski, E.S., and Vrtis, M., *J. Am. Chem. Soc.* **115**, 176 (1993).
- 4.9 Ekstig, B., Källne, E., Noreland, E., Manne, R., *Phys. Scripta* **2**, 38 (1970).
- 4.10 Peng, G., deGroot, F.M.F., Hämäläinen, K., Moore, J.A., Wang, X., Grush, M.M., Hastings, J.B., Siddons, D.P., Armstrong, W.H., Mullins, O.C., Cramer, S.P., *J. Am. Chem. Soc.* **116**, 2914 (1994).
- 4.11 Wang, X., Randall C.R., Peng, G., and Cramer, S.P., *Chem. Phys. Lett*, **243**, 469 (1995).
- 4.12 Randall, C.R., Froeschner, A.G., Cramer, S.P., Verhagen, M.F.J.M. and Adams, M.W.W., submitted to *Inorg. Chem.*
- 4.13 Hoyer, E., Bahr, C., Chan, T., Chin, J., Elioff, T., Halbach, K., Harnett, G., Humphries, D., Hunt, D., Kim, K.-J., Lauritzen, T., Lindel, D., Shirley, D., Tafelski, R., Thompson, A., Cramer, S., Eisenberger, P., Hewitt, R., Stöhr, J., Boyce, R., Brown, G., Golde, A., Gould, R., Hower, N., Lindau,

- I., Winick, H., Yang, J., Harris, J., Scott, B., *Nucl. Inst. & Meth.* **208**, 117 (1983).
- 4.14 Tsutsumi, K., Nakamori, H., Ichikawa, K., *Phys. Rev. B*, **13**, 929 (1976).
- 4.15 Dufek, P., Schwarz, K., and Blah, P., *Phys. Rev. B* **48**, 12672 (1993).
- 4.16 Soldatov, A.V., Ivanchenko, T.S., Kovtun, A.P., Della Longa, and Bainconi, S., *Phys. Rev. B* **52**, 11757 (1995).
- 4.17 private communication.
- 4.18 Bianconi, A., Dell, C., Ariccia M., Durham P.J., and Pendry, J.B., *Phys. Rev. B*, **26**, 6502 (1982).
- 4.19 Sayers, D.E. and Bunker, B.A., in "X-ray Absorption: Principles, Applications, Techniques of EXAFS, SEXAFS and XANES", edited by Konigsberger, D.C., Prins, R.. Wiley & Sons, New York, 1988. p. 211.
- 4.20 Lee P.A., Citrin, P.H., Eisenberger, P., and Kincaid, B.M., *Rev. Mod. Phys.* **53**, 769 (1981).
- 4.21 *International Tables for X-ray Crystallography, vol. III*; MacGillavry, C.H., Rieck, G.D., Eds., Kynoch, Birmingham, 1968. p. 171.
- 4.22 McKale, A.G., Knapp, G.S., Chan, S.-K. *Phys Rev. B* **33**, 841 (1986).
- 4.23 Rehr, J. J., Albers, R. C., *Phys. Rev. B* **41**, 8139 (1991).
- 4.24 Shrivastava, B.D., Gupta, G.D., and Joshi, S.K., *Phys. Lett. A*, **163**, 188 (1992).

Chapter 5. High Resolution X-ray Spectroscopy of Metalloproteins

5.1. Instrumentation and Initial Results

The site and spin selectivity of high resolution fluorescence spectroscopy could provide complementary information on both geometric and electronic structures for systems such as metalloproteins. Those selectivities could simplify the complex spectra of metalloproteins enormously and provide higher sensitivity to distinguish different sites of the same element in multinuclear clusters. The main obstacle of this application to metalloproteins is the low efficiency of the spectrometer. In this section, a paper accepted by the Journal of Synchrotron Radiation is included, which describes the new instrumentation on the high resolution x-ray fluorescence spectroscopy, and some first protein results obtained by this spectrometer. The spectra are analyzed in the same manner as for model compounds, but special concerns of photoreduction in protein experiments are address, and future prospects are discussed.

High Resolution X-ray Fluorescence and Excitation Spectroscopy of Metalloproteins - A New Technique for Site- and Spin-Selectivity

Xin Wang^{a,b}, Melissa M. Grush^{a,b}, Andrew G. Froeschner^a, Stephen P.
Cramer^{a,b}

^a Department of Applied Science, University of California, Davis, CA
95616.

^b Energy and Environment Division, Lawrence Berkeley National
Laboratory, Berkeley, CA 94720.

Abstract

A spectrometer has been developed with sufficient efficiency to make high resolution fluorescence experiments on metalloproteins possible. The resolution of this spectrometer can reach 0.45 eV at 7.1 keV emission energy. The focus images of this multiple curved-crystal array spectrometer are presented. The chemical sensitivity of $K\beta$ emission spectra can be used to identify chemical states, and the spin-polarized near edge structure provides a new measure of the spin density. The high resolution fluorescence metalloprotein studies should become routine with third generation synchrotron facilities, and the strength of both site- and spin-selectivity should complement the structural information from other spectroscopies.

Keywords: x-ray fluorescence; $K\beta$ emission; spin-polarization; metalloproteins.

1. Introduction

The combined application of x-ray absorption and emission spectroscopy to chemical and physical problems offers unique advantages over simple x-ray absorption or emission measurements (Åberg & Tulkki, 1985, Cowan, 1994). This rapidly developing field is variously known as resonant x-ray emission (RXES) (Mori, Kayanuma & Kotani, 1991), resonant x-ray fluorescence (RXFS) (Skytt, Guo, Wassdahl & Nordgren, 1995), resonant x-ray inelastic scattering (RXIS or RIXS or REXS) (deGroot, 1996; Krisch, et al., 1995), and x-ray resonant scattering or x-ray resonance Raman scattering (XRRS) (Carra, Fabrizio & Thole, 1995; Udagawa, Hayashi, Tohji & Mizushima, 1994). Regardless of the nomenclature, one essential part of the experiment is high resolution monochromatization of both the resonant x-ray excitation beam and of the scattered or emitted radiation. The first x-ray RRS was observed by Sparks (Sparks, 1974) with monochromatic Cu K α radiation incident on various metallic targets. The first synchrotron radiation RRS experiment was carried out by Eisenberger and coworkers (Eisenberger, Platzman & Winick, 1976), who studied the effect near the K edge of metallic Cu. Development of ever-brighter synchrotron radiation sources (Schlacter, 1994, Winick, 1995) has dramatically improved the sensitivity of these double monochromator experiments. Monitoring the emission has improved from low resolution measurements using solid state detectors to high resolution experiments with curved crystal (Stojanoff, et al., 1992) or grating (Nordgren, et al., 1989) spectrometers.

Chemical effects on the energies and shapes of x-ray fluorescence lines have been known since the 1920s (Lindh & Lundquist, 1924). These shifts can

be used to identify oxidation and spin states (Ekstig, Källne, Noreland & Manne, 1970; Peng et al., 1994). Shifts due to oxidation state changes can be used to conduct site-selective XANES or EXAFS measurements (Grush, Christou, Hämäläinen & Cramer, 1995). Shifts due to spin state changes can also be used for this purpose (Wang & Cramer, 1996c). The spin sensitivity of the emission spectrum can also be used to generate spin-selective XANES (Hämäläinen, et al, 1992; Peng, Wang, Randall, Moore & Cramer, 1994; Wang, Randall, Peng & Cramer, 1995) or spin-polarized EXAFS measurements (SPEXAFS). The resultant SPEXAFS effects at the K-edge (Grush et al. 1996a; Wang et al. 1996a) are 50-100 times stronger than those observed by x-ray magnetic circular dichroism measurements (Schütz et al., 1987; Kobayashi et al., 1995). Dramatic line-sharpening effects in x-ray scattering measurements allow observation of structure in excitation spectra that is normally unobservable (Hämäläinen, Siddons, Hastings & Berman, 1991).

High resolution fluorescence and scattering experiments on the metal clusters in proteins complements the electronic and structural information available from x-ray crystallography, EXAFS, and other spectroscopies. Because the metals are present at low concentration (30-1000 ppm), the efficiency of the collecting spectrograph is critical to the feasibility of such experiments. In this paper, we describe a curved crystal array for collecting x-ray emission and excitation spectra. This device has an energy resolution of 10^{-4} (DE/E) and collects sufficient solid angle to make metalloprotein experiments possible. We report Fe emission and excitation spectra of *Pyrococcus furiosus* rubredoxin that demonstrate the feasibility of applying these techniques to metalloproteins. These results also illustrate the spin-dependent electronic information obtainable. The significance of x-ray

photoreduction is illustrated with preliminary results on the Mn in Photosystem II. The potential for further improvements and prospects for biological applications are discussed.

2. Experimental apparatus and procedures

2.1. The high resolution fluorescence spectrometer

In order to study dilute systems such as metalloproteins, a multiple crystal array spectrometer was developed which captures a larger solid angle than previously possible (Figure 1). The incident beam is focused on the sample using the beamline optics. An array of spherically bent crystals on intersecting Rowland circles then diffracts the scatter or fluorescence back to a common spot on the detector. Because the diffraction occurs in near-backscattering Johann geometry on an 850-mm-diameter Rowland circle, very high energy resolution ($\Delta E/E = 10^{-4}$) can be obtained. An emission spectrum can be obtained by rotating the analyzer crystals while moving the detector (in this case, a NaI scintillation counter) simultaneously to track the diffracted beam. Alternatively, a position sensitive detector can be used, eliminating the necessity of having a mobile detector.

The previous spectrometer with a single analyzer (Stojanoff et al., 1992) used a mechanical crystal bending apparatus (Schulke & Nagasawa, 1986). However, the extra space occupied by crystal benders prevents efficient packing of multiple crystals into an array. We therefore switched to 'form-bent' crystals, each glued onto a spherically ground concave glass form with an 850-mm-radius. For Fe $K\beta$ emission, the 78 degree Bragg angle obtained

with Ge(620) crystals gives 0.45 eV resolution at 7.1 keV (Brennan & Cowan, 1992), while the Si(440) reflection at 83.5 degree used for Mn K β yields 0.35 eV resolution at 6.8 keV (Stojanoff et al., 1992). Each 'form-bent' crystal is placed in a circular opening machined from an aluminum plate and held in place with a set screw. The crystal holder is mounted on a computer-controlled Huber rotation stage operating the diffraction angle (q). Another goniometer at the bottom drives rotation in the horizontal plane (c). The six crystals are placed as close together as possible (Figure 1). The solid angle collected by each crystal is 0.28 msr.

Reduction of air absorption is essential because of the long paths taken by the fluorescence x-rays in this experiment. A plastic (PVC) vacuum tank was built to occupy most of the path between sample, crystals, and detector. 50 m Kapton windows were used on both ends of the tank and a vacuum of approximately 6 torr was obtained. Air absorption was further minimized by additional helium paths between the vacuum tank and detector, between the crystals and the tank, and between the beamline and the sample. The overall transmitted intensity of this spectrometer is 0.70 at 6.8 keV, the result of 19 m polypropylene, 150 m Kapton, 5.1×10^4 m air, and 7.1×10^5 m helium in the beam path. A Balzers He refrigerator with a 7 K copper cold finger was used to keep the sample cold and reduce x-ray damage.

2.2 Sample preparation and data collection

(NEt₄)[FeCl₄] (Gill, 1961) was a gift from Prof. Larry Que. Rubredoxin from *Pyrococcus furiosus* was prepared by published procedures (Blake et al., 1991) and kindly donated by Prof. Michael Adams. The concentration of the

protein was 22.5 mg/ml, corresponding to an Fe concentration of ~225 ppm. A Photosystem II sample originally poised in the S_1 state (Ghanotakis & Yocum, 1986, Ghanotakis, Demetriou, & Yocum, 1987) was generously provided by Prof. James Penner-Hahn.

Fe and Mn $K\beta$ spectra were recorded on the X-25 wiggler beamline at Brookhaven National Laboratory (Berman et al., 1992) with the spectrometer described above. The synchrotron radiation excitation beam was monochromated using a pair of Si(220) crystals and focused with a toroidal mirror to a 0.5 mm x 0.8 mm spot. Mn $K\beta$ spectra and Fe x-ray images were also recorded on beamline VI-2 at Stanford Synchrotron Radiation Laboratory (Hoyer et al., 1983) with a Si(111) excitation monochromator and the same fluorescence spectrometer.

The Fe spectra were calibrated by assigning the $K\beta$ peak of $(\text{NEt}_4)[\text{FeCl}_4]$ to 7058.0 eV (Peng, Wang, Randall, Moore & Cramer, 1994); Mn emission spectra used a value of 6491.7 eV for the main $K\beta$ peak of MnF_2 (Grush et al., 1995). The excitation energy was calibrated by reference to the first inflection point of Fe or Mn metal, 7111.2 eV and 6539.0 eV, respectively (Williams, 1986).

3. Results and discussion

3.1 Spectrometer focus quality

To evaluate the combined focus in our array spectrometer, images were recorded with a two dimensional position sensitive detector (Smith & Bo,

1995). This gas proportional chamber has an active area of 10 cm x 2 cm, with a position resolution of approximately 200 mm at 7 keV. Using this detector, the image of the fluorescence focus was recorded separately for each individual analyzer crystal, as well as for three crystals simultaneously.

The images of the diffracted beams collected from the three crystals are shown in Figure 2. Contours were drawn for the beam from each crystal while the other crystals were blocked. The finite source size of the excitation beam on the $(\text{NEt}_4)[\text{FeCl}_4]$ sample (1 mm vertical x 3 mm horizontal) and the spherical aberration of the 'form-bent' crystals contribute to the size and shape of the diffracted beam. In this geometry, the vertical axis is the energy dispersive direction on each Rowland circle. The individual beams focus to 1.5 mm x 2.1 mm (FWHM) for each crystal, and the combined beams stay within a 3.8 mm x 8.5 mm region. Thus, a small slit of 4 mm x 9 mm can be used to reduce the background from undesirable scattered x-rays.

3.2. Comparison of 'form-bent' and mechanically bent crystals

In Figure 3, we compare the emission spectrum of $(\text{NEt}_4)[\text{FeCl}_4]$ using a mechanically bent Ge(620) crystal to that with a 'form-bent' Ge(620) crystal. Even after the focus of the mechanically bent crystal was optimized using Fe $K\beta$ fluorescence, the Fe emission spectrum was broader than that observed with the 'form-bent' crystal. The observed FWHM of the emission spectrum improved from 7.2 eV to 5.3 eV, increasing the intensity at the $K\beta$ peak by 25%. We also found it difficult to bend Ge crystals to the desired radius without frequent breakage. We note, however, that bending Si(440) crystals

was less problematic, and improved resolution was not obtained with 'form-bent' Si(440) crystals.

3.3 Count rate for an Fe model compound

A typical count rate at the Fe $K\beta$ peak for pure $(\text{NEt}_4)[\text{FeCl}_4]$ with 3 'form-bent' crystals was ~ 3000 photons/sec with a background of only ~ 4 counts/sec. With an incident flux of 1×10^{12} photons/sec, it is a worthwhile exercise to determine where the photons have gone. If we assume that 53% of the incident x-rays are absorbed by Fe (calculated using absorption coefficients as tabulated in Marenkov, 1994), a total fluorescence yield of 34% (Krause, 1979), a $K\beta/K\alpha$ quantum yield ratio of 0.133, and 75% reabsorption of the emitted radiation, then approximately 5.1×10^9 photons/sec are emitted into 4π steradians. Since the spectrograph only intercepts 6.7×10^{-5} of the full solid angle and the windows and air paths absorb 50% of the x-rays, we can expect at most a count rate of 1.7×10^5 photons/sec. (The most recent version of this spectrometer includes thinner Kapton windows and a smaller air path, resulting in a transmission of 70%, as stated earlier in this manuscript, rather than the 50% used in this efficiency calculation.) This calculated count rate is still greater than 50 times that observed. However, as the $K\beta$ emission is distributed over more than 20 eV while the rocking curve width of the Ge crystal (71 mrad) (Brennan & Cowan, 1992, Zachariasen, 1945) corresponds to approximately 0.33 eV resolution, we conclude that the remaining 'lost' photons are a consequence of the high resolution of this spectrometer. For certain experiments where only resolution of $K\beta$ and $K\beta'$ features is necessary, an order of magnitude in count rate could be recaptured with a lower resolution instrument.

3.4 Fe K β emission spectrum of rubredoxin

In Figure 4, the K β emission spectrum (measured with an excitation energy of 7200 eV) of reduced *Pyrococcus furiosus* rubredoxin is compared with that from (NEt₄)[FeCl₄]. Both the protein and the model complex are high spin Fe compounds with approximately tetrahedral symmetry. The K β emission spectra are split into two regions, the main peak (K β) around 7057.9 eV and a satellite (K β ') at lower energy. The K β regions are very similar in the two spectra, but the position and intensity of the satellites differ. For (NEt₄)[FeCl₄], the K β ' satellite is stronger and better resolved, with a 14 eV energy separation from the main peak, while the rubredoxin has a weaker satellite ~13 eV lower in energy than the main peak. The weaker satellite in the protein spectrum may be due in part to the more covalent sulfur ligands as compared to chloride ligands in the model compound. As reviewed by Ekstig (Ekstig, Källne, Noreland & Manne, 1970), Peng (Peng, et al., 1994), and deGroot (de Groot F.M.F., Fontaine, A., Kao, C. C., & Krisch, M., 1994), the splitting of the K β main peak and satellite is due to the 3p3d exchange interaction. When 3d electrons are delocalized as in the case of covalent sulfur ligands, the smaller exchange interaction results in a smaller energy separation from the main peak and a weakened satellite. A more detailed analysis of these spectra will be presented elsewhere (Wang et al., 1996b). The important point is that the Fe K β spectrum of rubredoxin demonstrates that there is adequate sensitivity for recording emission spectra of metalloproteins. In many cases, there will be valuable chemical information in these spectra which makes more difficult excitation spectroscopy (see below) unnecessary.

3.5 Spin-polarized XANES

The predominately 'spin-down' vs. 'spin-up' nature of the $K\beta$ and $K\beta'$ regions, respectively, allows spin-polarized x-ray excitation spectra to be recorded. The fluorescence from either region can be monitored as a function of incident energy. In Figure 5, we show the first spin-polarized XANES of a metalloprotein (rubredoxin) recorded in this manner. There are several differences between the spin-up and spin-down spectra. The spin-down edge generally has sharper, better-defined features than the spin-up spectrum. There is a clear double-peak at the top of spin-down edge, while the spin-up edge has a single broad peak. Finally, there is a clear pre-edge peak around 7112.6 eV in the spin-down spectrum, which is generally described as a $1s \rightarrow 3d$ transition.

The $1s \rightarrow 3d$ transition provides a demonstration of the spin-polarized nature of these excitation spectra. In a tetrahedral environment, mixing of 4p and 3d orbitals gives this transition some dipole-allowed character. For high-spin Fe(II), a d^6 ion, the electronic configuration can be described as $e_g^3 t_{2g}^3$, and all of the 'spin-up' orbitals are filled. Transitions to the remaining t_{2g} spin-down levels are allowed, hence the ' $1s \rightarrow 3d$ ' transition in the spin-down spectrum. However, since there are no spin-up vacancies, the spin-up spectrum does not show a ' $1s \rightarrow 3d$ ' transition. The residual intensity in this region results from resonant Raman scattering (de Groot, et al., 1995). A more detailed discussion of the rubredoxin data with theoretical simulations is in preparation (Wang, et al., 1996b).

Ionic samples show clearer definition between the edge and pre-edge regions as compared to more covalent samples with similar geometry. This has been previously illustrated by comparing spin-polarized XANES from MnO_2 and MnF_2 (Hämäläinen, et al., 1992). As a contrast to the relatively covalent rubredoxin case, the spin-polarized XANES of MnF_2 are presented in Figure 6.

3.6 Photosystem II - a dilute challenge

A cluster of 4 Mn ions forms an essential part of the oxygen-evolving complex (OEC) of Photosystem II (Rutherford, Boussac, & Zimmerman, 1992). As the concentration of Mn in this system is quite low (typically ~ 40 ppm Mn), measurements on Photosystem II (PSII) illustrate the current sensitivity limit for this technique. The first Mn $K\beta$ emission spectrum of Photosystem II is shown in Figure 7. A count rate of ~1 count per second was obtained, requiring 8 hours of signal averaging to obtain the spectrum shown here. The beam was moved to a fresh spot on the sample every two hours. Mn $K\beta$ emission of Photosystem II poised in various states will be presented elsewhere (Grush et al., 1996b).

Photoreduction during exposure to bright x-ray sources is often a concern during metalloprotein experiments (George, Lowery, Solomon & Cramer, 1993; George et al., 1992; Murphy et. al., 1995; Debenham, et. al., 1996). Damage can be reduced by spreading the x-ray beam across a relatively large sample. Conversely, the situation is worse for this experiment, which involves point-to-point focussing.

Comparison of the PSII spectrum with Mn model complexes (Figure 7) shows that this sample contains predominantly Mn(II). It has been shown using conventional K-edge absorption measurements that Mn(II) is not a component of the resting 'S₁' state (Sauer, Yachandra, Britt, & Klein, 1992), and that the native Mn oxidation states should include Mn(III) (Kirby et al., 1981; Kusunoki et al., 1990; Penner-Hahn et al., 1990) and possibly Mn(IV) (Yachandra et al., 1993; Riggs, Mei, Yocum & Penner-Hahn, 1992). Most likely, this sample has been reduced by electrons produced during exposure to the x-ray beam.

With brighter beamlines, photodamage will become a concern for many systems. Careful monitoring of x-ray spectra for time-related changes as well as performing sample assays before and after x-ray exposure will be necessary in order to ensure the relevance of these x-ray measurements.

3.7 Future prospects

High resolution fluorescence experiments on metalloproteins are clearly starved for photons, and it is worth considering the impact of brighter sources. On third generation facilities such as the European Synchrotron Research Facility (ESRF) and the Advanced Photon Source (APS), high resolution fluorescence experiments on metalloproteins could become routine. The incoming photon flux on new undulator beamlines will likely improve by one to two orders of magnitude while still focussing to a sub-millimeter spot. Our current spectrometer has an efficiency of 10^{-7} with three crystals. Increasing the solid angle of the analyzers is possible by switching to six 6"-diameter crystals, improving the fluorescence at the detector by 50-fold,

and resulting in a total efficiency of 5×10^{-6} (using the $(\text{NEt}_4)[\text{FeCl}_4]$ complex as an example). The combined three to four order increase of both incoming photon and spectrometer efficiency could shorten the acquisition time for $K\beta$ emission spectra of metalloproteins to a few minutes, even for ≤ 50 ppm metal concentrations. However, the bright future of high resolution metalloprotein experiments is shadowed by the obstacles of photoreduction. With such a high photon brightness, the protein could easily be reduced before a single scan is completed. Photoreduction will become the limiting factor for these experiments. On-line monitoring through optical or other spectroscopies can be helpful to determine time-related changes. One possible solution to minimize photoreduction is to rotate a frozen protein solution during the measurements, requiring much higher homogeneity in sample preparation.

For spin-polarized experiments, the resolution of the curved crystal spectrometer is much better than necessary. Since the separation between the main peak and satellite is ~ 13 eV for Fe complexes, a detector with 10^{-3} energy resolution would be sufficient for measuring spin-polarized spectra. The development of ultra high energy resolution detectors, such as the bolometer (Legros, et al., 1995) and the superconducting tunnel junction detector (Frank, et al., 1996), may eventually eliminate the whole crystal spectrometer for spin-polarized study. It is, however, essential to have spectrometer resolution which is better than 1 eV in order to utilize the chemical shifts (~ 1 eV) in mixed valence and mixed spin state clusters for site-selective XAS.

4. Conclusions

The first high resolution fluorescence spectra of metalloproteins have been made possible by the development of a multiple crystal fluorescence spectrometer. The focus images of multiple form-bent crystals confirm that all diffracted beams are brought to a common focus within a region 3.8 mm (vertical) x 8.5 mm (horizontal) on the detector. The strengths of high resolution fluorescence metalloprotein studies are both site- and spin-selectivity and can complement the structural information obtainable from other spectroscopies. In addition, the spin-polarized near edge structure provides a new measure of the spin density. The current spectrometer has sufficient sensitivity for dilute protein experiments. With the combined two to three orders of magnitude improvement in photon flux and spectrometer efficiency, site-selective and spin-polarized EXAFS can become a powerful probe of multinuclear proteins in the near future.

Acknowledgements

We would like to thank Prof. Larry Que (University of Minnesota, Minnesota) for the $(\text{NEt}_4)[\text{FeCl}_4]$ sample, Prof. M. Adams and H. Huang (University of Georgia, Athens) for the *P.furiosus* rubredoxin sample and Prof. J. E. Penner-Hahn and P. S. deMarois (University of Michigan, Ann Arbor) for the Photosystem II sample. This work was funded by the National Institutes of Health (GM-48145) and the Department of Energy, Office of Health and Environmental Research. The National Synchrotron Light Source and the Stanford Synchrotron Radiation Laboratory are supported by the Department of Energy, Office of Basic Energy Sciences.

References

- Åberg T. & Tulkki J. (1985), *Atomic Inner-Shell Physics*, edited by Crasemann, B., Plenum, New York.
- Berman, L.E., Hastings, J. B., Oversluizen, T., Woodle, M. (1992). *Rev. Sci. Instrum.* **63**, 428-432.
- Blake, P. R., Park, J.-B., Bryant, F. O., Aono, S., Magnuson, J. K., Eccleston, E., Howard, J. B., Summers, M. F. & Adams, M. W. W. (1991). *Biochemistry*, **30**, 10885-10895.
- Brennan, S. & Cowan, P. L. (1992). *Rev. Sci. Instrum.* **63**, 850-853.
- Briand, J.P., Smionovici, A., Chevallier, P. & Indelicato, P. (1989). *Phys. Rev. Lett.*, **62**, 2092-2095.
- Carra, P., Fabrizio, M. & Thole, B.T. (1995). *Phys. Rev. Lett.* **74**, 3700-3703.
- Cowan, P.L. (1994). in *Resonant Anomalous X-Ray Scattering*, edited by Materlik, G., Sparks, C.J. & Fischer, K. pp. 449-472. North-Holland, Amsterdam.
- Debenham, M.J., Hao, Q., Hasnain, S.S. Dodd, F.E. and others (1996). *Synchr. Rad.* **3**, 14-19.

de Groot, F. M. F., Pizzini, S., Fontaine, A., Hämäläinen, K., Kao, C. C. & Hastings, J.B. (1995). *Phy. Rev. B* **51**, 1045-1052.

de Groot F.M.F., Fontaine, A., Kao, C. C., & Krisch, M. (1994). *J. Phys. Cond. Matt.*, **6**, 6875-6884.

de Groot F.M.F. (1996). *Phys. Rev. B* **53**, 7099-7110.

Eisenberger, P., Platzman, P.M. and Winick, H. (1976). *Phys. Rev. Lett.* **35**, 623-626;

(1976). *Phys Rev. B* **31**, 2377-2380.

Ekstig, B., Källne, E., Noreland, E., Manne, E. (1970). *Physica Scripta* **2**, 38-44.

Frank, M., Mears, C.A., Labov, S. E., Azgui, F., Lindeman, M.A., Hiller, L.J. & Netel, H. (1996). *Nuc. Instr. Meth.* **370**, 41-43.

George, S.J., Lowery, M.D., Solomon, E.I. & Cramer, S.P. (1993). *J. Am. Chem. Soc.* **115**, 2968-2969.

George, S.J., van Elp, J., Chem, J., Ma, Y., Chen, C.T., Park, J.-B., Adams, M.W.W., Searle, B.G., deGroot, F.M.F., Fuggle, J.C. & Cramer, S.P. (1992). *J. Am. Chem. Soc.* **114**, 4426-4427.

Ghanotakis, D. F., Demetriou, D. M. & Yocum, C. F. (1987). *Biochim. Biophys. Acta* **891**, 15-21.

Ghanotakis, D.F. & Yocum, C.F. (1986). *FEBS Lett.* **197**, 244.

Gill, N. S. (1961). *J. Chem. Soc.* **18**, 3512.

Grush, M. M., Christou, G., Hämäläinen K. & Cramer, S. P. (1995). *J. Am. Chem. Soc.* **117**, 5895-5896.

Grush, M.M., Horne, C.R. & Cramer, S.P. (1996a). In preparation.

Grush, M.M., deMarois, P. S., Daly, K., Penner-Hahn, J.E. & Cramer, S.P. (1996b). In preparation.

Hämäläinen, K., Siddons, D.P., Hastings, J.B. & Berman, L.E., (1991). *Phys. Rev. Lett.* **67**, 2850-2853.

Hämäläinen, K., Kao, C.C., Hastings, J.B., Siddons, D.P., Berman, L.E., Stojanoff, V. & S. P. Cramer (1992). *Phys. Rev. B* **46**, 14274-14277.

Hoyer, E., Bahr, C., Chan, T., Chin, J., Elioff, T., Halbach, K., Harnett, G., Humphries, D., Hunt, D., Kim, K.-J., Lauritzen, T., Lindel, D., Shirley, D., Tafelski, R., Thompson, A., Cramer, S., Eisenberger, P., Hewitt, R., Stöhr, J., Boyce, R., Brown, G., Golde, A., Gould, R., Hower, N., Lindau, I., Winick, H., Yang, J., Harris, J. & Scott, B. (1983). *Nucl. Inst. & Meth.* **208**, 117-125.

Kobayashi, K., Maruyama, H., Maeda, H., Iwazumi, T., Kawata, H. & Yamazaki, H. (1995). *Physica B* **209**, 779-780.

Krause, M. (1979). *J. Phys. Chem. Ref. Data* **8**, 307-327.

Krisch M.H., Kao C.C., Sette F., Caliebe W.A., Hämäläinen, K. & Hastings, J.B. (1995). *Phys. Rev. Lett.* **74**, 4931-4934.

Kusunoki, M., Ono, T., Inoue, Y., Susuki, M., Uchida, A., Matsushita, T. & Oyanagi, H. (1991). "Mn K-edge XANES Spectroscopy for water-splitting Mn-enzyme in photosynthesis. High quality pre-edge features in the S₁ and S₂ states." in *X-ray Absorption Fine Structure*, edited by Hasnain, S.S., pp. 174-177, Ellis Horwood Limited, West Sussex.

LeGros, M., Silver, E., Schneider, D., McDonald, J., Bardin, S., Schuch, R., Madden, N. & Beeman, J. (1995). *Nucl Instr. Meth.* **357**, 110-114.

Lindh, A. E. & Lundquist, O. (1924). *Ark. Mat. Astronom. Fys.* **18**, 14.

Marenkov, S.O. (1994). *Handbook of partial attenuation coefficients of characteristic X-ray radiation*, edited by Marenkov, O.S., Nova Science Publishers, New York.

Mori, A., Kayanuma, Y. & Kotani, A. (1991). *Prog. Theo. Phys.* **106**, 75-93.

Murphy, L.M., Dobson B.R., Neu M. Ramsdale C.A. and others, (1995). *J. Synchr. Rad.* **2**, 64-69.

Nordgren J., Bray G., Cramm S., Nyholm R., Rubensson, J.-E. & Wassdahl, N. (1989). *Rev. Sci. Instrum.* **60**, 1690-1696.

Peng, G., deGroot, F.M.F., Hämäläinen, K., Moore, J.A., Wang, X., Grush, M. M, Hastings, J.B., Siddons, D.P., Armstrong, W.H., Mullins, O.C. & Cramer, S.P. (1994). *J. Am. Chem. Soc.* **116**, 2914-2920.

Peng, G., Wang, X., Randall, C. R., Moore, J. A. & Cramer, S. P. (1994). *Appl. Phys. Lett.* **65**, 2527-2529.

Penner-Hahn, J.E., Fronko, R.M., Pecoraro, V.L., Yocum, C.F., Betts, S.D. & Bowlby, N.R. (1990). *J. Am. Chem. Soc.* **112**, 2549-2557.

Riggs, P.J., Mei, R., Yocum, C.F. & Penner-Hahn, J.E. (1992). *J. Am. Chem. Soc.* **114**, 10650-10651

Sauer, K., Yachandra, V.K., Britt, R.D & Klein, M.P. (1992). in *Mn Redox Enzymes*, edited by Pecoraro, V.L. pp. 141-175, VCH Publishers, New York.

Schütz, G., Wagner, W., Wilhelm, W., Kienle, P., Zeller, R., Frahm, R. & Materlik, G. (1987). *Phys. Rev. Lett.* **58**, 737-740.

Schlacter, A.S. (1994). "Third Generation Synchrotron Light Sources", in *New Directions in Research with Third-Generation Soft X-Ray Synchrotron Light Sources*, . edited by Schlacter, A. S. and Wuilleumier, F. J., pp. 1-22. Kluwer Academic Publishers, Dordrecht.

Schulke, W. & Nagasawa, H. (1984). *Nucl. Inst. Meth.* **222**, 203-206.

Skytt, P., Guo, J.H., Wassdahl, N. & Nordgren, J. (1995). *Phys. Rev. A* **52**, 3572-3576.

Smith, G.C. & Yu, B. (1995). *IEEE* **42**, 541-547.

Sparks, C.J., Jr. (1974). *Phys. Rev. Lett.* **33**, 262-265.

Stojanoff, V., Hämäläinen, K, Siddons, D.P., Hastings, J.B., Bermab, L.E., Cramer,

S.P. & Smith, G. (1992). *Rev. Sci. Instrum.* **63**, 1125-1127.

Taguchi, M. & Kotani, A. (1996). *J. Phys. Soc. Jpn.* **63**, 706-709.

Udagawa Y., Hayashi H., Tohji K & Mizushima T. (1994). *J. Phys. Soc. Jpn.* **63**, 1713-1720.

Wang, X., Randall, C. R., Peng, G. & Cramer, S. P. (1995). *Chem. Phys. Lett.* **243**, 469-474.

Wang, X., Cramer, S.P., Zang, Y., Que, L., Jr., Ankudinov, A. & Rehr, J. (1996a). In preparation.

Wang X., Huang, H, Adams, M, Kotani, A. & Cramer, S.P. (1996b). In preparation.

Wang, X. & Cramer, S. P. (1996c). In preparation.

Williams, G.P. (1986) in *X-ray Data Booklet*, edited by Vaughan, D., University of California, Berkeley.

Winick, H. (1995). *J. Elec. Spec.* **75**, 1-8.

Yachandra, V.K., DeRose, V.J., Latimer, M.J., Mukerji, I., Sauer, K., & Klein, M.P. (1993). *Science* **260**, 675-679.

Zachriassen, W. H. (1945). *Theory of X-ray diffraction in crystals*, edited by Zachriassen, W.H., Dover Publications, New York.

Figure captions

Figure 1. Schematic diagrams of the crystal array used for metalloprotein experiments: side view (left) and top view (right).

Figure 2. Illustration of the focus image achieved with 3 crystals simultaneously. The label at the bottom shows the photon counts corresponding to a given color. The horizontal and vertical axes in the picture are also the horizontal and vertical axes, respectively, for the position sensitive detector.

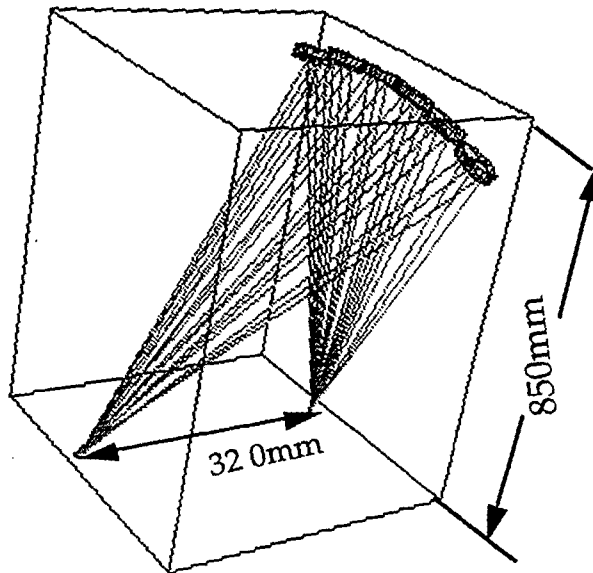
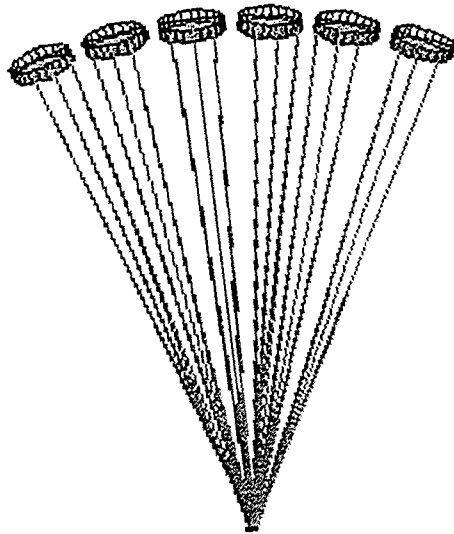
Figure 3. Improved resolution achieved with a form-bent Ge(620) crystal (solid line) as opposed to a mechanically bent crystal (dotted line), illustrated with the $K\beta$ emission spectrum of $(\text{NEt}_4)[\text{FeCl}_4]$.

Figure 4. Experimental Fe $K\beta$ spectrum of rubredoxin (dotted line) compared with the tetrahedral model complex $(\text{NEt}_4)[\text{FeCl}_4]$ (solid line).

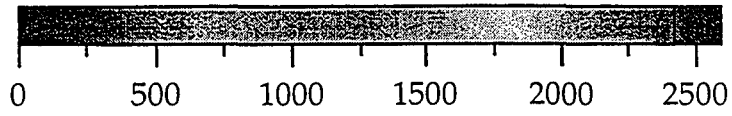
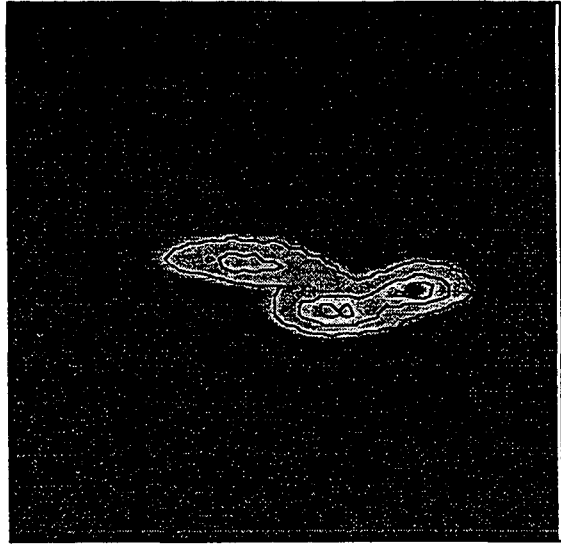
Figure 5. Spin-polarized Fe excitation spectra of rubredoxin. The spin-down transition (solid line) is compared with the spin-up transition (dotted line). The inset is the pre-edge region of both excitation spectra. The spin-down edge was measured by setting the analyzer crystals to the main $K\beta$ peak, 7057.9 eV, while the spin-up transition was monitored at 7044.9 eV. The raw data was smoothed over a 5 point range.

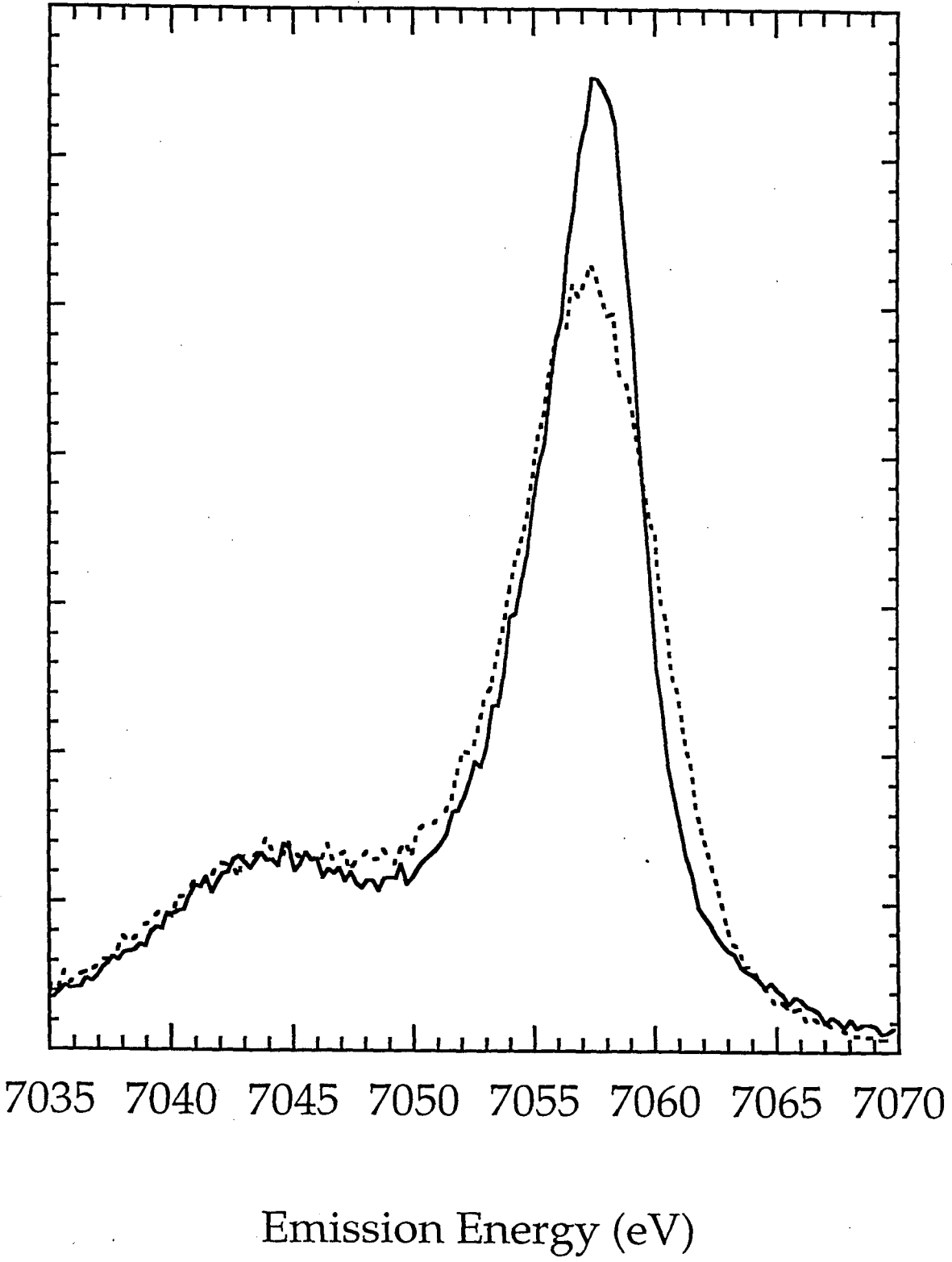
Figure 6. A demonstration of spin-selectivity using MnF_2 . Mn XANES using $\text{K}\beta$ detection (solid line) and $\text{K}\beta'$ detection (dotted line). The 1s to 3d pre-edge feature is only observed when the outgoing electron is spin down.

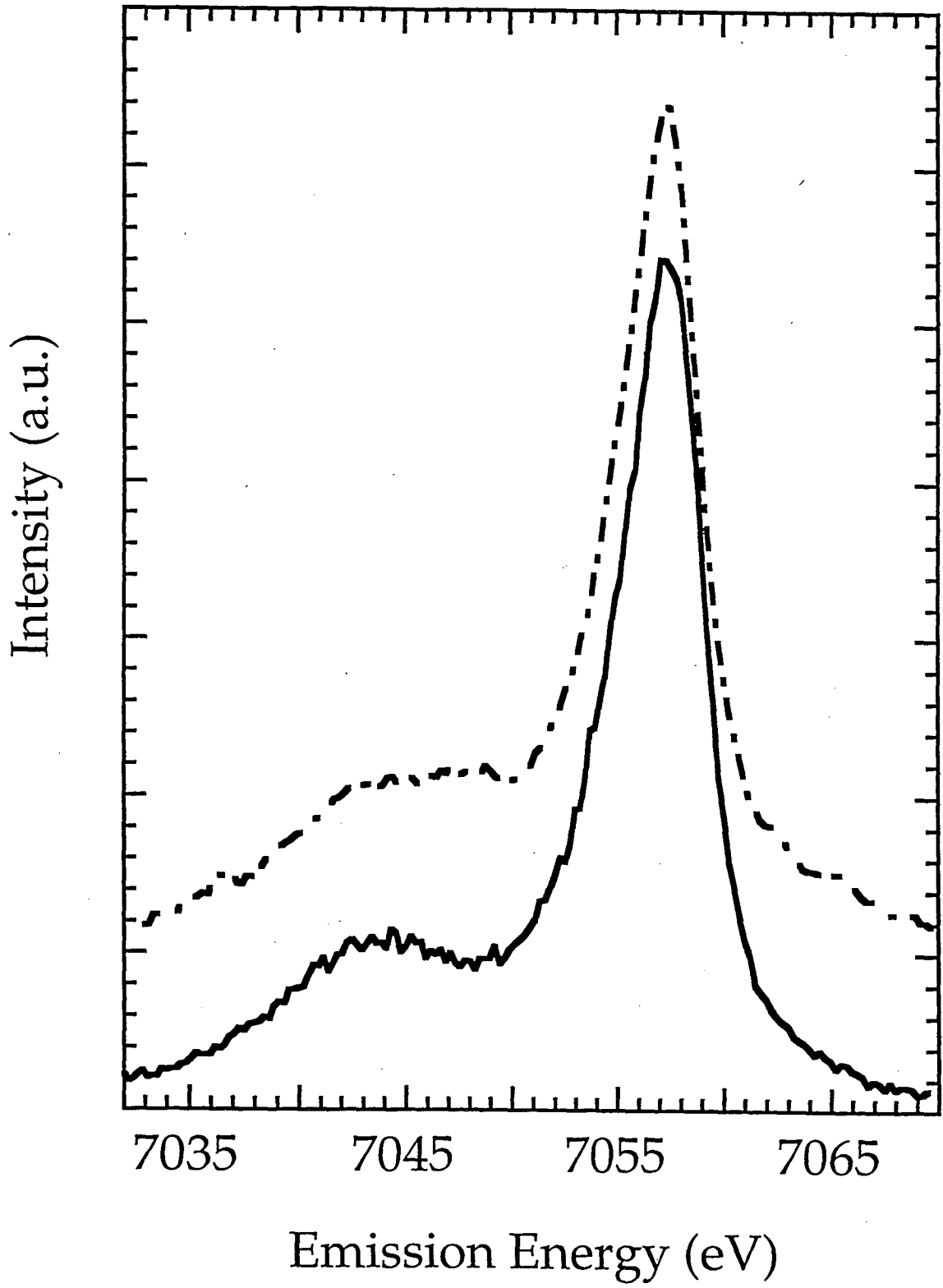
Figure 7. Experimental Mn $\text{K}\beta$ emission spectra of photoreduced Photosystem II (top, solid line) compared with Mn(II)(Cl)_2 (bottom, dotted line).

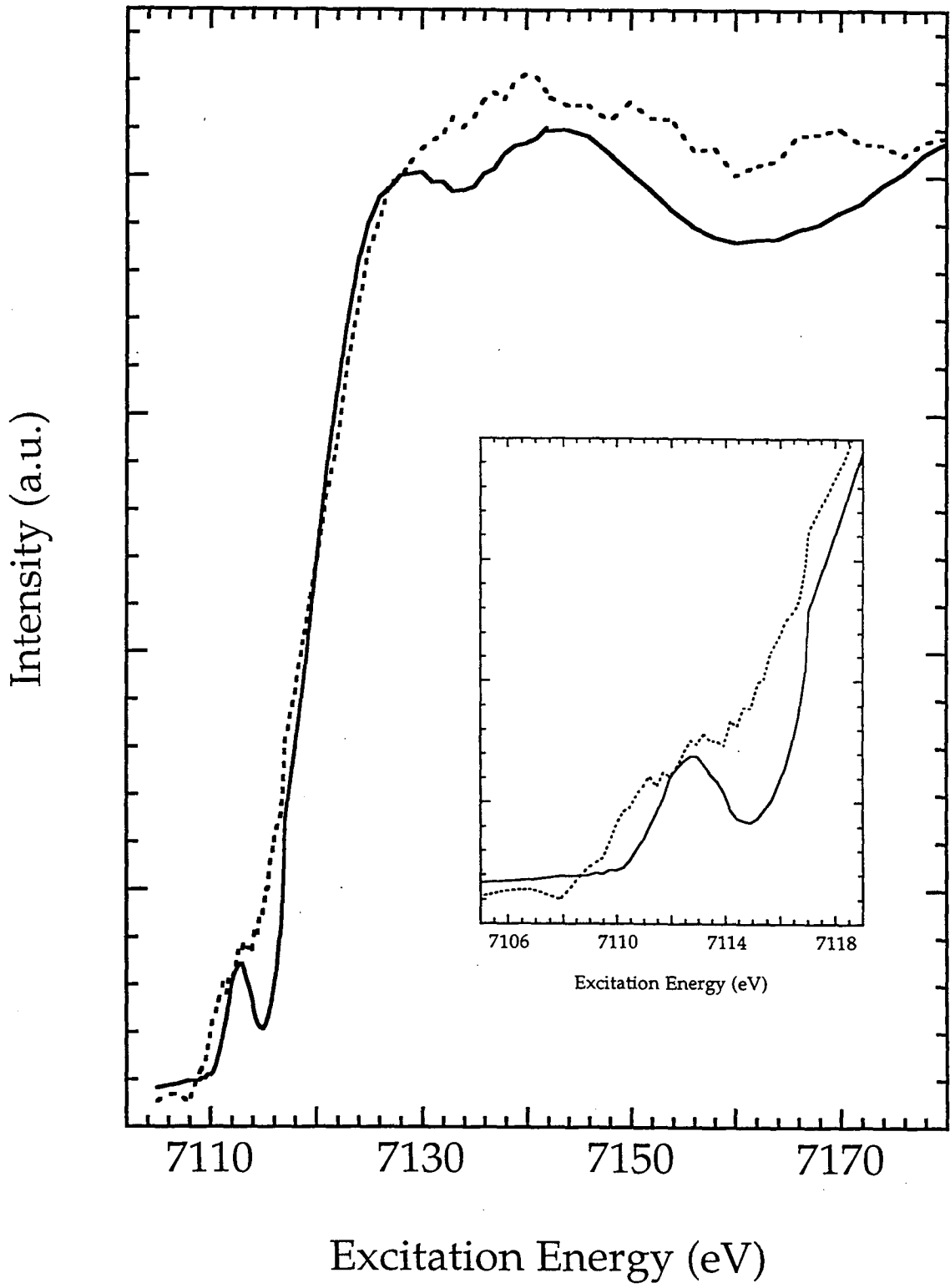


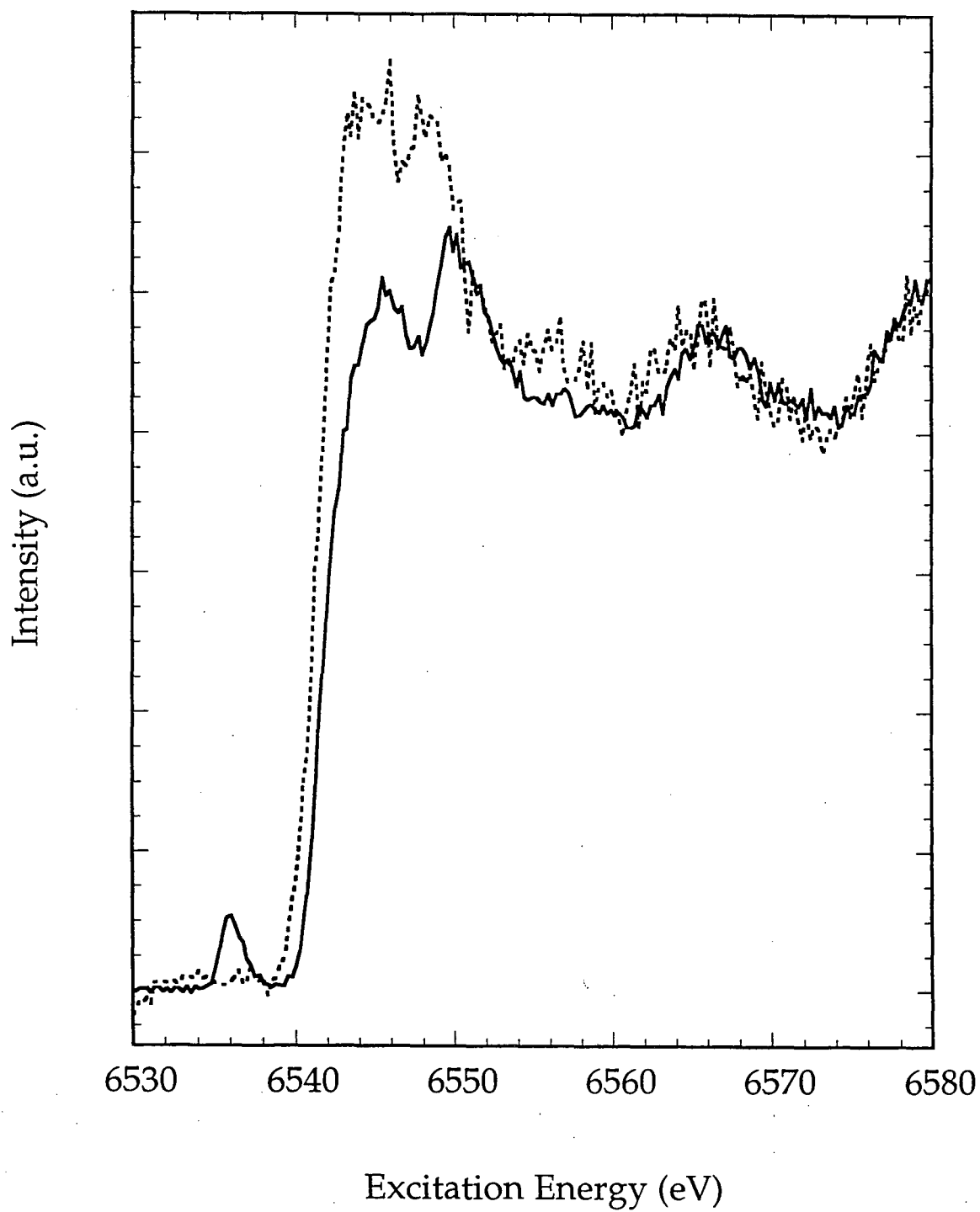
1 cm

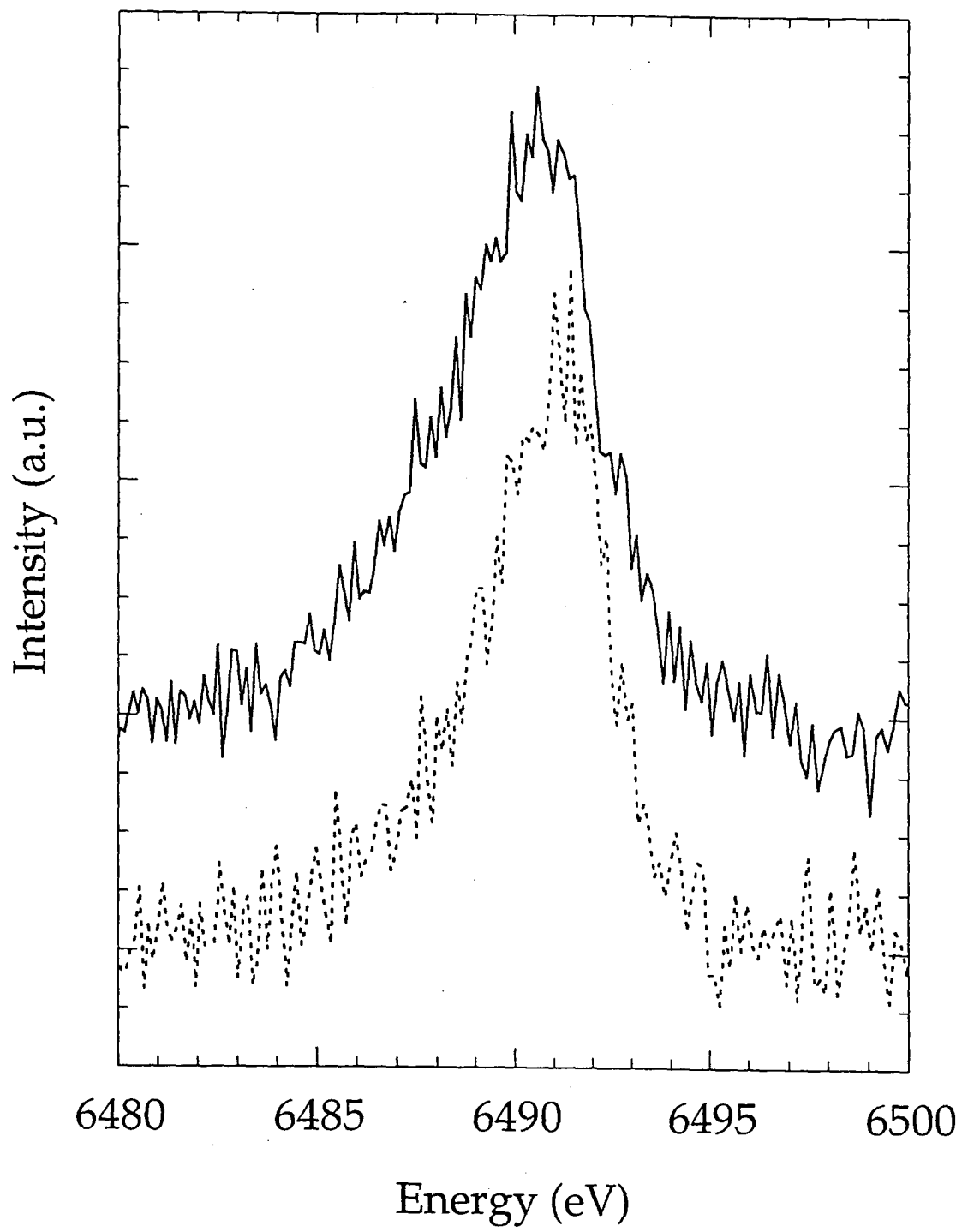












5.2 Experimental Results of Rubredoxin

In the first application of high resolution fluorescence spectroscopy on metalloproteins, the Fe-S cluster rubredoxin was used as an example to demonstrate the sensitivity of our current spectrometer, as well as the spin-polarization and line-sharpening effects of this novel technique. Some first initial results are discussed in the last section, but detailed analysis of $K\beta$ emission spectra with ligand field model, the influence of more covalent ligands, possible model to simulate the spin polarized excitation spectra, the life time disappearance effect, and the severity of photoreduction of synchrotron experiments on metalloproteins are discussed in this section.

5.2.1 $K\beta$ Emission Spectra

Using ligand field multiplet model, the Fe $K\beta$ emission spectrum of reduced rubredoxin is simulated in Figure 5.1. In the simulation, we used $10Dq=0.9$ eV and Fe(II) d^6 configuration in T_d symmetry as the ground state. Because of the very covalent sulfur ligands [5.1], the Slater integrals from calculation were reduced to 55% of their atomic values. The spin-up and spin-down emission spectra are constructed from the method discussed in Chapter 2.3. There are some agreement and discrepancies with the theoretical simulations. The main features of $K\beta_{1,3}$ from theory are in good agreement with experimental data, but the satellite intensity is somewhat too large in the calculated spectrum. Analysis of calculations for many possible transitions reveals that a large number of $3p^53d^6$ states are symmetry-allowed final states, especially in the case of a strong crystal field (high-spin). The weakness of the satellite may result from experimental broadening of this large number of low-intensity peaks, as seen by many transitions in the energy range 7043-7054

eV. Similar discrepancies have been found in $K\beta$ emission for higher oxidation states Mn compounds [5.2]. The disagreement between experiment and calculations suggests that when the valence electrons in the metal center (Fe in this case) are more delocalized, the configuration interactions between different occupations of 3d electrons can not be omitted. Since the 3d spin-orbit effects correlate with ligand field strength, the 3d spin-orbit coupling should also be included in the simulation. A more comprehensive theory, e.g. the charge transfer cluster model should be used for a detailed study in the case of covalent compounds. Inclusion of the charge transfer effects in Ni compound does show dramatic improvement between experiment and simulations [5.3].

Relaxation Effects

When taking into account the charge transfer effects in the calculation, there are complications regarding how it should be included. Once a 1s core hole is created, the most relaxed state including charge transfer is $1s^1 3d^7 \underline{L}$ with the lowest energy, which does not necessarily have a very large absorption cross section. In our calculation, we assume the ground state symmetry derived from the $3d^6$ configuration does not change upon the creation of a core hole, so the system react to this creation as staying in the same symmetry but derived from the $1s^1 3d^7 \underline{L}$ configuration. However, the state with the same symmetry in $1s^1 3d^7 \underline{L}$ often does not have the lowest energy, therefore in principle it can relax to the lowest state. These effects are totally omitted in the ligand field multiplet calculation, even with the inclusion of charge transfer effects. This complex problem relates to a more general question of the creation of core hole and decay processes, and its influence on the spectral shape through the different spectroscopic techniques. This may only be solved

by combination of resonant experiments, such as x-ray photoemission and absorption. Effectively it can be treated roughly through lifetime broadening.

Difficulties using Charge Transfer Calculation

There are also some practical difficulties to account the charge transfer effects. A detailed electronic structure of the ground state has to be known before any reasonable parameters can be used in the $K\beta$ simulation. The parameters which determine the relative energies and strength of hybridization among different electronic configurations are the charge transfer energy D , the correlation energy U , the core potential energy Q and the hybridization strength T . All these parameters have to be measured through other techniques such as XPS. For metalloproteins, these parameters are not generally available, due to the difficulty to conduct 2p or 3p photoemission experiments. Without any reasonable guess of so many parameters, agreement between experiment and calculation is just pure luck. Also, when taking into account the charge transfer effects by confining to only two-configuration approximation, there are already four-fold transitions we have to perform, in case of Fe(II), namely the $1s^13d^6 \rightarrow 3p^53d^6$, $1s^13d^7\bar{L} \rightarrow 3p^53d^7\bar{L}$, $1s^13d^6 \rightarrow 1s^13d^7\bar{L}$, and $3p^53d^6 \rightarrow 3p^53d^7\bar{L}$. In some cases, third configuration $1s^13d^8\bar{L}\bar{L}'$ should be also taken into account for a more accurate ground state description. To calculate all the wavefunctions and transition matrix elements of all possible transitions, it does require a large computer. The computer in our laboratory can not run those calculations.

Covalency Effects

To better our understanding of the covalency effects on experimental $K\beta$ emission spectra, a comparison of three Fe compounds with different

Figure 5.1 Experimental Fe K β emission spectrum of rubredoxin (top, dotted line) as compared to ligand field multiplet simulations (bottom). Plotted theoretical spectra are total fluorescence (dotted-dashed line), spin-up (dotted line) and spin-down (solid line) spectra.

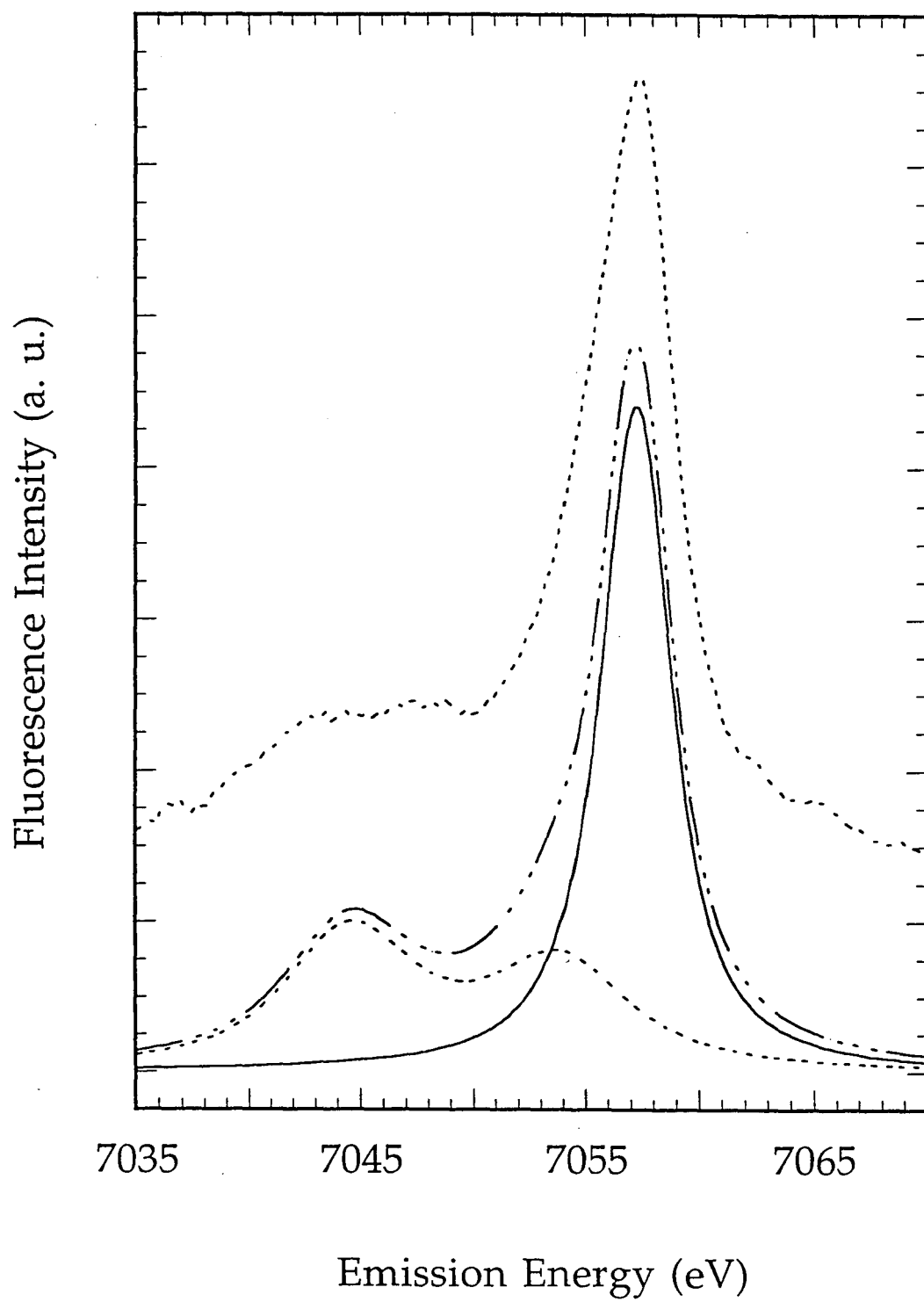
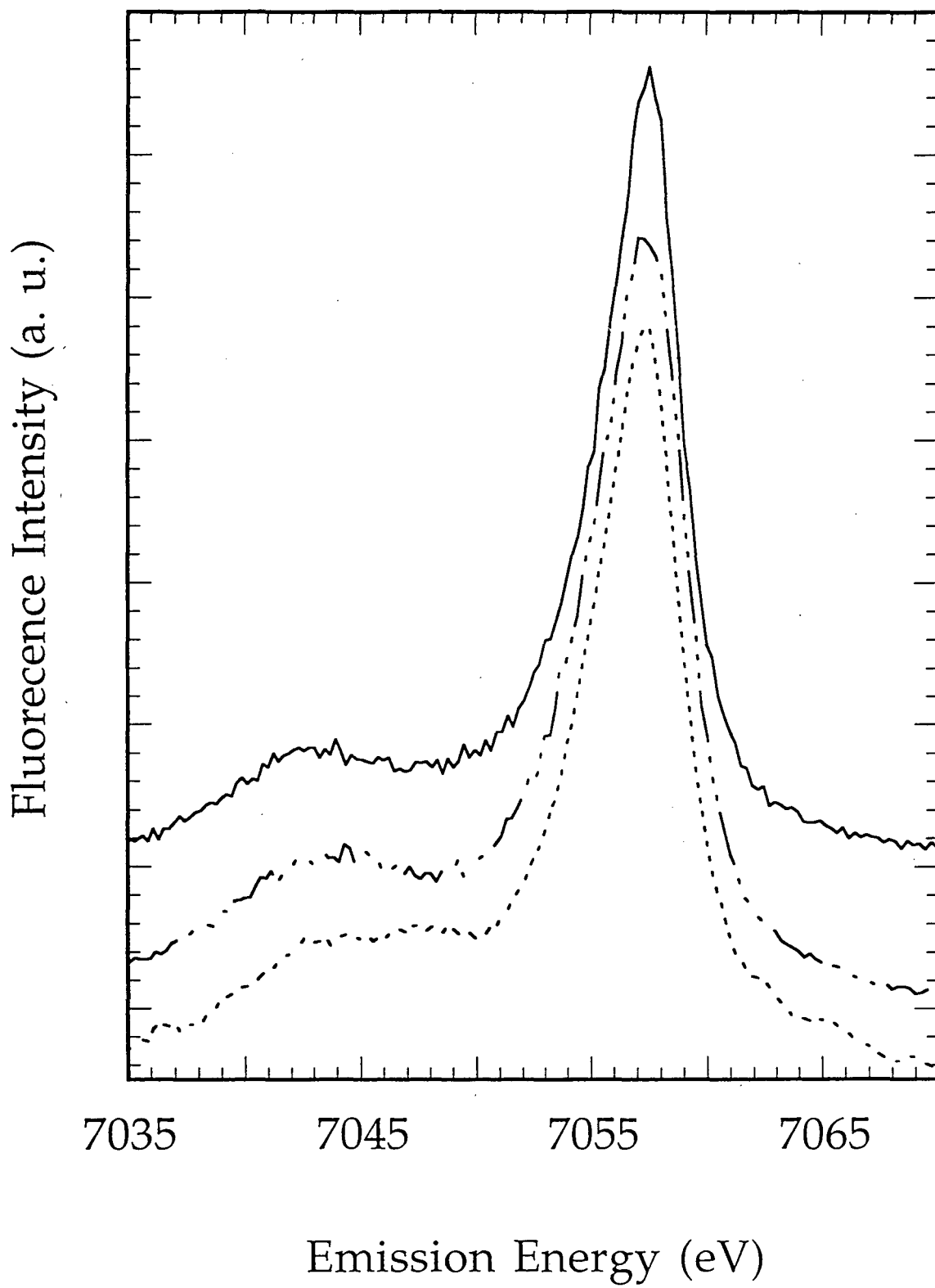


Figure 5.2 Covalency effects on experimental Fe $K\beta$ emission spectra. Plotted are Fe_2O_3 (top, solid line), $(\text{NEt}_4)[\text{FeCl}_4]$ (middle, dotted-dashed line) and rubredoxin (bottom, dotted line).



degrees of covalency are presented in Figure 5.2. After normalizing at the main peak, it is clearly shown that the satellite shifts its intensity to the higher energy side from Fe_2O_3 to rubredoxin, resulting in a smaller energy difference from the main peak. And the intensity of satellite also decreases gradually with the increase of covalency.

We would like to point out though, there are possible reasons to believe that the low S/N of the experiments could cause distortions on the spectrum, particularly at the satellite. For rubredoxin, 225 ppm Fe concentration gives a typical count rate around 50 photons/sec on the peak, as compared to 3000 photons/sec for $(\text{NEt}_4)[\text{FeCl}_4]$. It takes about 4 hours (8 scans) to generate a reasonable protein spectrum, and the S/N is still poor as compared to 0.5 hours emission from the model compound. The satellite which 'suffers' mostly from the low count rate and relatively high noise level could not be well resolved as that of the model compound. To get better data on protein samples, longer time data collection is necessary, but special care must be taken to preserve the sample integrity for long time beam exposure.

5.2.2 Spin-Polarized Excitation Spectra

Although the charge transfer effects, covalency effects and the relaxation effects complicate the detailed simulations for rubredoxin, the separation of spin polarized components in the emission spectrum remains intact. The main peak $\text{K}\beta_{1,3}$ still corresponds to ~85% spin-down transitions, and the satellite $\text{K}\beta'$ almost 100% spin-up. Setting analyzer crystals at those emission energies, first spin-polarized excitation spectra of a metalloprotein were obtained, and are presented in Figure 5.3.

As discussed in Chapter 5.1, there are three main differences between spin-up and spin-down K edge excitation spectra of rubredoxin: The pre-edge

feature which only appears in the spin-down spectrum because of the only available 3d spin-down orbitals; the sharper edge of the spin-down spectrum in general, and the double-peak feature on the top of the edge.

Those small but observable differences have their own significance to better our understanding of the electronic models we use for core spectroscopy interpretation. Recently, a spin-dependent linearized augmented plane-wave calculation of the MnF_2 band structure in the antiferromagnetic state has been reported by Dufek [5.4], but the agreement with the experimental excitation spectra is poor. Soldatov et. al. [5.5] have made a self-consistent full multiple-scattering analysis of the spin-dependent Mn K edge absorption for MnF_2 and MnO , but the results with MnO is still poor. More recently, Taguchi and Kotani [5.6] have used the charge transfer cluster model and a coherent second-order optical formula to calculate the spin dependent Mn K edge excitation of MnF_2 and MnO . I will discuss briefly of their findings for Mn compounds, and apply those to the spin-polarized Fe K edge excitation spectra of rubredoxin.

As shown in the work of Taguchi and Kotani, there are two important results from the cluster model and inelastic scattering calculations. First, the importance to include the core hole potential. When assuming the spin dependent density of states of Mn from band calculation, and using coherent the second-order optical process, the excitation spectra resemble the original density of states of the valence band, but differ from the experimental results. Since the core hole potential is not well screened by the charge transfer between metal 3d and ligand 2p states, the core hole potential act on the covalent band must be taken into account. This results in a double-peak structure on the top of the spin-down edge, instead of a slight shoulder when the core hole potential is ignored. Second important effect is the 3p lifetime

Figure 5.3 Experimental spin-up (dotted line) and spin-down (solid line) excitation spectra of rubredoxin.

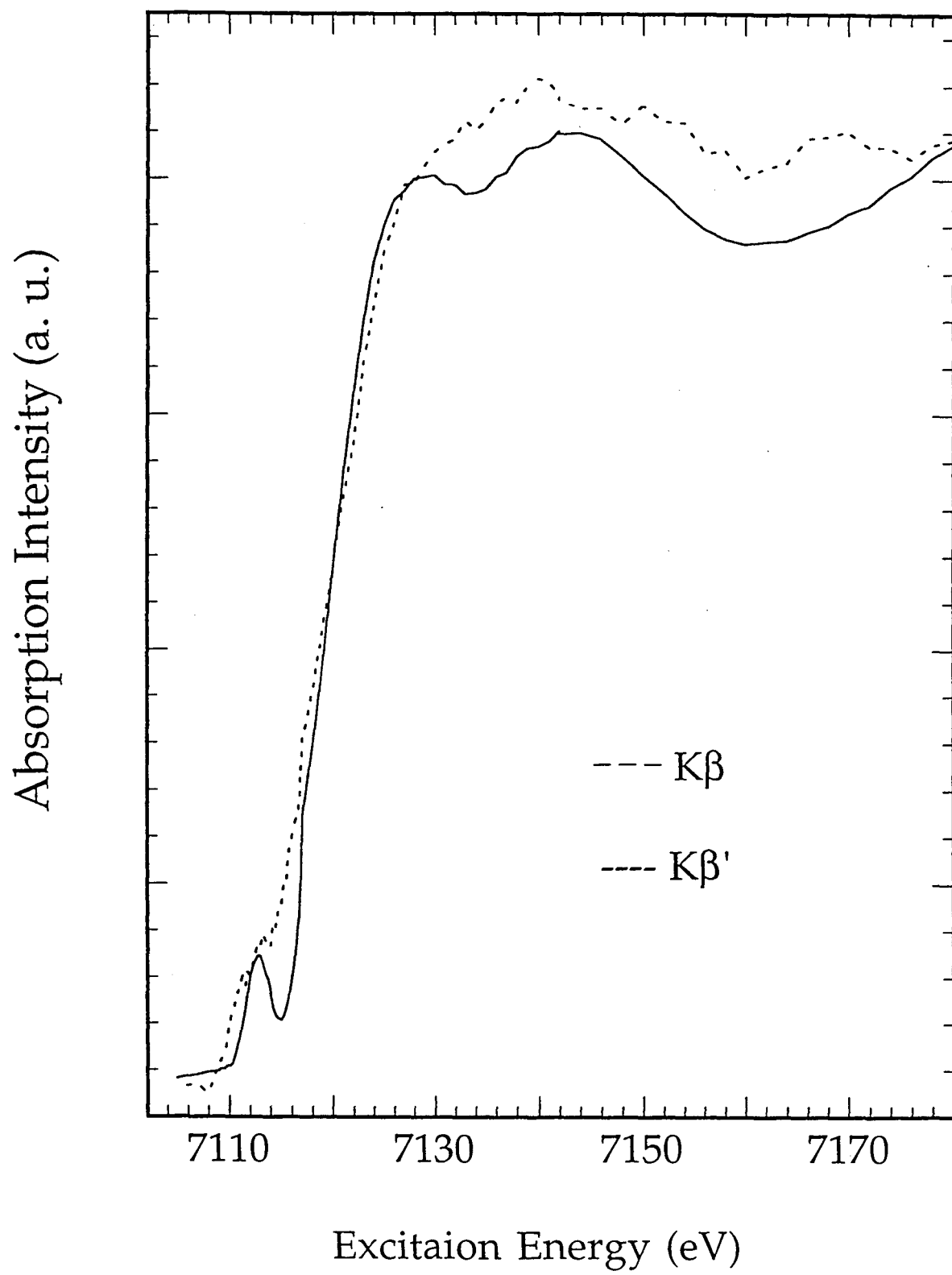
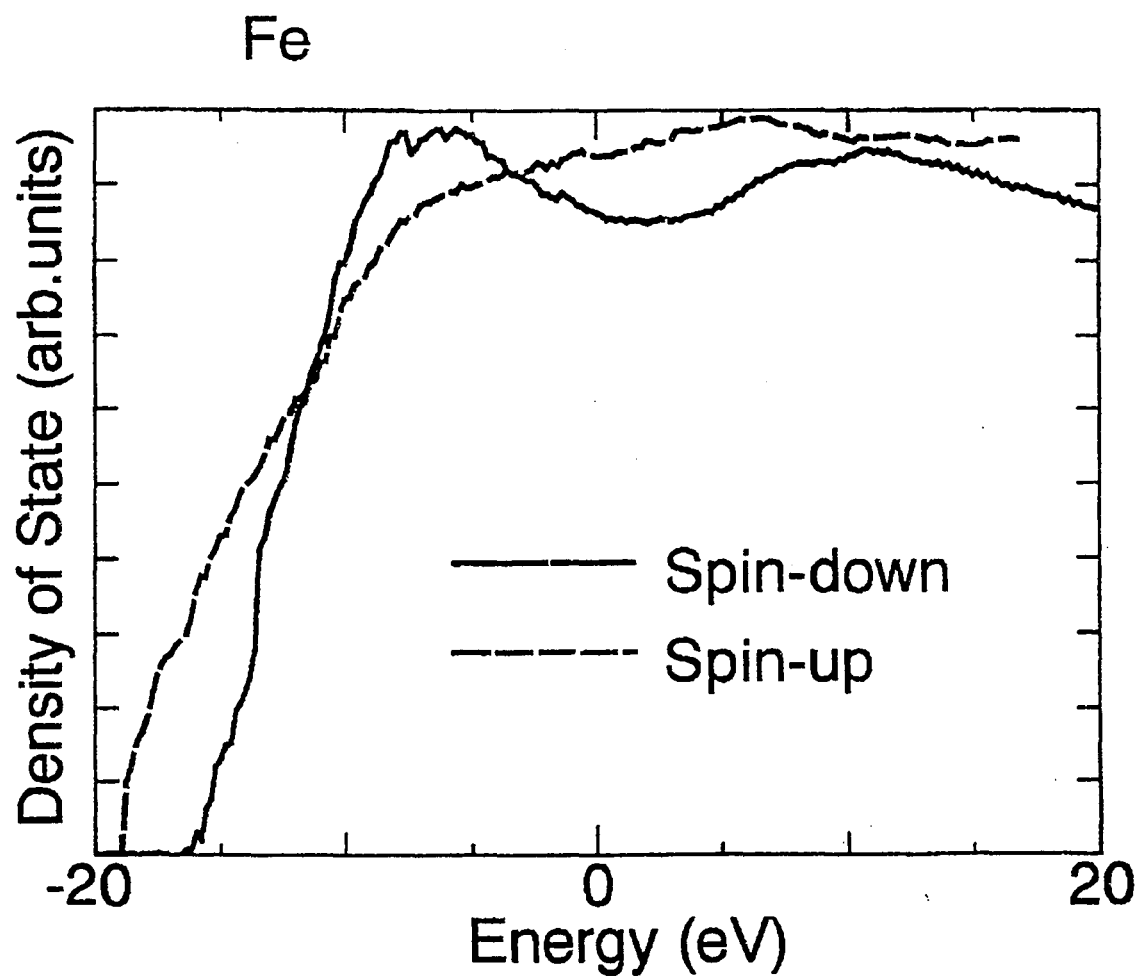


Figure 5.4 . Calculated spin dependent density of state for rubredoxin.



dependence on the multiplet terms. For 7P final state in Mn(II) (mostly spin-down), a 0.01 eV lifetime broadening has been found, which is much narrower than what was generally believed (normally about hundreds of meV). This longer lifetime gives rise to much sharper features in the spin-down spectrum than that in the spin-up, since the lifetime broadening for 5P of 0.6 eV was found to best simulate the experimental spectrum.

Those important effects can be used to explain the Fe K excitation edge features of rubredoxin. A similar calculation for the spin dependent density of states of rubredoxin have been performed with collaboration with Kotani group, and the result is shown in Figure 5.4. If we disregard the charge transfer between Fe(II) and ligand states, those spectra reduce to a single peak, and this shows again a strong hybridization effect on the Fe system. However, without information on the valence band and electronic structure, further simulations as for MnF_2 and MnO are impossible. There are quite pronounced differences already above the edge on the spin dependent density of state.

5.2.3 Line-Sharpening Effect

As discussed in Chapter 2.2, the $K\beta$ detected excitation exhibits sharper features than total fluorescence yield, because of the disappearance of 1s core hole lifetime. The broadening parameters used in the calculation from Kotani group prove how sharp the excitation spectra could be. We show the comparison of total fluorescence yield K edge Fluorescence spectra with the $K\beta$ detected one in Figure 5.5. Due to the limitation of experimental broadening (in our case, ~ 1.0 eV), the $K\beta$ excitation does show some improvement in resolution, though no drastic changes, as demonstrated by Hämäläinen [5.7].

Figure 5.5 Line-sharpening effect of rubredoxin. Plotted are total fluorescence yield excitation spectrum (dotted line) and $K\beta$ detected excitation spectrum (solid line).

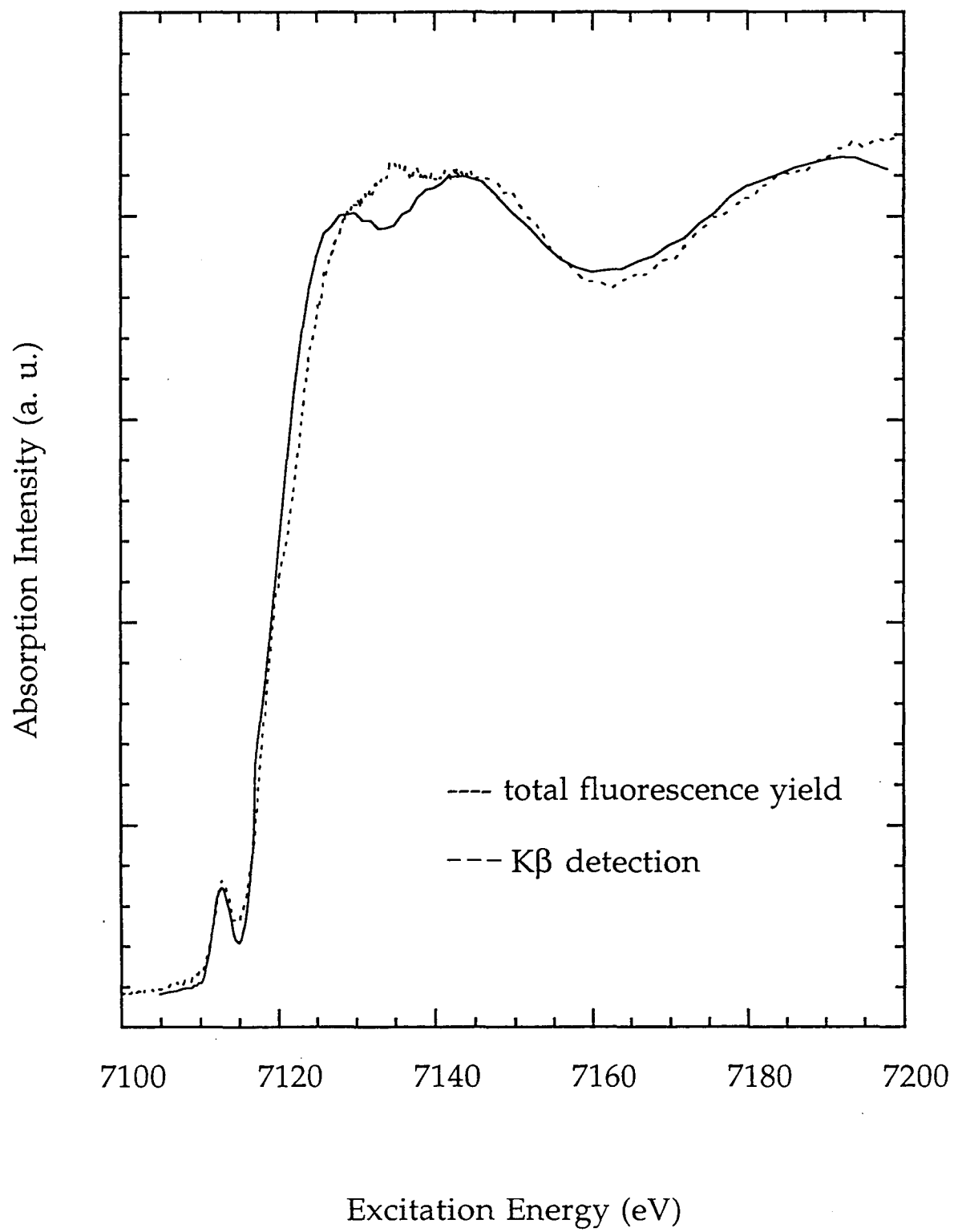
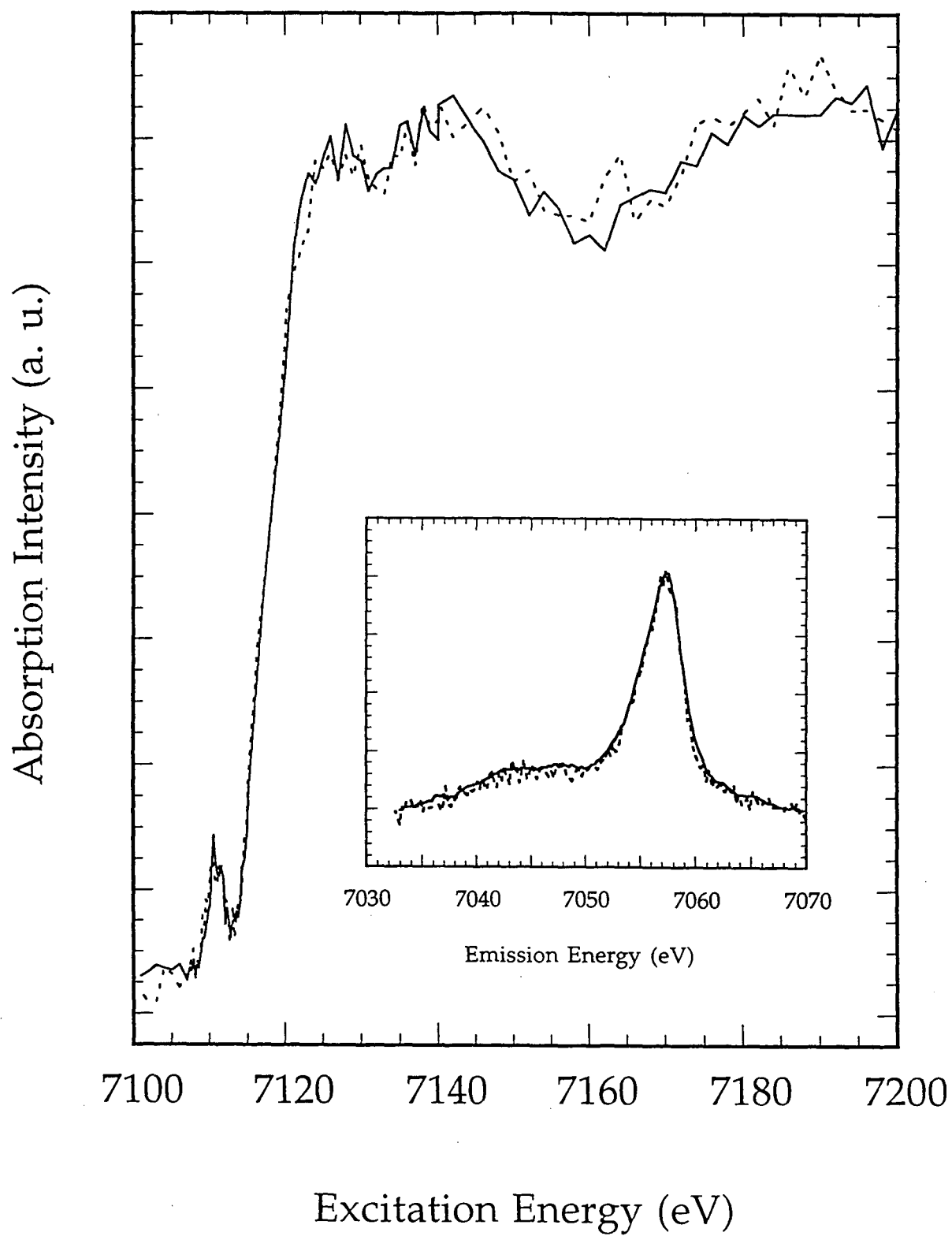


Figure 5.6 Photoreduction on rubredoxin. Plotted are oxidized (dotted line) and reduced excitation of rubredoxin (solid line). Inserted are $K\beta$ emission spectra.



5.2.4 Photoreduction

Photoreduction during exposure to bright x-ray sources is always a concern during metalloprotein experiments [5.8]. This is what happened to the oxidized rubredoxin. After on the beam of $\sim 10^{12}$ photon/s flux at 100 K for about 2 hours, the emission spectrum of oxidized became the same as the reduced one, and the edge position of the excitation spectrum was also shifted to lower energy. The edge of oxidized rubredoxin should be at higher energy, as found from conventional Fe K edge of rubredoxin [5.9]. Most likely, the sample has been reduced by the electron created during the x-ray exposure. The comparison of reduced and oxidized rubredoxin is shown in Figure 5.6.

With the development of new synchrotron facilities with a high photon brightness, the protein could easily be reduced before a single scan is completed. Photoreduction will become the limiting factor for these experiments.

References

- [5.1] George, S.J., van Elp, J., Chen, J., Ma, Y., Chen, C.T., Park, J.-B., Adams, M.W.W., Searle, B.G., deGroot, F.M.F., Fuggle, J.C. & Cramer, S.P., *J. Am. Chem. Soc.* **114**, 4426 (1992).
- [5.2] Peng, G., deGroot, F.M.F., Hämäläinen, K., Moore, J. A., Wang, X., Grush, M.M., Hastings, J.B., Siddons, D.P., Armstrong, W.H., Mullins, O.C., Cramer, S.P., *J. Am. Chem. Soc.* **116**, 2914 (1994).
- [5.3] de Groot F.M.F., Fontaine, A., Kao, C. C., and Krisch, M., *J. Phys. Cond. Matt.*, **6**, 6875 (1994).
- [5.4] Dufek, P., Schwarz, K., and Blah, P., *Phys. Rev. B* **48**, 12672 (1993).
- [5.5] Soldatov, A.V., Ivanchenko, T.S., Kovtun, A.P., Della Longa, and Bainconi, S., *Phys. Rev. B* **52**, 11757 (1995).
- [5.6] Taguchi, M. & Kotani, A., *J. Phys. Soc. Jpn.* **63**, 706 (1996).
- [5.7] Hämäläinen, K., Siddons, D.P., Hastings, J.B. & Berman, L.E., *Phys. Rev. Lett.* **67**, 2850 (1991).
- [5.8] Shulman, R.G., Eisenberger, P., Blumberg, and Stombaugh, W., *Proc. Natl. Acad. Sci. USA*, **72**, 4003 (1975).
- [5.9] Murphy, L.M., Dobson B.R., Neu M., Ramsdale C.A., and others, *J. Synchr. Rad.* **2**, 64 (1995).

Chapter 6. Spin-Polarized EXAFS using $K\beta$ Detection

This chapter consists of a paper under preparation for the Nature. It describes the spin-polarized EXAFS (SPEXAFS) effect observed for the first time in an antiferromagnetically coupled system. This effect is about 2 order of magnitude larger than that of conventional XMCD SPEXAFS, and has some important consequences for the study of magnetic ordering and properties in magnetic materials and metalloproteins.

Magnetic Structure Determination from X-Ray Spectroscopy - A method for Spin-polarized EXAFS using $K\beta$ detection

Xin Wang^{1,2}, Alexei Ankudinov³, John J. Rehr³, Yan Zang⁴, Lawrence Que,
Jr.⁴ and Stephen P. Cramer^{1,2}

¹Department of Applied Science, University of California, Davis, CA 95616

²Lawrence Berkeley National Laboratory, Berkeley, CA 95720

³Department of Physics, University of Washington, Seattle, WA 98195

⁴Department of Chemistry, University of Minnesota, Minneapolis, MI 55455

Abstract: The first spin-polarized EXAFS of an anti-ferromagnetically coupled system using $K\beta$ detection is reported. The $K\beta$ emission spectrum has been analyzed using the ligand field multiplet model, where the spin-up and spin-down components can be separated because of their different state symmetries. The satellite $K\beta'$ is almost 100% spin-up, while the main peak $K\beta_{1,3}$ is about 85% spin-down. The $K\beta$ SPEXAFS effect is therefore about 50-100X larger than the K-edge XMCD SPEXAFS, because of the greater spin polarization of the photoelectrons. This internally referenced technique is suited for antiferromagnetically coupled systems, as well as ferromagnetic and paramagnetic systems.

The interactions between the magnetic moments of metal centers are critical for a wide range of phenomena. Ferromagnetism, antiferromagnetism, and intermediate cases are important in the study and application of magnetic materials. Magnetically coupled metal clusters which form a weak bond are also present at the heart of many proteins (1). The new discoveries of giant magnetoresistance (2-3), perpendicular magnetic anisotropy (4) and oscillatory exchange coupling (5) in thin transition metal films and multilayers would have a major technological impact on the industry such as magnetic recording. Since the magnetic properties of individual ions are so critical in science and technology, different techniques have been developed for extracting this information. The most direct procedure is neutron diffraction, which could give information about the magnetic structure on specific groups of atoms (6), but the experiments require large single crystals which are not always available. Magnetically sensitive X-ray diffraction (7) is also possible in certain cases, but could not provide an element- and site-selective probe on the magnetic moment.

X-ray absorption spectroscopy (XAS) can be used to study the element specific electronic structure and magnetic moments. Photoelectron spin polarization effects in the EXAFS region (SPEXAFS) have generated considerable interest recently, both in experiments (8,9,10) and theory (11,12). The phenomenon was first observed in x-ray magnetic circular dichroism (XMCD) measurements with circularly polarized x-rays and an external magnetic field by Schütz (13). In L-edge absorption, it involves 2p to 3d transitions, and the XMCD effects of transition metals (14), thin films (15), multilayers (16) were investigated with great success. The effect is understood as different selection rules for transitions from the ground state to the final core hole multiplets (17). In K edge absorption, the polarization of incoming

photons is partially transferred to the spin polarization of the photoelectrons (about 10^{-2}), due to the influence of spin-orbit interaction on the transition dipole matrix element (18). Because of the extra exchange terms in the scattering potentials of magnetic neighbors, only the metal-metal interactions will appear in the spectrum, while the diamagnetic neighbor contributions will be invisible.

Despite the success of XMCD SPEAXFS, the technique is generally limited to concentrated ferromagnetic or paramagnetic systems. For antiferromagnetically coupled systems, the sites are 50% spin-up and 50% spin-down, eventually the dichroism effects are cancelled. Also, K edge XMCD SPEXAFS effects are weak signals ($\Delta u/u \sim 10^{-4}$), and experimental observation of such a small effect is quite difficult, especially for dilute systems such as metalloproteins.

Recently, a new technique of spin-polarized X-ray absorption has been demonstrated by Hämäläinen and coworkers (19). This method utilizes the separation of internally referenced spin-up and spin-down transitions by detecting different parts of $K\beta$ emission spectrum. The $K\beta$ X-ray emission spectrum (XES) arise from $3p \rightarrow 1s$ transitions. The main peak ($K\beta_{1,3}$) and satellite ($K\beta'$) ultimately derive from the excitation of a $1s$ electron anti-parallel or parallel to the $3d$ spin direction. Simulations with ligand field multiplet theory (20) confirms the spin-polarization assignment.

Here we report the first SPEXAFS of an antiferromagnetically coupled binuclear complex $[\text{Fe}_2\text{O}(\text{OH})(6\text{TLA})_2](\text{ClO}_4)_3$. By detecting at $K\beta_{1,3}$ and $K\beta'$ emission energies, respectively, the spin polarization can reach 85% and 100% for spin-down and spin-up electrons (21). Besides this 100-fold increase in spin polarization, $K\beta$ detected SPEXAFS is internally referenced. It therefore requires no circular polarized light or external magnetic field, and it is also

useful for antiferromagnetically coupled systems. The elemental specification and spin selectivity will greatly simplify the structure of complex proteins, and the sign of the effect could provide information on the nature of the magnetic coupling.

A schematic description for SPEXAFS using $K\beta$ detection is shown in Figure 1a. A Von Barth-Hedin prescription (22) and the X-ray crystallography data were used to construct the spin-dependent potentials. The two high-spin Fe(III) are antiferromagnetically coupled, each Fe atom carries a 5/2 spin moment with directions opposite with the other. In a single particle picture, when $K\beta'$ excitation is monitored, a 1s electron parallel to the 3d spin direction (spin-up, red) is excited from the absorber (atom A), therefore the photoelectron is antiparallel to the spin direction of the scatterer (atom B). Because the electronic density is symmetric in these two Fe sites, the contribution in $K\beta$ XES from one Fe is not distinguishable from the other, therefore monitoring certain $K\beta$ emission energies is recording the excitation of both the absorber and scatterer. The excitation of a spin-up 1s electron (red) of the scatterer (atom B) results in a photoelectron also antiparallel to its neighbor (atom A). The antiparallel interaction (spin-up EXFAS) with spin-oriented neighbor atoms is therefore enhanced in detecting at $K\beta'$. When $K\beta_{1,3}$ excitation is monitored, the parallel photoelectron (spin-down, blue) in both sites interacts with neighboring Fe atoms, therefore the parallel interaction (spin-down EXAFS) is recorded.

SPEXAFS effect primarily derives from spin-up and spin-down electrons scattering with different probabilities from magnetic neighbors. The theoretical calculations of spin-up and spin-down Fe-Fe backscattering amplitudes are presented in Figure 1b. The final state of EXAFS is formed with the outgoing electron waves superimposed on the backscattered waves.

The transition matrix element for the absorption process is determined by the overlap of the wave function for the core state and final state. All paths involved with absorber Fe atom will have small differences in phase shift for spin-up and spin-down photoelectrons since the core potential of absorber is spin dependent, but the effective backscattering amplitudes are the same for all diamagnetic neighbor atoms. Only when the potential of scatterer is also spin dependent, both the amplitude and phase would be different for spin-up and spin-down electrons. It is clear that when the wave vector k is between 3 to 8 \AA^{-1} , the spin-down amplitude is larger than spin-up. This theoretical prediction is consistent with the high resolution electron energy loss spectra (23), as well as XMCD SPEXAFS results (8), as the parallel interaction is always stronger than antiparallel interaction.

The SPEXAFS experiment was carried out at beamline 6-2 (24) in Stanford Synchrotron Research Laboratory using a pair of Si(111) monochromator crystals in focusing mode. The X-ray Near Edge Absorption Spectra (XANES) were obtained at beamline X-25 (25) in National Synchrotron Light Source at Brookhaven National Laboratory, with Si(220) monochromator. The high resolution curved-crystal spectrometer (26) was used to collect all the spectra. $[\text{Fe}_2\text{O}(\text{OH})(6\text{TLA})_2](\text{ClO}_4)_3$ was synthesized by published procedure (27). The sample was diluted with BN to 2% Fe by weight. All data were collected at 11K, and $(\text{NEt}_4)[\text{FeCl}_4]$ was used for emission and edge calibrations (28).

Experimental and theoretical $K\beta$ XES of $[\text{Fe}_2\text{O}(\text{OH})(6\text{TLA})_2](\text{ClO}_4)_3$ are shown in Figure 2a. The emission spectrum is split into two parts, the main peak $K\beta_{1,3}$ at 7057.8 eV and the $K\beta'$ satellite at 14 eV lower energy. A typical count rate at the $K\beta_{1,3}$ was 4200 c/s with background 3 c/s. A ligand field multiplet calculation was used to simulate the spectrum. The simulation

involves a $1s^13d^5 \rightarrow 3p^53d^5$ transition in O_h symmetry, with the ligand field strength $10Dq=1.2$ eV. All the Slater integrals are reduced to 70% of their atomic values. Since the excitation of a 1s spin-down photoelectron partitions 6/7 of the fluorescence transition intensity to $[^7S]$ symmetry, and the excitation of a 1s spin-up electron partitions 100% intensity of the $[^5S]$ symmetry plus 1/7 of the $[^7S]$ symmetry, it is possible to construct the spin-up and spin-down contributions separately by calculating transitions to $[^7S]$ and $[^5S]$ in $K\beta$ XES. From the composition of the spin-up and spin-down transitions presented in the spectra, it is clear that the satellite is 100% spin-up, while the main peak is around 85% spin-down.

Figure 2b shows the spin-polarized excitation spectra of $[\text{Fe}_2\text{O}(\text{OH})(6\text{TLA})_2](\text{ClO}_4)_3$. Since each Fe is in a distorted O_h environment, there are some mixings between Fe 3d orbital and 4p characters. In spectroscopic term, the K absorption edge of such a compound would have some pre-edge features, which results from the 'forbidden' $1s \rightarrow 3d$ transition (weakly allowed dipole). In the spin-down (blue) excitation spectrum, when the spectrometer monitoring at the main peak 7057.8 eV, the pre-edge feature indeed is distinctive; in the spin-up spectrum (red), achieved by setting the spectrometer at the satellite 7043 eV, the pre-edge feature disappears. This confirms again the spin assignment of the $K\beta$ XES. For a high spin d^5 system, all 5 spin-up 3d orbitals are occupied, therefore no spin-up transitions possible. All spin-down orbitals are still empty, so spin-down spectrum shows some distinctive pre-edge features.

X-ray crystallography shows that in the unit cell of $[\text{Fe}_2\text{O}(\text{OH})(6\text{TLA})_2](\text{ClO}_4)_3$, there are two unique molecules. Each molecule has an inversion center at Fe_2O_2 core. The model is drawn in Figure 3a, where only the first shell O and N atoms, the second shell Fe and the third

shell C atoms are illustrated. The averaging Fe-m-O bond length is 1.94 Å, and the averaging Fe-N bond length 2.21 Å. The Fe-Fe bond length is 2.95 Å, and the exchange interaction between those two sites has a strength J equals -57 cm^{-1} . In Figure 3b, the Fourier transform of experimental spin-up and spin-down EXAFS ($k=1-9 \text{ Å}^{-1}$) are shown. The EXAFS data was calibrated and deglitched in each raw data set before spline was taken, then weighted by its signal counts, and finally smoothed over a $k=0.2 \text{ Å}^{-1}$ interval. There are some distinct differences in the spin polarized EXAFS data, which is most easily interpreted in the Fourier transforms. Because of the limited range of data available (the S/N ratio decreases drastically with k), there are two major well-resolved peaks in the transforms. The feature at $r' < 2.0 \text{ Å}$ corresponds to the first shell coordination sphere, including O and N atoms, and that at $r' \sim 2.3 \text{ Å}$ corresponds to the Fe-Fe component. There is almost no difference in the backscattering amplitude of the first coordination contributions in both spin-up and spin-down EXAFS. The somewhat different amplitude at $r' \sim 1.1 \text{ Å}$ is due to background subtraction. For the Fe-Fe component, however, the amplitude of the spin-down EXAFS is larger than that of spin-up. This result was reproduced in data from several different experiments.

From theoretical calculations as shown in Figure 1a, it is predicted that parallel electrons have larger backscattering amplitudes than antiparallel ones. In the case of an antiferromagnetically coupled system, the spin-down EXAFS detects scattering by photoelectrons with opposite spins as the valence electrons of the x-ray absorber, i.e. the interaction with the magnetic neighbor is parallel. So the spin-down EXAFS will have larger backscattering amplitude, as we observed in our experiment.

In order to estimate the size of the effect, we performed Excurve fits on the spin-up and spin-down EXAFS using spin-independent potentials and

phase shifts. Including multiple scattering paths, the best fit for spin-up EXAFS gives 2 O at 1.85 Å, 4 N at 2.21 Å and 1 Fe at 2.96(1) Å. For spin-down EXAFS, all the other fitting parameters are the same except we find 1.1 Fe at 2.96(5) Å. The different coordination number of Fe-Fe component reflects the difference in backscattering amplitudes with spin-up and spin-down electrons - spin-down EXAFS has 10% more intensity. This 10% effect is about 2 order of magnitude bigger than the K-edge XMCD SPEXAFS. From the Fourier transform, it is clearly shown that there is no difference on the backscattering amplitudes of the first coordination contribution from spin-up and spin-down EXAFS. The somewhat different amplitudes at $r \sim 1.1$ Å are due to background subtraction, but on the Fe-Fe component, the amplitude of spin-down is about 10% larger than that of spin-up, which is due to the difference of the spin-dependent potentials of neighboring atoms. The 10% effect is much larger than the effect by using MCD, which is in the order of 10^{-4} .

SPEXAFS by $K\beta$ detection have broad applications in materials science and biological science. As a generalization of sum rules derived by Carra et. al. (29), one can obtain the spin moment of the ground state from the spin-up and spin-down signals (30). To further confirm the nature of the magnetic couplings, a ferromagnetically coupled system can be examined by the same technique. In that case, the spin-up EXAFS should be stronger than spin-down, and the sign of the SPEXAFS signal in the Fourier transform will be opposite as what we observed in the antiferromagnetically coupled system. The magnitude of difference should depend on the difference in the potentials, which is proportional to the spin moment of the magnetic atoms.

The extra spin selectivity and 2 order of magnitude more sensitivity will greatly reduce a complex system into metal-metal interactions and only magnetic neighbors are visible. The low efficiency of this type of experiment

is the main obstacle. Since the fluorescence yield is in the order of 30% for first row transition metals, and the spectrometer can only collect 0.01% solid angle of all emitted photons, the count rate for $K\beta$ SPEXAFS is still considerably low, especially at the satellite $K\beta'$. Also the satellite $K\beta'$ intensity is proportional to the unpaired electrons, for certain systems this intensity is too small to be useful, and this technique will not be applicable. With the development of third generation synchrotron sources, where incoming photon current can be expected to increase 2 order of magnitude, and the higher efficiency of collecting spectrometer, this method could become routine to study magnetic structures.

Figure Legends:

Figure 1 (a) Spin-polarized core potentials for Fe absorber and scatterer. Plotted are spin-up (dotted line, red) and spin-down (solid line, blue); (b) Theoretical backscattering amplitudes of spin-up (dotted line, red) and spin-down (solid line, blue) electrons in Fe-Fe paths from multiple scattering calculations including spin-dependent potentials.

Figure 2 (a) Experimental $K\beta$ emission spectrum of $[\text{Fe}_2\text{O}(\text{OH})(6\text{TLA})_2](\text{ClO}_4)_3$ (top, dashed line) with ligand field multiplets calculations (bottom). Plotted theoretical spectra are total fluorescence spectrum (solid line), spin-up transition (dotted line, red) and spin-down transition (solid line, blue); (b) Spin-polarized near edge structure of $[\text{Fe}_2\text{O}(\text{OH})(6\text{TLA})_2](\text{ClO}_4)_3$. Plotted are spin-up excitation spectrum (dotted line, red) when monitoring $K\beta'$, and spin-down excitation spectrum (solid line, blue) while monitoring $K\beta_{1,3}$.

Figure 3 (a) Structure of $[\text{Fe}_2\text{O}(\text{OH})(6\text{TLA})_2](\text{ClO}_4)_3$, only the first three shells coordination sphere are plotted; (b) Fourier transform of experimental spin-up (dotted line, red) and spin-down (solid line, blue) EXAFS.

Figure 4 Excurve fitting of spin-up (a, red) and spin-down (b, blue) EXAFS and their Fourier transforms using spin independent potentials. Plotted are experimental data (solid line) and simulations (dotted line).

Figure 5 Excurve fitting parameters.

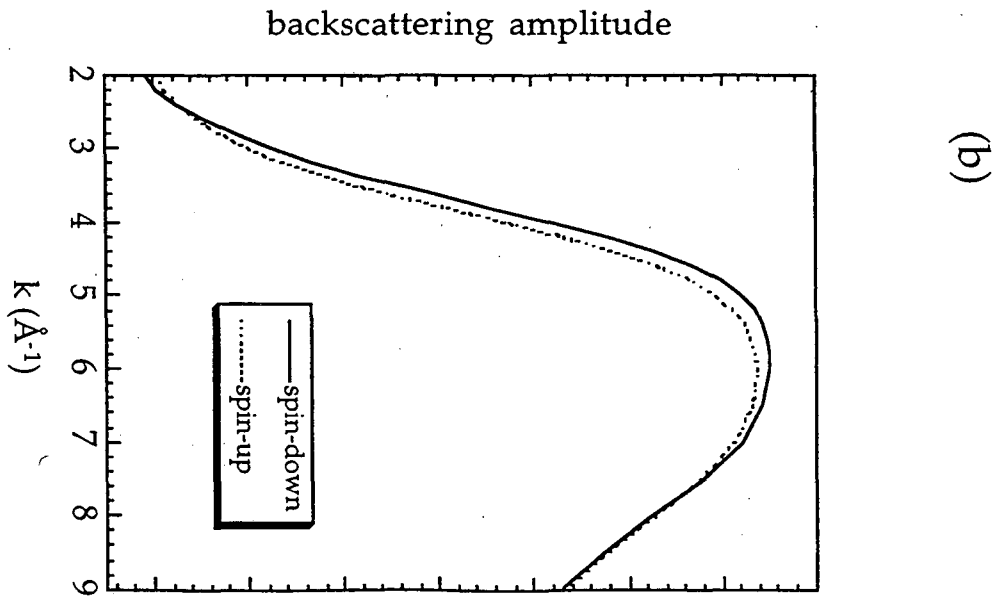
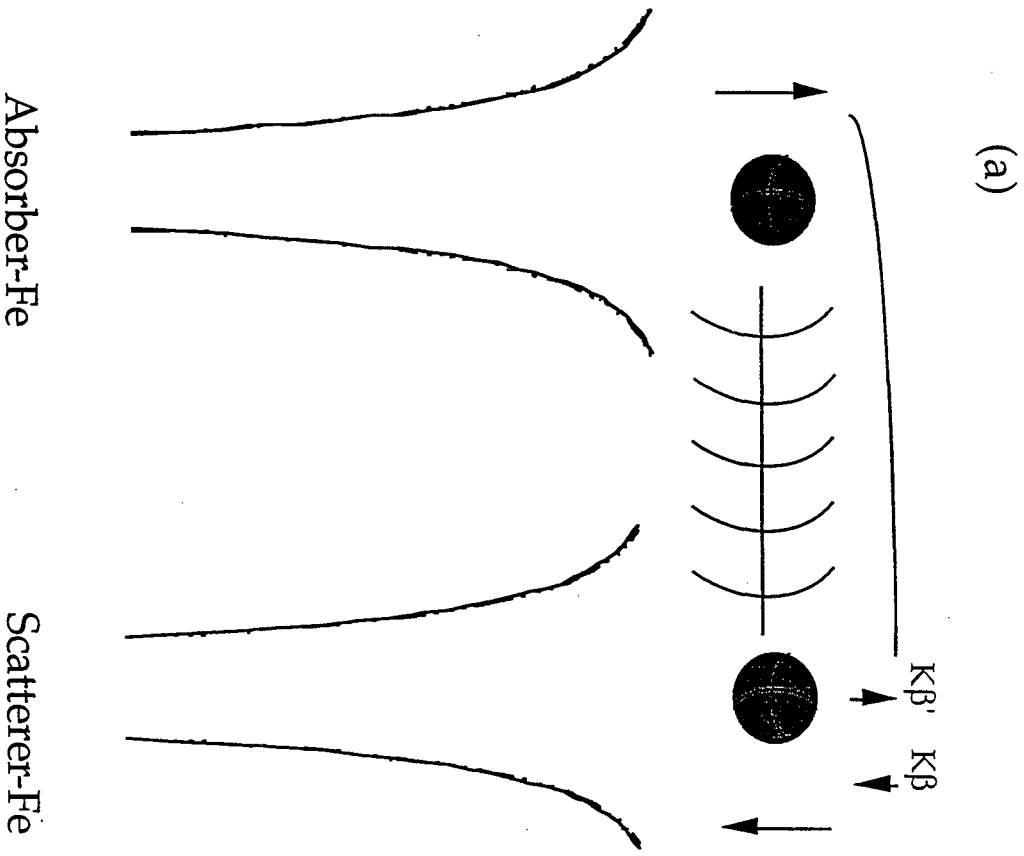
- (1) Bencini, A. and Gatteschi, D., '*Electron Paramagnetic Resonance of Exchange Coupled Systems*', Springer-Verlag, New York, 1988
- (2) Baibich, M.N., Broto, J.M., Fert, A., Dau, F.N.V., Petroff, F., Eitenne, P., Creuzet, G., Friederich, A, and Chazelas, J., *Phys. Rev. Lett.*, **61**, 2472-5 (1988)
- (3) Binasch, G., Grünberg, Saurenbach, F. and Zinn, W., *Phys. Rev. B*, **39**, 4828-30 (1989).
- (4) Carcia, P.F., Meinholdt, A.D. and Suna, A., *App. Phys. Lett.*, **47**, 178-80 (1985)
- (5) Parkin, S.S.P., More, N. and Roche, K.P., *Phys. Rev. Lett.*, **64**, 2304-7 (1990).
- (6) Blume, M., *J. App. Phys.* **57**, 3615-18; (1985) Blume, M. and Gibbs, D., *Phys. Rev. B* **37**, 1779-89 (1988).
- (7) Bergevin, F. De. and Brunel, M., *Phys. Lett.* **39A** 141-2 (1972).
- (8) Schütz. G, XAFS-9 conference.
- (9) Chakarain, V., Idzerda, Y.U., Kemner, K.M., Park, J.H. and Elam, W.T., *J. Appl. Phys.*, **79**, 6493-5 (1996).
- (10) Pizzini, S., Fontaine, A., Giorgetti, Ch., Dartyge, E., Bobo, J.F., Piecuch, M. and Baudalet, F., *Phy. Rev. Lett.*, **74**, 1470-3 (1995).
- (11) Brouder, C., Alouani, M. and Bennemann, K.H., *Phy. Rev. B*, **54**, 34-49 (1996).
- (12) Ebert, H., Popescu, V., and Ahlers, D., XAFS-9 conference.
- (13) Schütz, G., Wagner, W., Wilhelm, W., Kienle, P., Zeller, R., Frahm, R. and Materlik, G. *Phys. Rev. Lett.* **58**, 737-40 (1987).
- (14) Chen, C.T., Sette, F., Ma, Y. and Modesti, S., *Phys. Rev. B* **42**, 7262-5 (1990).
- (15) Van der Laan, G., Thole, B.T., Sawatzky, G.A., Goedkoop, J.B., Fuggle, J.C., Esteva, J.-M., Karnatak, R.C., Remeika, J.P. and Dabkowska, H.A., *Phys. Rev. B* **34**, (1986) 6529-31

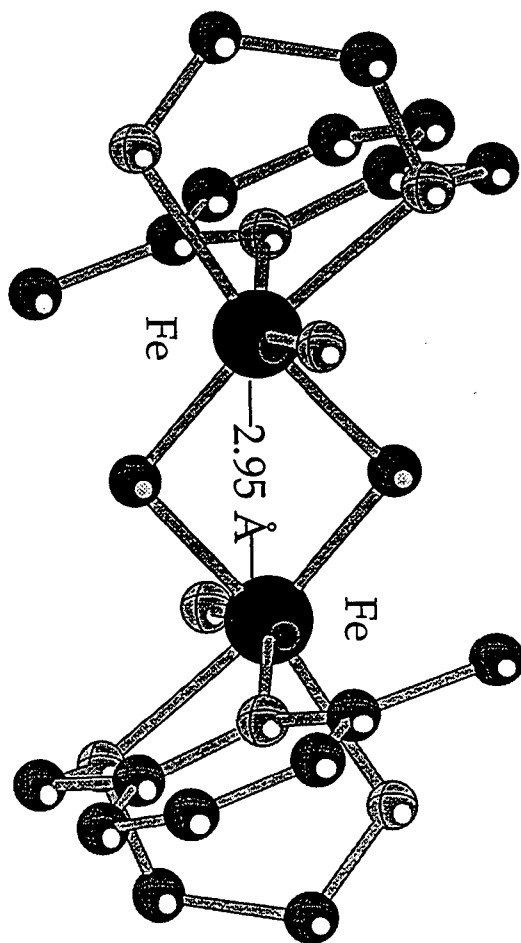
- (16) Baudelet, F., Dartype, E., Krill, G., Kappler, J.-P., Brouder, C., Piecuch, M. and Fontaine, A., *Phys. Rev. B* **43**, (1991) 3809-14 ; Stohr, J. and König, H., *Phys. Rev. Lett.*, **75**, 3748-51 (1995).
- (17) Van der Laan, G. and Thole, B.T., *Phys. Rev. B*, **43**, 13401-11 (1991).
- (18) Ankudinov, A. and Rehr, J.J., *Phys. Rev. B*, **52**, 10214-20 (1995); Brouder, C. and Hikam M., *Phys. Rev. B*, **43**, 3809-20 (1991).
- (19) Hämäläinen, K., Siddons, D.P., Hastings, J.B. and Berman, L.E., *Phys. Rev. Lett.* **67**, 2850-3 (1991).
- (20) Peng, G., de Groot, F.M.F., Hämäläinen, K., Moore, J.A., Wang, X., Grush, M. M., Hastings, J.B., Siddons, D.P., Armstrong, W.H., Mullins, O.C. & Cramer, S.P. *J. Am. Chem. Soc.* **116**, 2914-20 (1994).
- (21) Wang X., de Groot, F.M.F., and Cramer, S. P., submitted to *Phys. Rev. B*.
- (22) Ankudinov, A., Ph.D. Thesis.
- (23) Lamont C.L.A., Stenzel W., Conrad H., Bradshaw A.M. *J. Elec. Spectr.* **64-5**, 287-296 (1993).
- (24) Hoyer, E., Bahr, C., Chan, T., Chin, J., Elioff, T., Halbach, K., Harnett, G., Humphries, D., Hunt, D., Kim, K.-J., Lauritzen, T., Lindel, D., Shirley, D., Tafelski, R., Thompson, A., Cramer, S., Eisenberger, P., Hewitt, R., Stöhr, J., Boyce, R., Brown, G., Golde, A., Gould, R., Hower, N., Lindau, I., Winick, H., Yang, J., Harris, J. & Scott, B.. *Nucl. Inst. & Meth.* **208**, 117-25 (1983).
- (25) Berman, L.E., Hastings, J. B., Oversluizen, T., Woodle, M., *Rev. Sci. Instrum.* **63**, 428-32 (1992).
- (26) Wang, X., Grush, M.M., Freoschner, A. and Cramer, S.P., accepted by *J. Synchr. Rad.*.
- (27) Zang, Y., Pan, G.F., Que, L., Jr., Fox, B.G. and Münck, E., *J. Am. Chem. Soc.* **116**, 3653-4, (1994).

(28) Peng, G., Wang, X., Randall, C.R., Moore, J. and Cramer, S.P., *App. Phys. Lett.* **65**, 2527-9 (1994).

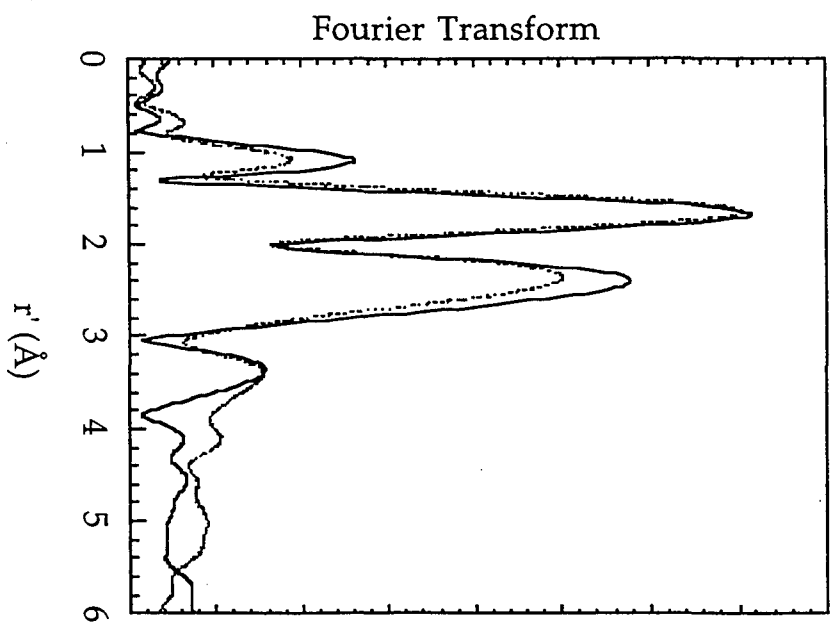
(29) Carra, P., Thole, B.T., Altarelli, M. and Wang, X.D., *Phys. Rev. Lett.*, **70**, 694-7 (1993).

(30) Ankudinov, A., Ph.D. Thesis.

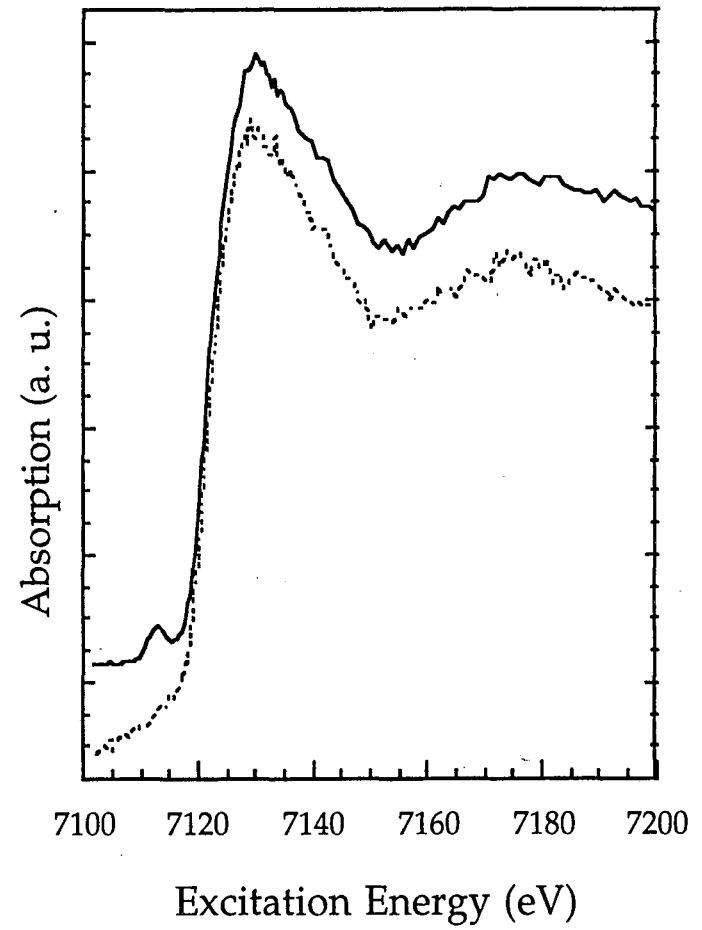
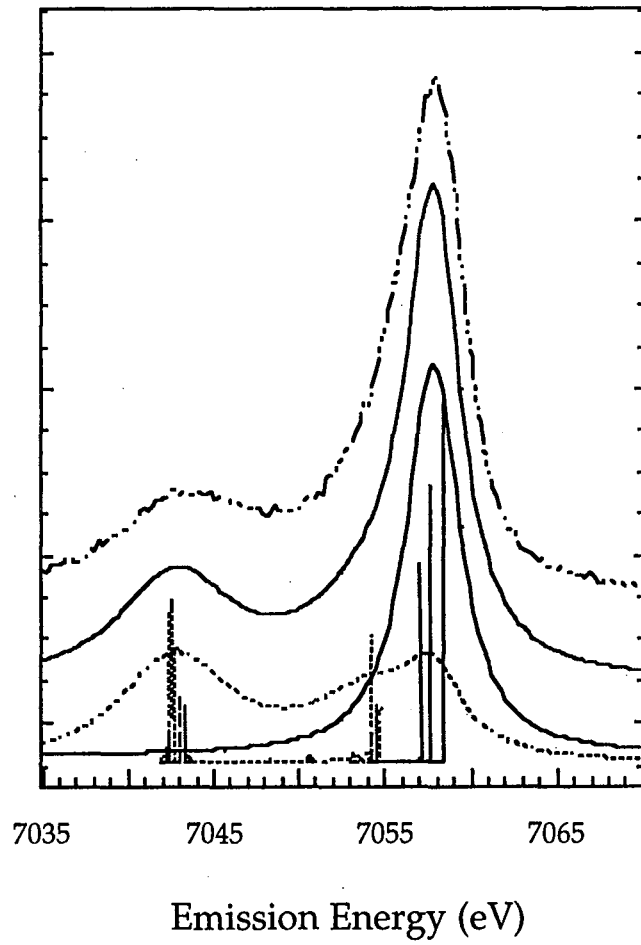


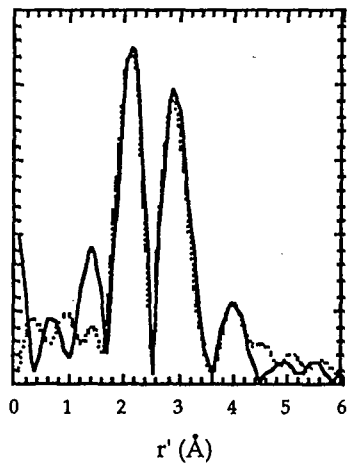
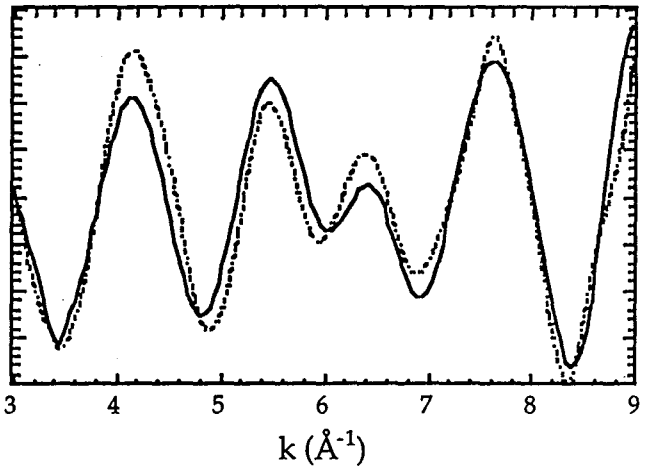
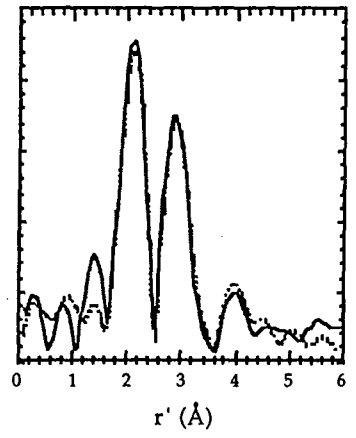
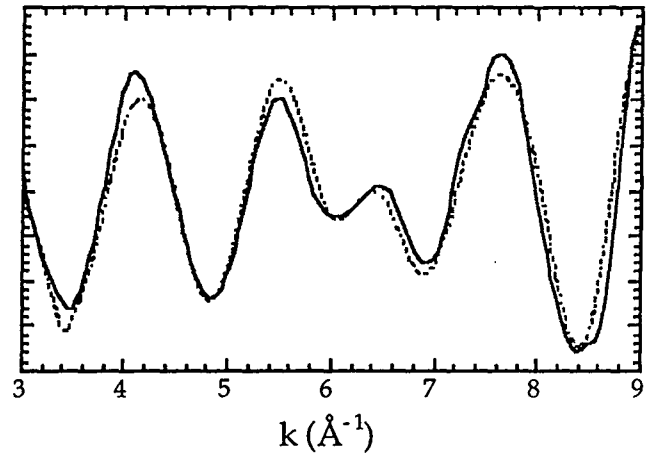


(a)



(b)





— experiment

.....excurve fit

EXCURVE Fe-X distances

	<u>Spin-down</u>			<u>Spin-up</u>			<u>Crystal</u>	
	N	R (Å)	$2\sigma^2$ (Å ²)	N	R (Å)	$2\sigma^2$ (Å ²)	N	R(Å)
Fe-O	2	1.89	0.043	2	1.89	0.043	2	1.95(av)
Fe-N	4	2.21	0.016	4	2.21	0.016	4	2.21(av)
Fe-Fe	1.1	2.96(5)	0.004	1	2.96(1)	0.004	1	2.95
Fe-C	9	3.36	0.096	9	3.36	0.096	9	3.35(av)

Appendix I. XMCD Spectra and Distortions of Fe²⁺ L_{2,3} Edges

This following paper was published on the Journal of Electron Spectroscopy and Related Phenomena, 78, 337 (1996). Using ligand field multiplet calculation, it discusses how the XMCD spectral shape changes with the ligand field distortion, and how to extract information from the spectra of the distortion parameter, as well as 3d spin-orbit coupling. The example of Fe²⁺ L_{2,3} edges is discussed in detail.

XMCD spectra and distortions of Fe²⁺ L_{2,3} edgesXin Wang ^a, Frank de Groot ^b and Stephen P. Cramer ^a^aDepartment of Applied Science, University of California, Davis, CA 95616^bSolid State Physics, University of Groningen, The Netherlands

Abstract: We have shown from ligand field multiplet calculation that the XMCD spectra shape changes drastically with the distortion parameter D_s . The temperature dependence study of XMCD makes it possible to determine both D_s and spin-orbit coupling.

1. Introduction

X-ray magnetic circular dichroism (XMCD) is a new experimental technique with promising futures for site-specific characterization of metals in complex. By observing the XMCD signal, we can investigate the magnetic and electronic structure of 3d transition metals and rare earth compounds. XMCD was predicted theoretically by Thole *et al.* (1) using ligand field multiplet calculations, and experimentally then demonstrated on L₃ and L₂ edges of transition metals (2-3). XMCD spectra of transition metals ions have been calculated in Oh symmetry (4). There are several powerful sum rules being developed (5) which allow determination of the average values for $\langle S_z \rangle$ and $\langle L_z \rangle$.

In this paper, we demonstrate that XMCD spectra shape changes drastically not only with a crystal field, exchange field and spin-orbit interactions, but also with the presence of distortion for a certain ground

state. When the distortion is in the same order of the spin-orbit interaction, the ground state character changes with the distortion parameter D_s , and some excited states cross the ground state. In some cases the energy splitting is very small, causing the XMCD spectra shape to be very sensitive to temperature.

2. Ground state character of tetragonal distortions

The effect of distortion on XMCD spectra is studied for high-spin Fe^{2+} L_{2,3} edge. In the ligand field multiplet calculation, the transition channels for d⁶ L edge can be approximated as $2p^6 3d^6 \rightarrow 2p^5 3d^7$. The ground state 5D_4 in spherical symmetry $O(s)$ is reduced to 5T_2 in the presence of a crystal field with octahedral symmetry O_h . A magnetic field along the z axis lower the symmetry further to C_4 and the exchange field is included by a Zeeman term in the Hamiltonian. As shown in Fig 1, which represents single particle picture, the 3d orbitals are split into t_{2g} and e_g with an energy difference of $10 Dq$. When there is a weak field along z and stronger field along x and y axes, the octahedron is elongated along the z axis, and the degeneracy of t_{2g} (d_{xy} , d_{yx} , d_{xz}) and e_g (d_{z^2} , $d_{x^2-y^2}$) are removed. The distortion is represented as the ligand field parameter D_s . The T₂, E, T₁, A₁, T₁ and T₂ levels which derive from the 5T_2 configuration through spin-orbit interaction (6) will split further, and each state gives different XMCD spectra. When D_s changes sign, the elongated shape changes into a compressed one, and the energy level ordering of xy and xz,yz orbitals reverses, therefore the ground state symmetry changes from e_g to b₂.

3. Results and discussions

The XMCD spectra calculated with different D_s values at $T=0\text{K}$ are presented in Fig 2. All the coulomb interaction and exchange integrals are scaled to 80%. The exchange field is included by a term $g\mu_B H S$ in the Hamiltonian with $\mu_B H=0.001\text{ eV}$. Crystal field is used as $10Dq=1.0\text{ eV}$, $Dt=0.0\text{ eV}$ to simplify the analysis. The core hole lifetime is taken into account by broadening the spectra with a Lorentzian of 0.3 eV and a Gaussian of 0.2 eV .

The XMCD spectra shape and intensity both change drastically with D_s . For $D_s=-24\text{ meV}$, there is no observable MCD effect at 0 K . With increase of negative D_s , the L3 edge shows a larger MCD effect around 711 eV and a well separated small peak around 709 eV . The intensity increase almost 50% at L3 from -30 meV to -48 meV , and L2 becomes much broader. For positive

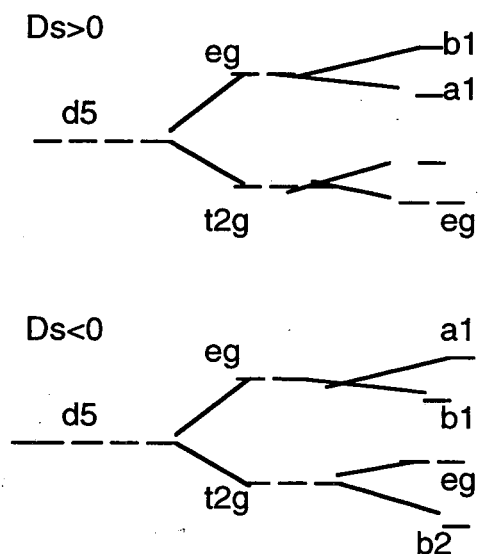


Figure 1. Ground state symmetry with the presence of tetragonal distortions.

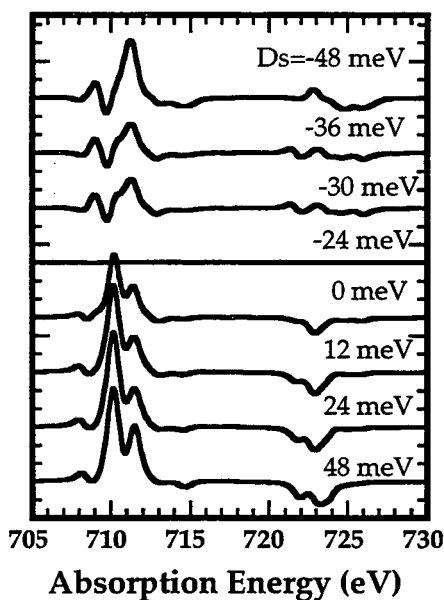


Figure 2. The XMCD spectra as a function of distortion D_s .

D_s , the XMCD spectra are very different. L3 peaks are much sharper around 710 eV, which is about 1 eV lower energy than the negative D_s . There is also a shoulder on 1.5 eV higher energy side. From $D_s=0$ to 48 meV, the MCD effect at L3 gradually increase, and become more distinguishable at L2.

Fig 3 presents the energy level diagram for square planar symmetry. The number shown on the top gives the approximate expectation values of $\langle S_z \rangle$ except for $D_s=0$, where $\langle S_z \rangle = -1$ and 1 are respectively -1.53 and 1.52 . For positive D_s , the lowest energy level remains lowest, which is consistent with that there is no "sudden" changes of the XMCD spectra. For negative values of D_s , there are three clear transitions; one near -8 meV, one around -24 meV and the last one at -42 meV. At $D_s = -8$ meV, the $\langle S_z \rangle = 0$ line

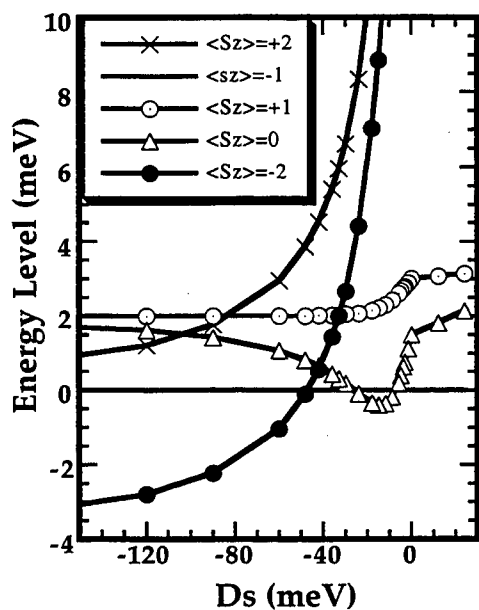


Figure 3. Five lowest energy level diagram as a function of D_s .

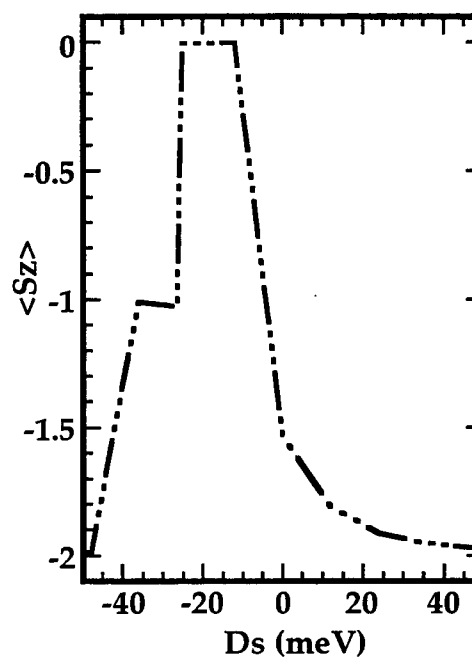


Figure 4. Ground state expectation value $\langle S_z \rangle$ as a function of D_s .

crosses the $\langle S_z \rangle = -1$ line and becomes the ground state due to the coupling of the ground states to the excited states. At $D_s = -24$ meV, the $\langle S_z \rangle = 0$ line crosses again and $\langle S_z \rangle = -1$ is the ground state. At $D_s = -42$ meV, a phase transition occurs where a 'spin-orbit' excited state with $\langle S_z \rangle = -2$ becomes the ground state. This is a similar effect as the high-spin low-spin crossings in the Tanabe-Sugano diagrams, but comparing 'spin-orbit' and 'D_s' instead of 'Coulomb exchange' and cubic crystal field.

As a result of the mixings around the transition points, the two lowest states cross around -8 meV and -24 meV, and possibly again at higher distortion. So in Fig 4, we show the expectation values of the spin moment in Z direction $\langle S_z \rangle$ at ground state. When the two lowest states cross, there is a jump in $\langle S_z \rangle$ at 0 K. The ground state $\langle S_z \rangle$ shows a strong dependence on D_s : between -8 meV and -24 meV, $\langle S_z \rangle = 0$ is the ground state, therefore no MCD effect will be observed for such a system, that the strongest dichroic effect is always observed at 0K is not correct here, as shown in Fig 5 and Fig 6. Higher energy levels with higher $\langle S_z \rangle$ values will give larger MCD. For $D_s = -26$ meV, $\langle S_z \rangle = -1$ is the ground state, and half of the dichroic effect is expected, and $D_s = -48$ meV, the ground state is almost $\langle S_z \rangle = -2$. When $D_s = 0$ eV, the ground state is $\langle S_z \rangle = -1.53$, therefore even without distortion, the ground state is a mixing of the different magnetic sublevels. Increase of positive D_s values gradually shift the ground state into a pure $\langle S_z \rangle = -2$ state.

Fig 5, 6 illustrate the temperature dependence for a given value of D_s . For $D_s = -12$ meV, as shown in Fig 5, there is almost no dichroic effect at 0K, but with an increase of temperature to 5K, a weak MCD spectrum is expected. When $D_s = -48$ meV, higher temperature reduces the MCD, as the higher level with lower $\langle S_z \rangle$ values. The temperature dependence XMCD study makes it possible to determine both spin-orbit coupling and D_s values.

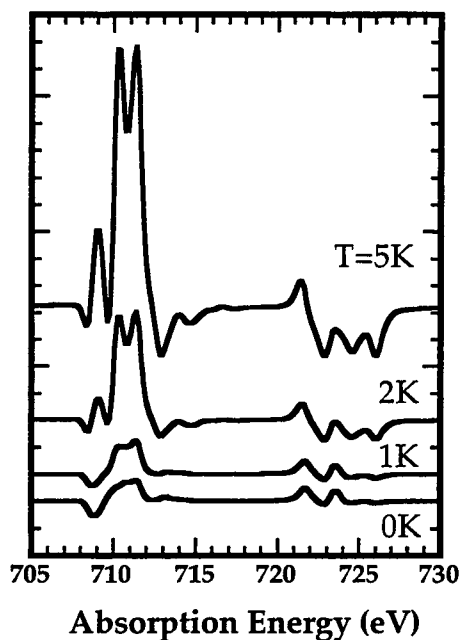


Figure 5. Temperature dependence of XMCD spectra at $D_s = -12$ meV.

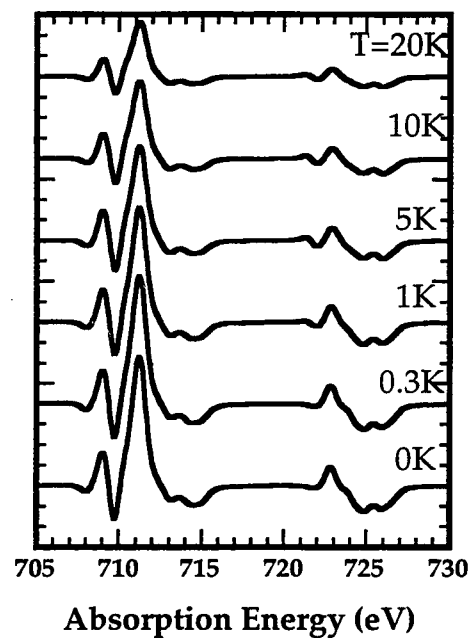


Figure 6. Temperature dependence of XMCD spectra at $D_s = -48$ meV.

4. Conclusions

From ligand field multiplet calculation, we have shown that for high-spin d^6 , the XMCD spectra shape changes drastically with the presence of distortions. The character of ground state changes when D_s changes sign, and mixings of different states could yield no dichroic effect at 0K for certain distortions. XMCD spectra also show a strong temperature dependence which allows determination of both spin-orbit coupling and D_s values. This calculation can be generalized to all 3d transition metals.

References

1. B. T. Thole, G. van der Laan, G. A. Sawatzky, *Phys. Rev.Lett.*, 55 (1985), 2086.
2. C. T. Chen, F. Sette, Y. Ma, S. Modesti, *Phys. Rev. B*, 42 (1990), 7262.
3. C. T. Chen, N. V. Smith, F. Sette, *Phys. Rev. B*, 43, (1991), 6785.
4. G. van der Laan, B. T. Thole, *Phys. Rev. B.*, 43 (1991), 13401.
5. B. T. Thole, P. Carra, F. Sette, G. van der laan, *Phys. Rev. Lett.* 68 (1992), 1943.
6. F.M.F. deGroot, *J. Elec. Spec.* 67, (1994), 529.

Appendix II: Manual for the Two-dimensional Position Sensitive Detector

2.1 Introduction

This document describes how to use the two-dimensional gas proportional detector (2.1), the corresponding electronics and software to take x-ray image data. The position sensitive x-ray detector in our group was developed by Dr. Graham Smith and coworkers in the instrument technology group at Brookhaven National Laboratory.

This document is divided into two major sections. Section 2.2 contains an overview of the detector, cabling diagrams, read-out electronics and operation procedures; Section 2.3 is a detailed description of the multiparameter software obtained from Canberra to collect data.

2.2 Two Dimensional Detector and Electronics

2.2.1 Overview of the detector

Multiwire proportional chambers are widely used as position sensitive detector of both photons and charged particles. The gas proportional chamber used in our group has an active area of 10 cm x 2 cm, and a 1mm Be window which gives good x-ray transmission. In normal operation, this detector provides two coordinates of information simultaneously, the lower cathode furnishing the X signal, and the upper cathode furnishing the Y signal.

The lower cathode of this detector is a printed circuit board with 40 zigzag shaped copper strips at 2.54mm pitch. 0.58mm above it, a grid of fine wires 12 mm diameter spaced 0.58 mm apart forms the anode plane. Another 0.58mm above it, a grid of 30 mm diameter wires at a pitch of 0.58 mm forms

the upper cathode plane. The beryllium window is 5.19mm above the upper cathode plane. The position resolution of the detector is about 150mm on both axes when an anode charge is just less than 1 pC, for 5.4 KeV x-rays absorbed in Ar/20% CO₂. When the anode charge is above 1 pC, position resolution begins to deteriorate, as shown in Figure 2.1.

Time digitalization using a delay line is the read-out technique used in this detector to measure the event positions, as in Figure 2.2. The induced signal from a cathode is collected by the specially designed delay line, where it divides into two signals. One half travels to a preamplifier and shaping amplifier at one end of the line, and the other half does likewise at the other end of the line. The time difference of these signals determines the event position in the detector. The block diagram (next section) shows that the timing signals from the two-dimensional detector feed the dual analog-to-digital converters (ADC), whose outputs are read by a front-end data multiplexing system (ND9900 multiparameter) under computer control.

2.2.2 Block diagram and operation conditions

The overall cabling diagram of the detector and the electronic is illustrated in Figure 2.3. Normal operating conditions are given as follows:

- (1) Research grade Ar/20% CO₂ gas mixing should be used for x-ray energy below 8 keV and high position resolution. For experiment involves x-ray above 8 keV, gas mixing of Xe/10% CO₂ should be used.
- (2) When detector operation begins from scratch, allow the gas to flow quickly (no more than tens of bubbles per second in oil bubbler) for about 15 minutes before switch on the high voltage. Slow down the flow rate to two bubbles per second.

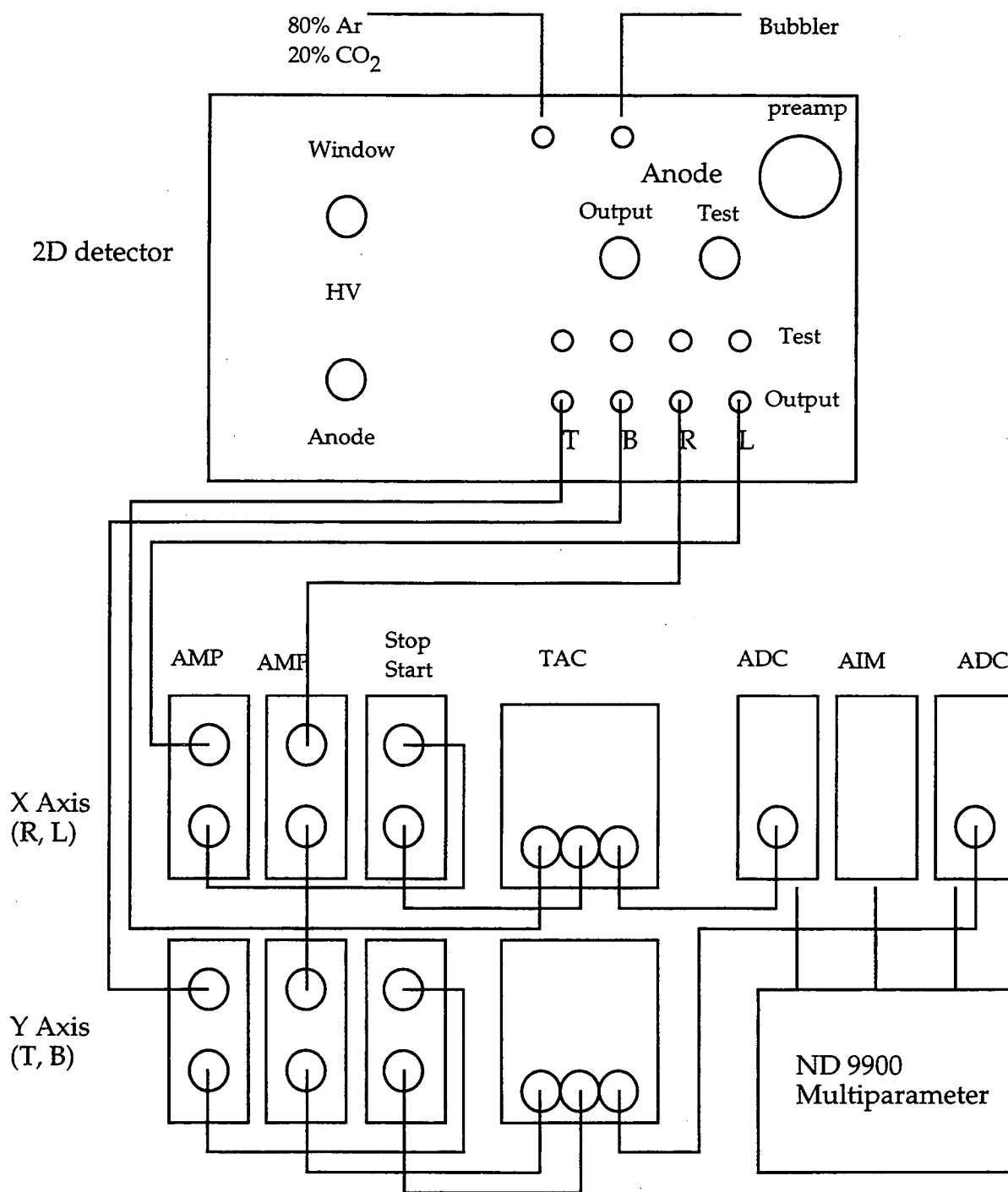


Figure 2.1 Block Diagram of 2D detector and electronics system.

- (3) The high voltage used are: Anode +1200 V, Cathode (window): -600 V. Increase the high voltage slowly and monitor the current to the anode wires. The anode wires should not draw more than 200nA at 1200V.
- (4) Never allow gas regulator output pressure to exceed ~15 psi.
- (5) Special preamplifier power cable should be used to connect to the detector to NIM (± 12 V).
- (6) For the anode high voltage power supply (channel A of Bertan 1755P) there are two toggle switches above the voltage control knob. When HV is on, the right hand toggle must be in the TRIP HOLD position, so a discharge in the detector will cut out the voltage.
- (7) The count rate for this detector can not exceed 1×10^5 per second.
- (8) The anode charge level of about 0.1pC is recommended for routine operation of the detector. The procedure of anode charge calibration is as follows: place an radioactive source (or x-ray beam) in front of the detector window; connect a square pulse generator's output to the Anode Test input on the detector; adjust the output of the pulse generator to 75mV peak to peak (it injects 0.1pC charge to the 1.33pF calibration capacitor on the anode preamp) ; monitor the anode signal output from its shaping amplifiers; raise the anode voltage so that the x-ray signals have the same amplitude as the pulser signal.

2.2.3 Electronics setting

All electronics should be at the following settings while taking data:

- (1) The gain on AMP/ZCD unit can be adjusted by the 4 dip switches on the front panel. The recommend settings are 1(U)2(D)4(U)8(D) for X and 1(D)2(U)4(U)8(D) for Y axes at about 0.1pC anode charge level; using negative input in both AMP. If it is deemed necessary to change the gain

Figure 2.2 Schematic diagram of a two-dimensional PSD using a dealy line encoding system.

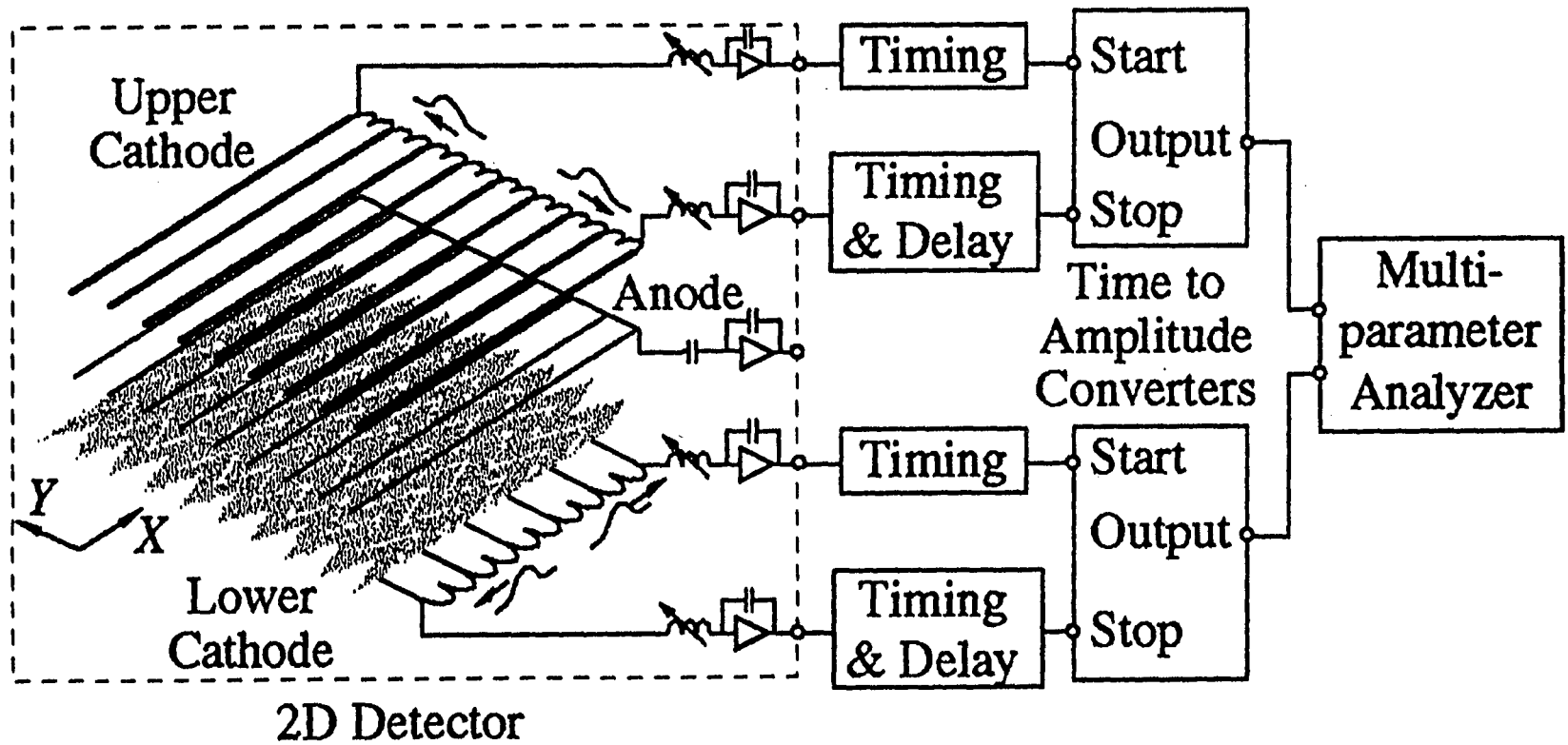
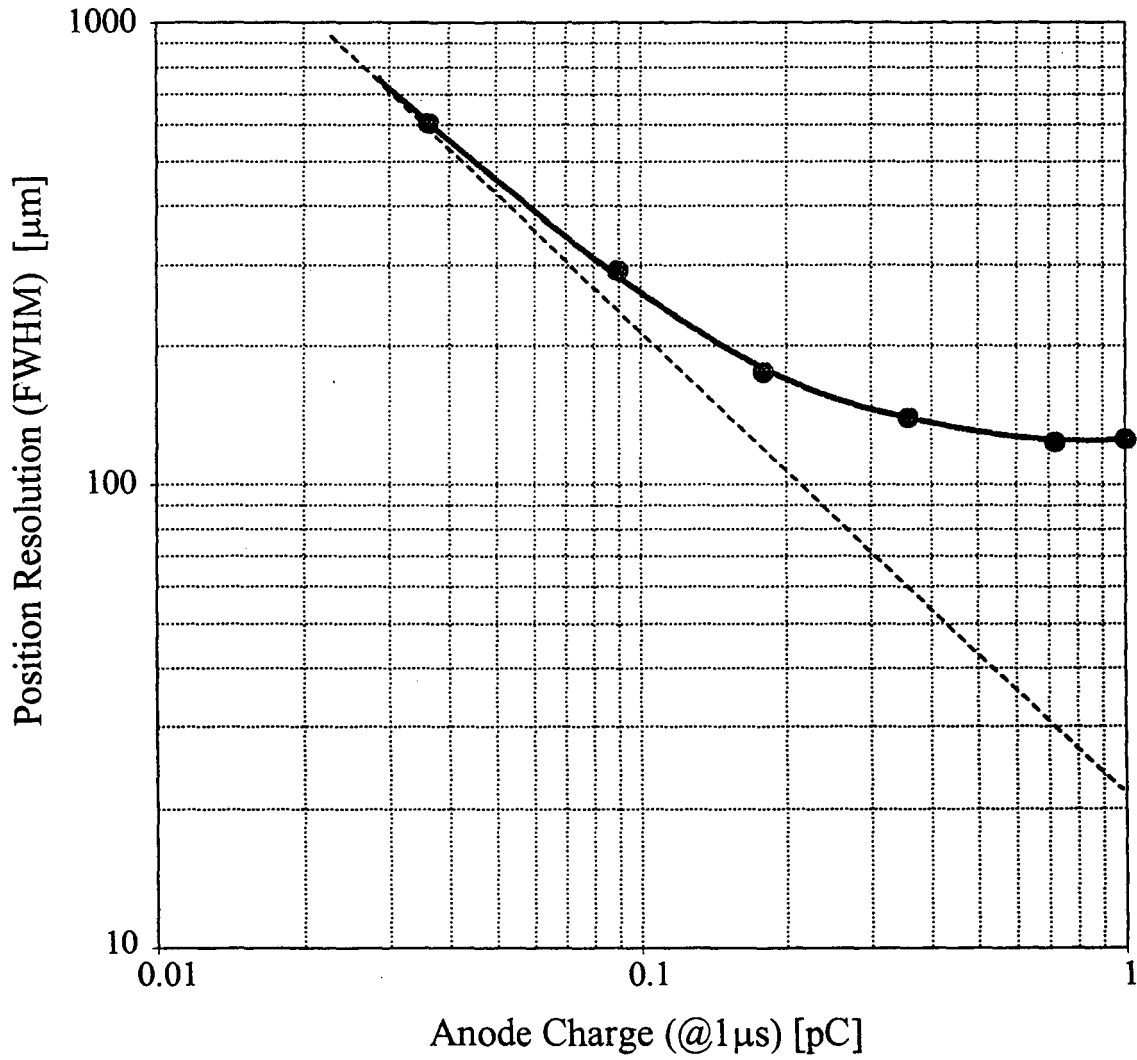


Figure 2.3 Position resolution along the anode wire direction as a function of anode charge.

Position Resolution as a Function of Anode Charge (5.4 keV X-rays, Argon/ 20% CO₂)



on the AMP/ZCD units, one should connect the output of the Monitor point to an oscilloscope and adjust the switches such that the majority of the x-ray signals are within 0.5 to 2V range.

- (2) The time range in both 2145 TAC should be 2 ms (20 ns x 100).
- (3) Jumper settings inside 8715 ADC is referenced to p. 23 in 8715 ADC user manual, the setup with 556 AIM.
- (4) The gain on both ADC should be at 4K; according to the range setting in the data acquisition software, choose range on each ADC accordingly. Data is collected in PHA mode to generate histograms. ADCs need $\pm 6V$ NIM.
- (5) There should be a 50 Ω terminator on one end of BNC which connects the transceiver box in the back of 556 AIM to the computer network card. Another 50 Ω terminator should also be used in the other end of this BNC.

2.3 Data Acquisition System

2.3.1 Overview of the system

The VAX/VMS (and a machine) ND9900 Multiparameter Acquisition System consists of ND9900 multiparameter multiplexer, ND556 AIM networked acquisition interface, and a software in workstation which can generate dual parameter display.

The basic flow of information is as follows:

- (1) Analog signals from detectors trigger conversions on the ADCs.
- (2) The multiparameter multiplexer decides whether the required coincidence conditions have been met; if so, it reads the data from the ADCs and generates a event packet.
- (3) The ND556 AIM interface on an Ethernet network tells the system CPU that its buffer had filled and the buffer is read out.

(4) Workstation system uses a software-generated spectral display.

After correct cabling, turn on the power switch on the crate, and login as "user" on milken. First thing is to check if network interface device is communicating with computer by typing:

Config/device

Apart from a list pseudo-ADCs, there should be a device name begin with "NI...". This should be the Ethernet address in the front of ND556 AIM. Also the green light "OK" in the front of the AIM should lit up steadily after initial checking and testing. If nothing like this happens, go back to check cable connection and terminators, as well as the crate power supply (need ± 6 V).

The command procedure DO_2X10.com can be used to display old data and collect new data. This is a modified version on the example file NDMPA_EXAMPLES:DO_DP_DEMO.COM, which was made to suit our detector application. It will create three configuration files: DP1, MONITOR1 and MONITOR2. For dual parameter display, DP1 is the histogram of the first parameter vs. the second; MONITOR1 is the histogram of the first parameter alone; MONITOR2 is the histogram of the second parameter alone.

2.3.2 Taking live data

We can use Do_2X10.com to histogram dual parameter data coming from an acquisition interface. The hardware needs to be set up as follows:

- (1) The outputs of two ADCs must be connected to the ADC1 and ADC2 inputs of the multiparameter multiplexer by ribbon cables;
- (2) The LIST output of multiplexer must be connected to either port of an AIM.
- (3) The setup of multiplexer must be as follows:
 - a. MPA mode to "2".

- b. INHIBIT to "REJ".
 - c. EXT+/INT/EXT- to "INT".
 - d. COMB/ANY/PAIR to "PAIR".
 - e. Switch 1 and 2 "ON"; 3-16 "OFF".
 - f. Set the Window control in the center of the scale.
- (4) Set the ADC switches to "COIN" and "ACQUIRE".

As for signals to test the acquisition system, using a single detector and amplifier; feed the output of the amplifier into both ADCS.

Now issue the command:

```
@Do_2X10
```

There will be a question of " where do you get the data". Answer the question with the Ethernet address in the front of AIM. For example, if the address is 6E2, and the list output of multiplexer is connected to port 1 on AIM, type

```
NI6E2:1
```

Configuration DP1 is created then in the Do_2X10.com procedure as following:

```
MCA create DP1 NI6E2:1/CH=64/ROW=256
```

This will create a data distributed in 64x256 dimensions, which is the closest simulation of the detector window 2x10.

If there is no dual parameter display window pop up on the screen, go to menu bar "Spectroscopy Assistant" to open up "file" under "detector": "DP1","MONITOR1" and "MONITOR2". The activity lights on the ADCs and multiplexer should be turned on after the program started, and with luck, data start to appear in DP1, MONITOR1 and MONITOR2.

To stop experiment, click on "Acquire off" on the display window, and use "save as" to save data. The data is an ASCII file, and can be viewed by command "list".

Further use of the programming of this system is referenced to User's Manual of ND9900 Multiparameter Data Acquisition System.

References

- 2.1 Smith, G.C., Yu, B., Fischer, J., Radeka, V. and Harder, J.A., *Nuc. Instr. Meth.*, **A323**, 78 (1992).
- 2.2 Smith, G.C. and Yu, B., *IEEE* , **42**, 541 (1995).

**ERNEST ORLANDO LAWRENCE BERKELEY NATIONAL LABORATORY
ONE CYCLOTRON ROAD | BERKELEY, CALIFORNIA 94720**